MULTIPATH AND GPS

C. BOSLOPER

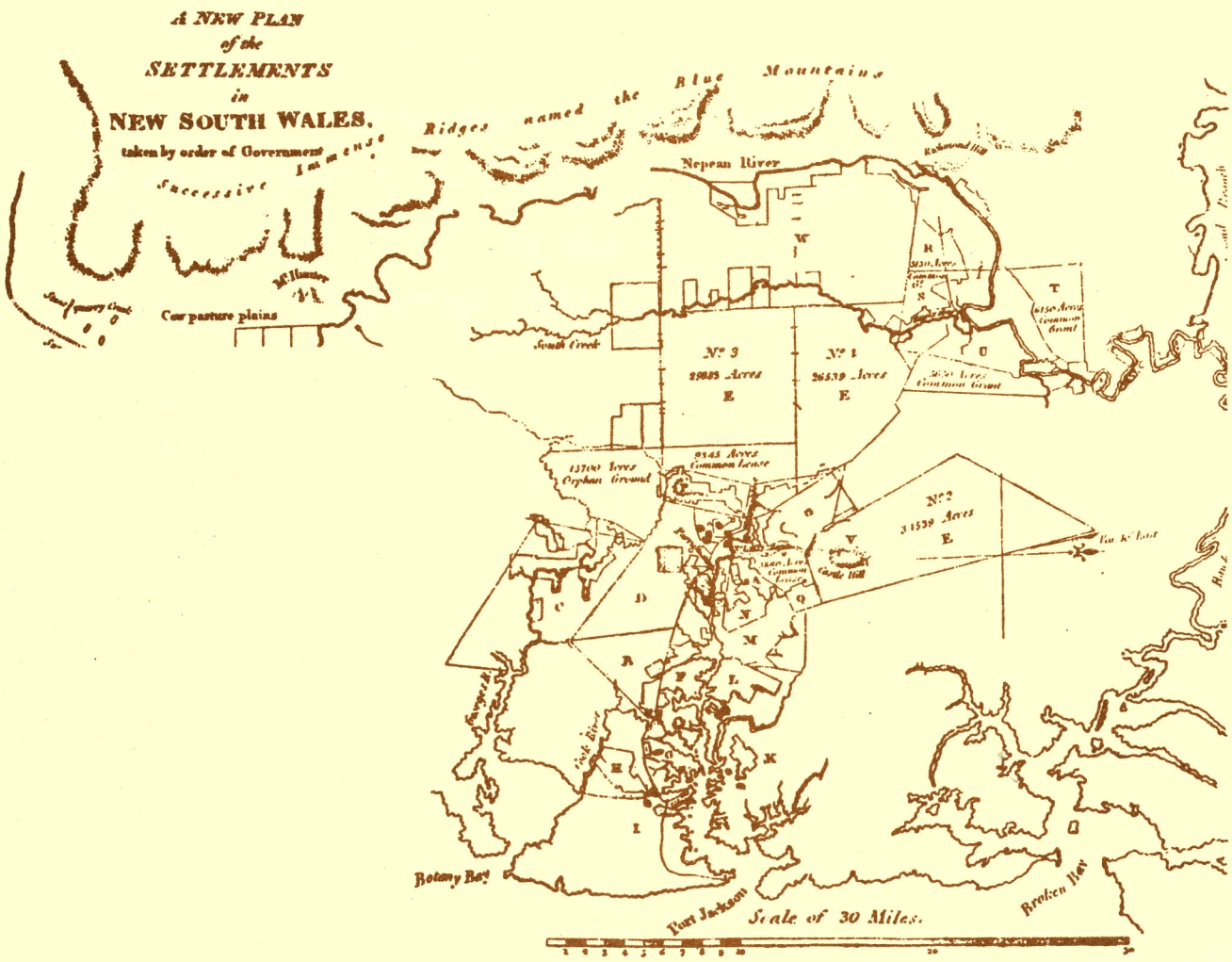

UNISURV S-39, 1990

Reports from

SCHOOL OF SURVEYING

THE UNIVERSITY OF NEW SOUTH WALES KENSINGTON, NSW AUSTRALIA 2033

UNISURV REPORT S-39, 1990

MULTIPATH AND GPS
Short Periodic Components of the Time Variation of the Differential Dispersive Delay

C. Bosloper

Received: November, 1990

SCHOOL OF SURVEYING
UNIVERSITY OF NEW SOUTH WALES
P.O. BOX 1
KENSINGTON N.S.W. 2033
AUSTRALIA

National Library of Australia

Card No. and ISBN 0 85839 057 4

TABLE OF CONTENTS

ABSTRACT

The multipath error in differential GPS positioning is reviewed. An indicator is developed for the estimation of the averaging time for observations from an individual satellite, required for the selection of the optimum observation duration of a session. This indicator, called the multipath index, makes use of the knowledge of the elevation angles of the satellites and their rates of change. A model is developed to describe reflection from an idealised point source, rather than specular reflection from a flat surface used in the classical model. This opens the way for utilising a vector of point sources or a matrix of point sources, permitting a better modelling of the antenna environment than with the classical model. Five hours of TI 4100 data, observed in a reflective environment, are analysed for multipath. Data of seven satellites observed at two sites of a 150 kilometre baseline on two consecutive days are used and the results are presented. The techniques used for the study include an analysis of the time variation of the differential dispersive carrier phase and pseudorange delay, by use of cross-correlation and spectral density functions. Another technique used is across-day averaging and differencing followed by a comparison of the relevant spectral density plots. Multipath simulations are carried out and are able to explain the variations occurring in the actual observations. Multipath simulations provide an effective tool for multipath analysis. Design parameters are suggested for an antenna adapter which will be able to measure the position errors caused by a long-periodic multipath effect, making use of small antenna shifts. Practical recommendations are given which help to reduce multipath in GPS observations.

1. INTRODUCTION

This study looks at one of the major remaining error sources in the geodetic use of the Global Positioning System (GPS), namely the cyclic carrier phase error caused by multipathing of the signal. The investigation is based on the analysis of the short-periodic components of the time variation of the differential dispersive delay on consecutive days.

Some specific definitions used in this thesis are in accord with current literature: the term **dispersive delay** will be used with the meaning of across-frequency carrier phase pathlength difference; the term **differential dispersive delay** will be used with the meaning of across-site across-frequency carrier phase pathlength difference. Both phase observables used to calculate the dispersive delay are scaled to units of length using the appropriate wavelengths.

In order to further explain these terms, a brief overview of the GPS system is given first. The GPS is a satellite based positioning system which gives the user a real-time point positioning capability to navigation accuracy, as well as allowing him to determine relative positions to accuracies as high as one tenth of a part per million and better (Bock, 1986a). A minimum of four satellites need to be visible simultaneously. This will be the case 24 hours a day and in all weather conditions, once all satellites are in place. At present the satellite constellation is not complete, resulting in restricted daily measurement windows for positioning to geodetic accuracy. Different windows apply to different parts of the world. The daily window has a fixed orientation in a sidereal reference frame. The satellites are in exact twelve hour orbits. Thus the window advances by four minutes

each day, repeating the satellite to receiver geometry after one sidereal day. Two carrier frequencies, L1 (1575.42 MHz) and L2 (1227.6 MHz), are transmitted by the satellites. The corresponding wavelengths are 190.3 mm and 244.2 mm. Some receivers use both, some use only L1. On each of these carriers a precise time transfer code, the P-code, is modulated. The L1 carrier is also modulated with a coarse acquisition code, the C/A-code. The use of the C/A-code, also called the standard access code, is less accurate than the use of the P-code and allows a cruder form of ranging. Its main use is to facilitate the acquisition of the signal in order to gain access to the "hand-over word" so that one can then use the P-code. With the P-code, precise navigation is possible in real-time at the 10-metre level. A navigation message with satellite ephemeris information can be read from the modulated carrier.

Geodesists require a much higher precision. Geodetic receivers get their accuracy by using the carrier itself, instead of the codes modulated upon it. The phase of the received Doppler shifted carrier is measured with a precision of two millimetres. This is achieved by, for example, multiplying the received code signal with delayed versions of a receiver generated identical code signal and subsequently achieving code correlation with the help of a delay lock loop (Refer to Chapter 5).

As microwave beams are not as directional as light beams it is possible that the received signal has components that have followed an indirect path (Refer to Chapter 2). This multipath effect will corrupt the range measurements. In Chapter 7 it is shown that the multipath effect impresses error signatures upon the data that are different for L1 and L2. Differencing the phase observables across frequencies can thus result in a multipath caused beat pattern. A form of across-frequency difference is already used in GPS analysis as a measure of the total electron content along the line of sight to the satellite. It has received the name "ionospheric delay" or, more general, "dispersive delay". The current

study shows that a considerable part of the changes in this across-frequency phase difference is caused by multipath.

The relative positioning accuracy of the GPS system is mainly restricted by ionospheric effects (phase advance and group delay), tropospheric and multipath effects. The rest of the error sources are all practically eliminated through differencing. In order to explain the approach taken in this study of multipath, the above mentioned terms need to be even more clearly defined. The dispersive delay is the difference, in units of length, between the delays of the L1 signal and the L2 signal. It is calculated by taking the difference between the scaled phase observable on the L1 frequency and the scaled phase observable on the L2 frequency, after converting each to units of length. This is the difference that is normally used as an indication of changes in the total electron content (Refer to Appendix B). The dispersive delay at a nearby station will almost be the same and the changes in each will be highly correlated. But the dispersive delays at each station are not necessarily identical. Differencing across sites will eliminate the common part of the delay, but will leave a residual part of the delay, often called the differential dispersive delay, or the differential ionospheric delay as in Georgiadou and Kleusberg (1988) and Kleusberg (1986). In short, the differential dispersive delay is the across-site difference of the dispersive delay.

The dispersive delay (the scaled phase difference between L1 and L2) can not be easily separated from multipath effects. In fact Georgiadou and Kleusberg (1988) point out that the dispersive delay is usually erroneously interpreted as solely caused by ionospheric effects and this assumption is used in the formation of the ionosphere-free observable and the ionospherically corrected observable. The inverse squares of the frequencies are used in this correction. However, a large part of the dispersive delay can also be due to multipath. The authors warn that correcting it as solely ionospherically caused, will lead to biased results.

Thus the terms "dispersive delay" and "differential dispersive delay" used in this thesis will be employed to indicate the way the observables are calculated and not the way they are caused. When referring to the underlying physical phenomena, I will distinguish between the ionospheric component and the multipath component of the differential dispersive delay, where necessary. But as far as possible and where clarity is necessary, the more cumbersome terms of across-frequency carrier phase pathlength difference and across-site across-frequency carrier phase pathlength difference are used. An effort to symbolise these through the text has been made by using the symbol # which can be imagined as composed of two f's for frequency minus frequency. The "across-epoch, across-site, across-frequency carrier phase pathlength difference" $\delta\Delta\#\#$ then clearly differs from the popular triple difference symbol $\delta\Delta\nabla\phi$ for the "across-epoch, across-site, across-satellite phase difference".

When the time series of the between-frequency differenced and across-site differenced delay is differenced across consecutive epochs, the time variation $\delta\Delta\#\#$ of the differential dispersive delay is obtained. All common effects are eliminated (Refer to Chapter 7) as well as the long periodic components of changes like ionospheric effects. The short periodic fluctuations, thought to be mainly caused by multipath, are highlighted.

Some TI 4100 data observed as part of the NSW GPS net (Dickson 1989) have been analysed for multipath. A 150 km baseline has been chosen featuring a highly reflective rooftop environment at one end and a bald and obstacle free hill at the other end. Three and a half megabytes of data from each station, covering about five hours, were used for each of two consecutive days (Refer to Chapter 9). This total of 14 megabytes of 3-second sampled data were cleaned and compressed to 30-second data by the preprocessor of the programme "DIPOP Version 2.0" (Santerre et al, 1987). Subsequently the data were differenced across frequencies,

sites and in some cases across epochs and days. After these manipulations the data were studied using cross-correlation and spectral density analysis techniques (Refer to Chapters 10 and 11).

Two multipath simulation studies are also included (Refer to Chapter 12). The first one builds a discrete and deterministic Fourier series from given periods and amplitudes, in order to study the time series plot of the resultant error signature as well as to study the spectral density. The second simulation models the fact that the satellite elevation is changing all the time at a varying rate and forms a discrete series of amplitudes at varying periods, using actual predicted satellite azimuths and elevations. In this simulation, a model is developed for a general type of reflection that describes a hemispherical reflection from an idealised point source or an edge diffraction (Refer to Chapter 8) and where specular reflection is modelled as a special condition. This simulation required a knowledge of the satellite azimuth and the azimuth of the assumed source of reflection. The satellite azimuth and elevation predictions were obtained as a by-product of commercial sky-plot software.

Chapters 2, 3 and 4 outline the multipath problem, Chapter 5 shows the way the problem is approached and Chapter 6 gives an overview of the literature on the general subject of multipath problems in accurate surveys. Chapters 7 and 8 show how to detect and quantify the multipath effect. Chapters 9, 10 and 11 analyse the multipath signature in an existing data set. Chapter 12 analyses some multipath simulation studies. Chapter 13 gives conclusions and makes a series of recommendations aimed at a reduction of multipath effects. Appendix A introduces some of the mathematical tools used in the analysis, Appendix B studies the ionosphere-free observable in the context of multipath and Appendix C describes the data preprocessor used.

2. MULTIPATH AS A PHENOMENON

Tranquilla (1985, p.557) describes multipath as a phenomenon brought about by reflective surfaces entirely decoupled from the antenna, resulting in a relative phase offset between different radio waves that arrive at a receiver, because they followed several possible routes although they had a common time origin. One can say the multipath error signature is caused by the interference between the direct and the reflected signals. If the reflected signal is of the same power as the direct signal, total fading alternated by moments with double signal power can be expected. The indirect signal strength could be larger again if there were multiple sources of reflection but, in general, the reflective surface absorbs part of the signal and the receiver antenna often has less gain closer to the horizon.

Multipath could, in principle, be reduced by increasing the radiating surface of the transmitting antenna, in order to reduce the beam width. Another approach would be to increase the directivity of the receiving antenna, towards a particular satellite. Both these solutions are useless in the case of the GPS, as the transmitter has to broadcast to many receivers and the receiver has to utilise the signal of various satellites. An increase of the frequency will also reduce the beam width and decrease the number of surfaces that are reflective. Too high a frequency brings about absorption problems through the atmosphere, like the water vapour effect (Benz, 1970 and Hagger, 1967). The frequency of about 1.5 Gigahertz used is a compromise: lower frequencies would be subject to larger ionospheric delays accompanied by a larger magnetic term. Thus multipath was not the largest concern when choosing the frequency during system design.

Two kinds of multipath have to be considered: satellite and receiver multipath.

2.1 Satellite multipath

Satellite multipath occurs when the transmitted signal bounces off from a part of the satellite, before being directed to the earth. By differencing observations to a given satellite between two receivers, most errors originating at the satellite cancel, but not the satellite multipath effect. Different errors at different receivers (Young, 1985, p. 423) must be expected through this effect. Young (1985) assumes the power of this multipath signal to be about 1% of the total transmitted power. There are various possible multipath surfaces on the satellite which can become of importance depending upon the satellite elevation. The simultaneous presence of more than one multipath effect can lead to an increased chance of non-coherence of the interfering signal. This could reduce the multipath problem through cancellation effects. But as the signals have a common time origin, it can also give rise to a beat pattern with a larger amplitude than what an individual reflection can account for (Refer to Chapter 8).

An important feature of a reflected signal is the change in the signal polarisation from right hand circularly polarised to left hand elliptically polarised (Refer to Chapter 5). A circularly polarised wave has components that are equal in amplitude and at quadrature in phase. An elliptically polarised wave has components that are unequal in amplitude and that have different phases. The receiver's right hand circularly polarised antenna will partially reject the left hand elliptically polarised signal and so reduce its relative strength.

As the satellite's solar panels track the sun, the satellite slowly rotates around its centreline through the course of a year, while it keeps its antenna array pointed to the earth's

centre. If the satellite multipath effect needs to be quantified, the measurements to a given satellite should be repeated at different times of the year. The satellite multipath effect is expected to be a few centimetres, for baselines of a few hundred kilometres (Young, 1985, p. 432).

2.2 Receiver Multipath.

If one looks around on a sunny day, apart from direct sunlight one will generally see many reflections of sunlight. For example the reflection from a section of the corrugated iron roof of a nearby shed, the reflection from a distinct spot on the side of a passing car, a reflection from the curved back window of a parked car (which seems to be visible from a lot of different angles), a reflection from the zinc cladding along the bottom of a chimney upon a house, the glare from the side cladding of another house and the glare from bitumen on the road and from the sand on a dirt track. With passage of time the intensities change depending upon the angle to the sun.

With radio waves from a satellite similar reflections occur simultaneously at a number of reflective surfaces. Some of these radio wave reflections are in phase with the direct waves at particular moments. Each site will have its unique environment of reflective surfaces; some sites will have almost none whilst other sites have a multitude. In Chapter 9 it is shown how advantage is taken of this between-site difference in reflectivity.

The effect of reflectivity on the received signal power depends upon the geometry of the transmitter, receiver and reflector and is unique for each site and satellite combination. As the satellite moves across the sky, the pathlength difference changes and an alternating fading and enhancement of the signal results, with a period dependent upon the carrier wavelength, the satellite elevation, the elevation rate and the geometry of the relative positions of the satel-

lite, reflective surfaces and the receiver. In radio astronomy it is known as the effect of "ground clutter" (Sukumar et al, 1987). What constitutes reflectivity is determined by the relation between the wave length and the roughness of the surface. In remote sensing one refers to Rayleigh's criterion: specular reflection occurs when the apparent heights of the surface irregularities **H** (corrected for look angle) are smaller than one twentieth of the wavelength and diffuse reflection occurs when these irregularities are larger than a quarter of the wavelength. The correction of the irregularities **H** for the look angle occurs by projecting their height onto the incident ray. In Sukumar et al (1987) the ratio between the power incident on a reflective surface and power reflected from the surface is given by:

$$\frac{P_r}{P_d} = \exp\left[-2\left(2\pi\frac{H}{\lambda}\right)^2\right] \qquad \textbf{(2.1)}$$

where P_r/P_d is the power ratio, valid for specular reflection from a rough surface,

H is the standard deviation of the roughness of the surface,

λ is the wave length.

This relationship indicates, when substituting **1/4** λ and **1/20** λ for **H**, that Rayleigh's criterion for an incident angle of zero degrees from zenith gives a one percent power ratio and below for the case of diffuse reflection and a 82% power ratio and above for the specular case. Between these two criteria lies a continuum where specular reflection changes into diffuse reflection.

Microwaves have a penetrating capability through dry soil of the order of a few wave lengths. A soggy spot just below the surface could be highly specular. As well as this, microwaves see obstacles that are progressively smoother than a quarter wavelength as increasingly specular and chicken wire with mazes of 10 mm would be perceived as a mirror for the L1 and L2 frequencies of GPS. A roof surface with coarse pebbles of 20 mm could be a fairly specular antenna environment for L2

Surface roughness	P_r/P_d		L2/L1 Power ratio
50 mm	L1	0.004	10:1
	L2	0.036	
37 mm	L1	0.05	3:1
	L2	0.16	
25 mm	L1	0.25	1.5:1
	L2	0.44	
12 mm	L1	0.73	1.2:1
	L2	0.84	
6 mm	L1	0.92	1.03:1
	L2	0.95	

Table 2.1 Surface roughness effect upon relative power ratio.

(1227.6 MHz) while it could be perceived as somewhat rougher by L1 (1575.42 MHz) (Refer to Table 2.1). In this case one could get an appreciable multipath signature from L2, but less from L1.

Generally, the phase of a horizontally polarised wave is reversed upon reflection (Shibuya, 1987, pp.196-197). A vertically polarised wave undergoes no phase reversal if the sum of the angles of incidence and reflectance is smaller than 90 degrees (Livingston, 1970, p.22).

A reflection originating from the edge of the first Fresnel zone will be a half wavelength out of phase with the direct signal and will cause fading. In microwave communications specular reflection and knife-edge diffraction are well known phenomena (Bachynski and Kingsmill, 1962; Livingston, 1970; Shibuya, 1987) and the ensuing signal interference is minimised by choosing a propagation path with first Fresnel zone clearance. Shibuya (1987, p.241) describes knife-edge diffraction as diffraction off a theoretically infinitely thin screen-shaped radio wave barrier which extends infinitely downwards and transversally. In the GPS situation it is unavoidable that objects (like the ground surface) are at times within the first Fresnel zone.

In order to obtain a feel for reflection effects a few examples were considered. When a satellite is close to zenith the azimuth can change as rapidly as 80 degrees per hour, but at lower elevations an azimuth change of 20 to 40 degrees per hour is more likely. Table 2.2 shows satellite elevation changes of an average 25 degrees per hour with a range from 40 degrees to zero degrees per hour, depending on the satellite's sky track.

A sufficiently smooth ground surface (like in a rooftop situation) can be seen as a large reflector by the antenna, limited only by the masking effect of the antenna's ground plane. Edge effects of the ground plane (Tranquilla, 1986) can make this masking effect less effective (see Fig. 4.6). If the rooftop is, say, six metres in all directions and the antenna height is 1.5 metres, the whole sky above 15 degrees mask angle can be seen specularly by the aerial, except for the limitations imposed by the effectiveness of the ground plane (Figure 2.1).

Satellite elevation	El. rate deg/hr	Hor. mpth. index (min*m)	Vert. mpth. index (min*m)
41.1	29.1	14.9	17.1
46.0	28.2	16.7	16.1
50.5	27.6	18.6	15.3
55.2	26.7	21.4	14.9
59.4	24.0	26.7	15.8
63.2	19.8	36.6	18.5
66.0	12.3	65.3	29.1
67.3	3.9	217.1	90.8
67.3	-5.1	166.0	-69.5
65.6	-12.6	62.8	-28.5
63.1	-18.6	38.8	-19.7
59.4	-23.4	27.4	-16.2
55.3	-25.2	22.8	-15.8
51.0	-27.0	19.2	-15.6
46.3	-28.5	16.6	-15.9
41.5	-27.6	15.8	-17.9
37.1	-27.3	15.0	-19.8

Table 2.2 Multipath periods as a function of elevation variables (Satellite 8, 12-9-87, 9:20 to 12:00 UT in 10 minute intervals). Multipath is denoted by mpth.

Table 2.2 shows typical multipath periods for horizontal and vertical reflective surfaces: the information of a 12 September 1987 pass of Satellite 8 has been used. The second column lists, at ten minute intervals, the rate of change of the satellite elevation. The periodicities in the third and fourth column are inversely proportional to the perpendicular distance to the reflective surfaces and are shown in minutes of time, for a distance of one metre, as a reflective surface multipath index. For example, for a reflection at the ground surface and an antenna height of two metres, these periodicities should be divided by two (the antenna height) and will give periods in minutes. A large change in the multipath period is evident when the satellite reaches zenith or a zero rate of elevation change. In fact, the multipath periodicity goes to infinity (Refer also to Table 12.1), leading to a bias in the phase observable for the duration of time that the elevation rate is zero. The passing through zenith is an instantaneous event, leading momentarily to a mathematical singularity through a division by zero. The calculation is derived in Chapter 8, using the classical multipath model, as proposed by Georgiadou and Kleusberg (1988).

Reflections of vertical surfaces don't cover such large areas of the sky. These surfaces must be higher than the antenna height by more than a quarter or one sixth of their distance to the antenna, in order to reflect anything above a 10 degree or 15 degree mask angle. The solid angle in which the antenna phase centre sees the reflective surface is equal to the solid angle that the reflective surface cuts out of the sky, forming a window from where reflections can originate. It would be possible to draw an azimuth and elevation window on to a skyplot in response

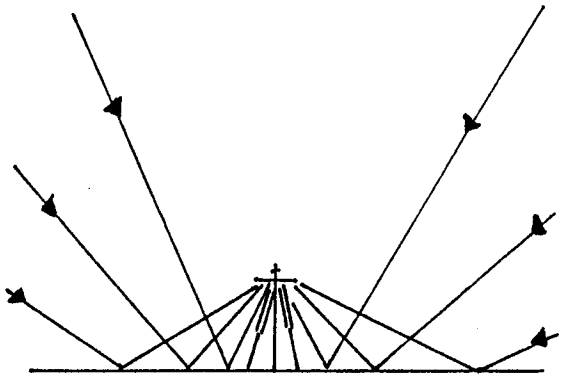

Figure 2.1 Reflection off a horizontal surface.

to the angular cross section of each reflector. The azimuth and elevation prediction of each satellite will then help to identify a period of multipathing danger, by showing when the satellite moves through this reflective window.

If the angular cross section, projected onto the sky by the reflective surface, is about 1/3 of a radian (in linear terms the cross section is then 1/3 of the distance to the reflective surface) and if a satellite tracks through this window at about 1/3 of a radian per hour (about 20 deg/hr), specular reflection can be expected for about one hour. The height of the vertical reflective surface is important. A vertical reflective surface six metres away with a one metre diameter has a cross section of 1/6th of a radian. Its top has to be at more than 1.5 metres above the antenna height at this distance to have a part of the sky above a 15 degree mask angle reflected at all. With a satellite moving through the reflective window at a rate of 20 degrees per hour this surface would only reflect specularly for about half an hour.

3. MULTIPATH AS A PROBLEM

In electronic distance measurement signal multipathing produces a constant excess path and its effect can be evaluated and averaged out. In GPS the excess path caused by multipath is ever changing and different for each individual satellite. This chapter looks briefly at the problems caused by multipath with respect to the following points: the total system noise, kinematic type surveys, precise surveys (as for crustal motion studies), biasing of baseline results, biasing of the ionospheric correction, cycle slip detection and ambiguity resolution.

3.1 Noise

The receiver-only noise has been shown to be 2 to 3 millimetres (Evans et al, 1985). Coco and Clynch (1986) even conclude that it could be as low as 0.7 millimetres. Other error sources are successfully eliminated through across-site and across-satellite differencing. The multipath effect can add short periodic (and long periodic) noise to the system. Thus the total noise will range from just above the receiver noise to the maximum error (as shown in Chapter 8) caused by multipath of 48 mm (L1) and 61 mm (L2), when a single reflective surface is present. In the case of multiple reflective surfaces (Refer to Chapter 8) the upper level of the multipath "noise" can be twice that after which the effect influences the ambiguity resolution. Some thoughts with regards to the long periodic multipath effects will be further elaborated in Sections 3.4 and 3.5.

3.2 Kinematic Type Surveys

The multipath periodicities generally range from a few minutes to tens of minutes (see Table 2.2 in Chapter 2). When carrying out kinematic surveys (or pseudo-kinematic surveys) it is most likely that the time span of the observations per

point is not long enough to average out long periodic multipath effects and, possibly, not long enough to average out short periodic multipath effects. Biases up to the order of magnitude mentioned above can therefore be introduced. The horizontal and vertical multipath indices of Table 2.2 in Chapter 2 and Table 12.1 in Chapter 12 give an indication of the necessary observation period required in order to capture one full multipath period for various distances to reflecting surfaces. The distinctive geometry of each satellite's relationship with reflective surfaces near the receiver antenna will produce a unique set of multipath periodicities for the particular pass of the satellite. These determine the optimum observation duration necessary in order to average out the multipath effect.

3.3 Precise Surveys as for Crustal Motion Studies

When surveys are repeated over long spans of time (e.g. crustal motion surveys), it is unlikely that the same satellites can be used. This means that different multipath signatures during the different re-surveys will bias the result. If the intention is to repeat the measurements in a shorter time interval (e.g. years rather than tens of years), the chance is greater that the same satellite configuration is still in existence. In this case the observations need to be carried out with a higher level of accuracy. When aiming at the highest accuracy, the multipath error becomes the limiting factor. This is mitigated by the fact that only the change in position and not the absolute position needs to be established. The multipath error can be tolerated if it can be made to repeat when the re-survey is carried out.
When the measurements are not repeated under the same satellite configuration, multipath can bias the results. Either the expected crustal motion should be large enough, by the time of the resurvey, to reach a level of statistical significance by which one can separate it from other noise and multipath influences, or the measurements should include a method to model, measure or eliminate the multipath effect.

3.4 Biasing of Baseline Solutions

The long periodic multipath effects with periods varying from 10 minutes to hours have the potential to bias the results when the observation duration is less than the multipath period. Of course, the intensity of each reflected ray will be attenuated to a certain degree by the properties of the reflective surfaces. Long periods arise during two situations, namely when the satellite reaches its culmination in elevation and exhibits an elevation change rate of zero for a while and when the satellite elevation becomes very large, close to zenith. Both the transit through zenith and the reaching of culmination at any elevation, lead to a theoretical multipath period of infinity. This causes a constant bias for a particular length of time. Multipath has a time varying period, depending upon azimuth and elevation (see Chapter 8) of the satellite. This leads to a phase shift in the multipath affected received satellite signal which not only has a particular but also an ever changing period. The consequence is a changing offset in the result which can not be solved for, but has to be either modelled, averaged out or measured.

3.5 Biasing of the Ionospheric Correction

Georgiadou and Kleusberg (1988) warn about the biasing of the ionospheric correction through the multipath effect. Wasseff (1989) also argues that the pseudorange and phase information should both be smoothed over a longer period before either data can be used to derive a more or less valid ionospheric correction. On the basis of the findings of Appendix B it is suggested however that during ionospherically disturbed periods of the solar cycle the ionosphere-free observable can be correct in principle, but during calm periods of the solar cycle the multipath effect and the ionosphere might account for comparable components of the dispersive delay changes. Normally the total dispersive delay and its changes are

interpreted as ionospherically caused and corrected in inverse proportion to the squares of the relevant carrier frequencies. This will result in a biasing of the results (Georgiadou and Kleusberg, 1988, p.178), unless the multipath component of the dispersive delay is in some way accounted for. During calm periods of the solar cycle it is probably better to use an ionospheric model rather than the dispersive delay to derive an ionospheric correction.

3.6 Cycle Slips and Ambiguities

Multipath, when causing extreme amplitudes in the phase values, can confuse the cycle slip detection procedures. This occurs especially in the presence of multiple reflecting surfaces. Cycle slip detecting procedures often use the widelane observable (Refer to Chapter 7) by subtracting the phase values of each carrier, in order to obtain an observable with an 862 mm wavelength. The two phase values are affected differently by multipath, which can lead to severe distortions of the widelane observable. Cycle slip detection methods often assume a linear phase velocity between successive epochs of observations (Lachapelle, 1987, p.150). Multipath corrupts this linearity and in extreme cases could be interpreted as a cycle slip. Cycle slip detection procedures also often use an ionospherically corrected observable for data validation through curve fitting. The ionosphere-free and the ionospherically corrected observable can be made useless by a strong multipath contaminant, as argued in Section 3.5 above. Coco and Clynch (1986, p.417) show that half the loss of lock instances during observations come about through multipathing of the signal causing total signal fade out. They conclude this by finding a repeat of this loss of lock one sidereal day later.

In summary, there are many reasons why multipathing of the signal causes problems in the baseline results. This thesis shows how this problem can be attacked from various angles.

4. SEPARATING MULTIPATH FROM OTHER EFFECTS

4.1 Phase Centre Variations

The prime observable in precision applications of the GPS is the phase of the L1 and L2 carrier measured at the receiving antenna. According to Tranquilla (1988) the standard that has been set for the accuracy of the phase measurement is about ten degrees or 10/360 x 200 mm, which is equal to 5 to 6 mm. This means that the phase characteristics of the receiving antenna should not deviate more than about five degrees each way from the ideal pattern produced by an isotropic point source (Fig. 4.1), when considering the near hemispherical phase pattern above a 10 or 15 degrees mask angle.

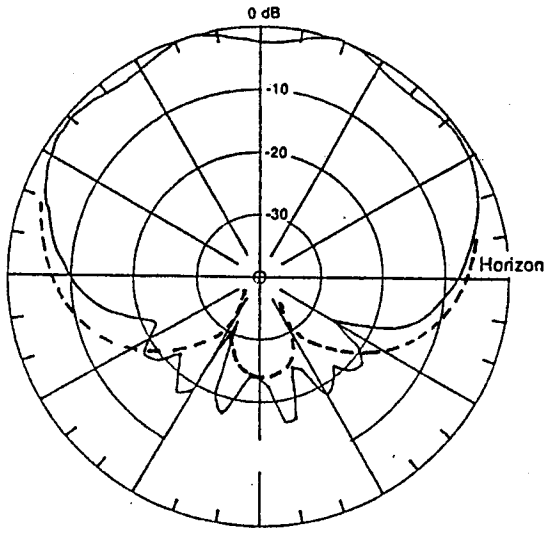

Figure 4.1 Antenna phase pattern (after Tranquilla, 1988).

For high accuracy surveys, the antennas should be calibrated and corrections applied at those azimuths and elevations where the antenna does not meet the criteria for the required survey accuracy. Severe constraints upon the phase pattern are imposed by the null forming near the antenna horizon, which is needed to cut out the influence of multipathing caused by general ground clutter. The effects upon the phase pattern are different for L1 and L2, so the antenna should be calibrated separately for each frequency. The maximum effect is of the order of 10-20 mm (Sims, 1985, p.229).

Sims describes the antenna calibration in detail. In a controlled environment the antenna is mounted at a certain distance from a transmitting source and rotated 90 degrees each way while phase measurements are taken.

The phase centre of a receiving antenna is described by the principle of reciprocity (Tranquilla, 1986, p.558). In the case of a transmitting antenna, the phase centre is the apparent source of radiation. The same antenna used as a receiving antenna will have identical phase centre properties. The radiated phase front is examined and the centres of curvature are calculated by the tangent-sphere technique. Only an ideal point source will give a spherical phase front. Normally, in the case of a finite radiator, the phase front is dimpled and distorted and thus non-spherical. Different arc segments of the equiphase contours will have different apparent centres of curvature. The phase centre can be described as a function of the observation angle, namely the angle of incidence of the satellite signal. The smoother and more spherical the radiated wave front is, the smaller the phase centre changes will be for these various angles of incidence. A high gain (directional) antenna gives a distorted phase front, achieved by constructive interference with another part of the antenna, which is often called a reflector or a ground plane. Deep nulls in the amplitude pattern are often a feature of high gain antennas. Extreme phase centre movements can occur with such antennas. As the GPS receivers need to acquire various satellites simultaneously, steered directional antennas are unsuitable. The antennas used are fixed antennas with a near hemispherical phase pattern above a certain elevation and with very low gain.

Stationary antennas, the phase centres of which move with the angle of signal incidence, exhibit similar effects as moving antennas. The change of the position error due to a moving satellite is a completely different effect than multipath and is entirely due to the antenna phase pattern.

A log spiral antenna at 1 Ghz can have a phase centre movement relative to its zenithal incidence angle (boresight) position of 0.3 metre at 10 degrees elevation (Tranquilla, 1986, p.560). A quadrifilar helix antenna (e.g. Wild-Magnavox WM 101/102) at 1 Ghz, can have phase centre movements of 3 mm at 10 degrees elevation.

In the absence of special measures, the antenna would "see" all the ground clutter below 10 degrees. This would raise the antenna noise level. A sharp cut off at 10° would be ideal but this would introduce very serious phase problems and result in large phase centre movements. Edge effects (Fig. 4.6) make any cut-off less efficient. Such diffraction effects can be reduced by placing an absorber on the ground plane's edge, made of electrically absorbing dielectric material. The requirement of having a low gain response near the antenna horizon is in conflict with the requirement of a stable phase centre.

For a monopole antenna, DeJong (1982) predicted the dependence of the phase centre upon the angle of signal incidence. In DeJong's approach, the variation of the position of the phase centre associated with the angle of signal incidence accounts for the elevation dependent change in phase measured at the antenna's terminals. By conceptually varying the phase centre, a constant relationship is obtained between the phase measured at the antenna's terminals and the phase of the wave front passing through the antenna's phase centre. The geometry is shown in Figure 4.2. The excess phase to be accounted for is ψ:

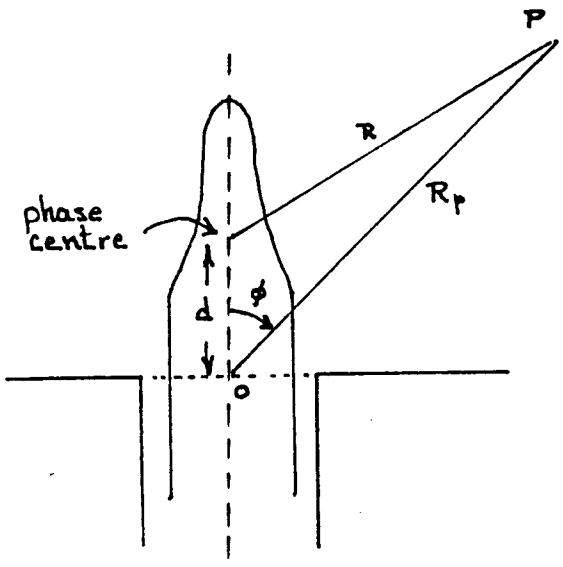

Figure 4.2 The monopole antenna (after DeJong, 1982).

$$\psi = k_o d \cos \phi \qquad (4.1)$$

where k_o is the wave number $2\pi/\lambda$,

d is the distance from the phase centre to the origin (O), which is the intersection of the monopole with the ground plane,

ϕ is the zenith angle of signal incidence,

ψ is the excess phase due to the phase centre position.

DeJong (1982) derives a value for the phase of the voltage observed at the antenna's terminal, in the form of the argument of the complex voltage vector V_R:

$$arg(V^R) = arg(Ai_\phi) + \psi + \frac{\pi}{2} + arg\left(\frac{Z_L Z_{im}}{Z_L + Z_{im}}\right) \qquad (4.2)$$

where V^R is the voltage across the terminals,

A is a complex vector that specifies the amplitude and phase of a plane wave at the origin as well as its state of polarisation,

$i_\phi = \cos \phi i_x - \sin \phi i_z$,

Z_L is a load,

Z_{im} is the input impedance of the antenna,

ψ is the excess phase due to the phase centre position.

The last two terms in the equation are constant. The excess phase ψ describes the dependence upon the angle of signal incidence. Tranquilla and Best (1986, p.741) criticize DeJong's assumption that the phase centre lies upon the vertical axis of the antenna. DeJong concluded this for reasons of symmetry. Tranquilla and Best show that this is not necessary, except at the zenith: only from this angle of incidence do requirements of symmetry demand the phase centre to be on the vertical axis of the antenna (Fig. 4.3). They derive the following relationship between points on equiphase contours, the angle of incidence and the x-axis intercept of the ray to the phase centre (Fig. 4.4):

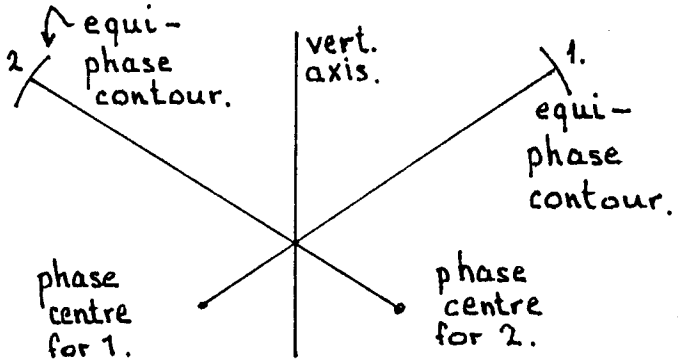

Figure 4.3 The antenna axis and the phase centre position (after Tranquilla and Best, 1986).

$$F(\alpha + \Delta\alpha) - F(\alpha) = d\,k_o[\cos(\alpha + \Delta\alpha) - \cos\alpha] \qquad \textbf{(4.3)}$$

where α is the elevation angle of incidence as seen from the origin,

k_o is the wave number $2\pi/\lambda$,

d is the x-axis intercept of the ray to the phase centre,

F(α) is a point on the equiphase contour.

For each point on the equiphase contour a unique value for **d** will be valid.

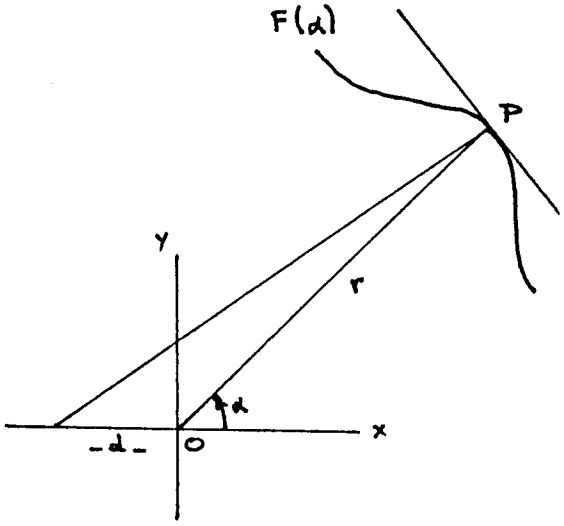

Figure 4.4 The x-axis intercept d of the ray to the phase centre (after Tranquilla and Best, 1986).

Geiger (1988) shows that the actual location of the phase centre is of no importance to the geodesist, who wants to know the range error resulting from the phase centre variation. This can be measured with respect to a mean centre. Geiger gives the following relationship:

$$\delta x = N^{-1} A^T \delta r(\theta,\lambda) + p^T e \qquad (4.4)$$

where **δx** is the position error,

δr is the angle of incidence dependent (carrier phase) range error,

A is the design matrix, expressing the (carrier phase) range as a function of the unknowns,

N is the matrix $(\mathbf{A}^T\mathbf{A})^{-1}$ of weight coefficients of the unknowns, assuming uncorrelated equally weighted (carrier phase) range observations,

$\mathbf{p}^T\mathbf{e}$ is the projection of the phase centre variation onto the ray to the satellite.

This approach reduces the problem to the measurement of the phase difference with respect to a mean phase centre and uses a stochastic approach to account for the departure from rotational symmetries of the characteristics of the tested antenna. Geiger uses a polynomial of sines and cosines and suggests the use of spherical harmonics to calculate the error function.

Geiger's investigations have led to the following conclusions with respect to different types of antennas:
The crossed dipole antenna only produces a constant error in height, the error function is not influenced by the angle of incidence and is thus independent upon the choice of satellite constellation. A calibration of the height offset solves the problem. The conical spiral antenna (e.g. Texas Instruments TI 4100) gives an angle of incidence dependent error in which a $\cos^2$ term contributes most. The quadrifilar helix antenna (e.g. Wild-Magnavox WM 101/102) has a constellation dependent offset with a constant part up to 5 mm and a stochastic part up to 1.5 mm. This aerial has more symmetry in its features than the conical spiral antenna and is thus

less constellation dependent than the spiral antenna. The micro-strip antenna is constellation independent but a constant horizontal offset does occur, so the antenna should always be used in the same orientation.

Dual frequency antennas have generally two phase centres. The movements of these are slightly correlated. Geiger (1988a) finds that there is a synchronisation term to be accounted for and that there is a constellation dependence. The effect of the synchronisation term is below 5 mm, while the rest of the error function is of the order of one millimetre. Geiger notes that the use of identical antennas at both ends of a baseline reduces the total error function.

4.2 Imaging

Ideally the phase centre of the antenna is the centre of the equiphase sphere. The latter is the best fit sphere to the surface of equal phase around the aerial if the antenna is transmitting. Unfortunately the surface of equal phase is generally not a sphere because of the presence of the ground plane, the electrical characteristics of the environment and manufacturing tolerances (Wells, 1986). Antenna imaging is an environmentally induced phase centre variation (Georgiadou and Kleusberg, 1988). This imaging is caused by induction from conducting material in the immediate vicinity of the antenna. The imaging arises through currents induced in the conductor. The antenna becomes electrically part of nearby conducting structures, in other words the antenna electrically couples with the conductor. According to Tranquilla (1986) the antenna forms an image in the conductor and this image contributes to the radiation pattern as if a separate antenna was present.

The resulting radiation pattern is complex. Rapid phase variations occur with changes in the incident angle of the satellite signal. The radiation characteristics are distorted and the surface of equal phase becomes irregular in shape.

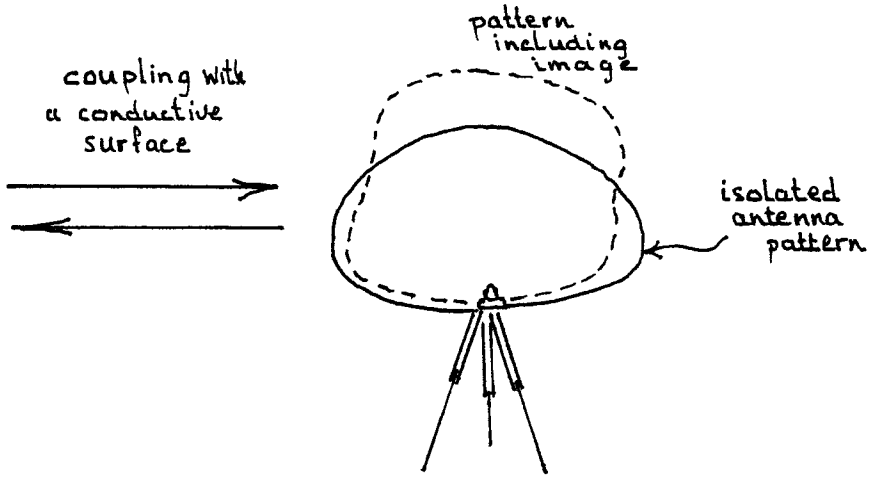

Figure 4.5 Antenna phase pattern distortion through imaging (after Wells, 1986).

The amplitude response pattern is changed (Fig. 4.5). In one instance this is done on purpose as mentioned before: the presence of the antenna ground plane results in lower gain in the vicinity of the horizon and reduces the reception of signals reflecting from below the ground plane horizon. But this is only partially true as shown in Figure 4.6. Edge currents distort this in reality.

The resultant radiation pattern must be considered as caused by the antenna and all its images. Imaging can be modelled as

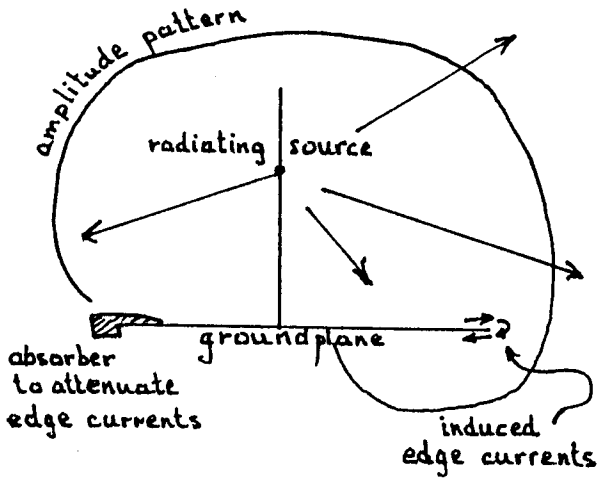

Figure 4.6 Ground plane edge currents (after Tranquilla, 1986).

an array phase centre movement (Tranquilla, 1986). The combined phase front must be considered, namely the interference pattern of all the sources that contribute. These degrade the phase front properties as a function of the angle of incidence of the satellite signal. The effective measurement point on the antenna varies as nearby objects influence the antenna's electrical characteristics. The coupling can be significant if objects are within a distance of about 10 wave lengths or a couple of metres for the GPS. Careful siting of the antenna can diminish the imaging problem.

Like multipath, imaging can not be separated from the data record. Also it can not be averaged out and thus will leave a bias in the measurement. But imaging does repeat itself the next day under the same circumstances for the same antenna-satellite-site-pair. This makes it possible to monitor station position changes with a high accuracy, as the bias is rather constant. Imaging, multipath and phase centre variations are all dependent upon geometry (Georgiadou and Kleusberg, 1988, p.176) and are thus difficult to separate.

As mentioned, rapid phase centre variations at changing incidence angles occur. It has been reported that the phase centre can move in an upwards direction by a decimetre at low incidence angles (Falkenberg, 1988). This degrades the phase centre stability. No results for antenna imaging are yet reported in GPS literature, but the effect is expected to be similar to phase centre variations. Antenna ground plane reflections should also be considered in the context of phase centre variations (Georgiadou and Kleusberg, 1988).

4.3 Multipath Testing in the Presence of Phase Centre Variations and Imaging

As phase centre variations have been shown to range between some millimetres and up to the order of a decimetre, problems arise in separating this effect from multipath which will be shown to cover a similar range. The cautious approach would

be to calibrate the antenna's phase pattern beforehand and apply corrections to the measurements carried out with the antenna. As well as this, sites should be avoided where conductive surfaces occur near the antenna. The multipath effect can then be better studied as the data can be assumed to be reasonably free of phase centre variation and imaging effects.

5. SUPPRESSION OF MULTIPATH

5.1 Multipath Discrimination by Choice of Bandwidth

This section explains what the concept of bandwidth encompasses and demonstrates what tracking is and how this is affected by the bandwidth of the code tracking loop. The question will be addressed whether the choice of bandwidth affects the multipath discrimination of the system. The material is presented by starting with an explanation of the tracking delay lock loop in order to lay the foundation for the quantification of the pseudorange multipath error presented in Chapter 8.2.

The "bandwidth" of a receiver refers to the bandwidth of the band pass filter in the code tracking delay lock loop. The time constant of the tracking loop (which is its integration time) is the inverse of the bandwidth (Hatch, 1986, p.1291). The code and carrier can be recovered when the receiver's reference code has been sufficiently delayed to match the received signal code. This is called "lock on". It can be maintained with slow user motion. Movements and accelerations cause changes in delay which could exceed the capacity of the filter bandwidth. Within the bandwidth the signal is successfully tracked by the delay lock loop. The bandwidth has to be narrow enough so that the bulk of the noise is rejected. Multipath is regarded as unwanted interference. Often the effect is too small to be eliminated and yet too large, to be acceptable as noise. An improvement is obtained in the noise performance of the tracking loop by decreasing the bandwidth, but then the tracking success of the delay lock loop suffers, especially under user accelerations. For this reason the TI 4100 offers a choice of four different bandwidths ranging from 0.7 Hz to 16 Hz, as shown in Table 5.1.

Mode	Bandwidth	Max. Acceleration	Data Rate
UD0	0.7 Hz	0 m/sec^2	3 seconds
UD1	5 Hz	6 m/sec^2	3 seconds
UD2	8 Hz	15 m/sec^2	1.2 seconds
UD3	16 Hz	40 m/sec^2	1.2 seconds

Table 5.1: Receiver bandwidths.

A stationary observer generally uses UD0. One can say that the receiver is tracking when the code correlating loop has aligned the receiver generated code to the signal received from the satellite. Spilker (1980, p.47) illustrates the code correlating delay lock loop, as shown in Figure 5.1.

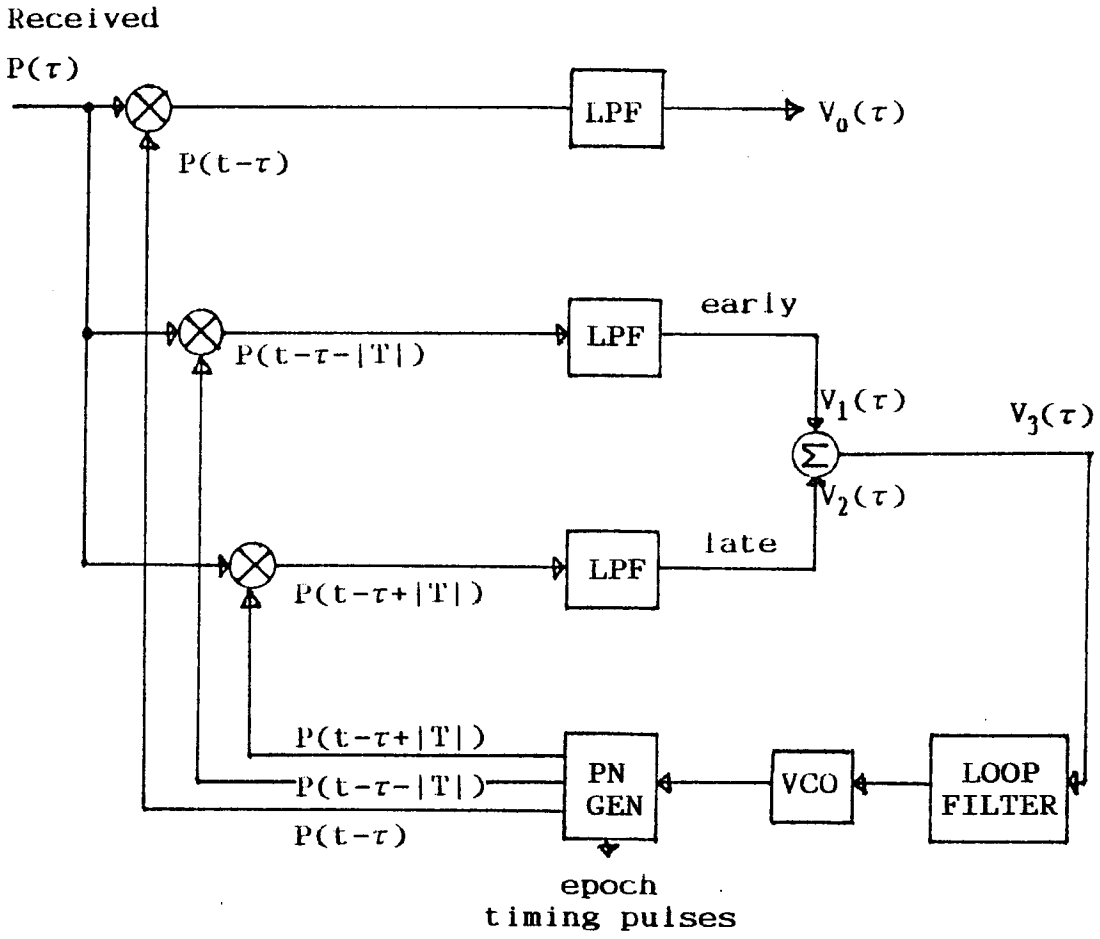

Figure 5.1 The tracking loop (adapted from Spilker, 1980).

The correlator alone can not determine the sign of the delay error of the reference signal and thus can not track the code by itself. A special technique is used instead, making use of a delay lock loop. The satellite signal is split and both components are multiplied with a receiver signal which is respectively advanced and delayed by half the 97.75 nanosecond chipping length. The output voltage of the early delay signal is subtracted from the output voltage of the late delay signal. In the case of perfect lock on, the difference in voltage output will be zero. When the signal goes slightly out of phase, a residual voltage in the early and late delay difference occurs, as the two delay voltages are now not equal (see Figure 5.2).

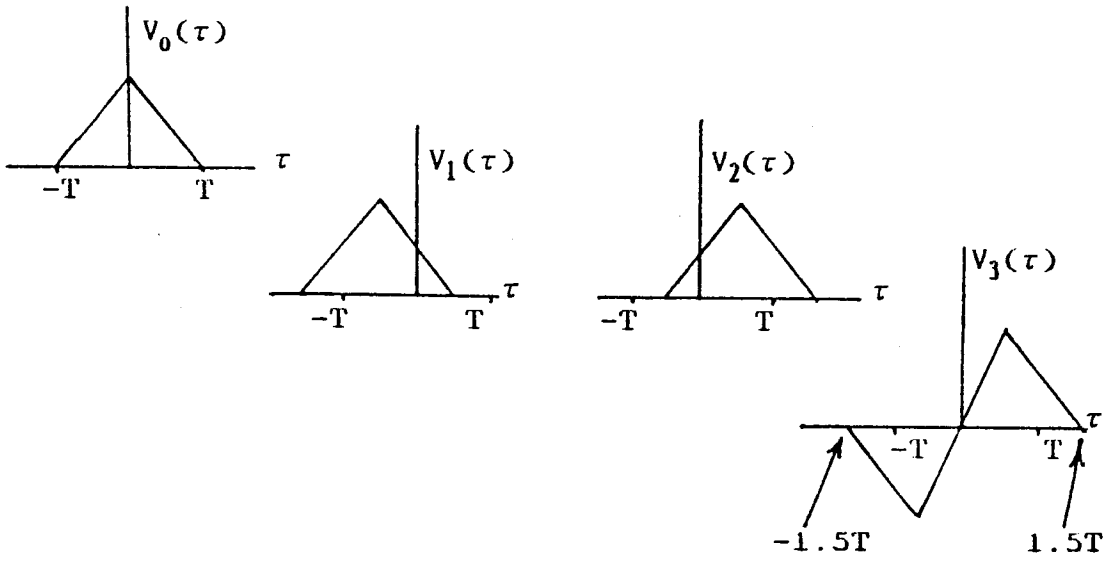

Figure 5.2 The corrective voltage (after Spilker, 1980).

The voltage difference drives a voltage controlled oscillator which speeds up or slows down the pseudo random noise generator in order to maintain lock. In this way "tracking" is achieved. The implementation is shown in Figure 5.1.

Under the following condition code alignment with the received signal is achieved:

$$D(\tau) = [\textit{late delay signal}] - [\textit{early delay signal}] = 0 \qquad \textbf{(5.1)}$$

where **D(τ)** is the early/late delay gate error function.

When signal multipathing is present, code alignment is achieved with the contaminated signal which is the resultant of the direct and indirect signals:

$$D(\tau) = [\textit{late delay signal}] - [\textit{early delay signal}] + \\ + \alpha\,[\textit{multipathed late delay signal}] \\ - \alpha\,[\textit{multipathed early delay signal}] = 0 \qquad \textbf{(5.2)}$$

where α is the relative signal strength of the reflected signal. Multipathing of the signal will leave a bias in the voltage difference between the early and late delay signals, so that the code correlation process is affected. When the voltage difference is not zero, the multipath caused residual voltage will drive the voltage controlled oscillator and achieve a change to the code generator until the voltage difference is zeroed. Chapter 8.2 will investigate how this affects the pseudorange results.

Raw data is normally processed by the internal filter of the receiver. Accelerations will cause positioning errors through filter lag (Lachapelle, 1987, p.151) and as such the integration time belonging to the tracking bandwidth is a variable affecting the measurement accuracy. Hatch (1986) suggests matching the sampling rate with the bandwidth (eg. a 67 millisecond sampling rate for a 15 Hz bandwidth) and reducing the amount of raw data subsequently by real-time curve fitting the carrier phase measurements over the desired sampling interval of for example 3 seconds.

Multipath rejection through the code correlating process will only occur when the multipath caused delay error exceeds 150 nanoseconds. Multipath can not be rejected by bandwidth changes in the 0.5 to 16 Hz range. It can only be averaged out over long periods, which could be seen as the equivalent to the use of extremely narrow bandwidths of 0.5×10^{-2} or 0.5×10^{-3} Hz, which is equivalent to the use of sampling rates of between one and various minutes. Following Hatch's suggestion mentioned above (Hatch, 1986), one could curve fit over a period of various minutes to filter out the short periodic multipath effects, but this still leaves the longer

multipath periods.

5.2 Suppression by Polarisation Discrimination

An important tool for the discriminating of a multipathed signal from a direct signal is the sense of polarisation of the received signal. Antennas exist which are sensitive to the sense of polarisation. First some definitions will be given to explain the different senses of polarisation. Horizontal polarisation means (Metcalf, 1986, p.1) that the

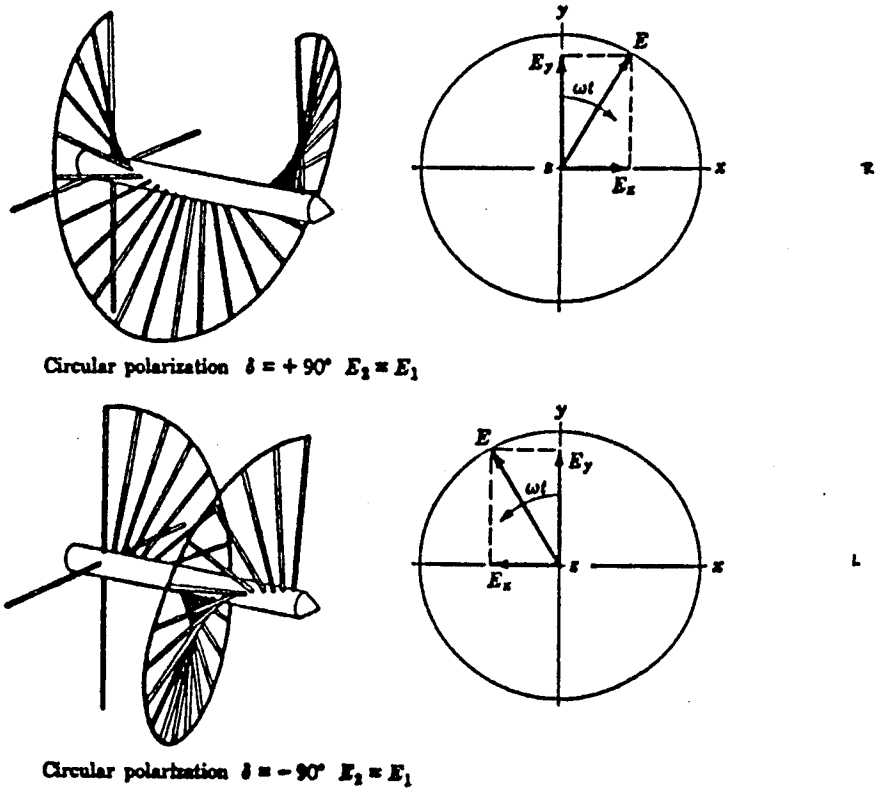

Figure 5.3 The left and right-handed helix (after Metcalf, 1986).

electric intensity vector E of the propagated wave is parallel to the ground, or more generally, parallel to the reflective surface. The E vector (as is the magnetic intensity vector H) is normal to the direction of propagation. When the E vector is perpendicular to the above defined horizontal direction the wave is called vertically polarised. These individual vectors are generally said to be linearly

polarised. Signals consisting of two components with equal amplitudes that are at quadrature in phase have circular polarisation. In other words when two linear E vectors are transmitted with one leading the other by $\pi/2$, the resultant electric intensity vector will rotate in response to the sequence of the amplitude variations of both its linear horizontal and vertical components (Fig. 5.3). In this way a circularly polarised wave is obtained containing either a right-handed (clockwise) helix or a left-handed (counter clockwise) helix of radiated electric field intensity vectors (Metcalf, 1986).

In the case of specular reflections from a plane surface, the ratio between the magnitude of the electric field vectors of the reflected wave and the incident wave is given by the Fresnel equations (Livingston, 1970, p.20). These equations give the reflection coefficients which are multiplied with the horizontal and vertical components of the incident wave to give the components of the reflected signal. If the wave arrives at the reflective surface under a certain angle of incidence, the resultant reflected wave will be constituted by the reflections of the different polarisation components of the incident wave's electric field vector. (If the media have very different magnetic permeabilities one should also take in account the magnetic field polarisation.) Schanda (1986) gives a thorough exposition of the matter. In a lossy medium it is necessary to take in account that the permittivities become complex quantities:

$$\epsilon = \epsilon' - j\epsilon'' \qquad (5.3)$$

Assuming that the air is near to a vacuum, with a refractive index of one and a reflecting medium that is a lossy dielectric with a refractive index **n**, the following equation applies:

$$n^2 = \epsilon_r' - j\epsilon_r'' \qquad (5.4)$$

The real term refers to the relative permittivity, the imaginary term refers to the complex component of the

relative permittivity and accounts for losses through conductivity. This last term influences the phase shift in the reflected signal before it combines with the direct signal. Snell's law is used to express the Fresnel equations in terms of the angle of incidence, by substituting the terms containing the angle of reflection (Livingston, 1970, p.21). The Fresnel equations for wave amplitudes are (Schanda, 1986; p.28-29):

$$E_{RH} = \sqrt{\frac{(p-\sin\delta)^2+q^2}{(p+\sin\delta)^2+q^2}}\, E_{IH} \qquad (5.5)$$

$$E_{RV} = \sqrt{\frac{(\epsilon_r'\sin\delta-p)^2+(\epsilon_r''\sin\delta-q)^2}{(\epsilon_r'\sin\delta+p)^2+(\epsilon_r''\sin\delta+q)^2}}\, E_{IV} \qquad (5.6)$$

with the following values for **p** and **q**:

$$p = \frac{1}{\sqrt{2}}\left[\sqrt{(\epsilon_r'-\cos^2\delta)^2+\epsilon_r''^2}+(\epsilon_r'-\cos^2\delta)\right]^{\frac{1}{2}} \qquad (5.7)$$

$$q = \frac{1}{\sqrt{2}}\left[\sqrt{(\epsilon_r'-\cos^2\delta)^2+\epsilon_r''^2}-(\epsilon_r'-\cos^2\delta)\right]^{\frac{1}{2}} \qquad (5.8)$$

where E_{RH} is the reflected wave's horizontal component,
E_{IH} is the incident wave's horizontal component,
E_{RV} is the reflected wave's vertical component,
E_{IV} is the incident wave's vertical component,
δ is the angle of incidence, as an elevation above the reflective surface,
ϵ_r' is the real term of the complex relative permittivity,
ϵ_r'' is the imaginary term of the complex relative permittivity.

The amplitude of the reflected signal is obtained by multiplying the incident wave amplitude with the absolute value of the complex reflection coefficient and by multiplying with an attenuation factor due to divergence caused by the curvature of the earth and the signal path (Poder and Andersen, 1965, p.85; Livingston, 1970, p.29). The reflected signal is

delayed because it travels a longer path, it also receives a phase shift at the reflection itself. Thus the total phase lag of the reflected wave is the sum of the phase shift at the reflection and the phase shift due to the pathlength difference (Shibuya, 1987, p.165). The phase shift at the reflection of the signal is obtained by calculating the argument of the complex reflection coefficient. Born and Wolf (1965, p.49) show that phase changes occur in both the horizontally and vertically polarised components. The phase shifts can be represented by:

$$\phi_{rh} = 2 \arctan\left(-\frac{\sqrt{\cos^2\delta - n^2}}{n^2 \sin\delta}\right) \qquad (5.9)$$

$$\phi_{rv} = 2 \arctan\left(-\frac{\sqrt{\cos^2\delta - n^2}}{\sin\delta}\right) \qquad (5.10)$$

where ϕ_{rh} is the phase shift in the horizontal component of the reflected wave,

ϕ_{rv} is the phase shift in the vertical component of the reflected wave,

δ is the angle of incidence, as an elevation above the reflective surface.

The phase shift at reflection is influenced by the ϵ'' term which is a function of the conductivity of the reflecting medium. Considering an operative wavelength of 1.5 GHz, the value for the conductivity decreases fast for increasingly dry soils, so that the real part of the complex permittivity term becomes much larger than the conductivity. The conductivity can be set to zero and the imaginary term ϵ_r'' of the permittivity in Eq.(5.4) neglected. The Fresnel equations Eq.(5.5) and Eq.(5.6) are then simplified and in this case become:

$$E_{RH} = \frac{(n^2-\cos^2\delta)^{1/2}-\sin\delta}{(n^2-\cos^2\delta)^{1/2}+\sin\delta} E_{IH} \qquad (5.11)$$

$$E_{RV} = \frac{n^2\sin\delta-(n^2-\cos^2\delta)^{1/2}}{n^2\sin\delta+(n^2-\cos^2\delta)^{1/2}} E_{IV} \qquad (5.12)$$

These equations agree with the ones used by Metcalf (1986,

p.6), Livingston (1970. p.21) and Shibuya (1987, p.166). However Metcalf reintroduces the complex term for n^2 as an approximation. Livingston (1970) shows how the ratio of conductivity versus relative permittivity is a thousand times smaller for soils than it is for water (see Table 5.2, which combines the information of various authors).

λ	Medium	ϵ_r'	σ	ϵ_r''
Metcalf (1986)				
10 cm	Sea water	69	6.5	(39)
	Dry soil	2	.03	
Schanda (1986)				
30 cm	Water	80		5
	Moist loam	10		1
Livingston (1970)				
15 cm to	Fresh water	75	1-20	
2 cm	Sea water	70	5-20	
	Low hills and rich soil	20	$3x10^{-2}$	
	Flat country + marshy soil	12	$8x10^{-2}$	
	Sandy, dry and flat	10	$2x10^{-2}$	
Poder and Andersen (1965)				
10 cm?	Sea water	69		39

Table 5.2 Permittivity and conductivity of various media where ϵ_r' is the real term of the complex rel. permittivity, ϵ_r'' is the imaginary term, σ is the conductivity in mhos/metre.

Livingston (1970) produces two graphs showing the reflected signal amplitude factors for horizontal and vertical polarisations as functions of the angle of incidence and as functions of the relative permittivity of the reflecting medium.

The vertical component loses a lot of intensity when reflecting of a horizontal surface with a high permittivity, while the horizontal component is only slightly attenuated. The unequal amplitudes will lead to what is called elliptical

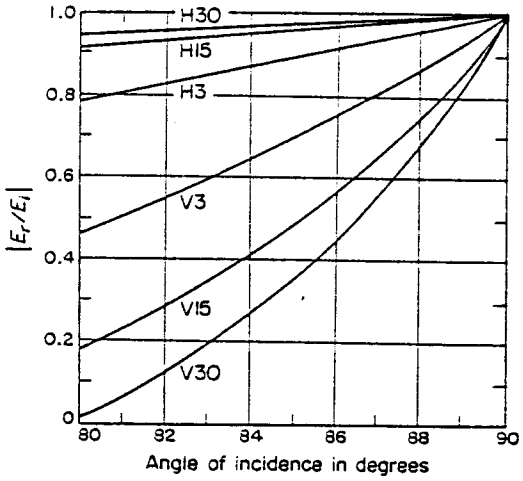

Figure 5.4 Reflection from soils (after Livingston, 1970).

polarisation. The small relative permittivity of 3 in the graph is for dry soil, while the larger one of 30 is for rich pastoral soil (Fig. 5.4). The curve V30 in Fig. 5.4 shows that, when the permittivity of the soil is quite high, the vertical polarisation component loses a lot of its signal strength, in comparison to the horizontal component H30. For dry soil (the V3 curve) the losses are less and horizontal and vertical polarisation components both have about half or more of their power reflected.

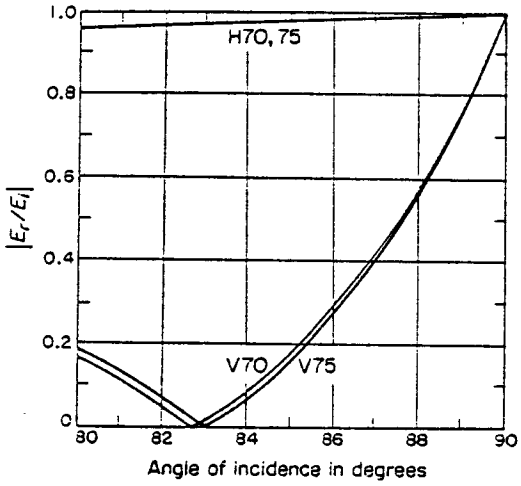

Figure 5.5 Reflection from water (after Livingston, 1970).

The relative permittivity of 70 applies to sea water (Fig. 5.5). The curves H70 and 75 (sea water and fresh water, respectively) show that the reflection coefficient for a horizontally polarised signal stays around 95 %. The vertically polarised signal behaves differently. When the grazing angle increases to the 5 degree level the amplitude of the reflected vertically polarised signal rapidly drops off and nulls, a further increase of the grazing angle sees the reflection coefficient rise again. Poder and Andersen (1965) use a value of $\epsilon = 69\text{-}j39$ for the complex relative permittivity in Eq.(5.4) for sea water, which agrees well with Metcalf (1986) and Schanda (1986) when a frequency of about 3 GHz is considered. Using this value Poder and Andersen deduced a phase shift of $\pi - 2.5\sin\delta$ at reflection from sea water with δ as the grazing angle. The phase shift also responds to the conductivity of the reflective surface. It is influenced by the imaginary term in the complex relative permittivity which is a function of frequency, magnetic permeability and conductivity (Livingston, 1970, p.21). Poder and Andersen show that a phase shift of close to 180 degrees occurs, when reflections take place off the surface of a conductive medium like sea water. Shibuya (1987, pp.196-197) shows that generally a horizontally polarised signal receives a 180 degree phase shift when reflecting of smooth surfaces (e.g. water, fertile land, dry soil, etc.).

Metcalf (1986) uses the simplified Fresnel equations (5.11) and (5.12) as starting point of his derivation. He reintroduces the full complex term for the relative permittivity and generates a graph (Fig.5.6) showing the theoretical multipath behaviour of a signal measured during air-to-ground transmission from an aircraft at 3000 meter altitude over seawater using signals of various polarisations. The diagram shows that a horizontally polarised signal exhibits strong nulls and a vertically polarised signal shallow nulls when the signal reflects off the water. This is due to the fact that the intensity of the horizontally polarised signal is only slightly reduced through the reflection and still has the power to almost extinguish the direct signal. In contrast

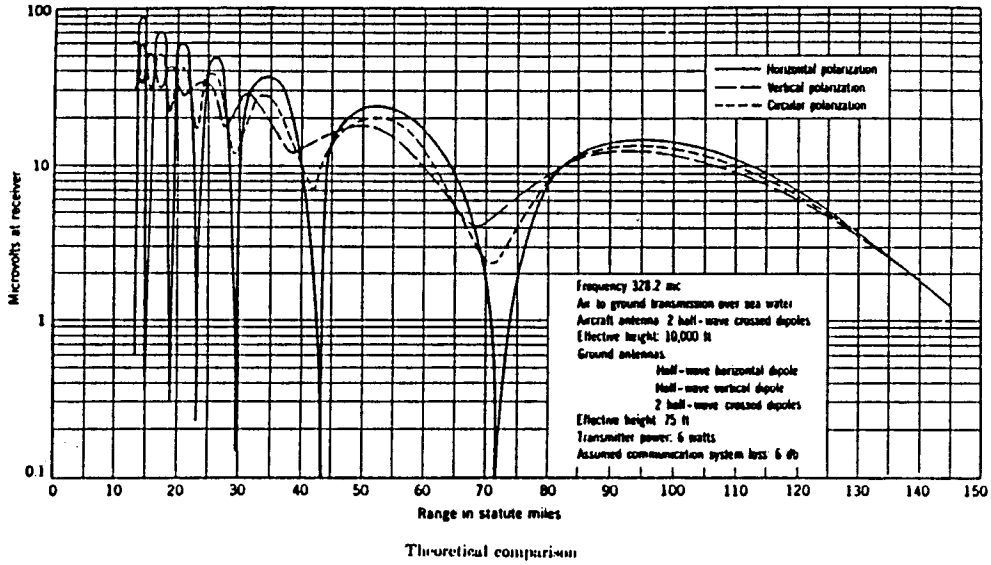

Figure 5.6 Signal polarisation and signal strength variations through reflections during an air-to-ground transmission over sea water from an altitude of 3000 m. The full, broken and dashed lines represent horizontal, vertical and circular polarisation, respectively (after Metcalf, 1986).

the vertically polarised component is much reduced in intensity after reflection and, thus, can only cause gentle swings in the received signal intensity. Metcalf (1986) shows that the circularly polarised signal has multipath nulls somewhere in between the extremes shown by the horizontally and vertically polarised signals.

Metcalf (1986) also shows a graph (Fig. 5.7) of the phase change brought about by the reflection coefficient for a vertically polarised wave in the case of reflection over sea water. It shows that the phase shift caused by the reflection coefficient for vertical polarisation is very sensitive to the "grazing angle" and drops from 180 degrees to 30 degrees in the first 10 degrees of the grazing angle. With a larger grazing angle it drops towards zero (Shibuya, 1987, p.196-197). But in contrast, a circularly polarised signal will

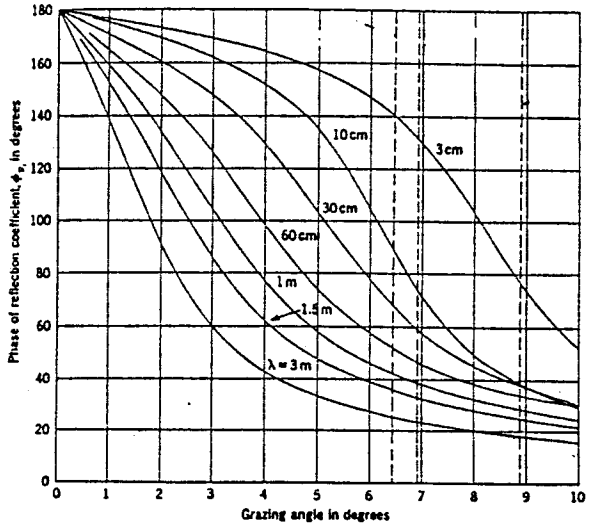

Figure 5.7 Reflection and the signal phase (after Metcalf, 1986).

reverse its sense of circular polarisation from right-handed to left-handed by virtue of its horizontal component swapping from being the lagging to being the leading electric intensity vector, after a grazing reflection from sea water. For reflections from very dry land "more elaborate expressions" are needed to calculate this phase shift, according to Poder and Andersen (1965). Shibuya (1987, p.196-197) shows some excellent graphs for reflections from sea water, damp ground, fertile soil and dry land. Apart from the behaviour of both senses of polarisation, these graphs also show the behaviour

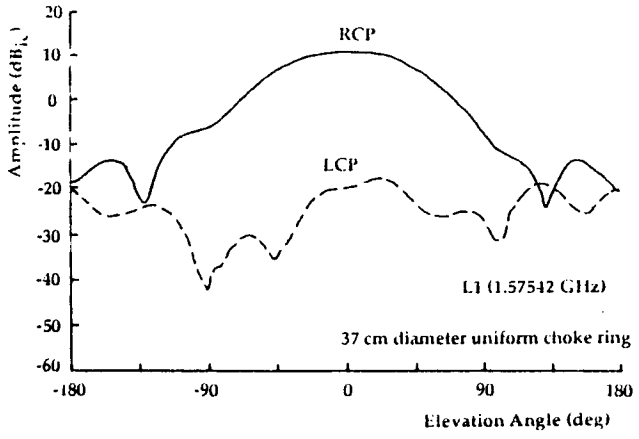

Figure 5.8 Polarisation discrimination by the antenna (after Tranquilla et al, 1989).

of the phase angle of the reflection coefficient.

Some antennas can transmit and discriminate these circular polarisations, for example crossed dipoles, the helix and wave guides with crossed slots. Tranquilla, Colpitts and Carr (1989) recently investigated various Dorne Margolin Model C146 antenna configurations. They showed that a 20 dB difference could be achieved, almost over the whole hemisphere, between the antenna response to a right-hand circularly polarised signal and a left-hand circularly polarised signal. Figure 5.8 shows the polarisation discrimination response for the above Dorne Margolin antenna using a 2λ diameter untapered choke ring. In summary it can be said that signal polarisation discrimination by the antenna is a very useful tool for the reduction of multipath effects.

5.3 Multipath Sensitivity of Various Antenna Designs

5.3.1 Gain of Antennas

An equation is derived which shows that the power ratio between a direct and a reflected ray is a function of three main factors that can be optimised resulting in a reduction of the antenna's multipath response. The relationship between the gain **G** of the antenna in the direction of an incident wave (the direct wave in this case) and the antenna's effective receiving area $\mathbf{A_e}$ is known from antenna theory (Skolnik, 1980):

$$A_e = \frac{\lambda^2}{4\pi} G \qquad \textbf{(5.13)}$$

It is also known that the power received by the antenna from the direct wave is equal to the product of the satellite signal power density and the antenna effective receiving area:

$$P_d = P_o A_e \qquad \textbf{(5.14)}$$

where $\mathbf{P_d}$ is the power received by the antenna from the direct wave,

P_o is the satellite signal power density.

The power density at a distance **R** of an antenna which radiates uniformly in all directions, is equal to the total transmitted power divided by the surface area $4\pi R^2$ of an imaginary sphere at radius **R** (Skolnik, 1980). The direct signal power P_d and the reflected signal power P_r can be written as (Tranquilla and Colpitts, 1988, p.8-9):

$$P_d = P_o \frac{\lambda^2}{4\pi} G_1 \qquad (5.15)$$

$$P_r = P_1 \frac{\lambda^2}{4\pi} G_2 \qquad (5.16)$$

where G_1 is the gain of the antenna in the direction of the direct wave,

G_2 is the gain of the antenna in the direction of the reflector,

P_1 is the power density of the reflected signal.

P_1 is equal to the transmitted signal P_o, modified by the reflector characteristics and transmitted in all directions with a particular gain G_r towards the receiving antenna:

$$P_1 = P_o A_a G_r \frac{1}{4\pi d^2} \qquad (5.17)$$

where A_a is the absorbing area of the reflector and **d** is the distance to the receiving antenna. The reflected signal power received by the antenna is then:

$$P_r = P_o A_a G_r G_2 \left(\frac{\lambda}{4\pi d}\right)^2 \qquad (5.18)$$

This means that the multipath sensitivity of an antenna can be reduced by minimising the following power ratio (Tranquilla and Colpitts, 1988):

$$\frac{P_r}{P_d} = \frac{A_a G_r}{4\pi d^2}\left(\frac{G_2}{G_1}\right) \qquad (5.19)$$

It is clear from Eq.(5.19) that this power ratio can be reduced by increasing the distance between the reflective

surface and the antenna, by minimising the gain ratio between the gain of the antenna towards the direct and indirect signals, or by reducing the reflective properties of the reflective surface. Careful antenna siting can meet the first condition. The second condition is met by what is called **beam shaping**. This means reducing the antenna's response in those directions where multipath is expected from. This can have detrimental effects upon the stability of the phase centre position and can not be exploited to its fullest extent when high accuracy is required, because of the induced phase centre variations (see Chapter 4). The last condition can be met by placing absorbent material over known reflective surfaces.

Yunck (1987) remarked that the most troublesome forms of multipath were those with low frequencies in excess of 10 minutes. This usually arose from reflective surfaces very near to the antenna, often the ground. Higher frequency multipath effects usually average themselves out very well. His proposal was that the ideal antenna phase centre should be made to be flush with a large flat back plane. This means the antenna had to be as flat as possible itself. It's field of view should still be cut off at 15 degrees above the horizon. This would be an ideal antenna design for fiducial GPS sites. Tranquilla proposed (Yunck, 1987) that these antenna characteristics could be achieved by using a non-flat RF absorbent back plane, sculpted in such a way as to cut the field of view below 15 degrees. But low frequency multipath from a horizontal surface can also occur when the satellite culminates at any elevation where its rate of elevation change becomes zero and its multipath period goes temporarily to infinity (theoretically). A satellite going through zenith will also momentarily cause low multipath frequencies from horizontal surfaces.

5.3.2 Types of Antennas

GPS antennas can be divided into six main types:

1) monopole,
2) dipole,
3) crossed dipoles (actually 4 orthogonal monopoles),
4) spiral helix (conical spiral, log spiral)
5) quadrifilar helix and
6) microstrip.

Most of the types are illustrated in Figures 5.9 and 5.10. A few examples are the following: the MITES antenna has crossed dipoles, the TI 4100 has a conical spiral antenna, the Wild-Magnavox WM 101 has a quadrifilar helix and the Macrometer II

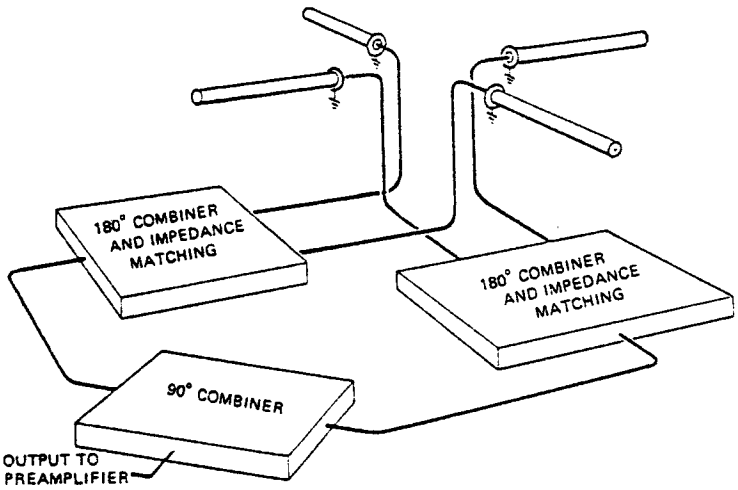

Figure 5.9 The crossed dipoles (after Greenspan, 1982).

a microstrip antenna. Microstrip antennas are now also used by Trimble, Geotronics, Ashtec and Topcon. The quadrifilar helix and the microstrip are the most popular antennas at the time of writing. The phase centre stabilities of most of the above antennas have been described in Chapter 4.1.

Wells et al (1986) give a good overview on antennas, which will be summarised here. The monopole, dipole and crossed dipole configurations are single frequency antennas which need a ground plane. Size variation of the ground plane design allows optimising of the antenna's multipath characteristics. The spiral helix antennas have good phase pattern

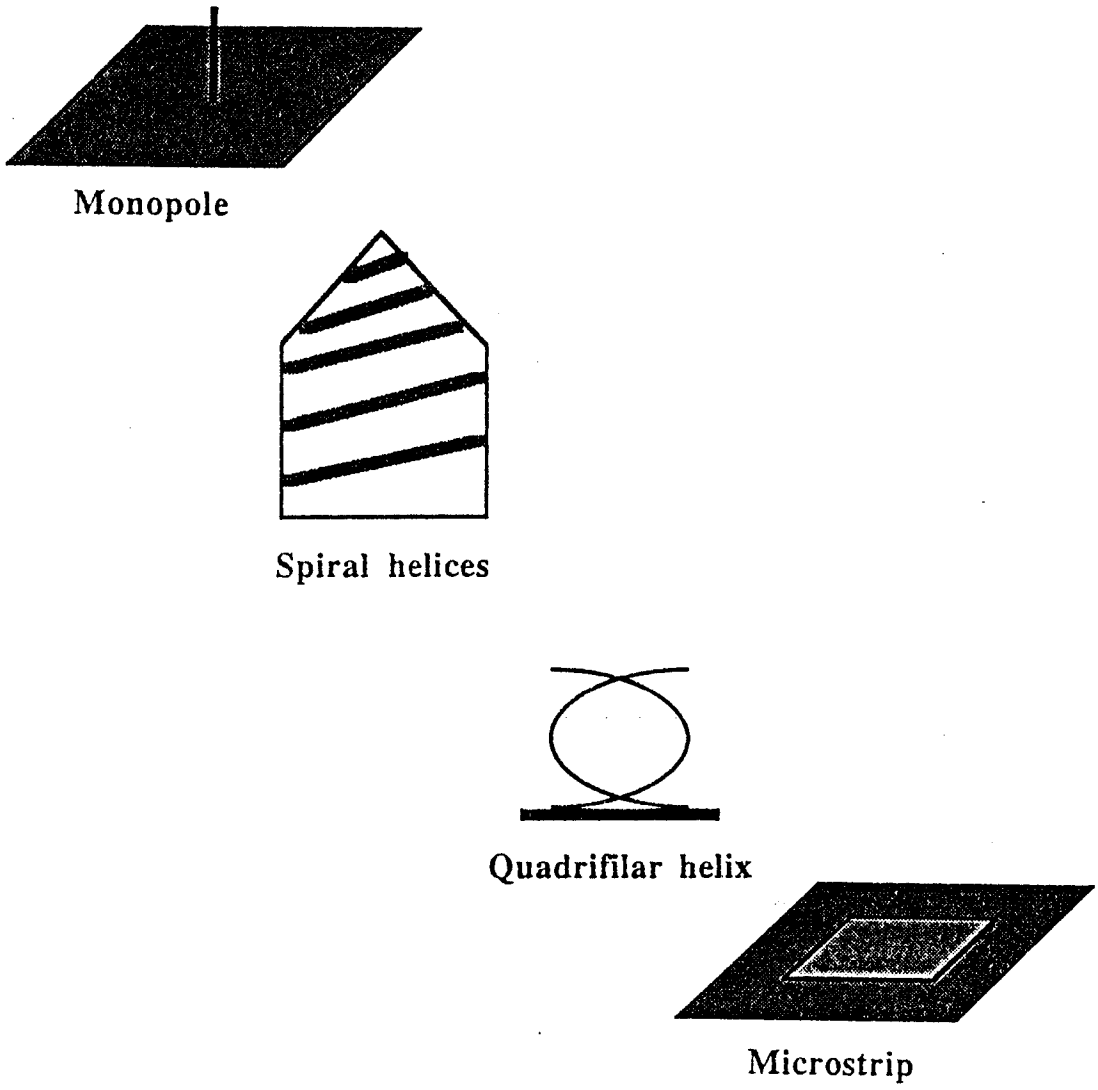

Figure 5.10 Other antenna types (after Wells, 1986).

characteristics and can operate on both GPS frequencies. They need to be oriented because their phase patterns are slightly azimuth dependent. The quadrifilar helix requires consistent orientation for the same reason. This antenna is generally a single frequency aerial, with good phase pattern characteristics and does not need a ground plane.

Although the microstrip antenna has a constant horizontal phase centre offset, the phase centre is stable at the millimetre level. This antenna comes closest to the "ideal" antenna as defined by Yunck (1987) with respect to its multipath characteristics, because its phase centre is flush

with the back plane. This rugged low gain antenna is suitable for single and dual frequency reception and requires a consistent azimuth when setting it up because of the above mentioned horizontal phase centre offset.

In order to exploit the GPS accuracy potential the trend will be towards calibration of the antenna phase patterns and real-time antenna phase pattern corrections by the receiver software. The design trend is towards setting phase stability specifications which require extremely small manufacturing tolerances, making the GPS antenna very different from a simple communications antenna. This demands very precise manufacturing techniques.

5.4 Thoughts about Correcting for Multipath

In Chapter 2 it was shown that the multipath period changes considerably over an hour. A horizontal and vertical multipath index was defined there which standardised the multipath period to the one that would occur if the reflective surface was situated one metre away. This was tabulated in Table 2.2 (Refer also to Table 12.1). (In order to obtain the actual multipath period this value must be divided by the perpendicular distance to the reflective surface.) The rapid change of the multipath period is the main reason why it is hard to devise a scheme to measure the multipath effect. The horizontal multipath period can change by 100 % in one hour on average and the vertical multipath period changes about 30 % in one hour on average, if observations are made sufficiently removed from the moments of the satellite's culmination in elevation. Otherwise the changes in multipath periods will be even larger. But the tables also show that over some periods of 10 minutes the multipath periods only change 10 % to 15 %. This suggests that if a method can be devised to measure the multipath effect for a particular site in this ten minute interval, a possible estimate of the momentary multipath period, amplitude and phase can be obtained.

The idea is to shift the antenna position in small steps to sample a full wavelength of the multipath error curve within the ten minute time bracket. An old fashioned "swing curve" would be obtained, by changing the antenna position 6 times by about 25 millimetres every 30 or 45 seconds through shifting it along a specially designed bar. This could be done in three dimensions sequentially and should take place in the shortest practicable time. In the vertical sense this could be achieved by adding spacers half a dozen times. This changes only the height of the antenna. In the horizontal sense a cross bar (in the following called **groma** after an ancient Roman surveyor's square) could be constructed with predetermined antenna positions: one position in the middle and three in each of the four cardinal directions. One arm of the groma could be positioned towards an obvious vertical reflective surface, if present, to maximise the effect.

Because the antenna position change is mirrored by its virtual image, the movement is doubled in its effect upon the phase pathlength difference. The groma does not have to be very large because of this. The projection of the bar upon the incident ray to the satellite should be $\lambda/2$. Short periodic multipath effects of periods of only a few to ten minutes are averaged out because of the observation duration itself but the longer periodic effects result in a bias. When the reflective surface is vertical, low satellites bring on the longest multipath periods. As we are only after the long periodic effect, projection angles larger than 45 degrees are less important. The movement along the horizontal bar will make a small vertical angle with the ray to the low satellite. When the reflective surface is horizontal, the satellites with high elevation angle bring about the longest multipath periods. The vertical movement of the antenna which is appropriate here will make only a small angle with the ray to the satellite. So a suggested spacing between the extreme antenna positions would be $\lambda/\{2 \sin(\pi/4)\}$ or 172 mm for L2 and 134 mm for L1. For a dual frequency receiver the larger size would be required, so this size should be the standard one. This recommended length should now be divided in say 6

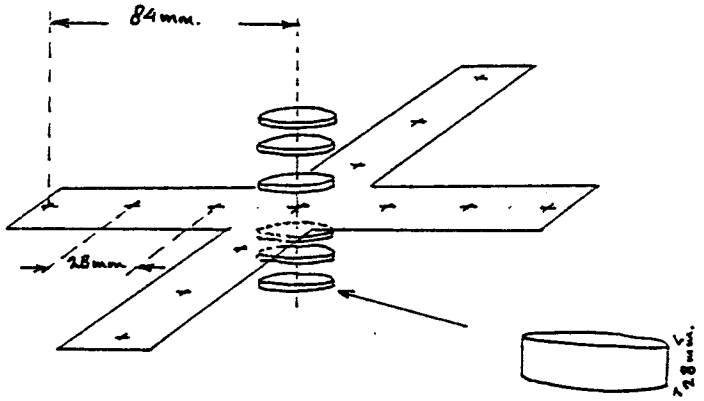

Figure 5.11 The proposed "groma".

sections of 28 mm. This results in 7 antenna positions. The same approach in a direction perpendicular to the first one would produce the other arm of the groma. The middle position will be in common in all three dimensions (see Fig. 5.11).

When the antenna positions have been observed with the GPS, they can be calculated and plotted in relation to the known relative antenna positions and thus generate a swing curve. A drawback is that, in order to obtain a result in three dimensions, 19 baselines per satellite have to be analysed. Obviously a short cut for the interpretation of the data is needed. One could use the knowledge of the satellite azimuth and elevation in order to calculate an expected (time tagged) phase change for the antenna shift and compare this directly with the observed one. After plotting the two perpendicular swing curves in the horizontal plane an intersection point of the two curves will become evident and the intersection of the two "zero lines" through the curves can be drawn (see Fig. 5.12). The difference between the two points is the horizontal offset due to signal multipathing from vertical reflective surfaces. The swing curve on the vertical axis yields the height offset due to multipathing off a horizontal surface. Theoretically this test will only be exact when the observation time approaches zero, but could yield reliable

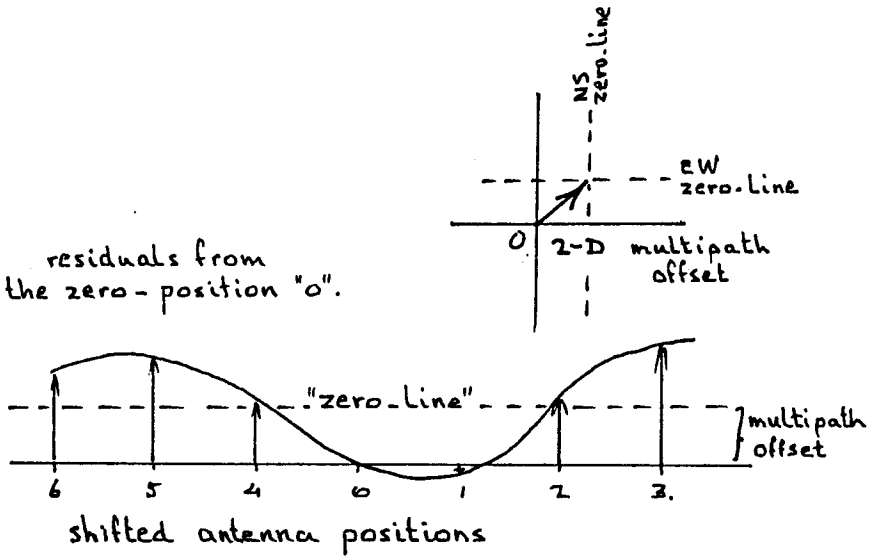

Figure 5.12 Construction of the zero-line of the multipath swing curve.

estimates if the antenna shifts can be done in thirty second intervals. The attractiveness of the method is that no identification and modelling of the reflective surface is required.

The most obvious way to correct the baseline results using this method is by observing the various antenna positions symmetrically around the original set up, in time and in space. The averaging of all the results comes about if the baseline is processed as if no antenna shifts had taken place. As a precaution, the three swing curves should be analysed in order to ascertain that no deep nulls have occurred through very strong reflections. This would invalidate the averaging process (Refer to Fig. 6.2).

6. REVIEW OF MULTIPATH EXPERIMENTS

In this chapter an overview of experiments related to signal multipathing will be given and conclusions drawn from these. The first section briefly reviews the problems encountered with multipath in electronic distance measurements with microwaves. The next section reviews the experiments undertaken in order to detect multipathing in GPS pseudoranges and the various ways that are proposed to cope with these. The third section outlines previous multipath investigations of the carrier phase signal and the conclusions that were drawn. The last section introduces the experiments carried out in connection with this project.

6.1 Multipath in Electronic Distance Measurement

Yaskowich (1964) investigated about 500 microwave EDM lines in the Canadian primary geodetic network. After defining ground swing as variations in the measured distance with changes in the carrier frequency he more closely investigated the 10% of the data set which featured the largest ground swing. He reported reflections from steel towers, ice, water, land and swamps and attempted to quantify the resulting errors with the help of values derived from coordinates that result from a geodetic network adjustment. He concluded that a lot of the observed ground swing curves were complex and did point to multiple reflections. This excluded the use of Poder's equation for ground swing, because the formula was then based upon a single reflection model. It was found that EDM lines with the most complex ground swing curves fit network adjustments better, suggesting that a process of averaging occurs.

Poder and Andersen (1965) reviewed the mathematical model of the multipath error and the approach taken in the mechanisation of the solution. They demonstrated the derivation for single and multiple reflections using a complex vector space. They showed that the phase changes that are added to the direct signal by the reflected signal will vary when the carrier frequency is altered. This will alter the relative phases between the direct and multipath signals. The changes of the carrier frequency will result in fading

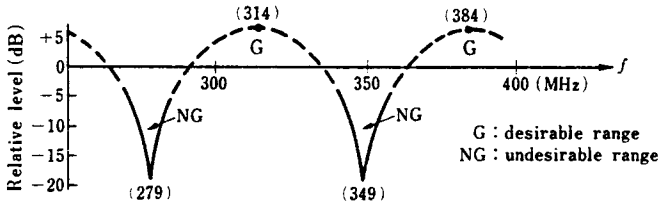

Figure 6.1 Signal fading through frequency variation (after Shibuya, 1987).

and enhancement of the combined signal (Fig. 6.1). One full period of this is called the groundswing curve. Often the ground swing curve is a sinusoid and the resulting distances are simply meaned. However, in cases of stronger reflections, the curve is not a sinusoid and deep nulls occur (Fig. 6.2). With the help of the reflection coefficient (Refer to Chapter 5.2) and a knowledge of the excess pathlength, the multipath error can be calculated for one full period of the error. The so determined error can then be subtracted from those parts of the observed ground swing curve where it is flat and steady (Poder and Andersen, 1965, p.94 and 95).

The total received signal comprises:

a. the direct signal and the two side bands of the modulation;
b. the multipath signal and its two modulation side bands, modified by a phase shift due to the excess path and a phase shift due to the complex argument of the reflection coefficient and multiplied by the relative signal strength

(which is the absolute value of the reflection coefficient).

Poder and Andersen (1965) suggested that a better solution to the multipath problem was to employ a shorter carrier wavelength so that the reflections become more diffuse. They also advised that it would be opportune to add extra redundancies to a survey network where a reflection problem was expected, so that the affected measurement could be eliminated, if necessary.

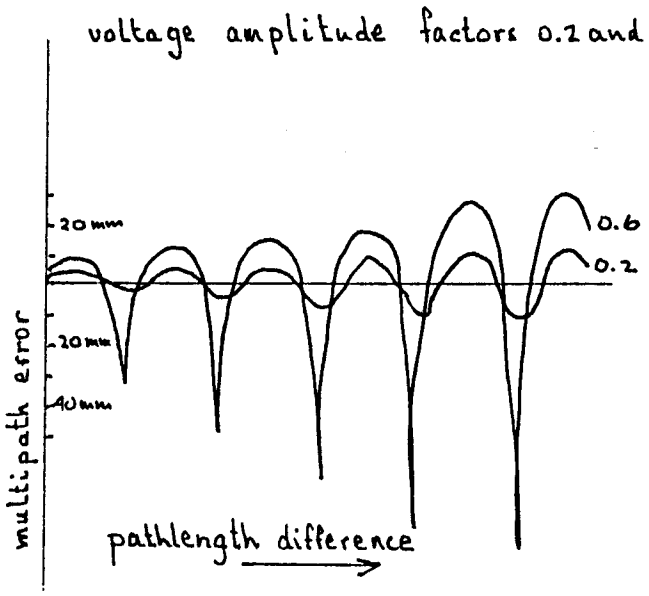

Figure 6.2 Fading due to strong reflections (after Merry and Rüther, 1986).

Küpfer (1968) found periodicities in the data he was using which indicated appreciable height changes over time in the reflective surface over which he had measured. Having measured over a lake, he suggested that microwave ducting had taken place in response to a refraction effect close to the lake's surface. In fact, the reflection didn't occur at the water surface of the lake but from an air layer just above it which varied in thickness as a function of time. He reviewed the main methods used to reduce the effect:

a. the tilting of the line of sight of the EDM instruments upwards by a few degrees in order to direct a lower gain

part of the receiver antenna into the direction of the expected reflection;

b. obtaining of ground swing curves by either changing of the height of instrument in order to change the excess path length (leading to possible signal fade-outs at critical instrument heights), or the variation of the carrier frequency.

Benz (1970) restated the fact that the ground swing curve only looks like a sine curve when the relative signal strength of the reflection is small compared to the signal strength of the direct signal. The ground swing curve becomes quite asymmetric when the reflected signal is very strong and shows deep nulls. He pointed out that the dual dipole parts of the transmitting antenna can be shifted relative to each other and they can be rotated relative to the horizontal plane in order to detect the presence of groundswing. In doing so, the directivity characteristics of the antenna are also changed. Phase changes of a quarter to one half of the wave length in the received signal occur when groundswing is present. If a measured distance does not change during the above procedure, no appreciable reflection is occurring. Otherwise remedial action can be taken.

Küpfer and Hossmann (1971) evaluated the acceptance of the method of varying the carrier frequency in order to obtain a ground swing curve and alluded to the possibility of varying the modulation frequency instead. For most EDM instruments manufactured up to 1971, the bandwidth was not very wide. But the instrument they were evaluating (WILD DI 60, SIAL MD-60) had a 150 MHz modulation frequency giving it a 300 MHz bandwidth. This was sufficient to obtain a ground swing curve.

Merry and Rüther (1986) investigated an instrument of which the carrier frequency could not be varied and showed that a change of phase can be achieved in the resulting distance by changing the instrument height. A height change can be found which will change the pathlength difference, brought about through reflection, by a full cycle. They also pointed out

that the received signal is the vector sum of all reflections and the direct signal. A fade-out can occur through destructive interference between the main beam and a major reflection, leaving the minor reflections free play to dominate the phase of the resultant. Characteristic for this is a drop in signal strength and an increased scatter in the observations.

Summarizing, it can be stated that the direct signal and its modulation side bands as transmitted by a microwave EDM instrument, are modified through reflection effects by the addition of the often out of phase indirect signal and its side bands which generally have an attenuated signal strength as well as a further reflection coefficient caused phase shift. This combined signal causes a beat pattern in the results which can be displayed as a ground swing curve. Ground swing in EDM has reportedly been caused by steel towers, ice, water, land and swamps. Often multiple reflections are suspected. There appears to be a tendency for the multipath effect to average itself out when the ground swing curves get more complex. In principle, the technique to detect and isolate multipath involves altering the relative phase between the direct and the combined direct and indirect signals, until at least a full period is seen in the plot of the results. The most popular method has been the altering of the carrier frequency. Signal fade outs can occur in cases of strong reflections. Averaging is then not the right approach. Another way to reduce the multipath effect has been to select ever higher carrier frequencies, in order to make the reflections more diffuse. It has been reported that the reflections do not necessarily originate from solid surfaces, they may be due to refraction driven microwave ducting of possible thermal origins. Apart from the variation of the carrier frequency, other methods to solve the multipath problem have been the changing of the antenna height or the slightly changing of the antenna alignment towards the receiver, or the changing of the directivity characteristics of the antenna through changes in the direction of polarisation of the transmitted signal. A further method to reduce multipath was the generation of a ground swing curve through the

changing of the modulation frequency instead of the carrier frequency.

6.2 Multipath in GPS Pseudoranges

In the case of GPS the signal originates from a point with a considerable elevation, which makes its multipath behaviour quite different from that of EDM. The reflection generally does not occur from a point half way between the transmitter and receiver. Multipath in the GPS generally occurs from reflective surfaces in the vicinity of the receiver (and perhaps of the transmitter) and the geometric relationship is different for each satellite, each site and each antenna position.

Spilker (1980, p.53) indicated that, if the multipath delay is more than one code bit (one wavelength at 10.23 MHz), the multipath signal is treated as if it was noise of the same power. In consequence, it would be successfully eliminated as if it were a jamming source. This occurs with the reflections of the C/A code when the delay is larger than 1.5 μsec and 150 nsec in the case of the P-code, on the condition that the receiver is already tracking the desired signal. But if the receiver was tracking the indirect signal rather than the direct one, then the error will be the full 150 nsec code length or about 45 metres.

Thornton et al (1984) mentioned the noise in the pseudorange signal and spoke of the method of fitting the carrier change in range record to the pseudorange record. The principle is shown in Figure 6.3. The first is a very accurate record of changes but is ambiguous with respect to its absolute values, the latter is very noisy but is close to a true absolute value of the range. By finding a best fit between the two records, a more accurate pseudorange can be derived for each epoch; an improvement is obtained by a factor $N^{-1/2}$, with N the number of points for which change in range values are available.

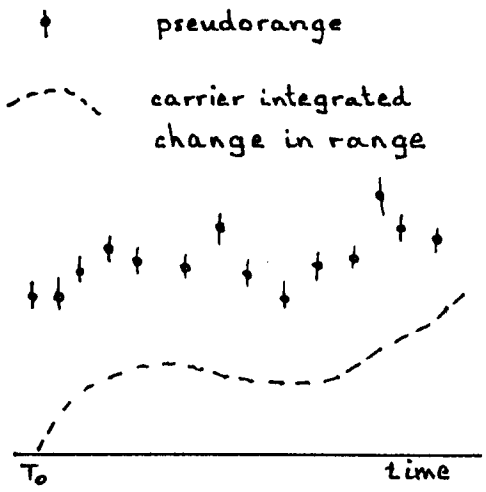

Figure 6.3 Carrier change in range fitted to the pseudoranges (after Thornton, 1984).

Bishop et al (1985), when trying to determine the ionospheric time delay by using GPS signals, came across problems caused by multipath. These authors carried out a test using different antenna environments. In one case the antenna was placed 10 metres from a trailer, in another test the antenna was placed on a box almost 2 metres high; in the third test it was placed on the ground, with a large ground plane. They concluded that the multipath effect could be identified by across day cross-correlation of the data. Elimination was suggested by low pass filtering, recognising that this was only useful, if the power spectra of the multipath effect and the ionospheric effect did not overlap with each other. In this case a matched filter could be applied to eliminate that part of the spectrum that corresponds most likely to multipath at the particular site. The method of calibrating pseudorange data with integrated carrier phase change in range data was confirmed. Bishop et al also recommended using various averaging periods depending upon the specific antenna environment.

Bletzacker (1985) was also of the opinion that the effect of pseudorange multipath could be reduced by a smoothing technique. He advocated subtracting the calibrated carrier phase from the individual pseudorange readings, in order to obtain an observable that scatters around zero. The

calibrated carrier phase is obtained by getting a best fit between the pseudorange readings and the carrier phase change in range values, which can lead to a pseudorange accuracy at the 0.3 metre level. Some necessary equations are given in Chapter 7.2.1. Bletzacker carried out some tests with different antenna environments whilst using short baselines in order minimise the tropospheric and ionospheric effects. He suggested to recalculate the results after removing data from low elevation satellites and to check the statistical significance of the ensuing changes in the results.

Bletzacker also mentioned differences in gain ratios between the L1 and L2 responses of the antenna at low satellite elevations. This antenna response asymmetry will complicate the pseudorange modelling. He suggested that the pseudorange multipath effects could be reduced by digital filtering of the pseudoranges, the use of radio frequency absorbent material on the antenna ground plane, the careful siting of the antenna and the use of signal diplexing to obtain the L1 and L2 signal using a single wide band antenna. Bletzacker pointed out that the L1 and L2 multipath periods should scale according to the ratio of their respective wave lengths, if they reflect off the same surface.

Meyerhoff and Evans (1986) showed a 20% improvement in pseudorange positioning accuracy by using Doppler change in range measurements to smooth pseudoranges. The smoothed pseudoranges used by these authors are actually integrated carrier phase data, which are given an initial offset by calculating a best value for a pseudorange. They corrected their data for, among other things, the ionospheric and tropospheric delay and clock corrections.

Evans (1986) went even further and suggested that the differences between the ionospherically corrected pseudorange and biased Doppler range could be used not only to detect multipath, but also to isolate it and statistically model it. He proposed the use of a Kalman filter to accomplish this. He commented that the occurrence of multipathing of the signal

was at times so destructive that loss of lock occurred. This could mean that the reflection was as strong as the direct signal and caused total fading. (Chapter 8 shows that this corresponds to a phase shift of 0.5 λ between the direct and indirect signals and a multipath induced error in the resultant of 0.25 λ just before fade out which is 7.3 metres for pseudoranges). Evans called for further tests on antenna and receiver design with respect to their multipath discrimination characteristics.

Evans and Hermann (1987) analysed the differences between ionospherically corrected pseudoranges and biased phase ranges and concluded that the standard deviation of these was 1.3 metres in a low reflective environment and 4 to 5 metres in a highly reflective environment. These tests involved various antennas in several configurations with respect to the following: siting, the use of absorbers, ground planes and low elevation antenna gain. They remarked that the TI 4100 antenna is of a design which has uniform gain even close to the horizon in order to increase the amount of satellites that can be received. This is now considered as undesirable because of the multipath sensitivity it creates.

Falkenberg (1988) named the various methods of multipath investigation: cross-correlation of pseudorange data or carrier phase data between two consecutive days; cross-correlation of observed data with a geometric model of signal multipathing; cross spectral density analysis by multiplying the spectral density functions of the data of two consecutive days of observations, in order to derive common frequencies; analysis of the time variation of the signal strength. He predicted results from tests relevant to hydrographic applications, with an oscillating mast assembly, which was positioned amongst eight reflector panels of 1.2 m squares.

Evans and Carr (1989) investigated pseudorange data from three GPS tracking sites equipped with TI 4100 receivers to determine the multipath characteristics of the sites. They

used 15 minute smoothed accumulated change in phase range values to recover multipath effects and signal noise by differencing the phase change record with actual observed pseudorange data. These differences were added to simulated pseudoranges, calculated from available orbit information. This information was used to solve for the orbit again and the results were compared with the starting values. They concluded that the multipath record used produced errors in orbit determination of up to 17 metres. According to the authors this was reduced to the 1 metre level when the five US GPS control stations were added to the data set. They concluded that the tracking sites with TI 4100 receivers (Australia, Argentina and the United Kingdom) must change to antennas with low gain near the horizon and use absorption material on the antenna ground planes.

In summary, it is clear that various tests have been carried out with different receivers and antennas with respect to pseudorange data. Short lines have been used in order to reduce other error sources. Pseudorange standard deviations of the order of one metre occurred at low reflective sites and standard deviations of up to five metres have been encountered at highly reflective sites. Antennas with and without low gain near the horizon have been used and with or without absorbing material on the ground plane. Pseudorange multipath detection has been mainly carried out using calibrated phase data which is compared with observed pseudoranges, as reported by Evans (1986) and by cross correlation of this data across consecutive days. Different elevation mask angles have been imposed upon the data to test the influence of the multipath component in the signals of low satellites. Multipath tests were reported which cross-correlated modelled pseudorange multipath effects with the observed pseudoranges, tests which used the cross spectral density function between two days of data and tests which monitored variations in signal strength in order to deduce multipath. Spread spectrum techniques keep the pseudorange multipath errors below one code bit unless the indirect signal is tracked. The periodicities of multipath errors in

L1 and L2 are in proportion to the 154/120 ratio of their relative frequencies. Multipath can cause errors in orbit determination of the order of 10 to 20 metres unless remedial action is taken.

6.3 Multipath in GPS Carrier Phases

Carrier phase multipath is considerably smaller (by about two orders of magnitude) than pseudorange multipath, but is significant when accurate surveys are required or when very short lines are used.

Georgiadou and Kleusberg (1988) used two short baselines in a multipath study. A 3.5 metre baseline was chosen with reflective surroundings, the other baseline was 24 metres with one site 15 metres away from any conducting material and the other end of the baseline was situated on a flat box on a corrugated trailer roof. The authors used a short baseline in order to decrease the across site differences in atmospheric delays and the effects of ephemeris errors. They conclude that the multipath error is much larger than the receiver noise and is the main error source on short distances. Averaging of the data over a longer period helps to eliminate the problem. The averaging time should be at least as long as the duration of one period of the longest multipath period present. As redundant data is collected during an observation session, the baseline solution will be obtained through an adjustment resulting in residuals. Kleusberg (1986, p.259) pointed out that most of the behaviour of these baseline adjustment residuals is already visible in the dispersive delay time series. Besides ionospheric causes this points to the effect of signal multipathing. The latter cause is important as shown by the across consecutive days cross-correlation (Georgiadou and Kleusberg, 1988).

Rocken and Meertens (1989) tested different antenna designs and different receivers. They tried mixing the antennas of a TI 4100, a Trimble 4000 SD, a Trimble 4000 ST and an Ashtec

XII, as well as a Dorne-Margolin (JPL choke ring) antenna assembly. Rocken and Meertens used distances ranging from 0.02 to 50 kilometres. When the TI antenna was lowered a change in baseline length was observed, probably due to a change in excess pathlength of a reflected signal. They found an 80 millimetre phase multipath amplitude in the data and observed a factor two reduction in multipathing when replacing the TI antenna with the Dorne-Margolin assembly. The noise of the Trimble receiver-antenna combination (±20 mm) was found to be half the noise of the TI 4100 receiver-antenna combination (±40 mm). The latter is mainly caused by the TI 4100 antenna. Another interesting conclusion was that a relative phase centre offset can be determined by swapping of the antennas types.

Tranquilla, Colpitts and Carr (1989) investigated a type of Dorne-Margolin antenna on a variety of ground planes. This antenna is meant to have a smooth hemispherical phase pattern, with a marked pattern cut-off near the horizon. The antennas are calibrated in a precise anechoic chamber, with measurements every five degrees in azimuth and elevation. As the received signal ought to be right hand circularly polarised, the antenna's response to left hand circularly polarised signals is important. A reflected signal reverses its polarisation, amongst other things. Comparisons were made with an antenna with a normal aluminium circular disk ground plane. This antenna showed 3 dB diffraction ripples throughout its phase pattern, as well as a 20 dB difference near zenith between its response to signals with opposite senses of circular polarisation, attenuating the response to reflected signals. The antenna configuration with the best multipath rejection characteristics as well as the best phase response was the uniform choke ring design with no tapering and a 2λ diameter. This antenna gave a smooth main beam tapering towards the horizon where a pronounced gain pattern cut-off occurs, which decreases the response to reflections without causing unacceptable phase centre variations. The left hand circular polarisation discrimination, which is important for multipath rejection, is uniform over the whole

hemisphere. No diffraction nulls occur at the horizon. The phase pattern is smooth and produces an accuracy of 3 millimetres.

Müller et al (1989) investigated existing data from some European fiducial stations. They found that the period of the multipath error in the pseudoranges was identical to the period of the multipath error of the carrier phase data. If a single dominant source of reflection is present, then the carrier phase multipath error can be deduced from the pseudo-range multipath error. They concluded that the utmost care should be taken in the siting of antennas as masts and wires can generate multipath even at distances of 45 metres.

In summary, it was shown that the behaviour of carrier phase baseline adjustment residuals of a session can already be predicted from the behaviour of the across-frequencies differenced carrier phase pathlength time series. The plots of both these quantities are very similar (Kleusberg, 1986, p.259). This leads to the conclusion that the largest components of the residuals are already present before the individual baseline adjustment and that they can be traced back to causes that affect both frequencies differently. The most likely causes are the ionosphere and geometry related phenomena. The latter is confirmed by the fact that high cross-correlation coefficients are often found in the dispersive delay time series between two consecutive days. Multipath, imaging and phase centre variations are all geometry related. Recent carrier phase multipath investigations (Georgiadou and Kleusberg, 1988) have been carried out over short baselines in order to eliminate the ionospheric component by maximising the ionospheric correlation between the two sites. Tests over longer lines have mainly been carried out in connection with antenna design investigations.

6.4 Proposed Investigation

As the Georgiadou and Kleusberg (1988) method of multipath

analysis was tested on short baselines, the following study analyses the strength of this method using data from a much longer baseline. Data of a 150 kilometre baseline was tested. After finding the across-day cross-correlation of the carrier phase differential dispersive delay time series unsuccessful over this distance, the time variation of this series, in the form of the across-epoch differenced differential dispersive delay time series, was subjected to a cross-correlation analysis. The report that follows describes the mathematical model and the analysis of the data of this test.

7. DETECTION OF MULTIPATH

7.1 Carrier Phase Multipath

7.1.1 Review

Most published methods used to demonstrate signal multipathing involve an investigation of pseudorange multipath, either directly or after a smoothing of pseudoranges with phase information (Evans, 1985, 1987; Bletzacker, 1985; Bishop, 1985). Pseudorange multipath is treated in Section 7.2. Bishop (1985) actually studied the effect of multipath upon the determination of the absolute ionospheric delay and concluded that carrier phase multipath was barely detectable. But for geodesists this "barely detectable" carrier phase multipath is a much larger nuisance than for people that are satisfied with the maximum accuracy obtainable from pseudoranges. When using single frequency receivers, a carrier phase multipath error is normally indistinguishable from a carrier phase change in range. A dual frequency instrument can distinguish a change in range from a dispersive delay or another change affecting each frequency differently.

Georgiadou and Kleusberg (1988) suggest using the differential ionospheric delay (the across-site, across-frequency phase observable) for multipath detection. In the absence of signal multipathing, this delay difference should be constant on short baselines. This requires the use of a dual frequency instrument. Any large variations in this observable would be an indication of multipath, because, if the cause of the variation would be ionospheric both sites would have to be almost equally affected. These authors demonstrated the

success of this method on a 3.5 metre baseline and on a 24 metre baseline.

The multipath study carried out in the context of this thesis shows that this method can be successfully used on baseline lengths of 150 kilometres, if the observable is once more differenced, in order to obtain the time variation of the across-site across-frequency carrier phase pathlength difference. This statement must be qualified by the fact that the observations used here were observed at a time of low solar activity (1987) and at night. The strength of the method using the time variation of the across-frequency across-site differenced carrier phase pathlength observable is remarkable. The results also suggest that the ionospheric changes over a fairly large area can be often more correlated than generally assumed.

7.1.2 Selected Multipath Detection Method

Considering the availability of dual frequency TI 4100 data, the following approach has been pursued. The TI 4100 continuously integrates the observed carrier phase. The resulting L1 and L2 phase observables can be found in the downloaded data for every 3 seconds and have to be multiplied by their appropriate wavelengths of 190.3 mm and 244.2 mm. Differencing of these scaled phase observables results in an across frequency carrier phase pathlength difference that is often called the "dispersive delay" or the "difference in ionospheric delay". The preferred term is the **across-frequency carrier phase pathlength difference.** The multipath signature is a very distinct beat pattern in this pathlength difference, which can be represented as the difference between two approximate sine curves (Georgiadou and Kleusberg, 1988). When the relative signal strength (between the direct and multipath signal) is close to 1, these sine curves start resembling sawtooth functions (Refer to Chapter 12.1). The above mentioned beat pattern consists of periodical enhancements and fading of the L1 and L2 signals. If there is

multipath, L1 and L2 are affected differently as they have a common excess path to travel but use different wavelengths. The so created beat pattern in the phase pathlength difference is modelled in Figure 7.1. This graph was generated using Eq.(8.15), a period of 50 minutes and a relative signal strength of 0.75 between the direct and multipath signals. The horizontal axis shows 1500 intervals of 30 seconds, the vertical axis shows the across-frequency multipath error signature in metres. If no multipath is

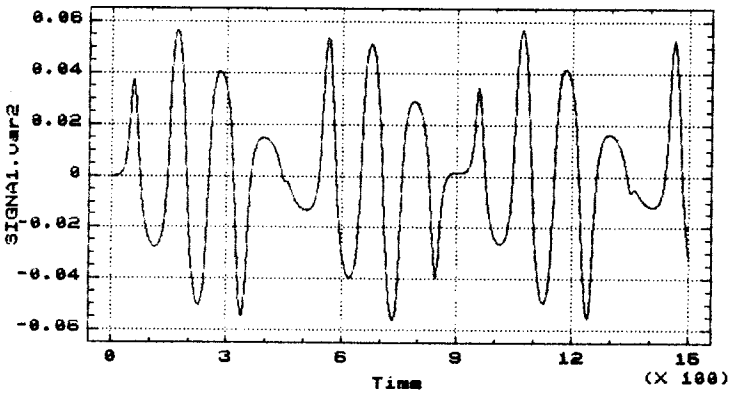

Figure 7.1 The multipath error signature, modelled by differencing the L1 and L2 error curves with amplitudes and periods that are different by a 120/154 ratio.

present, no second signal will superimpose itself upon the direct signal and no beat pattern will occur. If for argument's sake only the L1 signal undergoes reflection, an approximate sine wave beat pattern will occur as an across-frequency error signature. The opposite is also valid and the L2 signal could induce a sine wave beat pattern. If both, L1 and L2, are reflected (as normally is the case), the composite error signature of their difference will show a resonance. As evident in Fig. 7.1 every ninth half-cycle of L1 will be nearly in phase again with every seventh half-cycle of L2, illustrating the 120/154 ratio between the two frequencies. This is because the ratio 7/9 is within two thousandths of the 120/154 ratio. Complete resonance occurs at 77 cycles of L1 and 60 cycles of L2.

Every fifth peak in the beat pattern of Fig. 7.1 is reduced to little more than a point of inflection, preceded by a

subdued fourth peak. At first glance one sees three peaks and a squiggle, followed by a repeat. The maximum error occurs when the direct and indirect signals are 90 degrees out of phase, unless the reflection is very strong (see Chapter 8). After that, the error reduces again until the signals are in opposite phase, which creates a measure of fading of the signal depending upon the strength of the reflection. If the indirect signal is as strong as the direct signal (Chapter 8) and if the error signature is at one of its maxima, the maximum total dispersive delay error could be the sum of the possible maximum errors for each frequency. This is a quarter wavelength for each, totalling 108 millimetres. If more than one very strong reflecting surface is present, another 108 millimetre error could superimpose itself as well, at moments of resonance. Beyond that, ambiguities start to be affected. Because the L1 maximum occurs when the L2 signal is only at 120/154 times L1's phase, the maxima are often smaller and a further reduction takes place because the reflected signal is attenuated for reasons such as the antenna phase pattern response, the reflector's absorption characteristics and the antenna's opposite polarisation rejection. These issues have been treated in Chapter 5.

7.1.3 Differencing Techniques

If no multipath is present, the L1 phase observable gives a measure of the biased phase range to which the relevant ambiguity has to be added to obtain the true range, apart from a few other biases. These biases are the satellite clock offset, the receiver clock offset, the effect of the satellite ephemeris error upon the range and the tropospheric and ionospheric errors. Some of these biases are held in common with the L2 frequency: the satellite clock offset, the receiver clock offset, the effect of the ephemeris error and the tropospheric error. The two phase observables Φ^{L1} and Φ^{L2} can be expressed as:

$$\Phi^{L1} = \rho + c(dt - dT) + \lambda_1 N^{L1} - d_{ion}^{L1} + d_{trop} + mpth^{L1} + d_{eph} + \epsilon \qquad (7.1)$$

$$\Phi^{L2} = \rho + c(dt - dT) + \lambda_2 N^{L2} - d_{ion}^{L2} + d_{trop} + mpth^{L2} + d_{eph} + \epsilon \qquad (7.2)$$

Where: ρ is the true range,
c is the speed of light,
dt is the satellite clock offset,
dT is the receiver clock offset,
N is the ambiguity,
mpth is the multipath error,
d_{trop} is the tropospheric delay,
d_{ion} is the ionospheric delay,
d_{eph} is the effect of the satellite ephemeris error upon the range,
ϵ is the total random noise,
Φ is $\lambda\phi$ where ϕ is the observed phase.

Differencing of the two equations (7.1) and (7.2) leads to the across-frequency carrier phase pathlength differences $\#\Phi$.

$$\#\Phi = \Phi^{L1} - \Phi^{L2} \qquad (7.3a)$$

A new operator, namely #, is introduced to represent the across-frequency difference. The symbol can be imagined to stand for "f minus f". The operator is applied to Φ, as $\#\Phi$. Thus $\#\Phi$ stands for the difference between Φ^{L1} and Φ^{L2}. This differencing eliminates both the satellite and receiver clock offsets as well as the tropospheric error, the effect of the ephemeris error and the true range. Some of the remaining effects will be practically held in common with simultaneous observations recorded at another site. This across-frequency differencing will also eliminate an error like the time-variable receiver phase drift (Evans et al, 1985, p.253), which otherwise requires across-satellite differencing. Substitution of Eqs.(7.1) and (7.2) in Eq.(7.3a) results in:

$$\#\Phi = \#(\lambda N) - \#d_{ion} + \#mpth + \epsilon \qquad (7.3b)$$

The next step in generating a useful observable for multipath detection is the differencing across sites of the across-

frequency differenced carrier phase pathlength. This creates a linear combination of the ambiguities, which is a constant. It also eliminates the bulk of the across-frequency ionospheric delay difference at least as far as the common component at the two separate sites is concerned. Any changes in ionospheric conditions that correlate between the two sites will be eliminated. The two equations that are differenced across sites are:

$$\#\Phi^i = \#(\lambda N^i) - \#d^i_{ion} + \#mpth^i + \epsilon \qquad (7.4)$$

$$\#\Phi^j = \#(\lambda N^j) - \#d^j_{ion} + \#mpth^j + \epsilon \qquad (7.5)$$

Here the multipath effect at site j is (assumed) zero through the choice of one site without reflective surfaces. In Chapter 9 it is shown that one site in this study is a bald hill with no obstacles, in contrast to the rooftop site (i) with a dozen obstacles. Differencing across sites gives:

$$\Delta\#\Phi = \Delta\#(\lambda N) - \Delta\#d_{ion} + \Delta\#mpth + \epsilon \qquad (7.6)$$

The time variation of this observable is very interesting with respect to multipath. Differencing of this observable across the consecutive 30-second epochs eliminates the slow variations which are common to two consecutive epochs and emphasizes the short-periodic variations which are thought to be caused by multipath (Refer to Chapter 7.1.4). It is assumed that the ionospheric component of the across-site across-frequency differenced carrier phase pathlength is only slowly changing in time, compared to the short periodicities of the multipath effect and is differenced out. The cross-correlation of these time variation records between two consecutive days is studied in Chapter 10. Multipath is clearly identified, by consistently showing a significant peak in across-days cross-correlations at a lag of 240 seconds.

Differencing across epochs gives:

$$\delta\Delta\#\Phi = \delta\Delta\#mpth + \epsilon \cong \delta\#mpth + \epsilon \qquad (7.7)$$

For the 150 km baseline this assumption is shown to be applicable when one site has a very reflective environment compared to the other site. The shorter the line the more it is valid. Also the above argument assumes the slow varying components (which are differenced out) to be of ionospheric origin. The possibility that they are caused by multipath could be verified by a study of the spectral density of the across-site across-frequency time series, on two consecutive days.

In Eqs.(7.4) to (7.6) the operators # and Δ apply as follows to the ambiguities and the ionospheric delay difference:

$$\#(\lambda N) = \lambda_1 N^{L1} - \lambda_2 N^{L2} \tag{7.8}$$

$$\Delta\#(\lambda N) = \#(\lambda N^i) - \#(\lambda N^j) \tag{7.9}$$

$$\#d_{ion} = d_{ion}^{L1} - d_{ion}^{L2} \tag{7.10}$$

$$\Delta\#d_{ion} = \#d_{ion}^{i} - \#d_{ion}^{j} \tag{7.11}$$

Often, another observable is formed as a between frequency difference. The so-called "widelane phase observable" is obtained by direct differencing of the actual phase values, without multiplying them by their appropriate wavelengths. This results in a synthetic observable with a 0.86 metre wavelength which is useful for cycle slip detection and ambiguity resolution (see Appendix C):

$$\#^w\phi = \phi_1 - \phi_2 \tag{7.12}$$

Note the superscript "w". Another possible observable is the so-called "ionosphere-free phase observable". This one makes use of the fact that the ionospheric delay is proportional to the square of the frequency. It is of value in cycle slip detection and ambiguity resolution as well as in estimation of the ionospheric delay effect. It is treated in more detail in Appendix B:

$$\#^i\phi = \frac{f_1}{f_1^2 - f_2^2}(f_1\phi_1 - f_2\phi_2) = 2.546\phi_1 - 1.984\phi_2 \tag{7.13}$$

Note the superscript "i". This is also the observable used by King et al (1987, p.83) and Bock (1986b, p.286).

Blewitt (1989, 2nd page) and Kleusberg (1986, p.257) did multiply this phase observable by the L1 wavelength to obtain a value in metres:

$$\#^{i}\Phi = -\lambda_1(\#^{i}\phi) \qquad (7.14)$$

Further details are given in Appendix B. Neither of these variables is used in the actual multipath analysis, although they can be useful for data validation in the data cleaning stage (Appendix B).

7.1.4 Separation of the Ionospheric Component

The data in Chapter 10 shows consistent cross-correlation at a lag of 240 seconds between the time variation files $\delta\Delta\#\Phi$ of the differential dispersive delay on consecutive days of this 150 km baseline. On such a long baseline no or hardly any across-day cross-correlation is found in $\Delta\#\Phi$, the files that have only been differenced across sites and across frequencies. Across-epoch differencing is required. This leaves the question as to its meaning. It may be possible to derive from this phenomenon some statements about the magnitude of the multipath signature and the magnitude of the changes in the ionospheric component of the differential dispersive delay. More clearly, it may be argued that something can be deduced about the magnitude and frequency of the time variation of the across-site across-frequency multipath signature (the multipath component of $\delta\Delta\#\Phi$) and the time variation of the more random ionospheric component of the across-site across-frequency carrier phase pathlength difference (the ionospheric component of $\delta\Delta\#\Phi$).

In principle, these components are composed of one of eight possible combinations of the relative frequencies and amplitudes of the time variations of ionospheric or multipath changes. The dispersive delay can be seen as the sum of a

1	αM	HF	2	αM	LF
	ϵI	LF		ϵI	LF
3	αM	HF	4	αM	LF
	ϵI	HF		ϵI	HF
5	ϵM	HF	6	ϵM	LF
	αI	LF		αI	LF
7	ϵM	HF	8	ϵM	LF
	αI	HF		αI	HF

Table 7.1 Combinations of frequencies and amplitudes.

multipath (M) component and a more random ionospheric (I) component. Multipath (M) has either a slow time variation (LF) relative to differential ionospheric delay changes (I) or a fast time variation (HF). The multipath time variation has either a large amplitude (α) relative to the amplitude of the time variation of the differential ionospheric delay or a small relative amplitude (ϵ). In total there are eight possible combinations of α, ϵ, M, I, HF and LF. This is illustrated in Table 7.1. Of course if none of these (extreme) combinations fits the data, other means will have to be used to separate the ionospheric component from the signal multipath component. Fortunately, it appears that this approach is able to explain the behaviour of data on short as well as on long baselines.

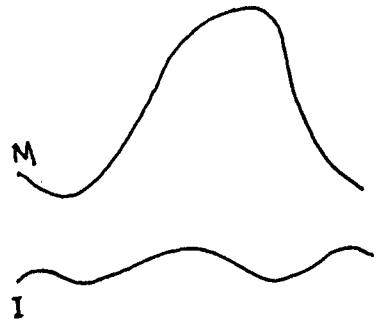

Figure 7.2 Case 2: αM LF and ϵI LF (large amplitude low frequency multipath and small amplitude low frequency ionospheric effect).

Case 2 (Fig. 7.2) is unlikely because a low frequency time variation of the multipath error will be differenced out in across-epoch differencing. A small amplitude ionospheric component will not alter this.

It is not likely that across-day correlation will occur in either the across-epoch differenced ($\delta\Delta\#\Phi$) or undifferenced ($\Delta\#\Phi$) files. This lack of across-day correlation is also to be expected in the combinations 4,6,7 and 8 of Table 7.1. Case 4 (Fig. 7.3) will see the multipath time variation differenced out again because of its low frequency, as far as it is not masked by the random high frequency changes of the ionospheric component. Most likely, no clear across-day cross-correlation will be detected.

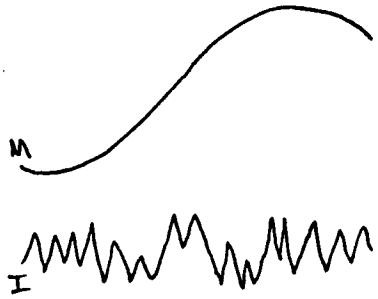

Figure 7.3 Case 4: αM LF and ϵI HF (large amplitude low frequency multipath and small amplitude high frequency ionospheric effect).

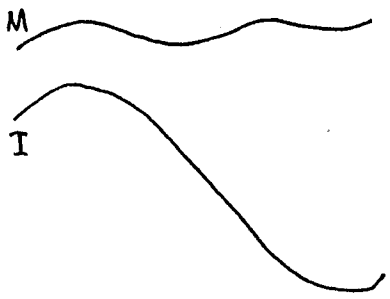

Figure 7.4 Case 6: ϵM LF and αI LF (small amplitude low frequency multipath and large amplitude low frequency ionospheric effect).

Case 6 (Fig. 7.4) results in the small amplitude and slow varying multipath signature being swamped by the large amplitude random changes of the low frequency ionospheric component. Again, no across-day cross-correlation will be detected. In Case 7 (Fig. 7.5) the small amplitude high frequency multipath signature is totally distorted by the large amplitude high frequency ionospheric change component. It will not be possible to detect across-day cross correlation. In Case 8 (Fig. 7.6) the large amplitude high frequency ionospheric component will totally obliterate the

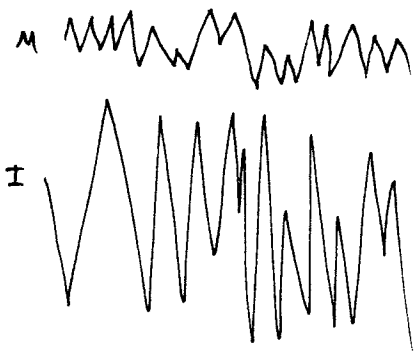

Figure 7.5 Case 7: ϵM HF and αI HF (small amplitude high frequency multipath and large amplitude high frequency ionospheric effect).

small amplitude low frequency changes of the multipath error signature. It will make it near impossible to detect a clear across-day cross-correlation. This leaves the discussion of cases 1, 3 and 5.

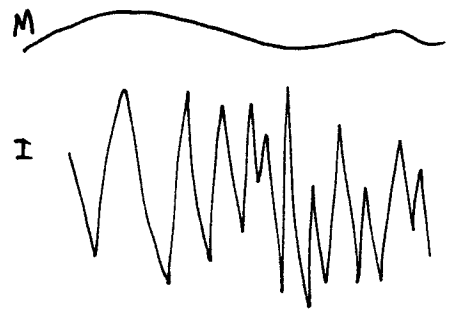

Figure 7.6 Case 8: ϵM LF and αI HF (small amplitude low frequency multipath and large amplitude high frequency ionospheric effect).

In Case 1 (Fig. 7.7) the small amplitude low frequency ionospheric component makes only a small impression upon the multipath signature. It is expected that the files already show across-day correlation before any across-epoch differencing. This does not occur on the 150 km line considered here, although it appears to reflect the situation on short lines. This leads to across-day cross-correlation between the data files without across-epoch differencing. The correlation phenomena for phase data, reported by Georgiadou and Kleusberg (1988), seem to be of this nature.

In Case 3 (Fig. 7.8) the small amplitude high frequency ionospheric component fails to make a large impression on the multipath signature and, again, an across-day correlation

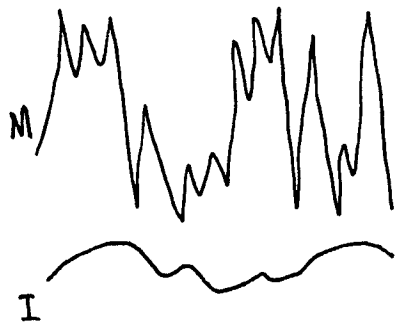

Figure 7.7 Case 1: αM HF and εI LF (large amplitude high frequency multipath and small amplitude low frequency ionospheric effect).

without across-epoch differencing is expected. This does not occur on the 150 km baseline in this study. In Case 5 (Fig. 7.9) the small amplitude high frequency multipath signature is hidden in the data files before across-epoch differencing.

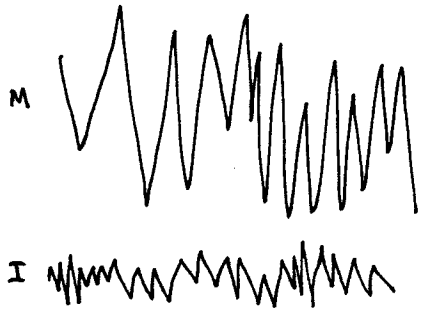

Figure 7.8 Case 3: αM HF and εI HF (large amplitude high frequency multipath and small amplitude high frequency ionospheric effect).

The slow time variation of the large amplitude ionospheric component results in the ionospheric component getting differenced out by across-epoch differencing.

The last case seems to apply to the 150 km baseline studied in this context. On this line the across-day cross correlation does not appear to occur until the across-epoch differencing is carried out. Thus, Case 5 seems to explain the success on long baselines of the method of multipath detection used in this thesis, which is based on the analysis of the short-periodic components of the time variation of the differential dispersive delay.

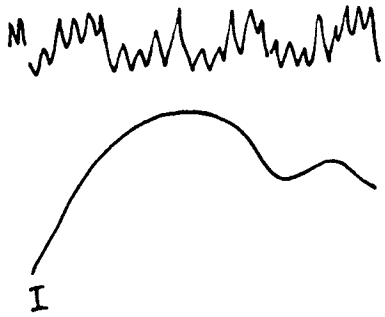

Figure 7.9 Case 5: ϵM HF and αI LF (small amplitude high frequency multipath and large amplitude low frequency ionospheric effect).

7.2 Pseudorange Multipath

7.2.1 Review of Existing Techniques

Pseudorange multipath has been studied by, among others, Evans (1986), Young (1985), Bletzacker (1985) and Bishop et al (1985). Evans (1986) used a modified version of a smoothing approach inspired by Hatch. The smoothing of pseudoranges with carrier phase change in range information is a feature of Hatch's pseudorange smoothing method, which is not intended to be used to study multipath but to reduce its effect upon pseudoranges. This method will be described here first. Hatch starts off with a weighted average of both pseudoranges $\mathbf{P_1}$ and $\mathbf{P_2}$ (Hatch, 1986, p. 1293), in order to bring about a linear combination of pseudoranges where the effect of the ionosphere is the same as in the carrier wide lane observable. The relevant carrier frequencies are used when weighting the two pseudoranges. Following that, they are divided by the sum of the two frequencies.

$$P(1) = (f_1 P_1 + f_2 P_2)/(f_1 + f_2) \qquad \textbf{(7.15)}$$

Indices in brackets, e.g. (1), (2), are epoch sequence numbers. The widelane phase observable (Refer to Eq.(7.12)) is:

$$\#^{w}\phi(1) = (\phi_1 - \phi_2) * 0.862 \qquad \textbf{(7.16)}$$

The operator # and the superscript "w" refer to the widelane across-frequency differencing of the actual phase observable. This is different from the differencing of the carrier phase pathlengths as shown in Chapter 7.1.3. The across-epoch

change in the scaled wide lane observable is added to the frequency weighted pseudorange:

$$\hat{P}(2) = P(1) + [\#^{w}\phi(2) - \#^{w}\phi(1)] \qquad (7.17)$$

This leads to an estimate of the next pseudorange, which is averaged with the next observed pseudorange.

$$\tilde{P}(2) = \hat{P}(2) + [P(2) - \hat{P}(2)]/2 \qquad (7.18)$$

where $\hat{P}$ is the estimated value,
and $\tilde{P}$ is the smoothed value.

Progressive averaging in Eq.(7.18) makes the actual observation contribute less and less while the expectation value gets more and more important. At the n-th observation only 1/n-th of the new observation's non-conformity contributes to the smoothed value (Hatch, 1986):

$$\hat{P}(n) = \tilde{P}(n-1) + [\#^{w}\phi(n) - \#^{w}\phi(n-1)] \qquad (7.19)$$

$$\tilde{P}(n) = \hat{P}(n) + [P(n) - \hat{P}(n)]/n \qquad (7.20)$$

As Hatch's combined observable is manipulated too much to be useful for multipath detection, Evans (1986) devised a method that uses the dual frequency information without Hatch's mixing of the frequencies. The pseudorange observation is corrected for the ionospheric group delay by using the dual frequency information. The carrier phase observable is corrected for phase advance. The change in phase range measurements are accumulated and form a biased phase range which basically represents the same information as the pseudorange, but with very much reduced noise. Subtracting these two values and removing the mean would give a variable which scatters about zero, but is based on one carrier frequency only. This observable represents the receiver noise and the pseudorange multipath because the other external error sources, that are held in common with the carrier phase observable, are removed by differencing. The problem with this method is that it uses the dispersive nature of the data to derive an ionospheric correction. Unfortunately a considerable part of the dispersion is caused by multipath. If this

component is as large as or larger than the ionospheric component of the dispersion, the actual dispersion is no longer a useful measure of the ionospheric electron content. However, when the ionospheric component is dominant, Evans' (1986) method obtains an ionospheric corrected pseudorange multipath time series without differencing between stations.

Bletzacker (1985, p.416) uses a similar method for a squaring receiver (SERIES-X). A squaring receiver delivers the carrier at twice the frequency. Because of this he divides the carrier phase by twice the frequency, before subtracting the resulting biased transit time from the pseudorange transit time. The observables used are double differences.

$$\Delta\phi_1 = c[P_1/(10.23_{10^6}) - \phi_{L1}/(2f_1)] \qquad \textbf{(7.21)}$$

$$\Delta\phi_2 = c[P_2/(10.23_{10^6}) - \phi_{L2}/(2f_2)] \qquad \textbf{(7.22)}$$

where $\mathbf{P_1}$ is the pseudorange **L1** code phase, etc.,
ϕ_{L1} is the **L1** carrier phase, etc.,
c is the speed of light and
Δ means difference.

The resulting observables are a form of carrier phase corrected, site-satellite double differenced, pseudorange phase pathlengths. Subsequently the mean is removed and the resulting systematic wander around the zero value is interpreted as the multipath signature.

Bishop et al (1985) mention that Jorgensen pointed out in 1978 that only one good value of the group delay is needed per pass to calibrate the accumulated phase advance information over the entire pass. About 30 minutes of filtered pseudorange data would supply this, free of pseudorange multipath. This would then be a reasonable bench mark against which to test individual pseudorange observations. This corresponds basically to Bletzacker's method.

7.2.2. New Method of Detection.

The method developed in this thesis differences the pseudoranges between frequencies (symbolised by #P). None of the above methods uses this approach for pseudoranges. The new method also removes common biases through differencing. The equations for the pseudoranges in each frequency are:

$$P1 = \rho + c(dt - dT) + d_{trop} + d_{eph} + d_{ion}^{L1} + Pmpth^{L1} + \epsilon \qquad (7.23)$$

$$P2 = \rho + c(dt - dT) + d_{trop} + d_{eph} + d_{ion}^{L2} + Pmpth^{L2} + \epsilon \qquad (7.24)$$

where: **P1** is the **L1** pseudorange,
P2 is the **L2** pseudorange,
ρ is the true range,
dt is the satellite clock offset,
dT is the receiver clock offset,
$\mathbf{d_{eph}}$ is the range error due to the ephemeris error,
$\mathbf{d_{ion}}$ is the ionospheric correction,
$\mathbf{d_{trop}}$ is the tropospheric correction,
Pmpth is the pseudorange multipath error,
ϵ is the total system noise.

The across-frequency difference between the pseudoranges results in:

$$\#P = \#d_{ion} + \#Pmpth + \epsilon \qquad (7.25)$$

The difference is of the order of five metres and represents the dispersive delay, consisting of a multipath component **#Pmpth** and an ionospheric component $\mathbf{\#d_{ion}}$. The following common biases are removed by the differencing: true range, satellite and receiver clock offsets, tropospheric error and range error due to the ephemeris error. In the context of this multipath study the true range is just another bias. The across-frequency differencing is followed by a differencing across sites:

$$\Delta\#P = \Delta\#d_{ion} + \Delta\#Pmpth + \epsilon \qquad (7.26)$$

Most of the ionospheric component of the dispersive delay is now differenced out. Only the differenced pseudorange multi-

path error remains because the ionospheric delay between two not too distant sites contains a significant common component. Across site differencing removes the bulk of this common component. Thus, $\Delta\#\mathbf{d}_{ion}$ is quite small when compared to the magnitude of the pseudorange multipath effect. This is supported by the fact that no across-epoch differencing is needed to show a high day to day cross correlation at a lag of 240 seconds. It may be concluded that the ionospheric component of the differential dispersive pseudorange delay is small compared to the pseudorange multipath component:

$$\Delta\#P \cong \Delta\#mpth + \epsilon \qquad (7.27)$$

In the case of pseudoranges, the bulk of the across-site, across-frequency pseudorange pathlength difference is actually the pseudorange signal multipath error required for this study.

This method is suitable for analysing long lines of the order of 100 kilometres or more for pseudorange multipath. The method proposed only requires two levels of differencing in order to calculate $\Delta\#\mathbf{P}$. This is analogous to the method developed by Georgiadou and Kleusberg (1988) for carrier phase multipath detection in short baselines.

8. THE MAGNITUDE OF MULTIPATH EFFECTS

8.1 Mathematical Model of Carrier Phase Multipath

If the amplitude of the direct satellite signal **V** is 1.0, the amplitude of the reflected signal can be represented by α, where α is the relative signal strength ($0 < \alpha \leq 1$). A wave may be represented graphically by a vector and the signal voltage detected at the antenna phase centre will be equal to the projection of this vector onto an appropriately defined axis (Bomford, 1971, p.656-657, Rüeger, 1990, p.176). When an

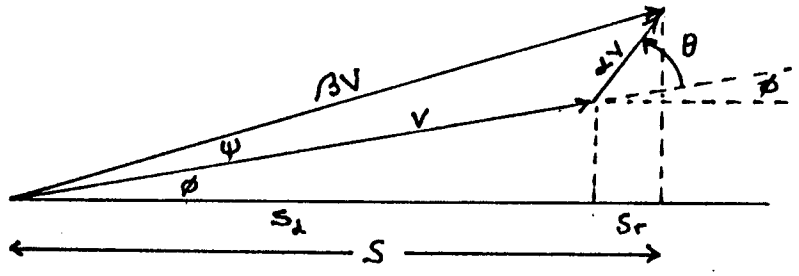

Figure 8.1 Vector representation of the direct and the reflected wave.

interfering wave is received because of a reflection, the received signal voltage at the antenna is equal to the projection of the vector sum of the instantaneous direct and reflected waves. The vector sum can be represented as:

$$\beta V_{\phi+\psi} = V_{\phi} + \alpha V_{\phi+\theta} \qquad (8.1)$$

where α and β are amplitude factors and **V**'s are unit vectors. The signal voltage received is the projection of the resultant, for which is valid (Fig. 8.1):

$$S = S_d + S_r \qquad (8.2)$$

where S_d and S_r are the signal voltages of the direct and reflected waves. In the subsequent development of the carrier phase multipath mathematical model, the formulation by

Georgiadou and Kleusberg (1988) is used as a starting point. If the phase of the direct signal **V** is ϕ and its amplitude 1.0, the signal voltage of the direct signal is:

$$S_d = \cos\phi \tag{8.3}$$

If the relative phase shift of the reflected wave is θ, the signal voltage of the reflected signal is:

$$S_r = \alpha \cos(\phi + \theta) \tag{8.4}$$

The signal voltage of the resultant is:

$$S = \beta \cos(\phi + \psi) \tag{8.5}$$

with β as in Eq.(8.1). Fig. 8.1 illustrates how a value for β can be derived using the cosine rule:

$$\beta = \sqrt{1 + 2\alpha \cos\theta + \alpha^2} \tag{8.6}$$

The angle ψ is the relative phase shift between the direct signal and the combined signal, which itself is the resultant of the direct and indirect signals (see Fig. 8.1).

The vector $\beta\mathbf{V}_{\phi+\psi}$ can be seen as the vector sum of two orthogonal components, one with magnitude $1+\alpha\cos\theta$ and the other with magnitude $\alpha\sin\theta$ which subtends the angle ψ.
From Fig. 8.1 it can be derived that:

$$\tan\psi = \alpha \sin\theta/(1+\alpha\cos\theta) \tag{8.7}$$

thus follows:

$$\psi = \arctan\left(\frac{\sin\theta}{\alpha^{-1}+\cos\theta}\right) \tag{8.8}$$

A derivation of the magnitude of the effect is evaluated on the basis of two cases. First there is the case of $\alpha \ll 1$. The second case is that of values of α that are rather larger, like 1/3, 1/2 tending towards $\alpha = 1$. Unfortunately, Georgiadou and Kleusberg (1988) do not dwell on $\alpha = 1$, where sawtooth-like phenomena come about.

8.1.1 Multipath with Small Voltage Amplitude Factors: $\alpha << 1$

If α is very small it can be shown that:

$$\psi = \arcsin(\alpha \sin\theta) = \alpha \sin\theta \qquad (8.9)$$

and that for small angles ψ the maximum ψ is obtained when θ equals 90 or 270 degrees. In this case (Fig. 8.2):

$$\psi_{max} = \arcsin\alpha \qquad (8.10)$$

It follows from the sum of angles in the shaded triangle in Fig. 8.2 that at ψ_{max}:

$$\theta = \pm(90^{o} + \psi_{max}) \qquad (8.11)$$

Equation (8.11) is rigourous. It follows from Fig. 8.2 that the shaded triangle has a right angle when ψ is at its maximum. Thus $\alpha/1$ is then equal to $\cos(180-\theta)$ or $-\cos\theta$. So θ is equal to $\pm\arccos(-\alpha)$ for extreme values of ψ.

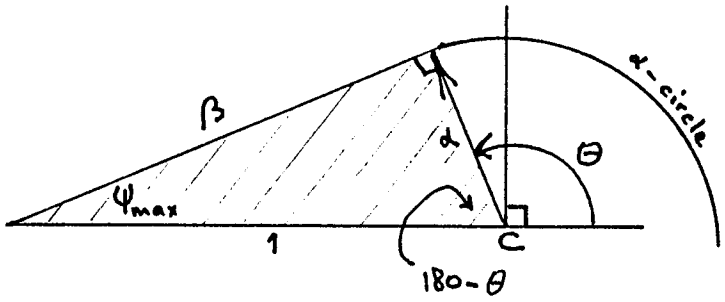

Figure 8.2 The maximum phase shift ψ_{max} as a function of α.

The angle ψ_{max} is the angle between the tangent to the α-circle and the line to the circle centre (see C in Fig. 8.2). This shows that the maximum multipath carrier phase error amplitude depends only upon the voltage amplitude factor (the relative signal strength) of the reflected signal. If α is known the maximum phase error can be quantified. For example, for α = 0.05 the value ψ_{max} is reached for arcsin α = 2.9 degrees. This is 0.008 if expressed as a fractional phase and would produce a maximum multipath error of 0.008 λ = 1.6 mm. The phase shift of the reflected signal at this point according to Eq.(8.11) is 92.9/360 = 0.26 or about 1/4 wavelength.

8.1.2 Multipath with Large Voltage Amplitude Factors: $0.25<\alpha<1.0$

In the case of $\alpha = 0.25$, ψ_{max} is reached for $\psi = \arcsin \alpha = 14.5$ degrees (the phase shift of the resultant). This gives a multipath error of 0.04 λ, or about 8 mm. The phase shift of the reflected signal becomes $\theta = 104.5/360 = 0.29$ or about 1/3 wave length at the time of the maximum error in the resultant.

It is of interest to investigate the behaviour of this model for even larger values of α between 1/2 and 1. It has been demonstrated before that ψ_{max} is the angle that the tangent to the circle described by the relative signal strength vector, makes with the line to the circle's centre (see C in Fig. 8.2). The equation (8.10) for ψ_{max} is rigourous and the value $\theta = 90 + \psi = \arccos(-\alpha)$ is reached at ψ_{max}. The larger α is, the more the tangent to the circle approaches a vertical line. The resultant signal strength vector $\beta V_{\phi+\psi}$ becomes shorter as ψ_{max} moves towards 90 degrees. The signal strength amplitude becomes small while the maximum multipath error approaches one quarter of a full cycle or $\lambda/4$. As the phase shift of the reflected signal is then about 180 degrees and not 90 degrees (as when α is small) the signal soon fades out, leading to a sawtooth effect (Refer to Fig. 12.8). To avoid singularities, it is useful to demonstrate this result with $\alpha = 0.99$. A ψ_{max} of 82 degrees will be reached for an excess path phase shift θ of 172 degrees. The phase shift ψ of the resultant $\beta V_{\phi+\psi}$ is then 0.23 times the wave length leading to a multipath error of 44 mm (L1) or 56 mm (L2). The resultant signal strength is still about 14%.

Poder and Andersen (1965) pointed out that a few strong reflections together can be stronger than the direct signal itself. It seems that the largest multipath errors occur when there is more than one reflected signal. One or a combination of a number of reflected signals (S_{r1} in Fig. 8.3) could have the effect of extinguishing the direct signal S_d, leaving free play to the resultant of the remaining reflections (S_{r2}

in Fig. 8.3) which will impose its full phase shift leading to the combined signal **S** (Merry and Rüther, 1986, p.259). However, Young (1985) suggests that multiple reflections are unlikely to be coherent. In this thesis it is shown that this might be valid sometimes but that a beat pattern may occur at other times. Such beat patterns are due to reflected signal phases not being random but having quite a deterministic component through their common time origin. Because of this they can be quite destructive (Refer to the simulation studies in Chapter 12).

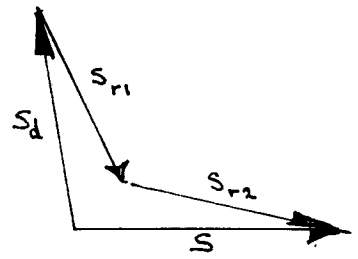

Figure 8.3 Multiple reflections.

8.1.3 Error Signature of Multipath

The error signature of multipath is studied by Georgiadou and Kleusberg (1988) by deriving a combined observable which eliminates the nuisance parameters like clock errors, the tropospheric error and the range error due to the satellite ephemeris error (Chapter 7.1.3). This observable

$$\#\Phi = \lambda_2\phi_2 - \lambda_1\phi_1 \qquad (8.12)$$

is also called the ionospheric delay difference, or the dispersive delay. As ϕ_1 and ϕ_2 each have a multipath induced phase shift, the observable can be rewritten as:

$$\#\Phi = \lambda_2(\phi_2 + \psi_2) - \lambda_1(\phi_1 + \psi_1) \qquad (8.13)$$

The multipath component of the across-frequency difference in phase pathlength is:

$$\#mpth = \lambda_2\psi_2 - \lambda_1\psi_1 \qquad (8.14)$$

Bishop et al (1985) showed that the amplitudes of the phase error variations ψ_{max} are equal for carriers of different frequencies, but that the periods of ψ_{max} variations will be different, in proportion to their frequency ratio and the

ratio of their phase centre heights above the ground plane. Thus this phase relationship can be substituted into the individual expressions for ψ. Allowing for the frequency ratio, Georgiadou and Kleusberg (1988, p.174) use $\theta_2 = 120/154\ \theta_1$ as the relationship between the phase shifts in each frequency and, using Eq.(8.8), arrive at:

$$\#mpth = \frac{\lambda_2}{2\pi}\left[\arctan\left(\frac{\alpha\sin 0.779\theta_1}{1 + \alpha\cos 0.779\theta_1}\right)\right] - \frac{\lambda_1}{2\pi}\left[\arctan\left(\frac{\alpha\sin\theta_1}{1 + \alpha\cos\theta_1}\right)\right] \qquad (8.15)$$

The current author neglects the phase centre effect. The division by 2π converts the angular values in radians to fractional phases and multiplication with the wavelengths results in units of metres for **#mpth** in Eq.(8.15). This equation expresses the multipath error signature as a function of the individual phase shifts of the **L1** and **L2** reflected rays. Resonance of this differenced observable occurs now and then, because of the 120/154 ratio between f_1 and f_2. Beats occur at 7/9 harmonics which differs less than one percent from the 120/154 ratio. In such cases and for small α values, the resultant across-frequency difference is at one of its maxima. Its amplitude can be written as:

$$\#mpth = [(\lambda_1 + \lambda_2)\ \arctan\ \alpha]/2\pi \qquad (8.16)$$

For voltage amplitude factors α near 1, a maximum value for the multipath error signature is reached of 1/4 times the sum of the wavelengths, because the maxima occur near θ = 180 degrees + $2k\pi$, where k is an integer. The maximum amplitude can be given as:

$$[(\lambda_1 + \lambda_2)\ \arctan\ \infty\ ]/2\pi = (\lambda_1 + \lambda_2)/4 \qquad (8.17)$$

As mentioned in Chapter 2, it is expected that a number of reflecting sources will contribute to the combined amplitude and phase received at the antenna. An inspection of the actual observation record will have to give the final say on any quantification of the multipath effect. In Chapter 10 it is shown that amplitudes of over 100 mm do occur in the

across-site across-frequency observation record, 50 mm variations are not uncommon and 5-10 mm variations are usual. The vector diagram in Fig.8.4 shows the effect of multiple reflections. From Fig.8.4, the multipath carrier phase error

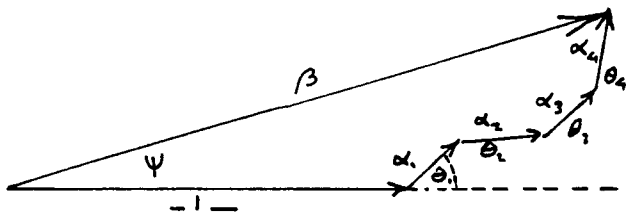

Figure 8.4 Vector sum of multiple reflections.

can be derived as:

$$\tan \psi = \Sigma\alpha_i \sin \theta_i / (1+\Sigma\alpha_i \cos \theta_i) \qquad \textbf{(8.18)}$$

The multipath component of the across-frequency differenced observable is:

$$\#mpth = (\lambda_1\psi_1 - \lambda_2\psi_2)/(2\pi) \qquad \textbf{(8.19)}$$

Substitution of Eq.(8.18) in Eq.(8.19) leads to the following across-frequency multipath error:

$$\#mpth = \frac{\lambda_2}{2\pi}\left[\arctan\left(\frac{\Sigma\alpha_i \sin 0.779\theta_i}{1 + \Sigma\alpha_i \cos 0.779\theta_i}\right)\right] - \frac{\lambda_1}{2\pi}\left[\arctan\left(\frac{\Sigma\alpha_i \sin\theta_i}{1 + \Sigma\alpha_i \cos\theta_i}\right)\right] \qquad (8.20)$$

This equation for a combination of reflections has been used in the multipath simulation study in Chapter 12.

After two levels of differencing a significant amount of noise is filtered out of Δ#Φ that would have affected both frequencies equally or both sites equally. The main remaining unknown is the twice differenced ionospheric delay, which is called the ionospheric component of the across-site across-frequency carrier phase pathlength difference.

The change in electron content at one site at night in a calm

year of the solar cycle is typically one half to one full unit of 10^{16} electrons per m^2 (Leitinger and Putz, 1988). A total electron content unit of 10^{16} electrons per m^2 is called one TEC unit. The TEC change at a nearby site will be heavily correlated. The correlation will be higher the closer the sites are. A change of electron content of one TEC unit brings about a change of 0.1 metre in the across frequency carrier phase pathlength difference (0.162 m in L1 minus 0.267 m in L2). This can be demonstrated as follows:

$$\#\Phi = \lambda_1 \left(\phi_1 + \frac{1.3436 N_{TEC}^{units}}{f_1^{Ghz}} \right) - \lambda_2 \left(\phi_2 + \frac{1.3436 N_{TEC}^{units}}{f_2^{Ghz}} \right) \qquad \textbf{(8.21)}$$

$$d(\#\Phi) = \frac{1.3436\ c}{10^9} \left(\frac{1}{f_1^2} - \frac{1}{f_2^2} \right) dN_{TEC}^{units} \qquad \textbf{(8.22)}$$

$$0.105\ dN_{TEC}^{units} = d(\#\Phi)\ metres \qquad \textbf{(8.23)}$$

where **c** is the speed of light.

Although the other site might measure a slightly different total electron content (TEC), the time variation of this difference would statistically be no more than 1.5 times the variation of TEC at an individual site. This assumes a worst case, where the TEC at both stations are not correlated at all. After the next level of differencing, it would be extremely unusual to find another 0.1 metre variation due to the effect of ionospheric changes upon the across-site across-frequency carrier phase pathlength difference, in particular, if night observations are used during a calm period of the solar cycle. This is the strength of this differencing technique.

It is possible that the change induced by the ionospheric delay variation on the once differenced carrier phase path-length difference observable #Φ is no more than a linear trend of 50 mm over a five hour period. The change in the twice differenced phase length observable Δ#Φ is expected to be smaller again. It would be wrong to read ionospheric

causes into the short term changes in the Δ## observables. These changes, as mentioned above, are too large to have ionospheric causes and appear to show across-day correlations. This is not true if extreme latitudes, equatorial regions, short period ionospheric scintillations or increased ionospheric activity are involved. In contrast, the randomness of ionospheric changes would ruin any across-day correlation. It is striking that the cross-correlation functions of δΔ##, the across epoch differenced Δ## files, without exception, show such a distinct peak in correlation at a 240 second delay in the observation records of two consecutive days (see Chapter 10). This leaves multipath as the major short periodic error source in these differenced observation files and the most likely cause of even fairly large (correlated) changes up to the order of about a decimetre.

8.1.4 Phase Shift θ of the Reflected Signal

Derivations of the phase angle of multipath are usually based on a vertical plane through the satellite, the receiver antenna and the reflector, in which the reflective plane is horizontal, vertical and, sometimes, skew (see Figs. 8.5, 8.6 and 8.7). The characteristic feature is that the azimuth to the satellite is the same or 180 degrees different from the azimuth to the point of reflection. The determining variables are then the perpendicular distance to the reflective plane

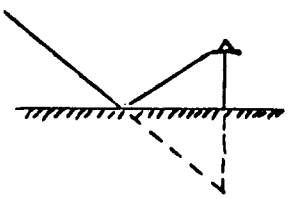

Figure 8.5 Reflection from a horizontal surface.

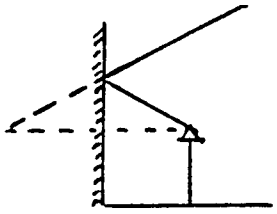

Figure 8.6 Reflection from a vertical surface.

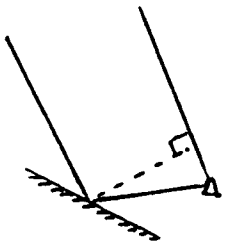

Figure 8.7 Reflection from a skew surface.

and the elevation of the satellite above the reflective plane.

Sometimes it is hard to pinpoint these variables but the distance to the reflector is roughly known as well as the elevation and azimuth of the satellite in a local topocentric coordinate system. A generalised formula is developed, which is capable of describing hemispherical reflections and edge diffractions as well as specular reflections in special cases when certain conditions are met. This gives a description of the pathlength difference, independent of the orientation of the reflective plane (see Fig. 8.8). In Fig. 8.8 **ΔH** is the vertical height difference between the antenna phase centre and the point of reflection.

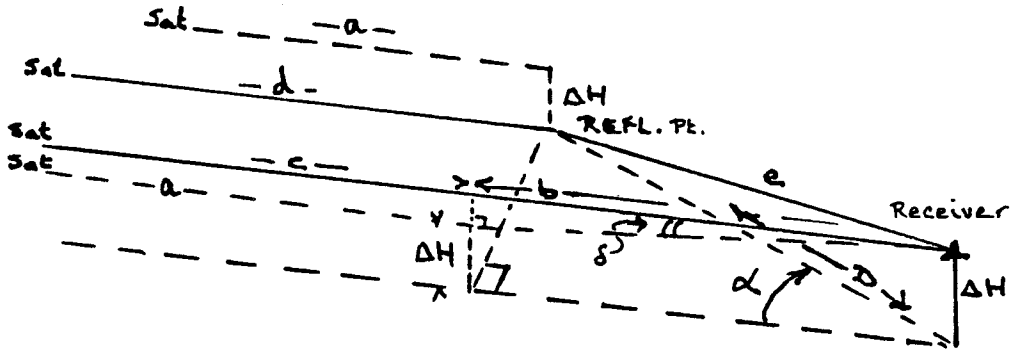

Figure 8.8 The excess pathlength d+e-(c+b).

The carrier phase pathlength difference can be written as a function of the azimuth and elevation of the satellite and the horizontal distance **D** and height difference **ΔH** to a suspected reflective spot. This formula is applicable for hemispherical reflections coming from an idealised point source. For an exploratory investigation of multipath this is very useful and less restrictive than methods that use the perpendicular distance to the reflective surface. For example, it allows the treatment of edge diffraction of the top of a cylindrical vent pipe situated near the antenna, where the pipe might not be high enough to give vertical reflections from satellites above the customary 15 degree mask angle. The antenna could be receiving such edge diffractions from the top of the vent pipe originating from satellites at various azimuths. The geometric treatment

involves basically the taking of differences between the satellite-to-reflector path length **d** and the satellite-to-antenna pathlength **c + b** and the adding to this of the path length **e** from the reflector to the antenna:

$$d + e - (c + b) = a - \Delta H \sin \delta + \sqrt{D^2 + (\Delta H)^2} - (a - b \sin^2 \delta + b) \qquad (8.24)$$

This results in the expression for the pathlength difference:

$$ep = -D \cos \alpha \cos \delta - \Delta H \sin \delta + \sqrt{D^2 + (\Delta H)^2} \qquad (8.25)$$

where **b** = **D** cos **α**/cos **δ**,

ep is the excess pathlength,

α is the angle between the satellite and the point of reflection,

D is the horizontal distance to the point of reflection,

δ is the elevation of the satellite.

The sign of the height difference **ΔH** is taken negative if the point of reflection is below the antenna phase centre.

The time variation of the phase shift (**dθ/dt**) has been derived as:

$$\frac{d\theta}{dt} = (D \cos \alpha \sin \delta - \Delta H \cos \delta) \frac{d\delta}{dt} + D \cos \delta \sin \alpha \frac{d\alpha}{dt} \qquad (8.26)$$

Horizontal specular reflection in a vertical plane through the satellite, the receiver and the point of reflection, follows as a special case, with **α** = 0 and **D** =**ΔHcot δ**. This leads to the pathlength difference for specular reflection from a horizontal surface:

$$ep = (1/\sin\delta)\,(|\Delta H|\cos^2\delta - |\Delta H|\sin^2\delta - |\Delta H|) \qquad (8.27)$$

which is equal to:

$$ep = 2\Delta H \sin\delta \qquad (8.28)$$

and agrees with Georgiadou and Kleusberg (1988, p.173). This has to be divided by the wavelength to obtain the phase

shift. If the latter is required in radians, it should also be multiplied by 2π.

The frequency of this (specular reflection) multipath error is the time variation of the phase shift:

$$\frac{d\theta}{dt} = \left(\frac{2\Delta H}{\lambda}\right) \cos\delta \frac{d\delta}{dt} \qquad (8.29)$$

The multipath period (in minutes) is obtained by taking the reciprocal value and division by 60. This is valid for any specular reflection from a horizontal surface ΔH below the phase centre of the antenna.

8.2 Mathematical Model of Pseudorange Multipath

Multipathing of the pseudorange signal is a multipathing of a modulated signal. Analogies exist in the treatment of ground swing in microwave electronic distance measurement (EDM) (Bomford 1971, Yaskowich 1964, Merry and Rüther 1986, Poder and Andersen 1965). In microwave EDM the equation for the phase shift was derived for a reflection from a mid point. The resultant of the side bands of a frequency modulated wave is in quadrature with the carrier. In GPS, the P-code, after it is modified by the satellite message through a modulo-2 addition, is modulated onto the carrier through a binary bi-phase modulation (Wells, 1986). In a normal phase modulation, the resultant of the side bands are in quadrature with the carrier, just like with frequency modulation, which would suggest that a similar approach to that in microwave EDM could be taken in the derivation of the multipath phase shift. But the bi-phase modulation in GPS is a flip-flop modulation (Spilker, 1980, Talbot, 1987), where the carrier phase is shifted in response to the code content of the P-code. This modulation can be seen as a kind of amplitude modulation with two phase states (Wells, 1988):

$$y = A(t) \cos(\omega t + \phi) \qquad (8.30)$$

Here the amplitude A(t) takes either the value +1 or -1, when

the binary P-code is 0 or 1, respectively. The result is either a phase shift of zero or one of 180 degrees.

Young (1985) has published an equation for the phase shift in the case of pseudorange (satellite) multipath valid for a reflected signal strength of 1 % of the direct signal. But his equation is valid only for a squaring receiver which recovers the carrier at twice the frequency. The factor two occurring in the terms referring to the carrier frequency, is expected to disappear in the derivation of an equation for a code correlating receiver.

Multipathing of the signal interferes with the code correlation process. The current author has not seen a direct equation which can be applied to a code correlating receiver. Spilker (1980) shows how the modulation described above is removed and the carrier and the code are recovered in a code correlating tracking delay lock loop. The synchronisation of the receiver occurs through an early/late delay gate implementation as shown in Figure 5.1 in Chapter 5. Bishop et al (1985) and Müller et al (1989) show a set of implicit equations for the code correlator, derived from a study by General Dynamics, which leads to graphs for the resulting group delay error. A knowledge of the description of the tracking delay lock loop given by Spilker (1980, p.47-48) is required in order to follow the treatment of the early/late delay gate error function in Bishop et al (1985, p.391-392) and Müller et al (1989, p.835-836). The derivation of the error function will be summarised below.

In Chapter 5 it is shown how the tracking loop determines the relative signal delay by splitting the received signal and multiplying it with an early delay and a late delay signal generated by the receiver's own code generator. These outputs of early and late delay are subtracted from each other and the result generates a correction signal which, through a voltage controlled oscillator, brings about the synchronisation of the receiver generated code with the received satellite P-code signal. For a synchronised signal

the early/late gate error function **D(τ)** is (see Eq.(5.1)):

$$D(\tau) = [\textit{late delay signal}] - [\textit{early delay signal}] = 0 \qquad \textbf{(8.31)}$$

D(τ) in itself is unitless, but is a measure of the voltage in the code correlating voltage controlled oscillator described in Chapter 5.1. When multipath is present code correlation is achieved with the affected resultant instead of the direct signal (see Eq.(5.2)):

$$\begin{aligned} D(\tau) = {} & [\textit{late delay signal}] - [\textit{early delay signal}] + \\ & + \alpha[\textit{multipathed late delay signal}] + \\ & - \alpha[\textit{multipathed early delay signal}] = 0 \end{aligned} \qquad \textbf{(8.32)}$$

where:

$$[\textit{late delay signal}] = R(\tau + \tau_d)\cos\psi \qquad \textbf{(8.33)}$$

$$[\textit{early delay signal}] = R(\tau - \tau_d)\cos\psi \qquad \textbf{(8.34)}$$

$$\begin{aligned} \alpha[\textit{multipathed late delay signal}] = \\ = \alpha R(\tau+\tau_d-\delta)\cos(\theta-\psi) \end{aligned} \qquad \textbf{(8.35)}$$

$$\begin{aligned} \alpha[\textit{multipathed early delay signal}] = \\ = \alpha R(\tau-\tau_d-\delta)\cos(\theta-\psi) \end{aligned} \qquad \textbf{(8.36)}$$

and where:

$$\psi = \arctan\left[\frac{\alpha R(\tau - \delta)\sin\theta}{R(\tau) + \alpha R(\tau - \delta)\cos\theta}\right] \qquad \textbf{(8.37)}$$

$$R(x) = 1 - \frac{|x|}{T} = 1 - \frac{|x|}{97.75} \qquad \textbf{(8.38)}$$

with **R(x) = 0** for **|x| > T**.

The variables used are:

τ_d = **T/2** = 97.75/2 nsec early/late delay,

ep is the excess pathlength,

δ = **ep/c**, the time taken along the excess path (with **c** the speed of light),

T is the pseudo random noise chipping time (reciprocal of 10.23 Mhz),

τ is the group delay error,

$\theta = 2\pi(\mathbf{ep})/\lambda \quad (=2\pi \mathbf{f}\delta)$,

α is the voltage ratio between the indirect and direct signals,

$\mathbf{x}$ is the time variable in the code cross-correlation function $\mathbf{R}$, like τ, as in Eqns.(8.33) to (8.37).

Once the excess pathlength **ep** is known, the phase shift θ of the indirect signal and the multipath caused delay δ can be obtained. If a value is adopted for the voltage amplitude factor α (the signal strength ratio) one can work out an expression for the phase shift ψ of the resultant of the direct and indirect signals which contains the group delay implicitly. A set of implicit equations for the group delay τ can be obtained as graphically illustrated by Bishop et al (1985). The graph is presented in Fig. 8.9. The equation in Bishop et al (1985) for the multipathed early delayed signal contains an error in the sign of δ [Eq.(5) in Bishop et al, 1985]. Müller et al (1989) display this equation correctly [Eq.(4a) in Müller et al, 1989]. It is illustrative to look at this implicit equation for those values of $\mathbf{R}(\mathbf{x})$ where $|\mathbf{x}| < \mathbf{T}$. The particular form of the equation is in this case:

$$-\eta|\tau+49|+\eta|\tau-49|-\gamma\left|\tau+49-\frac{ep}{c}\right|+\gamma\left|\tau-49-\frac{ep}{c}\right| = 0 \qquad \textbf{(8.39)}$$

where:

η is a function of the phase shift of the combined signal containing the group delay implicitly: $\eta = \cos\psi$,

γ is a function of α, θ and ψ which itself is a function of the group delay: $\gamma = \alpha\cos(\theta-\psi)$,

τ is the group delay in nanoseconds.

The terms of Eq.(8.39) are absolute values of functions of the group delay, from which the group delay has to be solved, leading to two extreme values for the group delay for each value of the phase shift of the multipathed signal. Such a solution creates part of the envelope of the gate error function as illustrated by Bishop et al (1985) and Müller et al (1989) (see Fig. 8.9).

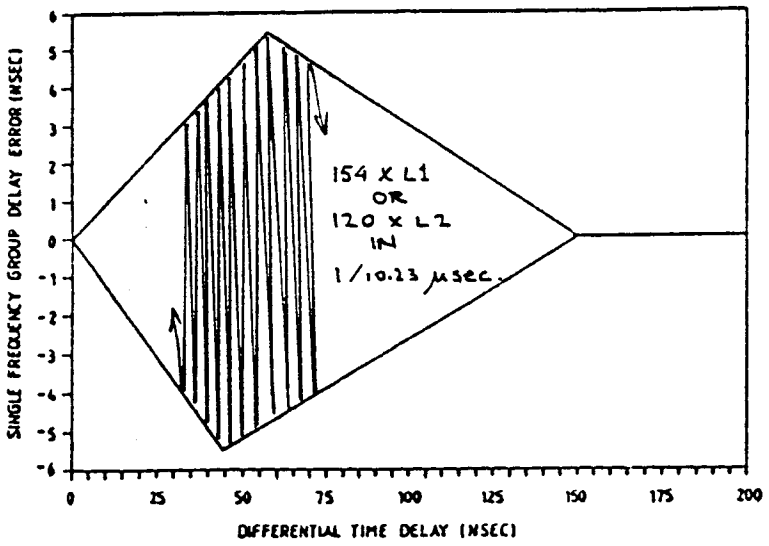

Figure 8.9 The early/late delay gate error function for α = 0.11 (after Bishop et al, 1985).

The early/late delay error envelope "opens up" when multipath is present and its amplitude is then determined by the relative signal strength of the indirect signal. The maximum multipath caused amplitude of the group delay error is generally expected to be 24 nanoseconds (one quarter of the P-code chip length) or 7.3 metres (Spilker, 1980, p.53), but theoretically the code correlator will not reject an out of phase signal until the multipath delay reaches 150 nanoseconds or 45 metres.

It appears that in response to a change in the voltage amplitude factor α the θ-value (on the horizontal axis in Fig.8.9), at which the maximum of the envelope figure occurs, will change. This is analogous to what happens with the multipathed carrier phase signal. Figure 8.9 illustrates how the maximum group delay error (5.5 nanoseconds for a relative signal strength α of 0.11) is situated at about 50 nanoseconds differential time delay. For an α value of near 1 the position and amplitude of this maximum will be different. The position of the maximum in the group delay will be shifted forward on the differential time delay axis (Spilker, 1980, p.53) and result in a multipath error of 24 nanoseconds or 7.3 metres. The amplitudes of these maxima are determined by the envelope of the early/late delay gate error

function (Fig. 8.9). The amplitude of the envelope is determined by the voltage amplitude factor of the indirect signal or, in other words, the strength of the reflection.

While the relative delay between the modulation on the direct signal and the modulation on the indirect signal goes from 0° to 360° the error function undergoes 120 maxima for the L2 signal and 154 maxima for the L1 signal. The pathlength difference has to change a full 30-odd metres for the error function to run its full cycle within the envelope. During this the carrier can repetitively run through a 0.2 metre pathlength difference and as such bring about a pseudorange change between the two extreme values allowed by the code correlation gate error function envelope.

9. TESTS IN A REFLECTIVE ENVIRONMENT

Data of TI 4100 observations at Mulley Geodetic Station from 12-9-87 and 13-9-87 were used in this multipath study, part of a 1987 GPS network across New South Wales. This network extends from the Queensland border in the north to the Victorian border in the south, over a distance of about 800 kilometres (Dickson, 1989). Each station was observed throughout a five hour window. Four TI 4100 receivers were used (rented from Nortech of Canada), creating a double chain of quadrilaterals along the eastern 200 km of New South Wales. In consequence the stations on the centreline of the double chain were occupied on four consecutive days. This makes it possible to cross-correlate data between consecutive days and to study the effect of signal multipathing. A station with a highly reflective environment happened to be one of these stations: Mulley Geodetic Station, on the roof of the building of the Land Information Centre (previously the Central Mapping Authority) in Bathurst, NSW. Another station on this centreline was Junction Geodetic Station. The network's baselines were processed in 1987 and the raw TI 4100 data sets stored in Nortech binary format.

9.1 Station Description

The geodetic station **Mulley** has been chosen for this multipath study as it is a station on a rooftop with many potentially reflective obstacles. In order to use the bias eliminating strength of differencing techniques, the line to the geodetic station called **Junction** was chosen as the latter is not expected to be affected by multipath. Junction Geodetic Station is situated on top of a bald, obstacle free hill.

The Figures 9.1 and 9.2 show the difference in noise of the pseudorange observations at each station on 12-9-87 for Satellite 9. The vertical axis shows the across-frequency pseudorange delay pathlength differences **#P** in metres. The

horizontal axis shows the number of 30-second sampling intervals. The TI 4100 recorded an observation every 3 seconds, these were sampled at intervals of 30 seconds by the software (see Appendix C), beginning at 20:22 AEST and finishing at 01:38 AEST. Fig. 9.1 refers to Mulley, displaying a 4 metre wide band of noise. Fig. 9.2 refers to Junction, displaying a 2 metre wide band of noise.

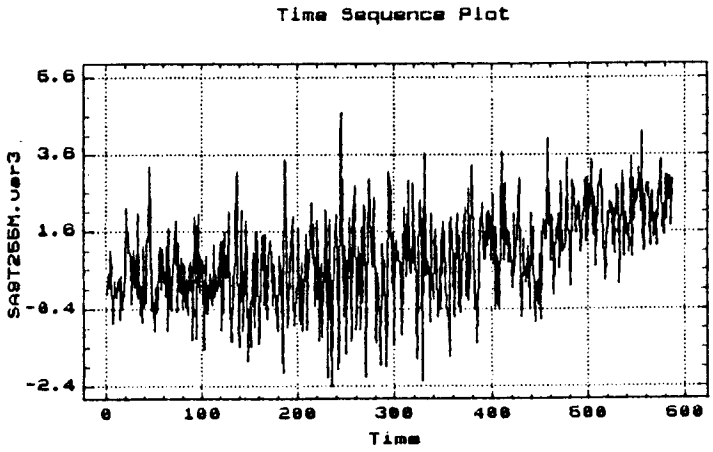

Figure 9.1 Pseudorange record #P, at Mulley (Satellite 9).

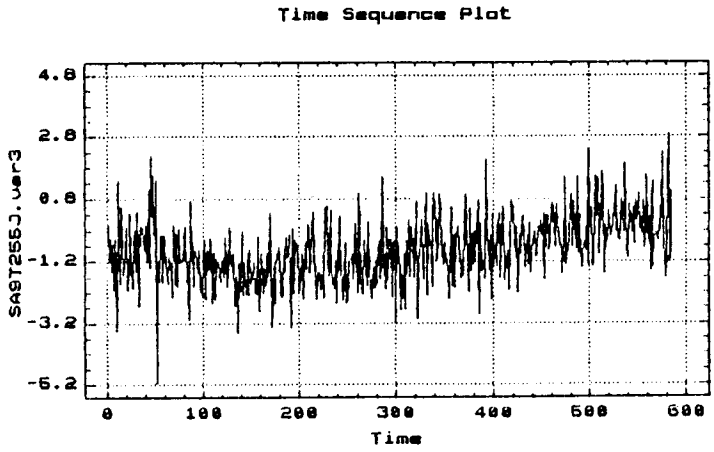

Figure 9.2 Pseudorange record #P, at Junction (Satellite 9).

Often an offset from zero has been noticed in TI4100 **#P** time series, possibly due to delays resulting from **P1** and **P2** code generation in the receiver (Kleusberg, 1990). The offsets from zero in Figs. 9.1 and 9.2 are firstly caused by subtracting the first value from all further values as described in Chapter 9.3.4. The across-frequency carrier phase pathlength difference #Φ changed more than one metre

during the observation session. This happened at both stations, as shown in Figs. 9.3 and 9.4. The vertical axis shows the across-frequency carrier phase pathlength differences #$ in metres, the horizontal axis shows the number of 30-second sampling intervals. The correlation is obvious. The same trend is displayed in the pseudorange

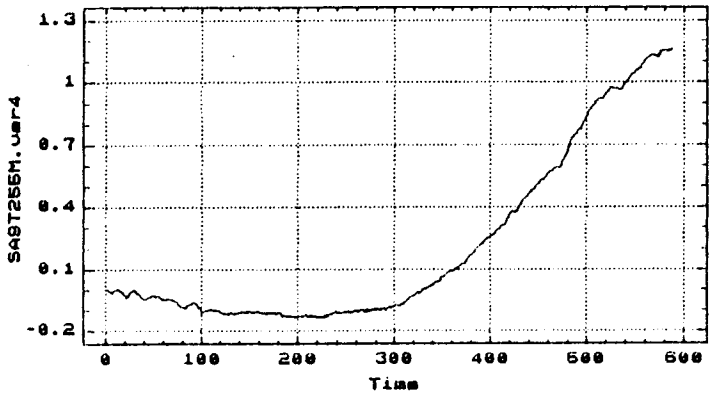

Figure 9.3 The carrier phase record #$ at Mulley (Satellite 9) displaying the ionospheric effect.

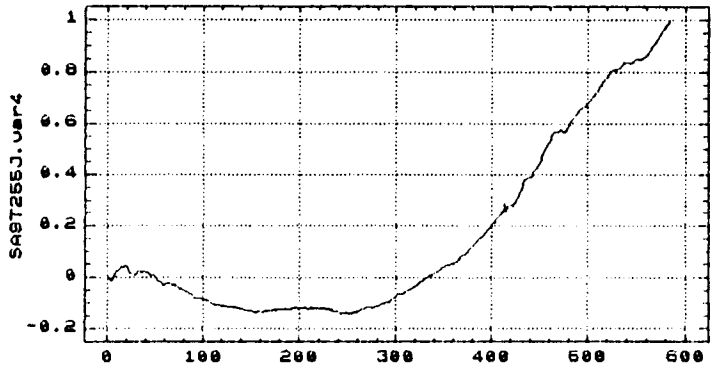

Figure 9.4 The carrier phase #$ record at Junction (Satellite 9). Again, the ionospheric effect is visible, changing the pathlength difference.

records #P of Figs. 9.1 and 9.2. This is the ionospheric effect, brought about by both the elapsing of time (the recombination of ions and electrons while the day progresses) and the change in the elevation of the line of sight to the satellite. The effect of the latter can be three times the at-zenith value of the ionospheric delay. The time variation of this gradual change is noisier at the station Mulley. The Figures 9.5 and 9.6 show the difference in noise of the

carrier phase observations at each station. The vertical axes show $\delta\#\Phi$, the across-epoch across-frequency phase pathlength differences. The units on these axes are millimetres. The legend at the top of the axis shows that they should be multiplied by 1/1000 to obtain metres. These figures refer to Satellite 9 but are quite representative. They suggest that

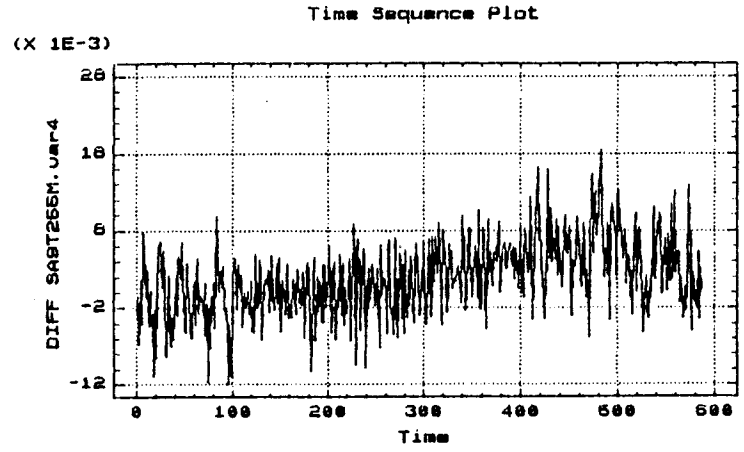

Figure 9.5 Carrier phase noise of about 10 mm in $\delta\#\Phi$, at Mulley (Satellite 9).

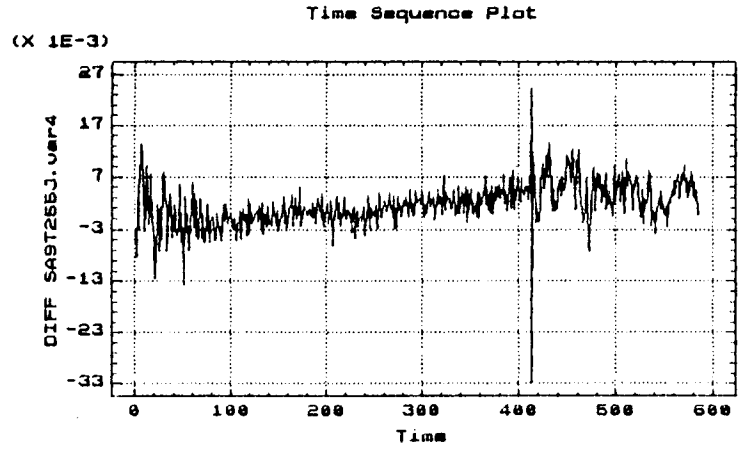

Figure 9.6 Carrier phase noise of about 5 mm in $\delta\#\Phi$, at Junction (Satellite 9).

the choice of stations was reasonably successful: in both the cases of the pseudoranges and the carrier phases, the noise at Junction is about half that of the noise at Mulley. It is therefore justified to assume that multipathing only occurs at the rooftop station, difference the data with the Junction data and qualify the conclusions later as being biased to some extent by this assumption. The results reported in Chapter 10 include these across-site differenced

observations as the starting point of the analysis.
The rooftop station Mulley has a variety of obstacles: five chimneys, two vents, two cylindrical objects with a conical top, two concrete pillars, 60 metres of handrails surrounding the observation site, as well as a two metre high wire aerial at a distance of about 14 metres. A locality sketch for the rooftop station Mulley is given in Fig. 9.7. It illustrates possible sources of reflections, apart from the roof surface itself.

9.2 Data Description

The TI 4100 data, used in this multipath study, comprised about 5 hours of observations on two stations on each of two

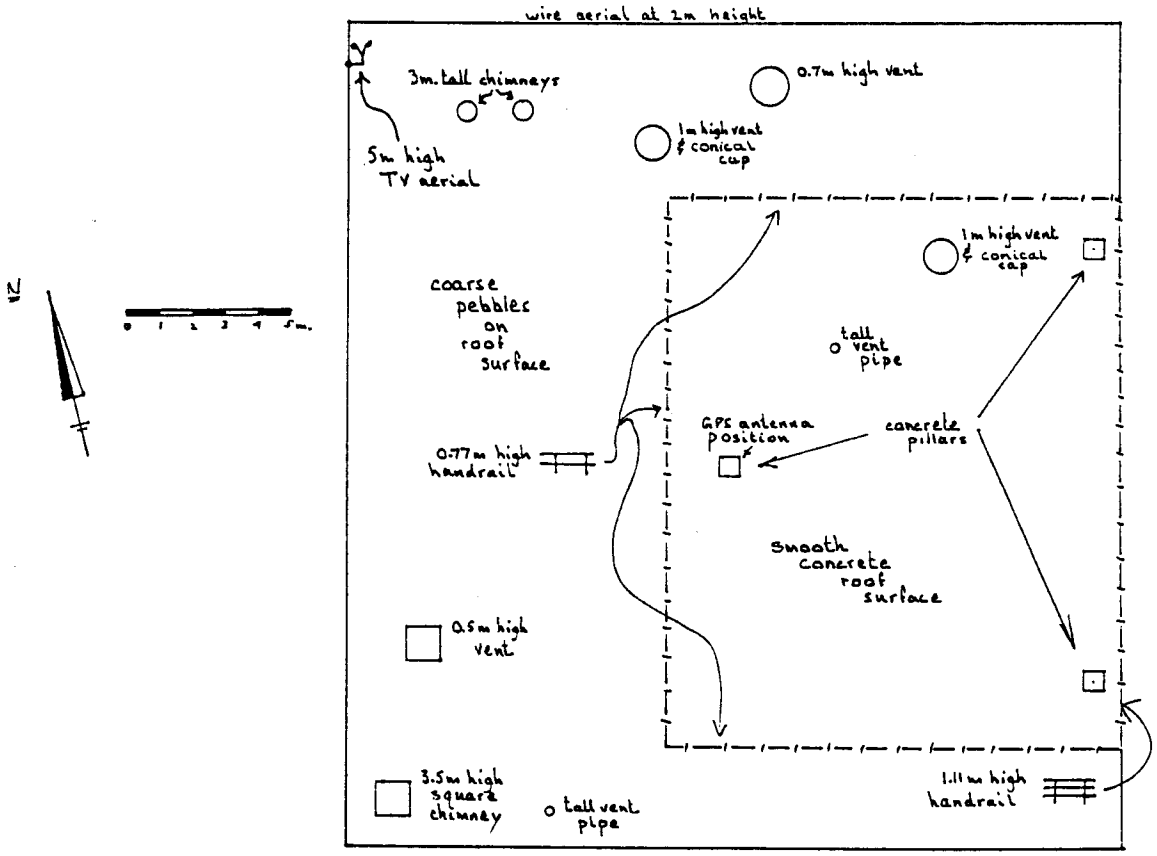

Figure 9.7 Locality sketch of the rooftop station at Mulley.

AZIMUTH, ELEVATION & TIME

Station : MULLEY — Latitude = 33.2600 South
Cut-off Elevation = 15 — Longitude = 149.3400 East
Date :12/ 9/1987 — Time 19.0000 --> 3.0000 — Zone = 10.0000

Time	Satellite 03		Satellite 06		Satellite 08		Satellite 09		Satellite 11		Satellite 12		Satellite 13	
	Az	El	Az	El	Az	El	Az	El	Az	El	Az	El	Az	El
19.00			232.1	28.4	28.5	31.4								
19.10			227.5	30.6	31.1	36.3								
19.20			222.4	33.3	33.6	41.1								
19.30			217.6	35.6	37.1	46.0								
19.40			213.0	38.3	41.1	50.5			1.2	19.4				
19.50			208.0	41.1	46.2	55.2			1.4	24.3				
20.00			202.5	44.0	52.6	59.4			1.5	29.4				
20.10			197.3	46.5	61.4	63.2			1.5	34.5				
20.20			191.5	49.5	73.0	66.0			1.5	40.1				
20.30			185.4	52.4	86.4	67.3	225.4	16.5	1.4	45.4				
20.40			179.0	55.4	101.0	67.3	222.3	19.6	1.4	51.1				
20.50			171.3	58.3	114.2	65.6	219.3	23.1	1.3	56.5				
21.00			163.1	61.2	124.6	63.1	216.3	26.4	1.3	62.4				
21.10			153.2	63.5	132.6	59.4	213.4	30.1	1.5	68.3				
21.20			142.1	65.6	138.4	55.3	210.6	33.5	2.5	74.2			334.4	16.5
21.30			129.1	67.3	142.3	51.0	208.2	37.5	6.2	80.1			332.4	21.1
21.40			114.6	68.1	145.1	46.3	205.5	41.5	21.4	85.4			330.3	25.4
21.50			100.3	67.5	146.5	41.5	203.3	46.1	124.5	87.0			327.4	30.0
22.00			86.4	66.3	147.4	37.1	201.2	50.4	154.5	81.5			324.4	34.3
22.10			74.3	64.1	147.5	32.4	199.1	55.1	159.3	76.2			321.0	38.5
22.20			64.1	61.1	147.4	28.1	197.2	60.0	160.3	70.5	215.0	16.1	316.5	43.0
22.30			55.3	57.4	147.0	23.5	195.3	64.6	160.0	65.3	213.4	20.1	312.0	47.1
22.40			48.3	53.5	146.0	19.4	193.6	70.1	159.0	60.2	212.4	24.3	306.2	51.1
22.50			42.4	49.4	144.4	15.3	192.5	75.2	157.3	55.2	212.1	28.5	299.4	54.5
23.00			37.4	45.1			192.2	80.5	155.5	50.2	211.5	33.3	291.4	58.1
23.10			33.4	40.4			195.2	86.2	153.6	45.4	212.1	38.0	282.3	61.1
23.20	304.5	18.0	30.1	36.1			352.1	88.0	151.5	41.1	212.6	42.5	271.4	63.3
23.30	300.5	21.3	27.1	31.3			1.2	82.2	149.3	36.5	214.4	47.3	259.4	65.0
23.40	296.3	24.4	24.4	26.5			1.4	76.4	147.1	32.5	217.3	52.1	246.5	65.5
23.50	291.5	27.5	22.3	22.1			1.2	70.5	144.4	28.5	221.4	56.5	233.5	65.4
0.00	286.5	30.5	20.5	17.4			0.4	65.1	141.6	25.1	227.5	61.0	221.3	64.5
0.10	281.3	33.4					0.1	59.2	139.1	21.3	236.3	64.4	209.6	63.2
0.20	275.5	36.1					359.3	53.4	136.1	18.1	248.3	67.2	199.4	61.3
0.30	269.6	38.4					359.1	48.0			263.1	68.4	190.4	59.1
0.40	263.4	40.5					358.4	42.3			278.4	68.2	182.3	56.4
0.50	257.1	42.5					358.3	37.1			292.3	66.2	175.1	54.1
1.00	250.2	44.3					358.2	31.5			303.3	63.0	168.3	51.3
1.10	242.1	46.0					358.2	26.4			311.5	58.5	162.1	48.5
1.20	236.0	47.2					358.3	21.3			317.6	54.2	156.2	46.1
1.30	228.4	48.2					358.5	16.4			322.4	49.3	150.4	43.3
1.40	221.1	49.2									326.2	44.3	145.2	41.0
1.50	213.3	49.6									329.1	39.3	140.0	38.3
2.00	205.5	50.3									331.4	34.4	134.6	36.1
2.10	198.2	50.5									333.5	29.4	129.6	33.4
2.20	190.3	51.1									335.5	24.6	125.0	31.2
2.30	182.6	51.2									337.4	20.2	120.1	29.0
2.40	175.2	51.2									339.3	15.5	115.3	26.5
2.50	167.4	51.1											110.4	24.2
3.00	160.0	50.5											106.0	22.2

Table 9.1 Satellite azimuth and elevation predictions for Mulley on 12-9-87.

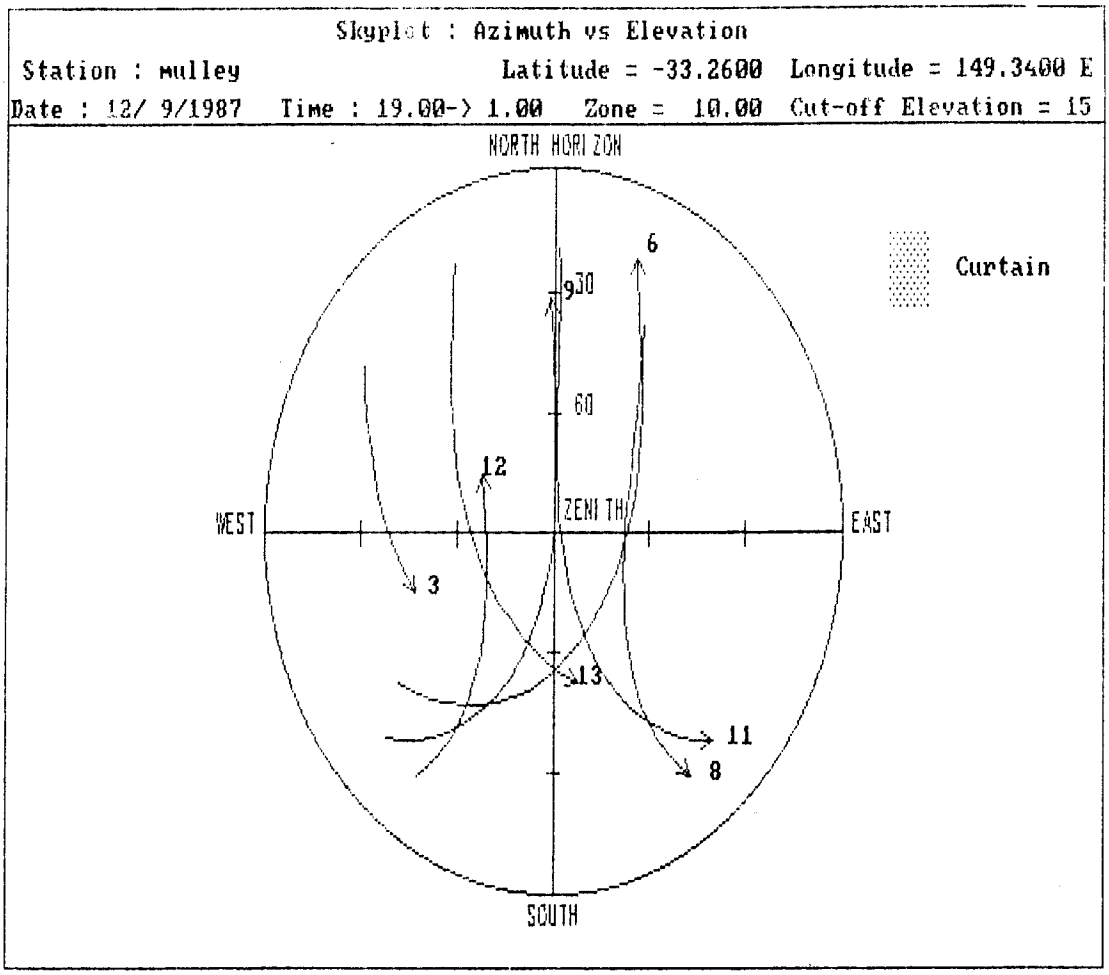

Figure 9.8 Skyplot for 12 September 1987, 19:00 to 01:00 EST.

days. The azimuth and elevation information of the 7 observed satellites are shown in Table 9.1. A skyplot of these azimuths and elevations is displayed in Fig. 9.8 (for 12-9-1987). As mentioned before, the data was stored in Nortech binary format. A few utilities, supplied by the School of Surveying of the University of New South Wales, made it possible to read the binary files and extract the necessary data. The source code required some changes and the output format of these utilities was altered to enable input into the data cleaning part of the DIPOP (Santerre et al, 1987) preprocessor. The utility DATCARD, which reads the so selected Nortech binary pseudorange and phase information, was shortened and called NTDATOBS. The utility EPHCARD, which reads the Nortech binary ephemeris information, was amended and called

NTEPHOBS. After these alterations, it was possible to read the individual station TI 4100 data, discard some unnecessary information and put the remainder into a new format which could be read by the preprocessor PREGE of DIPOP 2.0 using its "short UNB" format.

9.3 Preprocessing

The need for the use of the preprocessor is explained in more detail in Appendix C, where details are also given about the data preprocessing. In short, the result is a file which has been checked for bad data and cycle slips and which returns the validated raw data or a compacted version of the raw data. As the TI 4100 samples at a 3 second rate, it stores a phenomenal amount of data, which can be compacted by sampling without much loss of information. Evans (1986, p.576) sug-

		Pseudoranges		Carrier phases	
Time	ID	P1	P2	Φ1	Φ2
36479.00	6	.0587002775	.0587002881	-992212.42893	1673841.75236
36479.00	8	.0548032683	.0548032805	-1120916.78801	1642952.75261
36479.00	9	.0690085184	.0690085265	-787246.50472	1401515.93902
36479.00	11	.0588783642	.0588783760	-464397.17127	1937677.61114
36509.00	6	.0586681635	.0586681695	-941618.27448	1713265.76426
36509.00	8	.0547825517	.0547825552	-1088273.69137	1668388.91121
36509.00	9	.0689601704	.0689601758	-711074.83225	1460870.44753
36509.00	11	.0588070396	.0588070532	-352032.25686	2025234.65538
36539.00	6	.0586361005	.0586361054	-891102.17701	1752628.95069
36539.00	8	.0547622521	.0547622584	-1056294.22011	1693307.96853
36539.00	9	.0689117345	.0689117415	-634769.60923	1520329.00629
36539.00	11	.0587359514	.0587359669	-240040.51689	2112500.90584
36569.00	6	.0586040839	.0586040917	-840665.59448	1791930.17931
36569.00	8	.0547423727	.0547423809	-1024978.93632	1717709.45884
36569.00	9	.0688632153	.0688632237	-558331.31743	1579891.26262
36569.00	11	.0586651023	.0586651175	-128425.37050	2199473.71218
36599.00	6	.0585721184	.0585721295	-790310.09221	1831168.22570
36599.00	8	.0547229192	.0547229259	-994329.25271	1741592.31060
36599.00	9	.0688146103	.0688146216	-481760.60806	1639556.72640
36599.00	11	.0585944975	.0585945111	-17190.41317	2286150.27632
36629.00	6	.0585402095	.0585402178	-740037.15489	1870341.93771
36629.00	8	.0547038856	.0547038949	-964346.14281	1764955.74361
36629.00	9	.0687659246	.0687659352	-405057.73916	1699325.13461
36629.00	11	.0585241331	.0585241462	93660.38305	2372527.47747
36659.00	6	.0585083531	.0585083594	-689848.24195	1909450.17552

Table 9.2 Sample of a data file at Junction, on day 256 (September, 1987).

gests it is sufficient to use a 30 second sampling rate for a multipath study. This was done in this study by allowing the preprocessor DIPOP to sample the data at 30-second

intervals, in order to reduce the total of 14 megabytes of data to a more manageable level of 0.8 megabytes. Thus nine out of ten measurements, collected at the 3-second data rate, were omitted.

Four files were created by the preprocessor, one for each day and each of two stations:

MUL255.PRE	197 kb	JUN255.PRE	201 kb
MUL256.PUR	204 kb	JUN256.PUR	213 kb

These files contain GPS time tags, pseudorange transit times (in seconds) in L1 and L2 and accumulated phase observations in L1 and L2, as well as a satellite identification number. A sample of this data is shown in Table 9.2. The time is shown in GPS seconds, ID is the satellite PRN number, **P1** and **P2** are pseudorange transit times in seconds and **Φ1** and **Φ2** are continuous cycle counts.

9.3.1 Differencing Across Frequencies

The utility "IDIFFER" was written by this author for the conversion of transit times into pseudoranges by multiplication with the speed of light as well of the phases into biased pathlengths by multiplication with the relevant wavelengths. After that the L1 and L2 pseudoranges were differed across frequencies by the utility. Then the L1 and L2 carrier phase biased pathlengths were differenced in the same way. Four files resulted, of about 170 kb each, which represent this across-frequency differenced information **#Φ**:

MUL255D.LOK
JUN255D.LOK
MUL256D.LOK
JUN256D.LOK

A sample of the information in one of these files (Mulley, day 255, 12 September, 1987) is shown in Table 9.3. The time is shown in GPS seconds, ID is the satellite PRN number, **#P** is in metres and **#Φ** is in cycles. The **#Φ** observable, as shown in Chapter 7, eliminates the clock offsets of both the satellite and receiver, as well as the true range and tropos-

Time	ID	#P	#Φ
557039.0000	6	4.8781	1357554.177315
557039.0000	8	3.6811	618093.362652
557039.0000	9	2.7533	1810940.977480
557039.0000	11	4.6986	1721906.130742
557069.0000	6	3.5613	1357554.177711
557069.0000	8	2.1847	618093.361495
557069.0000	9	3.2920	1810940.977075
557069.0000	11	4.9081	1721906.115680
557099.0000	6	3.6811	1357554.178248
557099.0000	8	2.4241	618093.365353
557099.0000	9	2.9329	1810940.970445
557099.0000	11	5.4767	1721906.106749
557129.0000	6	4.5489	1357554.178377
557129.0000	8	4.3095	618093.363628
557129.0000	9	3.6511	1810940.966505
557129.0000	11	5.1176	1721906.095427
557159.0000	6	5.7760	1357554.177421
557159.0000	8	4.3095	618093.363757
557159.0000	9	3.8606	1810940.968236
557159.0000	11	5.5665	1721906.077256
557189.0000	6	3.8905	1357554.175984
557189.0000	8	4.6387	618093.358167

Table 9.3 Sample of across frequency differenced data (#P and #Φ) for Mulley, on day 255 (September, 1987).

pheric correction. In addition, the effect of the satellite ephemeris error upon the range is eliminated.

9.3.2 Individual Satellite Files

The four files of #Φ values are subsequently split into individual satellite files. For this purpose the utility "READSAT" was written, which generates 7 files for each station for each of two days. A total of 28 files were obtained, for example SA3T255.MUL, or generally SA*T25&.MUL or .JUN. A list is given in Table 9.4.

9.3.3 Preparation for Across-Site Differencing

A utility "GAPHUNT" was written in order to identify spots of discontinuities (missing data) in the time series of #Φ

(through constellation changes etc.). After these were identified, corresponding bits of data were removed in the simultaneously observed observations at the other station. This provided matching time series for across-site differencing of the data.

Satellite ID	Day 255 Mulley	Day 255 Junction	Day 256 Mulley	Day 256 Junction
*	SA*T255.MUL	SA*T255.JUN	SA*T256.MUL	SA*T256.JUN
3	24 kb	24 kb	21 kb	21 kb
6	28 kb	28 kb	30 kb	30 kb
8	19 kb	19 kb	21 kb	21 kb
9	43 kb	42 kb	42 kb	42 kb
11	13 kb	15 kb	17 kb	17 kb
12	12 kb	14 kb	12 kb	12 kb
13	27 kb	28 kb	25 kb	25 kb

Table 9.4 A listing of individual satellite files for each day. Day 255 and 256 refer to 12 and 13 September 1987, respectively.

9.3.4 Differencing Across Sites

The necessary differencing was carried out by the utility "DIIFDIF". The resulting 7 files of Δ#Φ for day 255 and 7 for day 256 are listed in Table 9.5.

These files represent the across-site across-frequency pseudorange and carrier phase pathlength difference records. From these files the first readings in each column were subtracted from all the following readings in the same column to eliminate the large numbers as shown in Table 9.3. The large numbers are a linear combination of ambiguities.

9.3.5 Importing Data into a Statistics Programme Package

The data was now ready for importing into the statistics software package STATGRAPHICS for graphing and analysis. In

M3J255D.DIF	24 kb	M3J256D.DIF	21 kb
M6J255D.DIF	28 kb	M6J256D.DIF	30 kb
M8J255D.DIF	19 kb	M8J256D.DIF	21 kb
M9J255D.DIF	42 kb	M9J256D.DIF	42 kb
M11J255D.DIF	13 kb	M11J256D.DIF	17 kb
M12J255D.DIF	12 kb	M12J256D.DIF	12 kb
M13J255D.DIF	27 kb	M13J256D.DIF	25 kb

Table 9.5 Listing of files of across-site across-frequency pseudorange and carrier phase pathlength differences for individual satellites.

order to be able to compare the data across different days, the files are edited within the statistics pack for time tag mismatches, so that each file starts at the same time tag on the different days. Gaps in the observational record are entered as blank data, in order to have the same amount of data on each day, without disrupting the time continuity for the frequency analysis.

The resulting time series are inspected in various steps:

--- time series plots of the pseudorange and phase results of $\Delta\#P$ and $\Delta\#\Phi$ as well as $\delta\Delta\#\Phi$, the across epoch differenced values of these,

--- calculation of the cross-correlation function of the data of two consecutive days,

--- calculation of an estimate of the spectral density through a Fourier transformation of the data and the display of the data in the form of a periodogram, for spectral analysis in the frequency domain.

More information on "time series", "autocorrelation function", "cross-correlation function", "spectral density function" and "periodograms" may be found in Appendix A.

Time series plots, cross-correlations and estimates of spectral density were obtained for both the pseudorange and carrier phase data from each satellite on each of the two days. These results are presented in Chapters 10 and 11.

10. ANALYSIS OF CARRIER PHASES

TI 4100 data was collected on 12-9-87 (day 255) and 13-9-87 (day 256) between 10:44 UT to 15:38 UT (20:44 AEST to 01:38 AEST) as described in Chapter 9. In this chapter a page of graphs will be presented in a standard format, for each satellite record. The page will show seven graphs (e.g. Figs. 10.1a to g). The top two (a,b) are the **time series** plots of the Δ#Φ record, the across-site across-frequency carrier phase pathlength differences. The left one is for day 255, the first day, the right hand side one is for day 256, the second day of observations. The horizontal axis shows the time in the form of numbered consecutive sample intervals of 30 seconds. This means record number 120 refers to an observation one hour after the start of the record. The vertical axis shows the recorded Δ#Φ amplitude in metres. At times the column legend shows an exponent like xE-3. This means the values shown along the vertical axis should in this case be multiplied by 1/1000 in order to obtain metres.

The two graphs below (c and d) depict δΔ#Φ, the **across-epoch differences** of the graphs above, across consecutive 30-second intervals. The first day is again on the left and the second day on the right. The horizontal and vertical axes are the same as indicated for the graphs above.

The next two graphs (e,f) further down the page generally show the **periodograms** for each day (which give an estimate of the spectral density function) and, occasionally, the autocorrelation function. The left one is for day 255, the right one for day 256. The periodogram is a frequency domain representation of the data, where each ordinate shows the amount of variance contributed by the data at that frequency (see Appendix A.4) or, in other words, the total energy of the series at that frequency. The horizontal axis of the periodogram shows the natural logarithm of the frequency, with the frequency expressed as the number of cycles per sampling interval. The data sampling interval is 30 seconds. In order to obtain the period in minutes, one reverses the sign, takes the exponential function and divides by two. Table 10.1 indicates the period in minutes for the various logarithmic values along the horizontal axis. The frequencies that are displayed span from 1/n-th of a cycle per sampling interval (where n is the total number of samples) to the Nyquist frequency of half a cycle per sampling interval. The vertical axes of these periodograms show the total variance of the series at a particular frequency, expressed by its base 10 logarithm.

The **autocorrelation function** (see Appendix A.2), occasionally given instead of the periodogram, includes the same information as the periodogram but in the time domain instead of the frequency domain. Along the horizontal axis of the autocorrelation function one finds the lags used for the calculation of each ordinate, in units of 30-second sampling intervals. The vertical axis shows on a scale from 0 to 1 the correlation coefficient valid for the lag on the horizontal axis.

The last plot (g), at the bottom of the page, is the **cross-correlation function** indicating the correlation between the data of the two consecutive days. The lag number is again given in units of 30 seconds and the vertical axis shows the cross-correlation coefficient on a scale from 0 to 1.

ln c/s.i.	prd. min.	ln c/s.i.	prd. min.
-0.7	1.0	-3.7	20.2
-0.9	1.2	-3.9	24.7
-1.1	1.5	-4.1	30.2
-1.3	1.8	-4.3	36.8
-1.5	2.2	-4.5	45.0
-1.7	2.7	-4.7	55.0
-1.9	3.3	-4.9	67.1
-2.1	4.1	-5.1	82.0
-2.3	5.0	-5.3	100.2
-2.5	6.1	-5.5	122.3
-2.7	7.4	-5.7	149.4
-2.9	9.1	-5.9	182.5
-3.1	11.1	-6.1	222.9
-3.3	13.6	-6.3	272.3
-3.5	16.6	-6.5	332.6

Table 10.1 Key to the horizontal axis of the periodogram; ln c/s.i. means the nat. log of cycles per sampling interval, prd. min. stands for period in minutes.

The periodograms generated by the statistics programme STATGRAPHICS (Figures 10.1e and 10.1f) show the horizontal axis in units of the natural logarithm of the number of cycles per sampling interval. The vertical axis shows the (base 10) logarithm of the variance of the p-th harmonic in square metres per cycle per sampling interval (m^2/Hz if the sampling interval was one second). The logarithms are used in order to highlight the frequencies of interest and to compress the highest frequency information, which usually represents the system noise. The (far) right hand side part of a periodogram curve represents the total variance of the noise at that frequency interval. In the lower frequency part of a periodogram curve (on the left side) the frequency sampling grid becomes quite wide and the likelihood increases that only one of the peaks of the L1-L2 multipath error signature is captured. In order to see the dual peak feature of the multipath error signature, the ratio between the values on the grid lines of the overtone series has to be such that a valley can occur between two grid lines that have a ratio of about 120/154. The frequencies on the grid lines have the ratios n/(n-1), for example 1/2, 2/3, 3/4, 4/5 etc.

To get a grid density twice as fine as 4/5, about 8/9 is required. This means that on the left of the ninth value plotted on the periodogram, only single peaks can be expected (or two high values next to each other) in response to the multipath error signature in the differenced phase observable between L1 and L2.

Further on the left in the periodogram, the frequencies of detected sinusoids become so small that one can only speak of a detected trend. Thus the periodogram cuts out at a frequency of 1/n cycles per sampling interval, where n is the number of samples. On the right, the periodogram terminates at the Nyquist frequency of half a cycle per sampling interval.

For satellites 8, 11 and 13 a further experiment was carried out. The data of the second day was lagged by 240 seconds in order to siderealy synchronise the records of the two days, which originated under the same satellite-to-receiver geometry. The mean of the two records was calculated as well as the difference. The averaging could be expected to enhance the common periodicities while the differencing would remove these. Four plots for each of the satellites 8, 11 and 13 are displayed in Chapters 10.3.5, 10.5.5, 10.5.10, 10.7.5 and 10.7.10, namely the averaged timeseries, the differenced time series as well as their corresponding periodograms (or occasionally their autocorrelation functions).

The satellite identification numbers used here are the so-called PRN numbers. This identifies which of the 37 seven-day segments of the P-code pseudo-random-noise signal is used by the satellite at that moment (Wells, 1986). Other identification numbers for the satellite, like the launch sequence number, are not used in this report. Satellites 6, 8, 9 and 11 were used from 20:44 to 21:21 AEST, the next constellation was formed by Satellites 6, 8, 9 and 13 which lasted till 22:56 AEST. Then Satellites 6, 3, 9 and 11 were used until 00:06 AEST after which Satellites 3, 9, 12 and 13 were used until 01:38 AEST (Refer to Table 9.1).

10.1 Satellite 3

10.1.1 Time Series Plot of Satellite 3 Data

The observations for satellite 3 were recorded from 13:04 UT to 15:38 UT and have been compacted to 309 samples. In order to correlate the time series plots with the table of ten-minute satellite elevations and azimuths (see Table 9.1), the reading at the first occurring 10-minute interval will be identified: observation 13 in Figs 10.1 a,b,c and d was recorded at 23:09:59 AEST. The plot of the time series of Δ#Φ (the across-site across-frequency carrier phase pathlength difference) for day 255 (Fig. 10.1a) and day 256 (Fig. 10.1b) show fairly wild fluctuations in the first 70 minutes with peak-to-peak changes of 244 mm on the first day and 110 mm on the second day. After the first 70 minutes the signal calms down to 40 mm peak-to-peak variations on each day. This is accompanied by a high frequency spectral content of about 10 mm amplitude. The sudden changes in the times series records lead to a few questions. The primary suspicion would be that the differencing did not remove clock effects and other biases sufficiently to conclude that the record is mainly caused by multipath. But when studying the other Δ#Φ plots it becomes clear that many of these large amplitude fluctuations occur again on the next day, often at exactly the expected sidereal time interval of 23 hours and 56 minutes (four minutes earlier each next day). This excludes ionospheric effects and clock rate variations and clearly points to a cause which depends on the satellite-to-receiver geometry.

In Figures 10.1a and 10.1b there is a sudden drop that ends in a clear trough. The day 255 drop in Figure 10.1a amounts to 170 mm over a time span of 10 minutes. The day 256 drop in Figure 10.1b amounts to 100 mm over a 6 minute period. The trough is reached at GPS time 570209 on day 255 and between GPS time 51539 and 51569 on day 256. This is equivalent to 14:23:29 UT on day 255 and 14:19:14 UT on day 256. The difference is 4 min 15 sec. There are many examples of deep

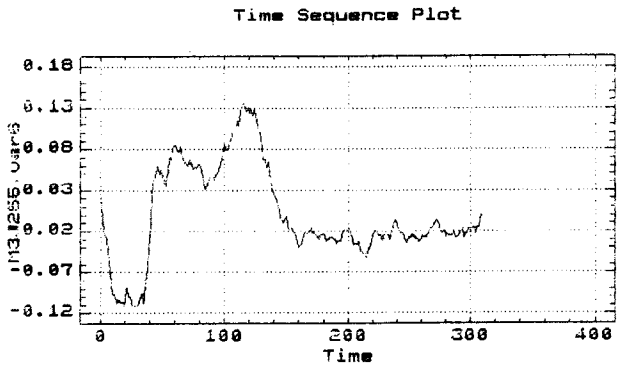

Fig. 10.1a Δ#Φ (255).

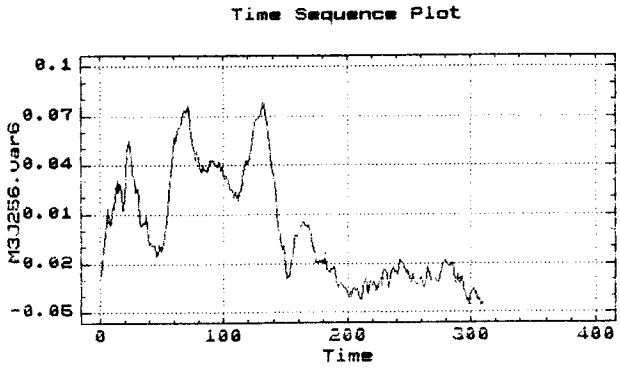

Fig. 10.1b Δ#Φ (256).

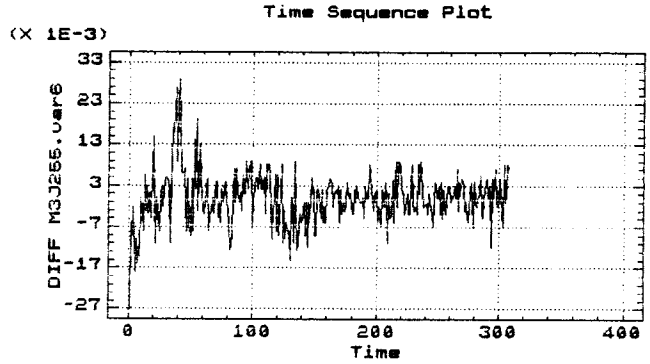

Fig. 10.1c δΔ#Φ (255).

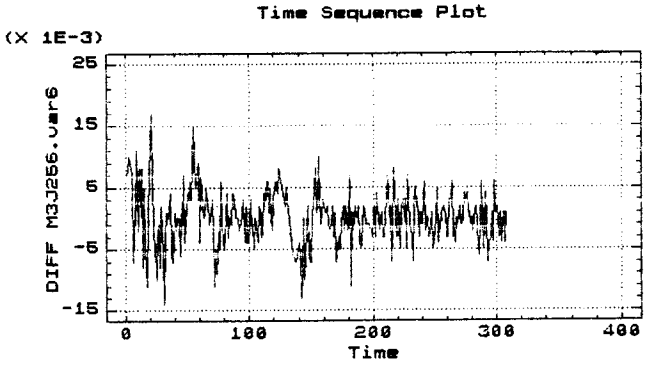

Fig. 10.1d δΔ#Φ (256).

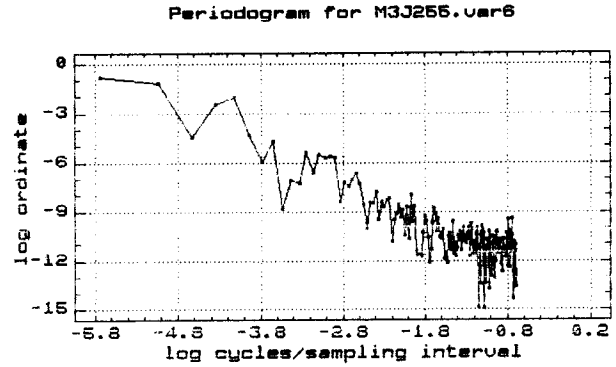

Fig. 10.1e Frequencies.

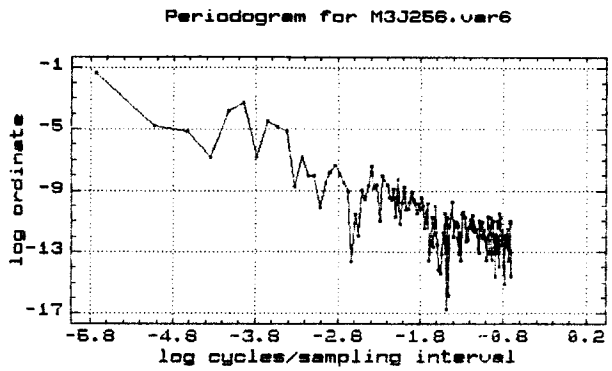

Fig. 10.1f Frequencies.

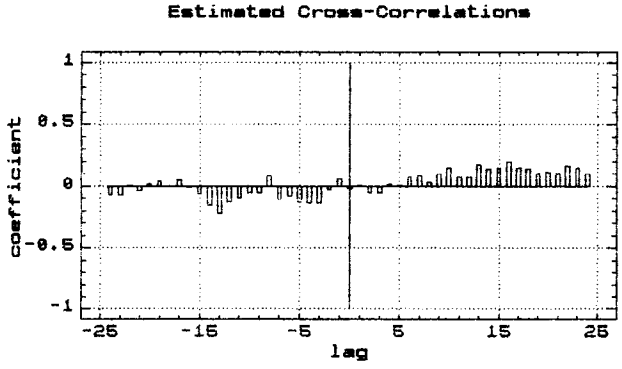

Fig. 10.1g Cross-correlations
Sat.3, days 255 and 256.

troughs in all the data, which reappear exactly after one sidereal day. The elevation of the satellite is around 36 degrees at this time and the rate of change of the angle of elevation is about 15 degrees per hour. This means the sharp change in the phase record is not caused by the satellite culminating in elevation or going through zenith.

10.1.2 Across-Epoch Differencing of Satellite 3 Data

The across-epoch differencing that precedes the cross-correlation calculation produces the two plots of $\delta\Delta\#\$$ time series in Figures 10.1c and 10.1d, which show some similarities in the beat pattern. These are plots of differentials, which indicate the necessary increments to get from the last observation to the next one. In most cases, the differences do not change more than 10 mm from one 30 second epoch to the next and a lot of the changes are only half that. Extreme changes reach about 30 mm.

10.1.3 Cross-Correlation Function of Satellite 3

Although at first sight the phase plots of the two days (Figures 10.1a and 10.1b) do not seem to exhibit matching recurring patterns, they do look similar as far as spectral content is concerned. Furthermore, some of the strong nulls do recur at the right lag. It is only through the calculation of the cross-correlation function that the evidence is produced: there is a distinct isolated peak, although a low one, at the lag of 240 seconds. For this calculation, the files represented in Figs. 10.1a and b had to be differenced once more, this time across consecutive epochs, as shown in Figures 10.1c and 10.1d. The cross-correlation function of the data of this satellite (Fig. 10.1g) shows that for negative lags (advancing) there appears to be correlation at any time. For positive lags, there appears to be mainly negative correlation and for a lag of 240 seconds there is a

clear but small solitary peak in the function which is emphasized by two large negative sidelobes.

10.1.4 Spectral Density of Satellite 3 Data

On the right side of the periodogram (Figs. 10.1e and 10.1f) the high frequency part of the spectral density (or noise) can be found. It is evident that the amplitudes are concentrated below a level of 0.1 mm (the log ordinate is -8 which indicates the total variance in m^2) at frequencies above 0.16 cycles per 30-second sampling interval. The ln cycles (remember the natural logarithm is used on the horizontal axis) per sampling interval are between -1.8 and -0.7, which indicates periods of 3 minutes or less (Refer to Table 10.1). Amplitudes closer to a millimetre or more (log of total variance around -6) are found at frequencies with periods up to 8 minutes and amplitudes of centimetres (log of total variance around -4) occur with periodicities up to about 20 minutes. There are distinct peaks in the periodograms of both days in various of these brackets; but as is shown in the multipath simulations in Chapter 12, the L1-L2 multipath error signature can be identified by dual peaks that are 120/154 different in frequency (or where the natural logarithms of the cycles per sampling interval are 0.25 apart). The overriding test criterion then is that this double peak should recur on the next day.

The periodograms of the Δ#♦ time series of both days exhibit a relative maximum at a 30 minute period (-4.1 on the horizontal axis in Figs. 10.1e and 10.1f) without a second peak occurring in the periodogram perhaps because the overtone series grid is not fine enough at this frequency to capture another frequency at the 120/154 ratio. In the area between periods of 8 and 22 minutes (-2.8 and -3.8 on the frequency axis) some clear peaks occur, but it is hard to identify them as dual peaks at the right ratio. The peaks that do appear as single peaks on both days (Figures 10.1e and 10.1f) are at periods of 20, 12, 5.5 and 4.5 minutes (at

-3.7, -3.2, -2.4 and -2.2 on the graph). The first two have an energy at the 10 mm level, the others appear to be well below the millimetre level.

10.2 Satellite 6

10.2.1 Time Series Plot of Satellite 6 Data

The observations for satellite 6 were recorded from 10:44 UT to 14:06 UT and have been compacted to 405 samples. In order to correlate the time series plots with Table 9.1, the reading at the first occurring 10-minute interval will be identified: observation 13 in Figs. 10.2a,b,c and d was recorded at 20:49:59 AEST. The Δ#* time series plot for day 255 (Fig. 10.2a) shows sudden changes, with amplitudes over 100 mm and a sudden drop of about 170 mm which appears to also occur in the next day's record. There is a very regular periodicity at first sight in the record of the second day (Fig. 10.2b). The peak-to-peak variation appears to be about 30 mm, upon which is superimposed some small variations with 2-5 mm amplitudes and periods of a few minutes. From 12:56 UT (564959 GPS seconds) to 13:22 UT (566519), there is a sudden 120 mm drop in the first day's record. From 12:51 UT (46259) to 13:19 UT (47939) there is a sudden 180 mm drop in the second day's record. In average this is a repeat of a similar phenomenon about 4 minutes earlier the next day.

During this time the satellite elevation increases from 36.1 to 49.4 degrees and the azimuth drops from 42 to 30 degrees. The rate of change of the elevation is about 25 to 30 degrees per hour. The sudden change in the phase record can once again not be explained by the satellite going through zenith or the elevation rate of change becoming zero. It must be assumed that multiple reflections occur which, for a short period, are suddenly all in phase and coherently add their amplitudes. This could explain, why a similar thing occurs at about the same time on the next day, though 4 minutes earlier. This provided a second indication that it would be

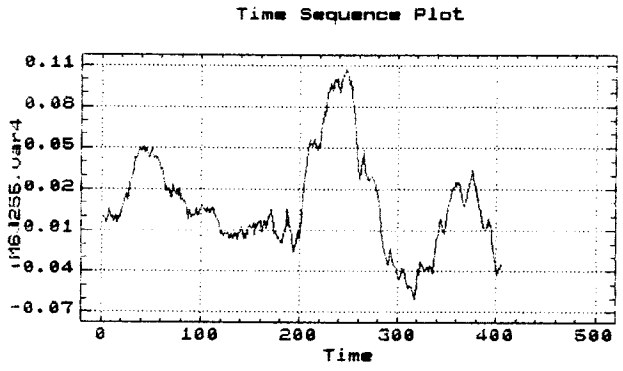

Fig. 10.2a Δ#Φ (255).

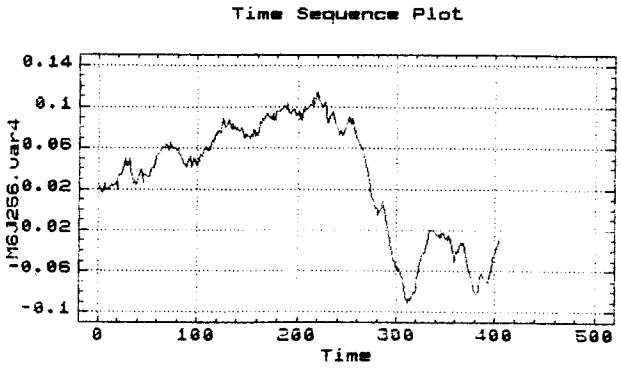

Fig. 10.2b Δ#Φ (256).

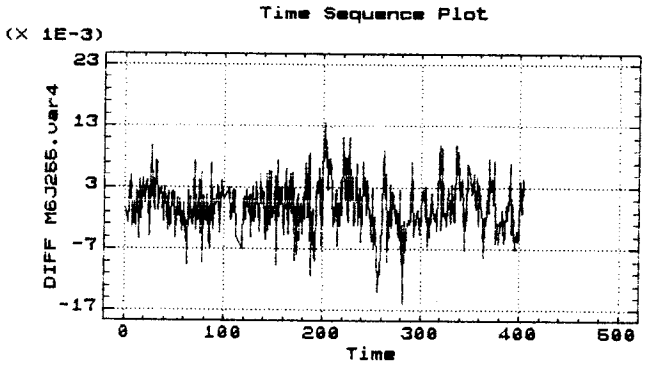

Fig. 10.2c δΔ#Φ (255).

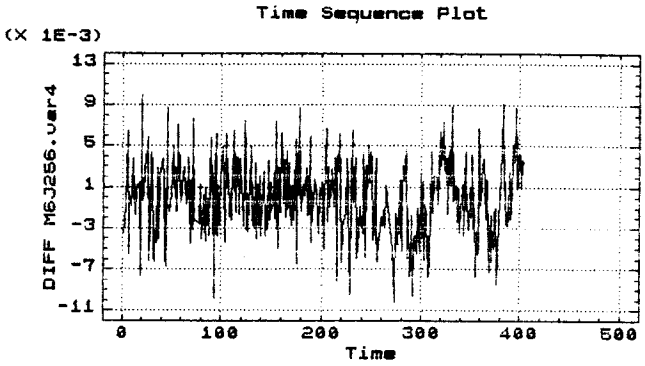

Fig. 10.2d δΔ#Φ (256).

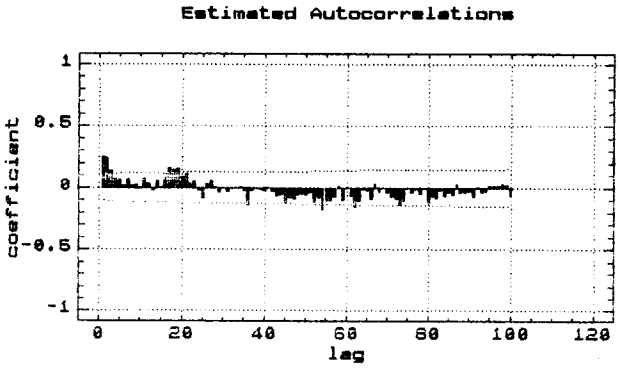

Fig. 10.2e Autocorrelations.

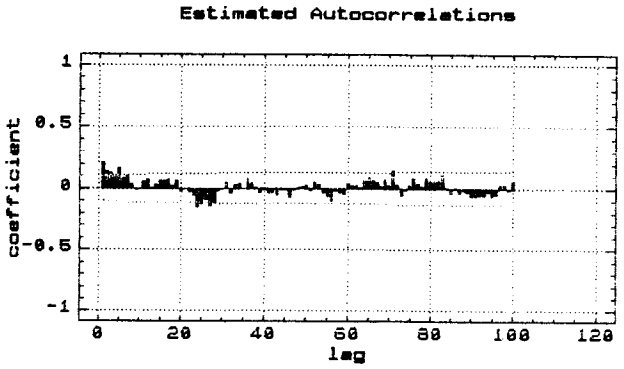

Fig. 10.2f Autocorrelations.

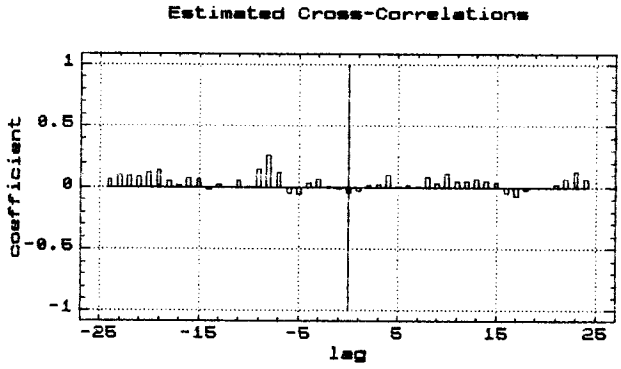

Fig. 10.2g Cross-correlations
Sat.6, days 255 and 256.

of interest to carry out a simulation of multiple reflections and to analyse the resulting spectral content.

The amplitudes in Figs. 10.2a and b could also suggest a very strong single reflection. When the relative signal strength α (between the direct and the multipath signal) is close to 1, the sine-curve nature of the constituent L1 and L2 multipath error curves degenerate each into a sawtooth pattern. The sudden change in the phase record through the appearance of the peak in Fig. 10.2a is contrasted by the slow ascension to a peak in Fig. 10.2b. The result of two differenced sawtooth functions can show exactly such a feature under particular surface roughness characteristics (Refer to Chapter 12.1).

With the satellite at the particular azimuths mentioned above, a few obstacles on the rooftop site can be identified as possible sources of reflections. In roughly the same direction a narrow chimney, a large cylindrical structure with a conical top, a big circular vent and the wire aerial as well as 14 metres of hand rails at a distance of 8 metres can be found. However, the main reflective surface would be expected to be the roof surface itself.

10.2.2 Across-Epoch Differencing of Satellite 6 Data

The $\delta\Delta\#\Phi$ plots in Figures 10.2c and 10.2d show a beat pattern with a periodicity of about half an hour. The whole spectral width of the beat is about 10 mm, but as this is a plot of differentials, they work accumulatively. The densest part of the plot is no wider than 3 mm for day 255 and 256, which is the average change from epoch to epoch. Extreme changes are about 15 to 20 mm in magnitude. This record is then subjected to a cross-correlation calculation.

10.2.3 Cross-Correlation Function of Satellite 6

The Δ#⁕ record in Figure 10.2a does not seem to show clear features that recur in the next day's record (Fig. 10.2b), apart from the sharp drop mentioned before. However, the cross-correlation function (shown in Fig. 10.2g) of the across epoch differenced records in Figures 10.2c and 10.2d indicates a clear peak at a lag of 240 seconds.

10.2.4 Spectral Density of Satellite 6 Data

The changes in Δ#⁕ appear to be too abrupt (the sharp corners require infinite Fourier terms) to capture them as sinusoids at the particular frequencies of the grid of the overtone series. The Fourier transform of the spectral density calculation failed through lack of sufficient RAM on the PC used, to handle the infinite Fourier terms. The first half of the file of day 256 was then analysed instead. The aim was to investigate the regular oscillations visible in this plot within the constraints of this narrowed spectral window.

The resulting periodogram in Figure 10.3 gives a classical example of the dual peak feature that belongs to the L1-L2 multipath error signature. Because two frequencies are combined in this error signature, the resulting spectral record will reflect the presence of both frequencies when multipathing of the signal occurs. Between the values -2.5 and -2.1 (the "ln cycles per sampling interval" values on the horizontal axis of the periodogram in Fig. 10.3) there are four peaks. The first and the third are an exact 120/154 frequency ratio of each other, just as the second and the fourth peak are. L1 is the higher frequency and generates the right hand side peak of each dual pair. Reference may be made to Table 10.1 for the conversion of the logarithmic values on the horizontal axis of the periodograms to periods in minutes. A frequency ratio of 120/154 is equivalent to a difference of 0.25 on the natural logarithm scale. In the low frequency section two peaks occur which feature components at

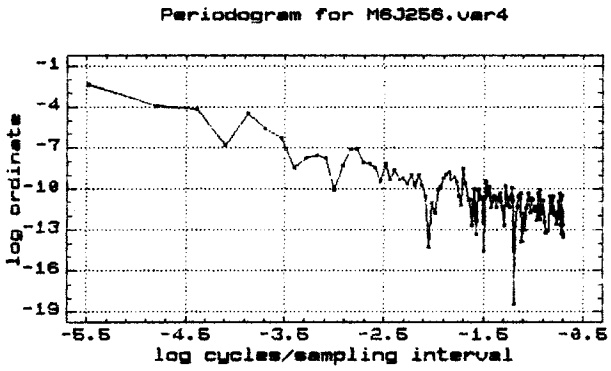

Figure 10.3 Dual peaks caused by the L1 (right) and L2 (left) multipath error signature.

the right frequency ratio with each other (-2.85 and -3.1), suggesting possible multipathing with an amplitude in the millimetre region and an L1 period of about 8.5 minutes. There is a lone peak (-3.9) in the very low frequency section of the periodogram where the grid is too wide to capture another frequency at the right ratio of 120/154. This peak thus could also indicate multipathing. It has a period of 25 minutes and an apparent energy of the order of 10 mm. At the high frequency end of the periodogram (Fig. 10.3) the noise of the differenced observable can be found and its energy is surprisingly low: well below 0.1 mm.

10.3 Satellite 8

10.3.1 Time Series Plot of Satellite 8 Data

The observations for satellite 8 were recorded from 10:44 UT to 12:56 UT and have been compacted to 265 samples. In order to correlate these time series plots with Table 9.1, the reading at the first occurring 10-minute interval will be identified: observation 13 in Figs. 10.4a,b,c and d was recorded at 20:49:59 AEST. The Δ#◆ time series plots of satellite 8 (Figs. 10.4a and 10.4b) show very distinct peaks and troughs. Almost every peak and trough in the Satellite 8 record of day 255 (Fig. 10.4a) seems to have its counterpart in the record for day 256 (Fig. 10.4b). The two timeseries plots exhibit an overall similarity as well. It looks as if

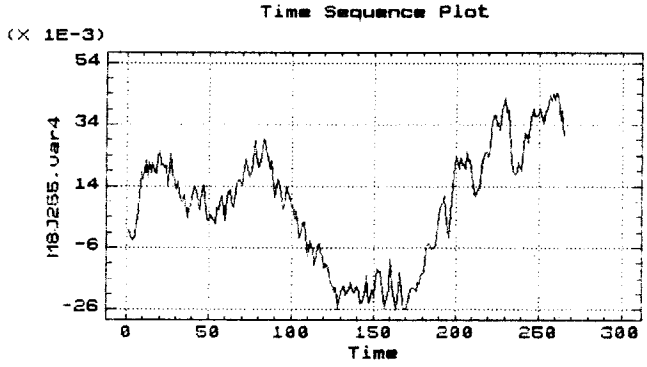

Fig. 10.4a Δ#Φ (255).

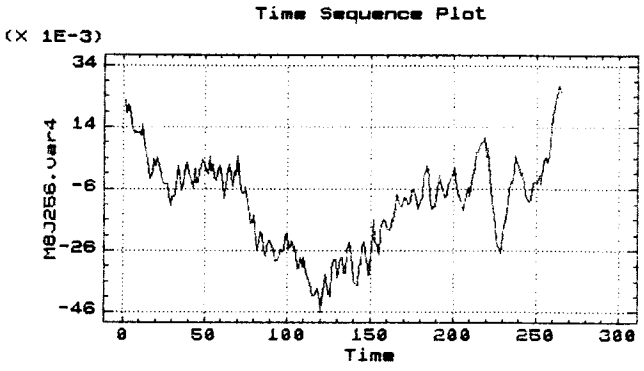

Fig. 10.4b Δ#Φ (256).

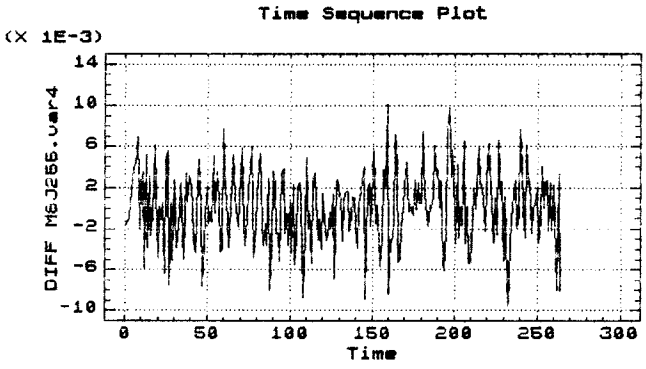

Fig. 10.4c δΔ#Φ (255).

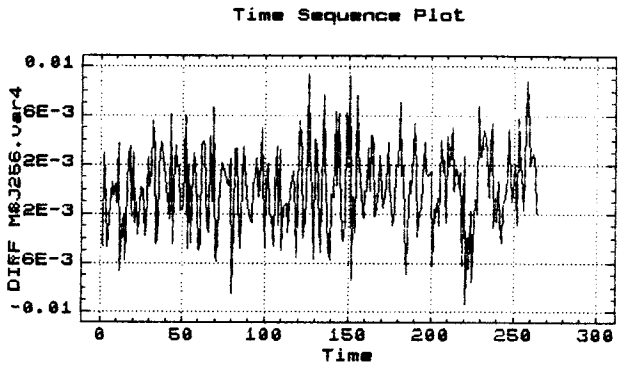

Fig. 10.4d δΔ#Φ (256).

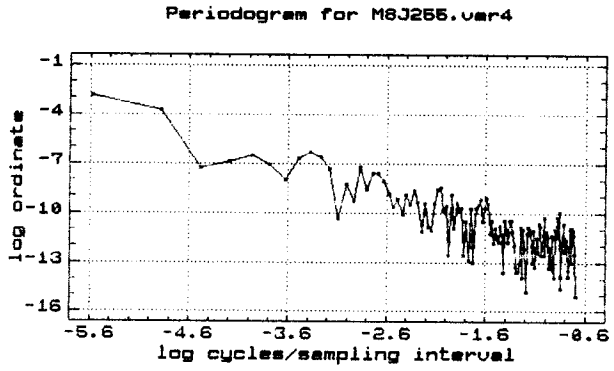

Fig. 10.4e Frequencies.

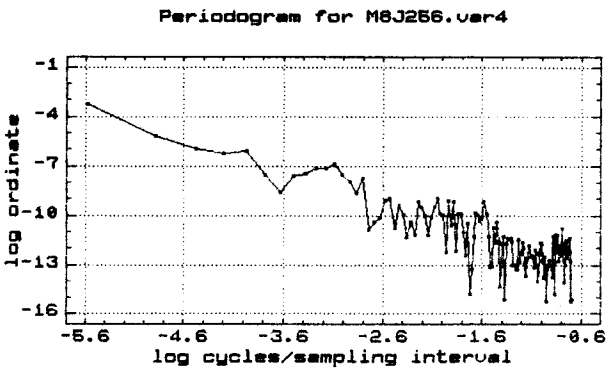

Fig. 10.4f Frequencies.

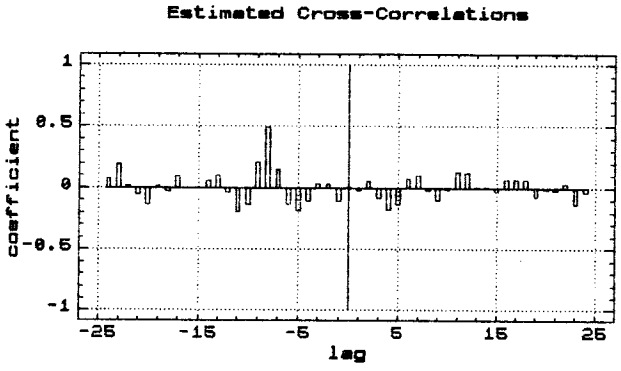

Fig. 10.4g Cross-correlations Sat.8, days 255 and 256.

particular sections of one plot only differ from the other plot through subtle changes in the trend of the subsections. The repeatability of spikes of a few millimetres amplitude at a 240 second lag is amazing and indicates that they are not due to noise. The sole differences in the two similar graphs may be produced by the reflective surfaces carrying more dust or moisture on one of the two days or through day to day differences in ionospheric variations. The ionospheric variations referred to here are the changes that are not occurring equally along the lines of sight from the satellite to the two (150 km) separated sites, as the common variation is removed through the across-site differencing.

If the cause is ionospheric, the effect on the across-site across-frequency phase pathlength difference, as shown in the time series plots of Figures 10.4a and 10.4b, is no more than 20-30 mm. Proof is provided by the recurrence of much of the variations 23 hours and 56 seconds later, identifying these as multipath-caused and leaving only the remainder to be explained by ionospheric variation differences between separate sites.

Over a two hour period, this variation is such that during part of the time the signal amplitude plot is 10 to 15 mm below the previous day's curve and it changes once or twice to being 15 mm above the previous day's curve, over an hour. Variations of 15 mm in the L1-L2 record correspond to electron content changes of the order of 1/10 of a TEC unit.

After inspection of these two remarkable time series plots it can be stated that 3/4 or more of the total variation of 80 mm in both plots is caused by multipath. One quarter of the variation in one day's plot is due to the difference between the ionospheric changes occurring between the 150 km separated sites because, through the across frequency differencing, the clock offsets and the tropospheric effects as well as the ephemeris error effects and the time-variable receiver phase drift effects (Evans et al, 1985, p.253) have been eliminated or greatly reduced. The across-site differencing of

simultaneously observed data reduces the remaining effects even further, leaving mainly the effect of unequal changes in the ionosphere between the two sites and signal multipath as the variables in the time series plot of the Δ#Φ observable.

The time at which the rate of change of the satellite elevation is zero is about 10:30 to 10:40 UT. The first Satellite 8 record is at about 10:22 UT (37319 GPS seconds), which means that during the following twenty to thirty minutes the periods of any multipath effects will be quite long, in the area of a few hours, before they become shorter again. After a while the multipath index (Refer to Chapter 2) for horizontal surfaces reduces to an average of about 13 to 16 metre minutes. (This value has to be divided by the height above the horizontal surface, to obtain the multipath period in minutes.) At this time both plots show a "swing" of about two cycles over a 25 minute interval. This can be explained by multipathing off a horizontal surface about 1 to 1.3 metres below the antenna phase centre. Fourteen small spikes occur in a 25 minute period suggesting a 1.8 minute periodicity. If a horizontal surface were to cause this it would have to be situated 7 to 9 metres below the antenna phase centre. The vertical multipath index is obtained by multiplying the horizontal index by the cotangent of the satellite elevation (Chapter 12). With the satellite elevation going from 37 to 15 degrees, the vertical multipath index changes from 21 to 48. In order to generate 1.8 minute periods, a vertical surface would need to be at a distance of about 11 to 27 metres. There are three tall chimneys at a distance of between 12 and 14 metres (see Fig. 9.7), which could specularly reflect satellites with low elevation.

10.3.2 Across-Epoch Differencing of Satellite 8 Data

Most of the information in the time series plots of the across-epoch differenced data in Figures 10.4c and 10.4d can be found in a 10 mm wide band. A large amount of data is within a band no wider than about 4 mm. A beat pattern with

about four beats over two hours is evident. This is valid for the Satellite 8 records of days 255 (Fig. 10.4c) and 256 (Fig. 10.4d). If a deterministic correction for this beat pattern were possible, in a case where multipath can be identified and modelled, it is likely that the remaining signal after correction would have a spectral width of 2 mm to 3 mm in the $\delta\Delta\#\Phi$ plot. These across-epoch differenced files are used to calculate the cross-correlation function.

10.3.3 Cross-Correlation Function of Satellite 8

The cross-correlation function (Fig. 10.4g) of the two across-epoch differenced time series (Figs. 10.4c and 10.4d) shows the highest correlation coefficient encountered in this multipath study: the full two hour record of observations for Satellite 8 yields a cross-correlation coefficient of 0.5, for a lag of 240 seconds. Figure 10.4g shows that the peak at 240 seconds is 3 to 4 times higher than any other peak in the function. This points to a strong component in the phase difference record which repeats itself after 23 hours and 56 minutes and to a cause which depends on the geometry between the satellite and the receiver. Similar results have been obtained by Georgiadou and Kleusberg (1988).

10.3.4 Spectral Density of Satellite 8 Data

The periodograms in Figures 10.4e and 10.4f exhibit peaks at periods of 25 minutes. The same peaks are also clearly visible in the $\Delta\#\Phi$ time series plots in Figures 10.4a and 10.4b. The periodogram for day 255 (Fig. 10.4e) shows four peaks between periods of 18 to 6.5 minutes, but when considered together with day 256 (Fig. 10.4f), they don't stand out as clear dual L1-L2 peaks. (Refer to Table 10.1 for a conversion between logarithms and periods). The spectral density plots in Figures 10.4e and 10.4f do have maxima between the logarithmic values -3.38 and -3.0 that occur on both days and can be explained as periodicities with the

120/154 ratio. These periodicities would be 10 to 13 minutes, with an energy in the millimetre region. There are some fairly high common peaks in the spectral density function estimate of each day, with L1 periods of about 2 minutes. The noise is again below the 0.1 mm level.

10.3.5 Across-Day Averaging and Differencing

Across-Day Averaging

In order to emphasise the agreement between the two time series of Figures 10.4a and 10.4b, the time series were both averaged across the two days, allowing for a lag of 240 seconds and a **(ΣΔ#Φ)/2** plot was made of the result (Fig. 10.5a). This appears to emphasise the spikiness, as well as the long periodic swing over the two hour session. The plot strengthens all that is common between the two original time series and reduces what is different.

Across-Day Differencing

Subsequently, the two original time series were differenced across the two days, allowing for the 240 second lag. This emphasises all that is different after one full sidereal day. The result, **DΔ#Φ**, is shown in Fig. 10.5b. The most striking feature of Figure 10.5b is the significant reduction of the spikiness of the time series. Both the original time series (Figs. 10.4a and 10.4b) and the averaged time series (Fig. 10.5a) have a strong spikiness. This leads to the assumption that this spikiness in the time series of Satellite 8 is clearly a feature of signal multipathing. The across-day differencing with a 240 second lag results in a W-curve with overlayed five millimetres noise and some remaining multipath error signature stumps. The long periodic variation is thought to have an ionospheric cause. It represents a ripple through the data with a 20 mm amplitude (40 mm peak-to-peak) and a period of a little over an hour. The possible explanation for this would be a half a TEC unit difference in the ionospheric changes between sites. Because the two sites are separated by 150 km, the ionospheric changes will not be

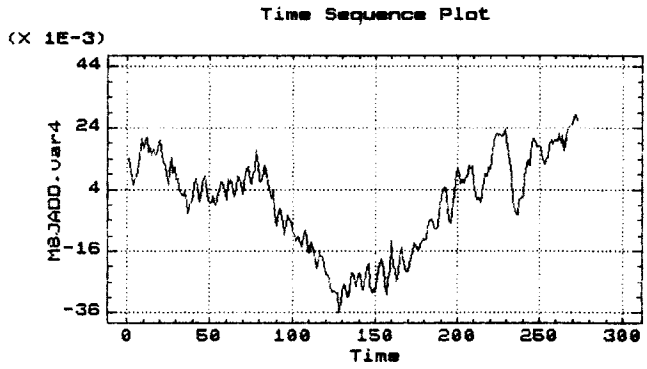

Fig. 10.5a Across-day averaged time series for Sat. 8.

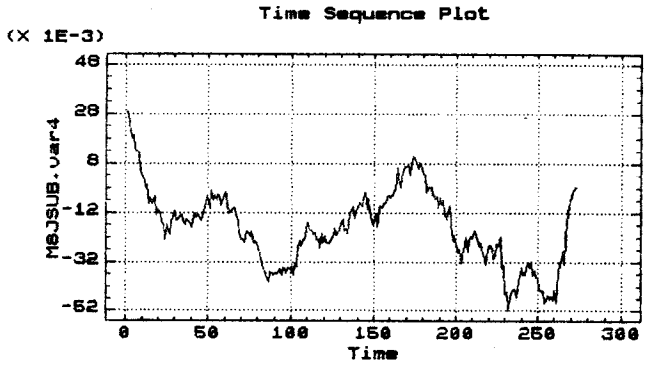

Fig. 10.5b Across-day differenced time series for Sat. 8.

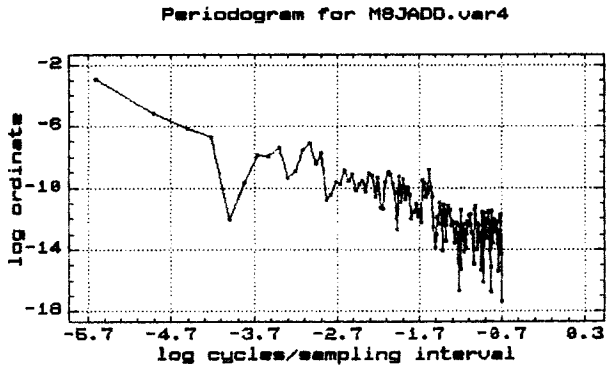

Fig. 10.5c Spectral density of the averaged series.

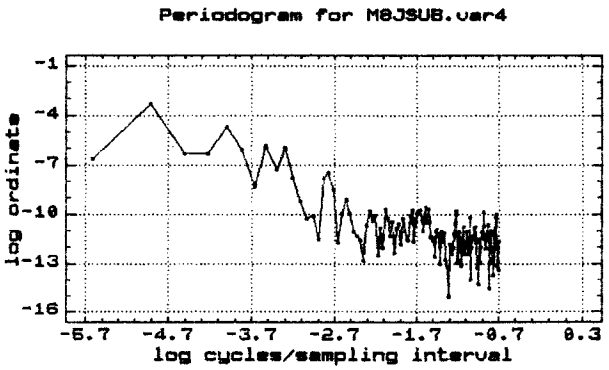

Fig. 10.5d Spectral density of the differenced series.

identical, although they will still show some correlation over the time span of the observational session.

Across-Day Spectral Density

The spectral density estimates of the across-day averaged (Fig. 10.5a) and the across-day differenced time series (Fig. 10.5b) show a couple of interesting features. In the differenced time series (with a 240 second lag) in the periodogram of Figure 10.5d, the long periodic 2 1/2 hour oscillation (of -5.7 log cycles) disappears and a peak occurs at 67 minutes, with a density 10 X stronger than in the original time series. In the periodogram of the across-day averaged time series (Fig. 10.5c) the 2 1/2 hour period stands out as strong as before the averaging. This suggests that the periodicity in the averaged series is caused by multipathing of the signal with a strong relative signal strength between direct and reflected signal. The one hour period in the across-day differenced series is probably an indication of the slower changes in the ionosphere across the 150 km distance and is probably quite random and entirely unique to this data set.

10.4 Satellite 9

10.4.1 Time Series Plot of Satellite 9 Data

The observations for satellite 9 were recorded from 10:44 UT to 15:38 UT and have been compacted to 589 samples. In order to correlate these time series plots with Table 9.1, the reading at the first occurring 10-minute interval will be identified: observation 13 in Figs. 10.6a,b,c and d was recorded at 20:49:59 AEST. The Δ#$ plots of Satellite 9 in Figures 10.6a and 10.6b show matching spectral content when comparing the first one-third of the record of day 255 (Fig. 10.6a) with the first one-third of day 256 (Fig. 10.6b). The sharp 30 to 70 mm peaks then give way in the second one-third to gentler 20 mm oscillations with little 2 mm spikes superimposed. In the last one-third of both day's records

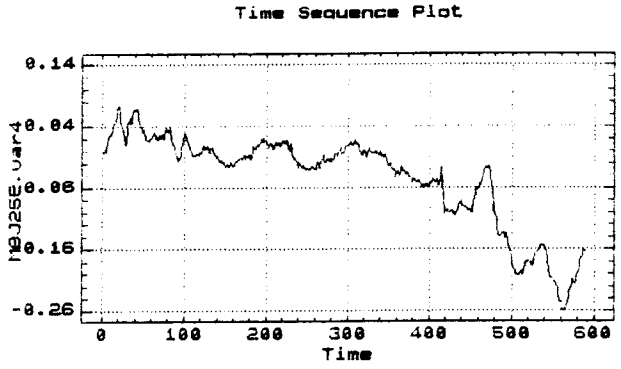

Fig. 10.6a Δ#₹ (255).

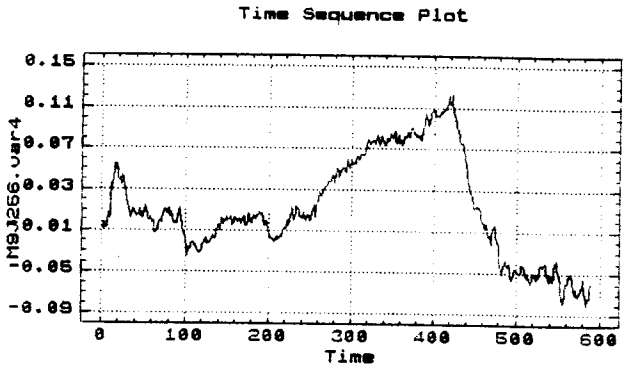

Fig. 10.6b Δ#₹ (256).

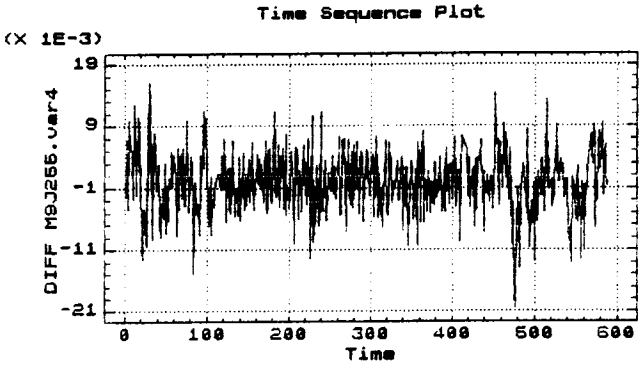

Fig. 10.6c δΔ#₹ (255).

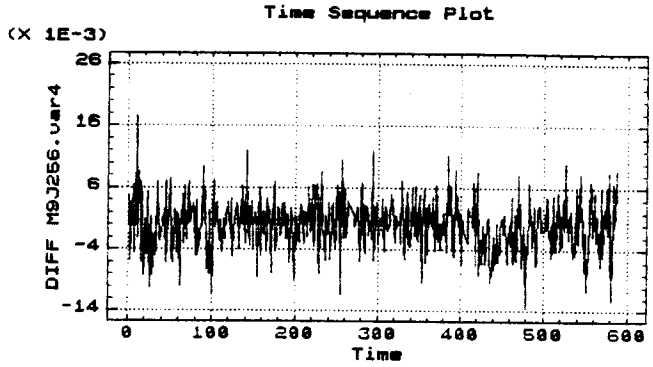

Fig. 10.6d δΔ#₹ (256).

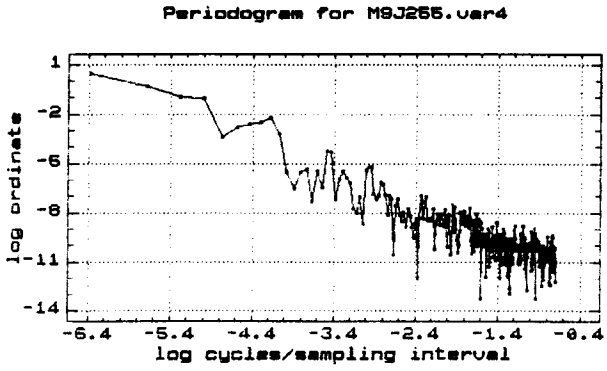

Fig. 10.6e Frequencies.

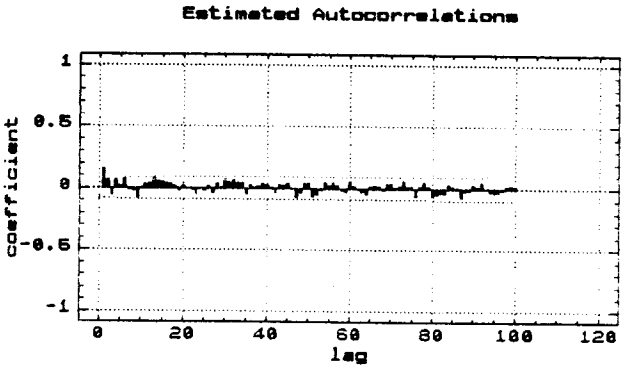

Fig. 10.6f Autocorrelations.

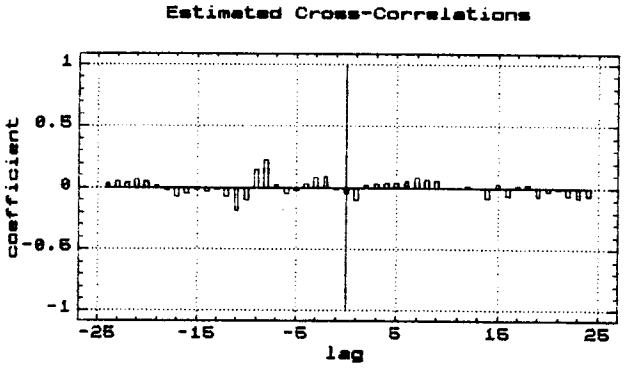

Fig. 10.6g Cross-correlations
Sat.9, days 255 and 256.

there are some sharp and sudden changes with larger amplitudes. The day 255 data shows a sustained downward trend in the plot, while day 256 shows a gradual rise followed by a steep drop of 170 mm. This steep drop find its counterpart in day 255 which is 180 mm. (The difference in vertical scale between Figures 10.6a and 10.6b hide the fact that the steep drops are of equal size.) The total peak-to-peak variation is 200 mm on day 256, while for day 255 it is 340 mm over an observation session of about five hours duration.

Between 13:10 UT and 13:20 UT the point is reached where the rate of elevation change of the satellite becomes zero (between 47400 and 48000 GPS seconds). This is close to the middle of the plot, at the 312th interval in the time axis. Any multipath error signature here would have a very long period. As there are still little 2 mm spikes visible near this elevation culmination point, they must indicate the system noise. The main other explanation would be multipathing off a vertical surface, in which case the apparent 2 minute periodicity would indicate a vertical surface at a distance of about 5 metres. (The vertical multipath index is about 10 to 11 metre minutes here.) With the satellite nearly going through zenith, multipath could be generated by edge diffraction from the top of the thin chimney pipe 5 metres away.

10.4.2 Across-Epoch Differencing of Satellite 9 Data

The time series plots of the across-epoch differenced records $\delta\Delta\#\Phi$ in Figures 10.6c and 10.6d show a band with a dense part of about 5 mm wide which oscillates itself in a band 10 mm wide. Some similarities between the two consecutive days are clearly visible and will be further highlighted by the cross-correlation function. The total width of these plots is no more than about 30 mm even when all the outliers are included. Thus the large drops in the time series of Figures 10.6a and 10.6b are generally composed of a sequence of steps of a few millimetres at a time that are consistently negative.

10.4.3 Cross-Correlation Function of Satellite 9

The cross-correlation function of the Satellite 9 data in Figure 10.6g over five hours of observations shows a strong peak at a lag of 240 seconds. This indicates that there is a strong component in the data that depends upon the satellite to receiver geometry. This peak becomes even more pronounced when the data of the middle session is considered separately. This narrowed spectral window is discussed at the end of the Section 10.4.4.

10.4.4 Spectral Density of Satellite 9 Data

The Fourier transform for the observation record of day 256 in Figure 10.6b failed. The sharp sudden drop in the record needs infinite terms in the Fourier series. The observation record for day 255 in Figure 10.6a did lend itself to the calculation of an estimate of the spectral density in the form of a periodogram displayed in Figure 10.6e. There are some clear dual peaks visible at the correct frequency ratio of 120/154. The main peaks are listed with respect to the natural logarithm of their frequencies: -3.5 (16.5 min) for L1, with a second peak at -3.75 (21 min); -3.0 (10 min) for L1 with a second peak at -3.25 (13 min). A further possible combination can be found at -2.35 (5 min) corresponding with a peak at -2.6 (6.7 min). Because of the dual peak feature it is possible to identify these peaks positively as caused by signal multipathing. But without the spectral density estimate for day 256 there is no objective proof that it recurs the next day.

At lower frequencies, where the overtone grid is not dense enough to capture both the L1 and L2 frequency together, a couple of sole peaks can be found: at -4.2 (33 min) with a 0.1 metre total energy and at -5.0 (91 min) with a 0.3 metre total energy. They are possibly caused by transformation of the sharp drop of 180 mm (after sample number 420 in Figures

10.6a and 10.6b) into sinusoids.

Narrowing of the Spectral Window.

The five hour record is too long to look at individual short duration occurrences of multipath through analysis of the full cross-correlation function. It is assumed that there will be patches of multipath through the data and that cross-correlating the full five hour data set will smooth the cross-correlation function. This smoothing is caused by the contributions of the time intervals where random fluctuations rather than multipath occur. It is amazing that sharp high correlation coefficient peaks were found at all when analysing the session in its full length. The 150 kilometre line length makes this even more remarkable.

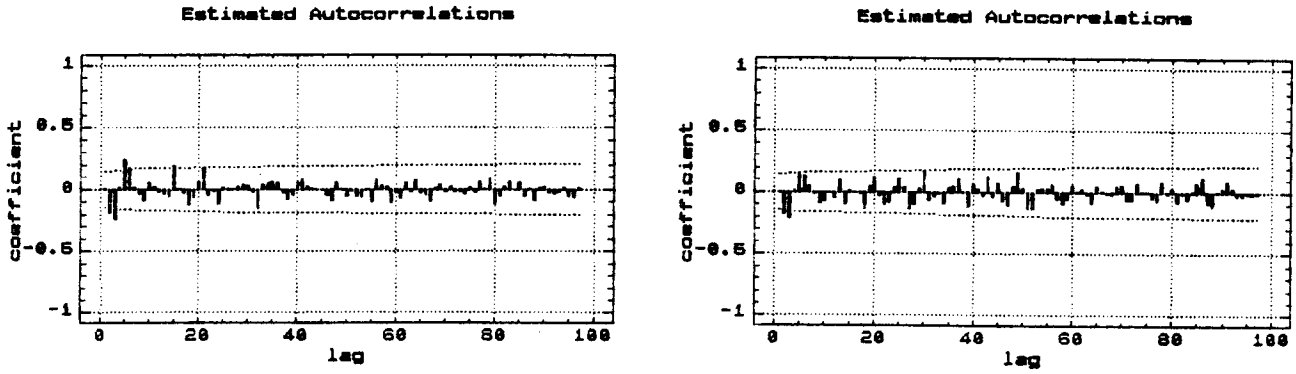

Figure 10.7a and b Autocorrelation functions for the middle of the Satellite 9 data session.

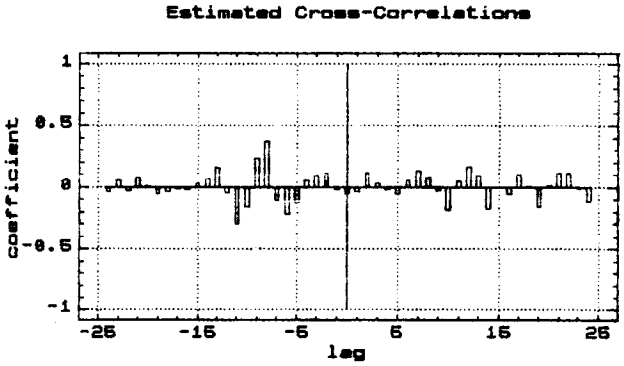

Figure 10.7c Cross-correlation function for the middle of the Satellite 9 data session.

The middle of the Satellite 9 session was analysed separately. All the same it was still not possible to carry out an estimate of the spectral density because of the sharp features in the time series. The cross-correlation function (displayed in Figure 10.7c) shows a high peak at a 240 second lag with an amplitude of one and a half times the cross-correlation coefficient of the total session. The peak in the cross-correlation function stands out strongly and features two negative side lobes. These side lobes occur when the data window gets smaller: they are a convolution of the square data window and the observational record. When there is a large amount of data, the side lobes become less dominating.

In place of the periodograms, the autocorrelation functions for the middle session were calculated. The plot (Fig. 10.7a) for day 255 shows periodicities at the fifth and sixth 30 second lag and the 15th and 21rd. These represent periods of 2.5, 3, 7.5 and 10.5 minutes. The plot for day 256 (Fig. 10.7b) shows periodicities of 2.5, 3, 6.5, 10, 12.5, 15, 18.5, 21.5 and 24.5 minutes. Some of these appear to be harmonics of a period of just over 6 minutes.

10.5 Satellite 11

Satellite 11 has been observed in two different sessions, separated by a gap of about 1¾ hours because of a change in the choice of constellation. The first session (A) has about a half hour of observations, the second session (B) has about one hour of observations. Satellite 11 culminates at about 11:50 UT at a satellite elevation of about 87 degrees. The Satellite 11 data stops about 36 minutes before this culmination moment and starts again about one and a quarter hour after it. Thus signal multipath periodicities in the two sessions are not affected by a zero rate of change of the elevation.

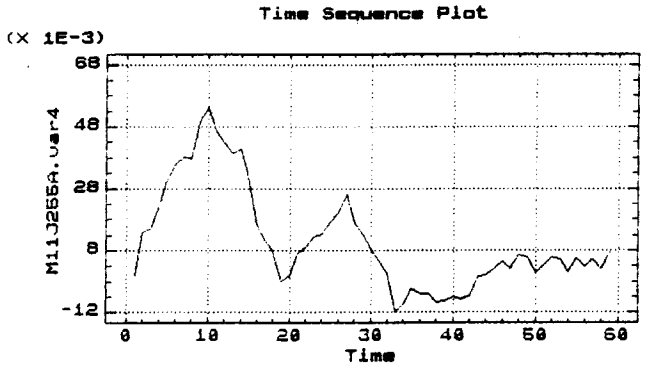

Fig. 10.8a Δ## (255).

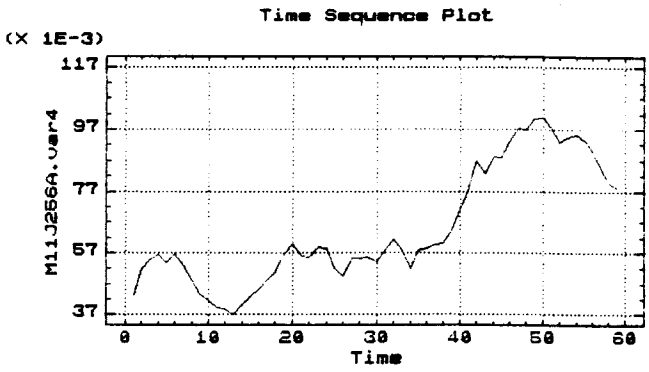

Fig. 10.8b Δ## (256).

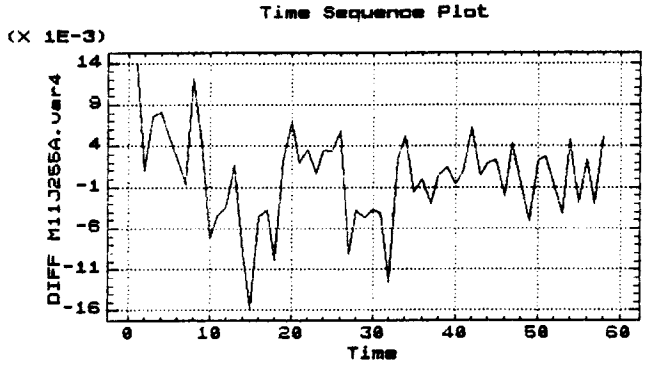

Fig. 10.8c δΔ## (255).

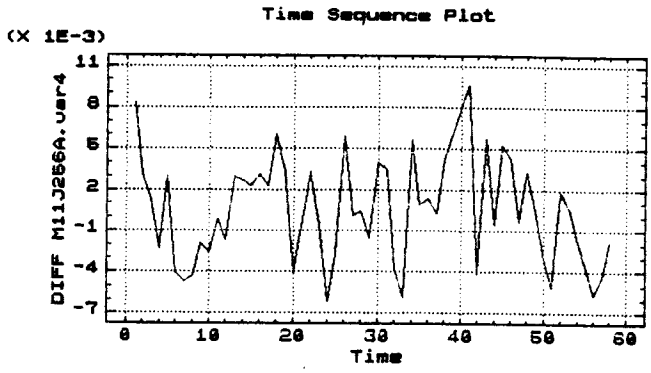

Fig. 10.8d δΔ## (256).

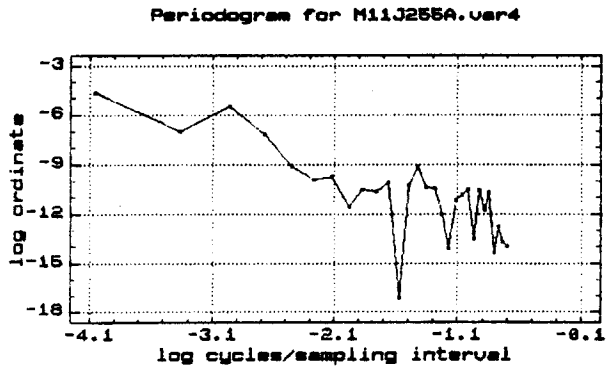

Fig. 10.8e Frequencies.

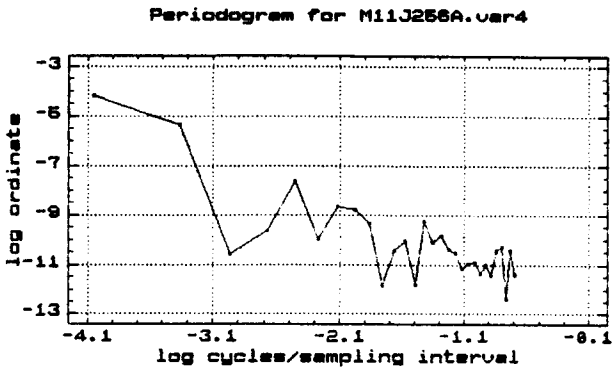

Fig. 10.8f Frequencies.

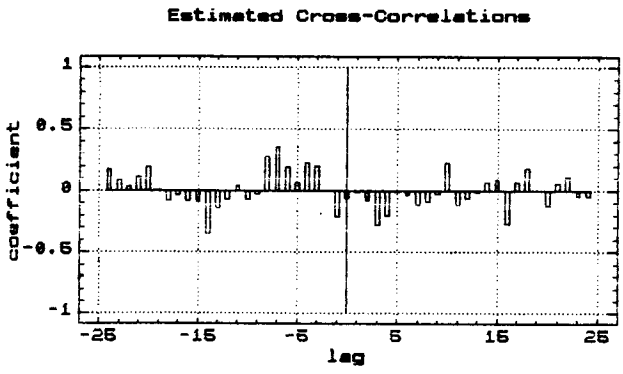

Fig. 10.8g Cross-correlations Sat.11(A), days 255 and 256.

10.5.1 Time Series Plot of Satellite 11 Data (Set A)

The observations for Satellite 11 (data set A) were recorded from 10:44 UT to 11:13 UT and have been compacted to 59 samples. In order to correlate these time series plots with Table 9.1, the reading at the first occurring 10-minute interval will be identified: observation 13 in Figs. 10.8a,b,c and d was recorded at 20:49:59 AEST. The amplitude behaviour of the Δ## time series plots for data set A of Satellite 11 for both days look quite different (see Figs. 10.8a and 10.8b). In the plot of day 255, 50 mm peak-to-peak oscillations occur in the first half of the record while the variations reduce to 10 or 5 mm in the second half of the session. The plot of day 266 starts with 20 mm to 10 mm oscillations which then increase their amplitudes to 40 mm. There are similarities in the spectral content as far as frequency is concerned, but the opposite amplitude behaviour masks this.

10.5.2 Across-Epoch Differencing of Satellite 11 Data (Set A)

Most of the data in both across-epoch differenced records δΔ## are found in a band no wider than 10-15 mm. The spectral content of Figures 10.8c and 10.8d is remarkably similar as far as amplitude and frequency is concerned. This will be treated objectively by determining the cross-correlation function.

10.5.3 Cross-Correlation Function of Satellite 11 Data (Set A)

The highest peak of the cross-correlation (Fig. 10.8g) between the two across-epoch differenced records occurs at a delay of 210 seconds. A slightly smaller peak is evident at a lag of 240 seconds. This suggests that the best fit lag for

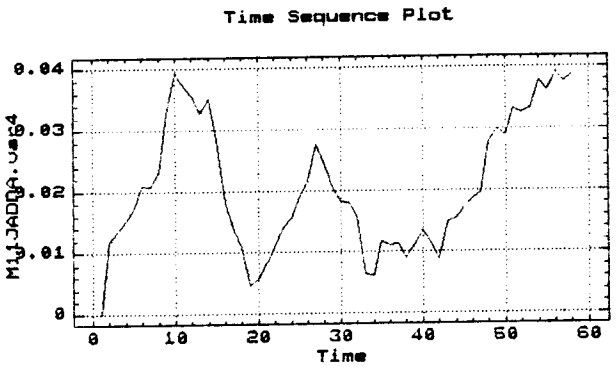

Fig. 10.9a Across-day averaged time series for Sat. 11(A).

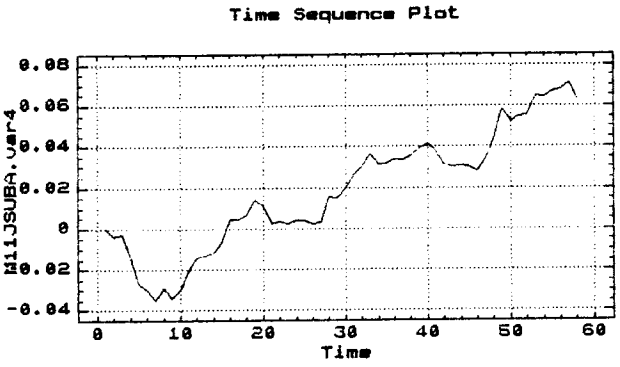

Fig. 10.9b Across-day differenced time series for Sat. 11(A).

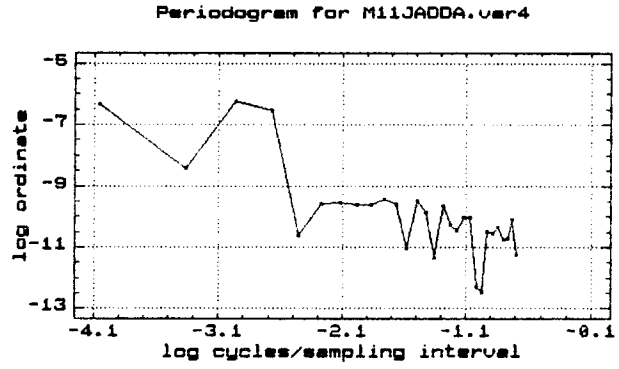

Fig. 10.9c Spectral density of the averaged series.

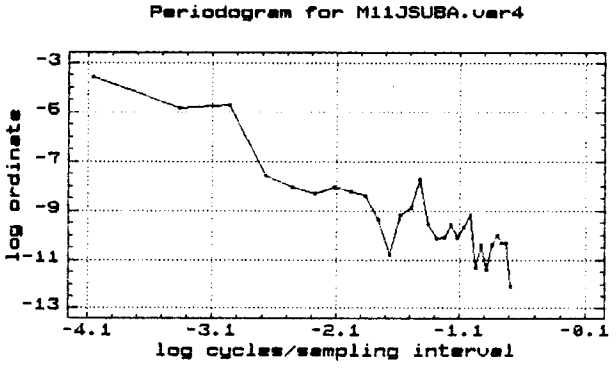

Fig. 10.9d Spectral density of the differenced series.

highest correlation between the records of two consecutive days is somewhere between 210 and 240 seconds. Some strong negative side lobes are also evident. They arise because of the small data window of 59 observations, as explained in Appendix A.4.

10.5.4 Spectral Density of Satellite 11 Data (Set A)

In the periodograms of Figs. 10.8e and 10.8f there are some distinct peaks in the spectral density estimate. It is harder to find peaks which are common to both plots and which are accompanied by second peaks at the frequency ratio of 120/154. Both periodograms show a high spectral density estimate at -4.1 (30 min) and at -3.2 (12 min) with amplitudes of 10 mm and 1 mm at the longer and shorter period, respectively. Some additional periodicities are found at 3.2, 2.7 and 1.8 minutes.

10.5.5 Across-Day Averaging and Differencing (Data Set A)

The largest peak in the across-day cross-correlation function shown in Fig. 10.8g suggests that there is a multipath component in the differential dispersive delay time series. The across-day differenced time series, **DΔ#♦** (Fig.10.9b), still shows the variations evident in both undifferenced **Δ#♦** observables (Figs. 10.8a and b). This suggests that these variations, although occurring on both days, are not of equal amplitudes. A change in surface reflectivity or conductivity between the two days could explain this 9 minute period, also evident in the spectral density functions (Figs. 10.9c and d) of both the averaged and differenced files, **(ΣΔ#♦)/2** (Fig. 10.9a) and **DΔ#♦** (Fig. 10.9b), respectively. The differenced file shows an upward trend of 100 mm across the half hour session, which could represent the change in across-site ionospheric behaviour between the two days. The phenomenon can be explained by one full TEC unit of change (across-day)

in the ionospheric variation trend between the two days and between the 150 km separated sites.

10.5.6 Time Series Plot of Satellite 11 Data (Set B)

The observations for Satellite 11 (data set B) were recorded from 13:04:29 UT to 14:06 UT and have been compacted to 124 samples. In order to correlate these time series plots with Table 9.1, the reading at the first occurring 10-minute interval will be identified: observation 12 in Figs. 10.10a,b,c and d was recorded at 23:09:59 AEST. The amplitudes and frequencies of Δ## in Figures 10.10a and 10.10b look very similar. Many peaks and troughs recur at a 240 second lag as the cross-correlation function will show. There are some similarities with the Satellite 8 records of Figures 10.4a and 10.4b which exhibited an even more startling agreement between the peaks. In this record of Satellite 11 the first day's data can perfectly overlay the second day's data if a "swimming" effect is removed. The latter is expected to be caused by the ionosphere and amounts to about 20 mm in this case. This phenomenon can be explained by a difference in the change of TEC between the two sites of about one fifth of a TEC unit (of 10^{16} electrons per m^2) over a period of one hour. It is interesting that the frequency component is highly correlated whilst the amplitudes of the peaks vary from 20 mm to about 5 mm. The frequency content is not corrupted because the spikes are added, just before reception, at the receiver end through signal multipathing.

10.5.7 Across-Epoch Differencing of Satellite 11 Data (Set B)

In the time series plots of Figures 10.10c and 10.10d the δΔ## data is contained in a 20 mm band on day 255 and in a 10 mm band on day 256. There is a strong beat pattern visible in the record of the first day.

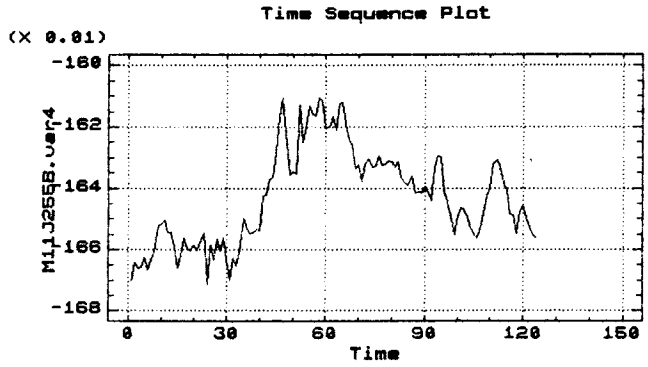

Fig. 10.10a Δ#⊕ (255).

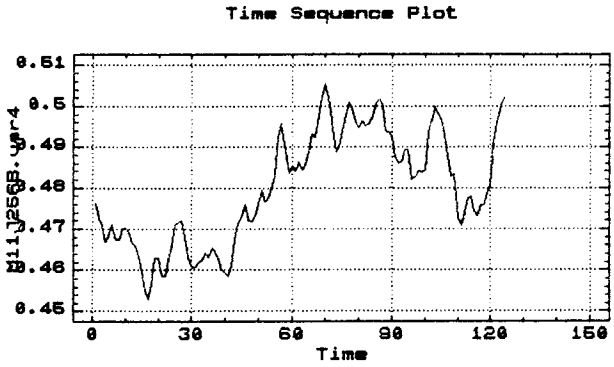

Fig. 10.10b Δ#⊕ (256).

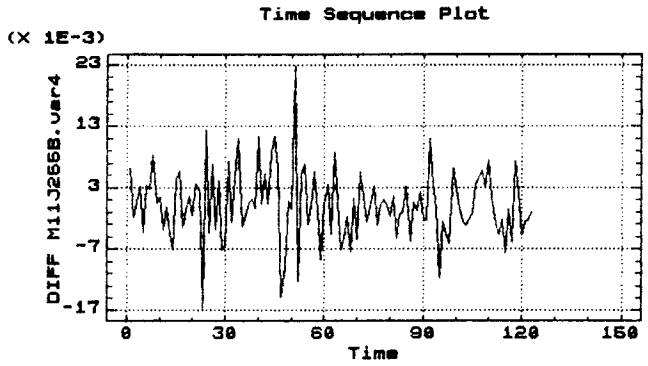

Fig. 10.10c δΔ#⊕ (255).

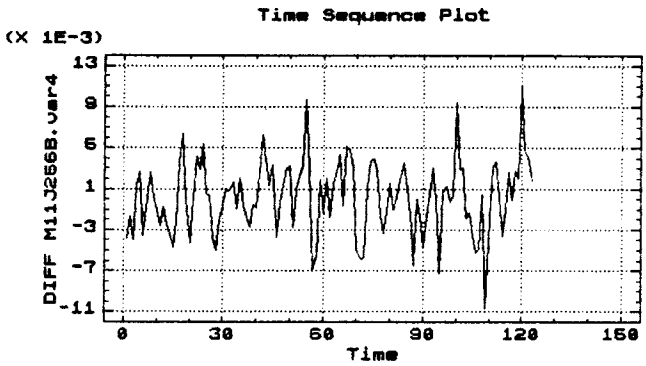

Fig. 10.10d δΔ#⊕ (256).

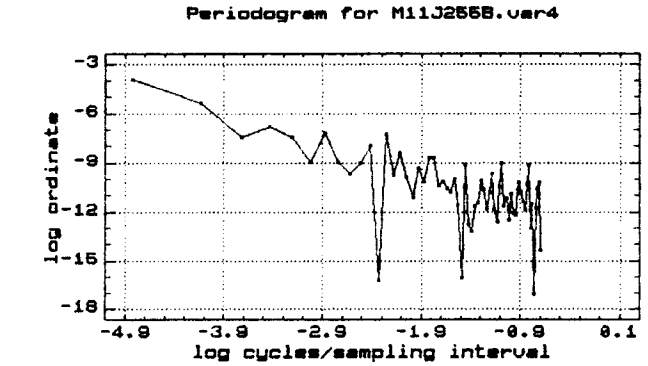

Fig. 10.10e Frequencies.

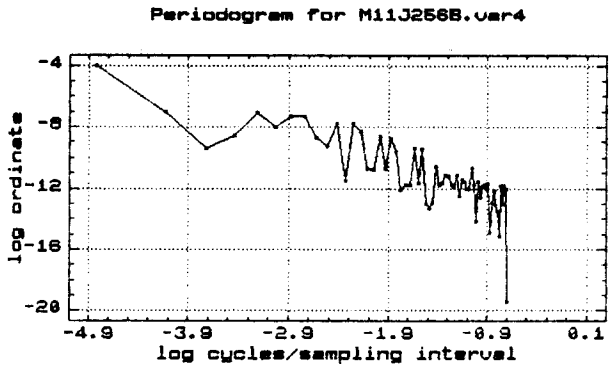

Fig. 10.10f Frequencies.

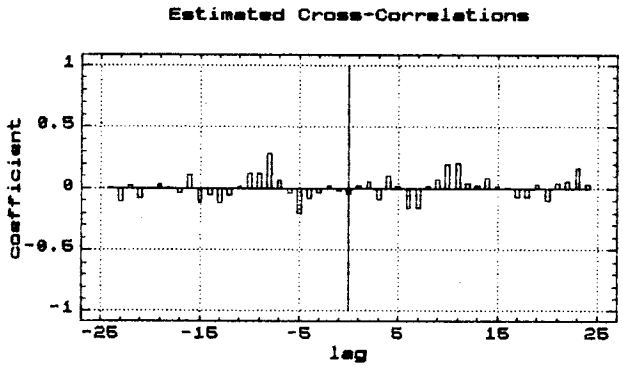

Fig. 10.10g Cross-correlations Sat.11(B), days 255 and 256.

10.5.8 Cross-Correlation Function of Satellite 11 Data (Set B)

The cross-correlation function of data set B (Fig. 10.10g) shows the highest peak at a lag of 240 seconds, confirming that the cause of this across-day correlation has a sidereal period. The phenomenon of the (random) occurrence of some other peaks in the cross-correlation function is considered in Section 10.6.3.

10.5.9 Spectral Density of Satellite 11 Data (Set B)

The estimates of the spectral density function in Figures 10.10e and 10.10f show very distinct peaks, but it is hard to find dual peaks that are common to the two days. Strong periodicities are evident between 2.5 (-1.6 log cycles) and 4.5 (-2.3) minutes. The other main common peaks are at a period of 9 minutes (-2.9) and 30 minutes (-4.1). The values in brackets are log cycles per sampling interval, using the natural logarithm (see Table 10.1). The remaining peaks appear only on one day.

10.5.10 Across-Day Averaging and Differencing (Data Set B)

The across-day averaging (Fig. 10.11a) enhances the 8.2 minute period (-2.8 ln cycles per sampling interval) as shown by the spectral density function of the averaged file (Fig. 10.11c). The across-day differencing (Fig. 10.11b) appears to suppress the 8.2 minute period (the large spikes are not as prominent) and enhances a period of about two minutes. The spectral density function (Fig. 10.11d) of the differenced file DΔ## still shows a peak though at -2.8 ln cycles. It appears that on the first day a high frequency (2 minutes period) multipath effect occurs as well as the 8 minute period. On the second day only the 8 minute period (at varying intensity) recurs. The intensities of possible

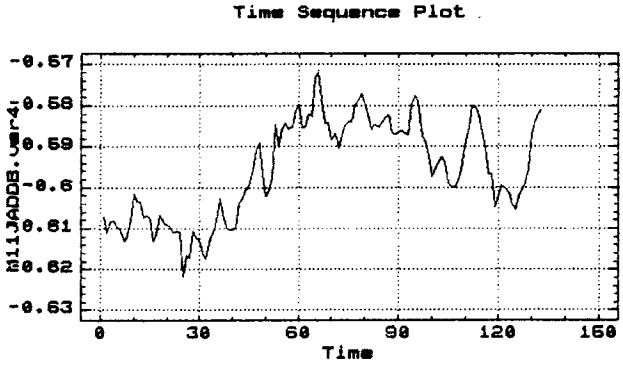

Fig. 10.11a Across-day averaged time series for Sat. 11(B).

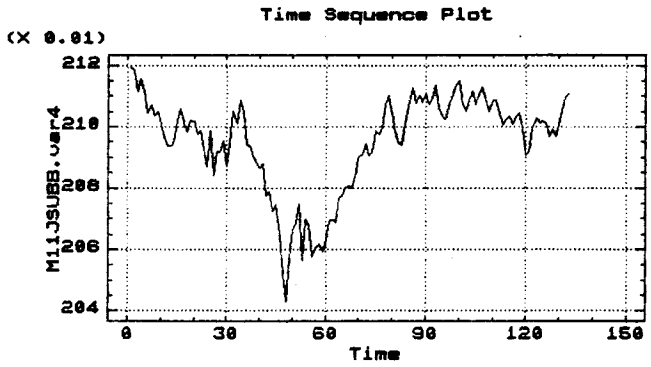

Fig. 10.11b Across-day differenced time series for Sat. 11(B).

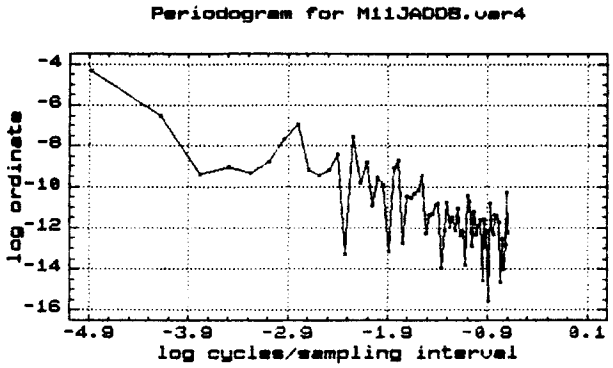

Fig. 10.11c Spectral density of the averaged series.

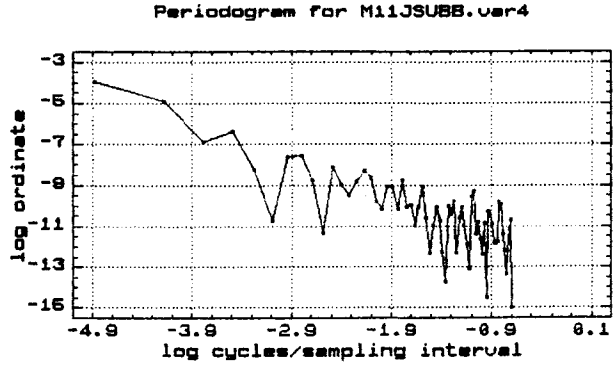

Fig. 10.11d Spectral density of the differenced series.

reflections are also not equal as the range of the data in the differenced file (80 mm) is larger than in the averaged file (50 mm).

10.6 Satellite 12

10.6.1 Time Series Plot of Satellite 12 Data

The observational session for Satellite 12 lasted for one hour: the observations were recorded from 14:39 UT to 15:38 UT and have been compacted to 119 samples. In order to correlate these time series plots with Table 9.1, the reading at the first occurring 10-minute interval will be identified: observation 3 in Figs. 10.12a,b,c and d was recorded at 00:39:59 AEST. The Δ## time series plots of days 255 and 256 (Figs. 10.12a and 10.12b) start with very small peaks and troughs within a 5 mm band. After half an hour, this changes into oscillations with amplitudes of over 20 mm and a trend that results in a rise of 40 mm or more. There is a dramatic 60 mm change after the first 20 minutes on day 255 (Fig. 10.12a). In the data of day 256 (Fig. 10.12b) no similar change is found. There is some agreement between the trends in the rest of both plots as well as in the overall oscillation pattern. But there is much less high frequency signature in these plots when compared with the time series plots of the other satellites. The changes in these plots over the one hour period could be explained by ionospheric changes that differ between the two 150 km separated sites: about half a TEC unit would suffice. A periodicity of about 10 minutes would explain most of the remainder. Considering an applicable multipath index of around 14 metre minutes, reflections from a horizontal surface in conjunction with an antenna height of about 1.5 metres could fully explain this 10 minute periodicity.

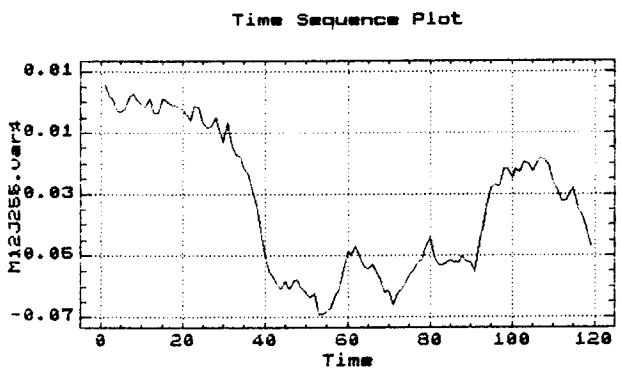

Fig. 10.12a Δ#$ (255).

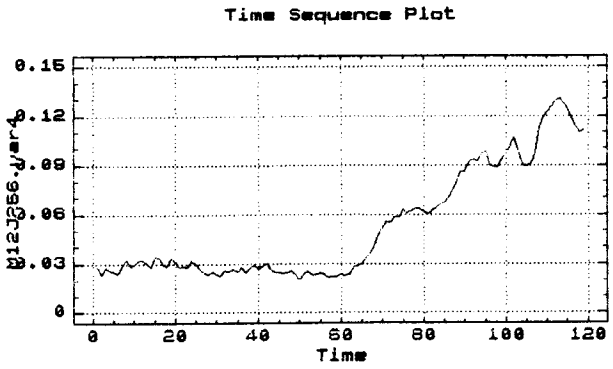

Fig. 10.12b Δ#$ (256).

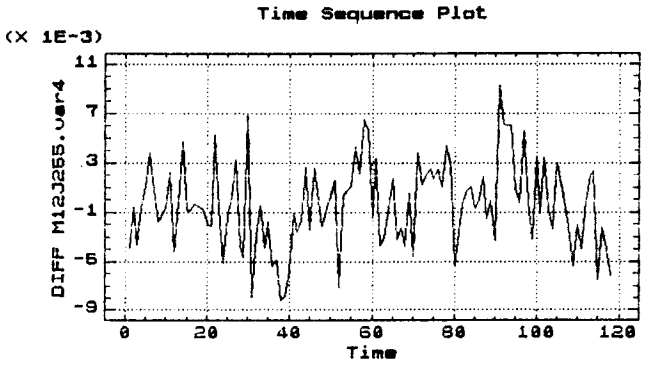

Fig. 10.12c δΔ#$ (255).

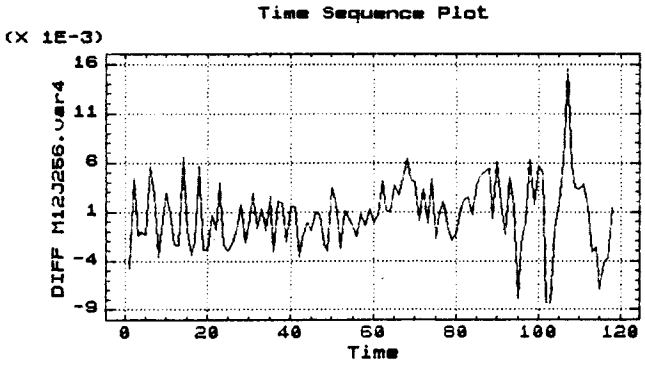

Fig. 10.12d δΔ#$ (256).

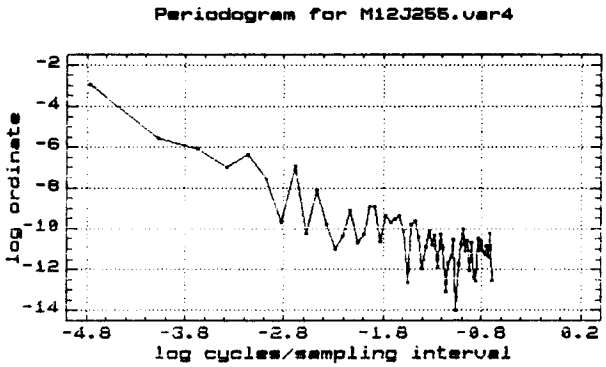

Fig. 10.12e Frequencies.

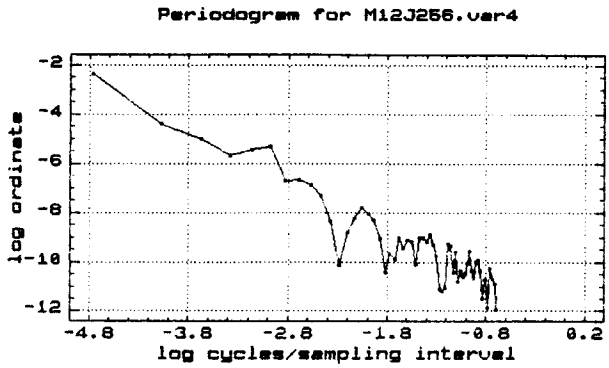

Fig. 10.12f Frequencies.

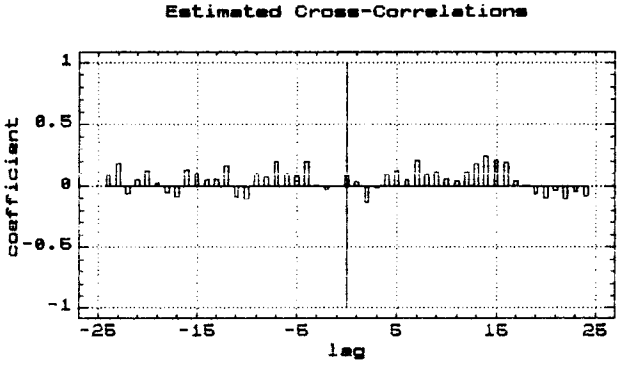

Fig. 10.12g Cross-correlations
Sat.12, days 255 and 256

10.6.2 Across-Epoch Differencing of Satellite 12 Data

The across-epoch differenced records δΔ## are displayed in Figures 10.12c and 10.12d and stay mostly within a band of about 12 mm for day 255. For day 256, the same is valid except for some larger variations at the end. In the middle of the record of day 256, the changes stay within a 5 mm band (Fig. 10.12d).

10.6.3 Cross-Correlation Function of Satellite 12

The cross-correlation function in Figure 10.12g shows a maximum at delays of about 2 to 4½ minutes, but there is no clear peak at the exact 240 second delay mark. Correlation coefficients are just as high at advances (the right hand side of Fig. 10.12g), in particular at 7 minutes which is the fourteenth 30-second advance. Although the result of this cross-correlation function does not conclusively show multipath, the maximum at a lag of seven 30-second intervals (210 seconds) does not deny it either. When the cross-correlation results of all 7 satellites are averaged, all the other lags appear to have rather random cross-correlation coefficients, while the lag at 240 seconds always shows a substantial and positive cross-correlation.

10.6.4 Spectral Density of Satellite 12 Data

The estimates of the spectral density, the periodograms in Figures 10.12e and 10.12f, show peaks at the logarithmic values -3.15, -2.7, -2.45 and -2.13. These values correspond to periods of 12, 7½, 6 and 4 minutes, respectively. Two peaks have the expected ratio of 120/154 and occur in the records of both days; these are at -2.7 and -2.45 and correspond with a 6 minute L1 period.

10.7 Satellite 13

For Satellite 13 (like for Satellite 11 before) there is a gap of about an hour and a quarter separating two observation sessions. This is because TI 4100 receivers only observe the optimum 4 satellites at any one time. Both sessions are of about 1½ hours duration. The moment of culmination for this satellite is at 13:45 UT or at about 49500 GPS seconds, which falls well within the one and a quarter hour gap separating the two sessions A and B. Satellite 13 culminates at an elevation of about 65 degrees at this time. In consequence, signal multipath periodicities in the two sessions are not affected by a zero rate of change of the satellite's elevation angle.

10.7.1 Time Series Plot of Satellite 13 Data (Set A)

The observations for Satellite 13 (data set A) were recorded from 11:26:29 UT to 12:55:29 UT and have been compacted to 179 samples. In order to correlate these time series plots with Table 9.1, the reading at the first occurring 10-minute interval will be identified: observation 8 in Figs. 10.13a,b, c and d was recorded at 21:29:59 AEST. Figures 10.13a and 10.13b, the Δ## time series plots of both days, exhibit a similar upward trend over the 1½ hour period. Variations of 60 mm from this trend line can be observed in both plots. The second halves of the sessions show a lot of similarities: the intervals between five of the six deep troughs are exactly the same on the two days. Large changes occur in the first half of the plot of day 255 (Fig. 10.13a), where the changes in the plot of day 256 (Fig. 10.13b) also reach their largest amplitudes. The possibility of movement of personnel around the receiver randomly obstructing the multipath error signature and of handling of equipment introducing strong but short momentary reflections can not be disregarded. This could explain the difference between the start of the records of the two days. But more probable is the possibility of the ocurrence of a very strong reflection. The amplitude of the

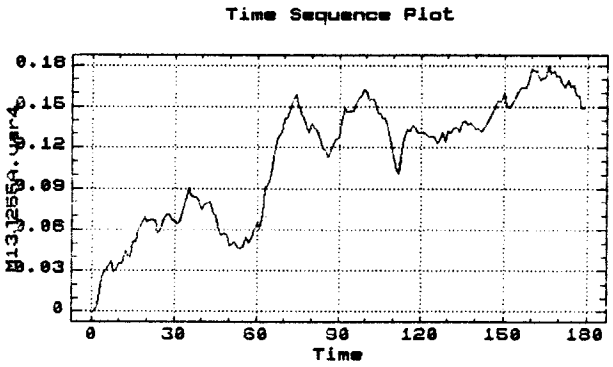

Fig. 10.13a Δ#₹ (255).

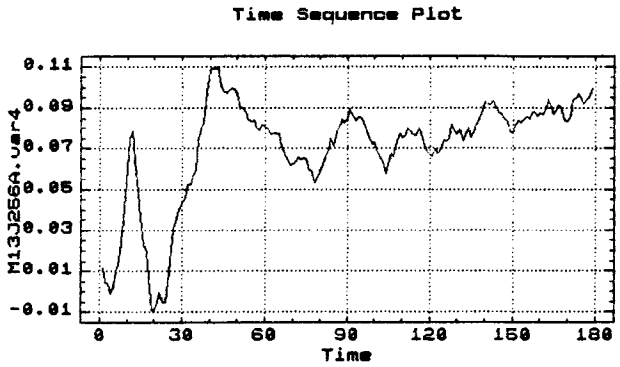

Fig. 10.13b Δ#₹ (256).

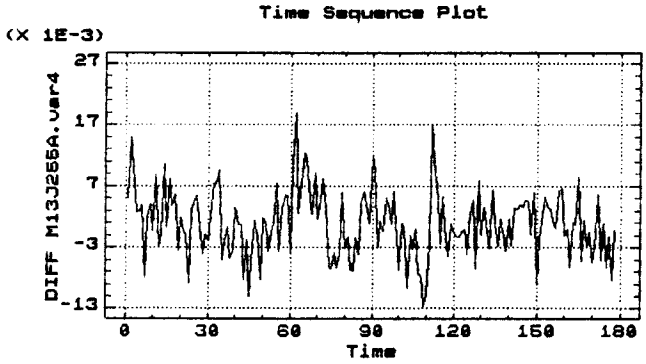

Fig. 10.13c δΔ#₹ (255).

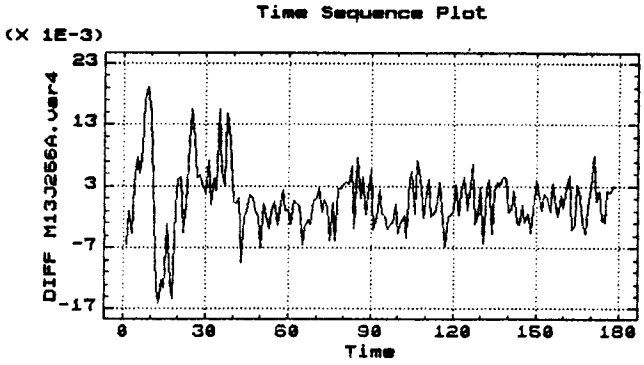

Fig. 10.13d δΔ#₹ (256).

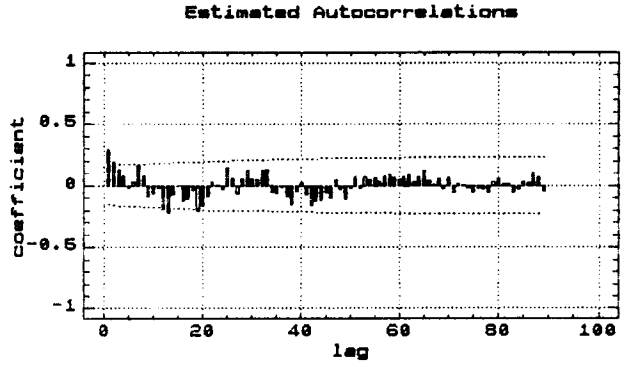

Fig. 10.13e Autocorrelations.

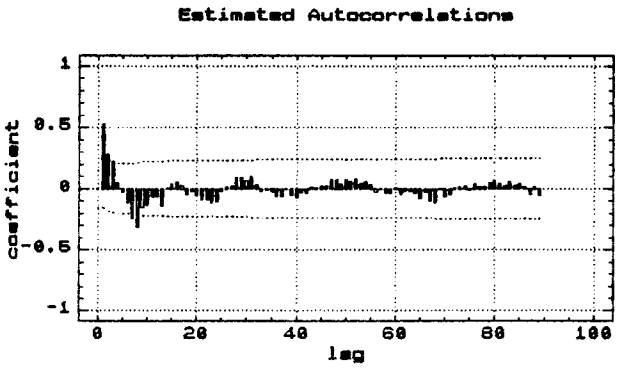

Fig. 10.13f Autocorrelations.

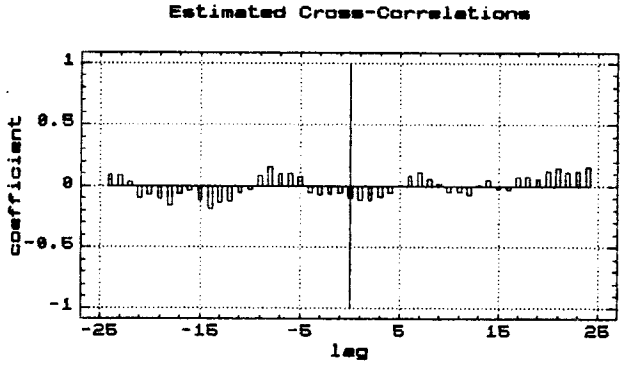

Fig. 10.13g Cross-correlations
Sat. 13(A), days 255 and 256.

day 256 Δ## time series is large and suggests a relative signal strength near 1 between the direct and the multipath signal. In such a case both the L1 and L2 error curves approximate sawtooth patterns. The across-frequency difference will consist of the difference between two sawtooth functions and will result in a pattern as shown in Fig. 12.9. This explains the sharp 90 mm variation at the start of the record in Fig. 10.13b.

10.7.2 Across-Epoch Differencing of Satellite 13 Data (Set A)

The across-epoch differenced record δΔ## of day 255 (Fig. 10.13c) shows a beat pattern and a 20 mm band of data about it. The day 256 plot (Fig. 10.13d) exhibits initially a 20 mm wide band, but the data soon settles into a band that is often smaller than 10 mm over the one and a half hour period.

10.7.3 Cross-Correlation Function of Satellite 13 Data (Set A)

The cross-correlation function in Figure 10.13g shows a peak at a delay of 240 seconds delay with a 0.15 correlation coefficient. This indicates that there is a component in the data that repeats itself after the passing of a sidereal day. The 240 second lag always seems to feature a relative peak, while there is no such consistent behaviour at other lags. The negative sidelobes are a feature of the Fourier transforms of the data window (Refer to Appendix A.4).

10.7.4 Spectral Density of Satellite 13 Data (Set A)

The statistics programme package was unable to compute the spectral density of this sample because the sharp features in the data time series would require infinite Fourier series. Consequently the time series could not be decomposed into the

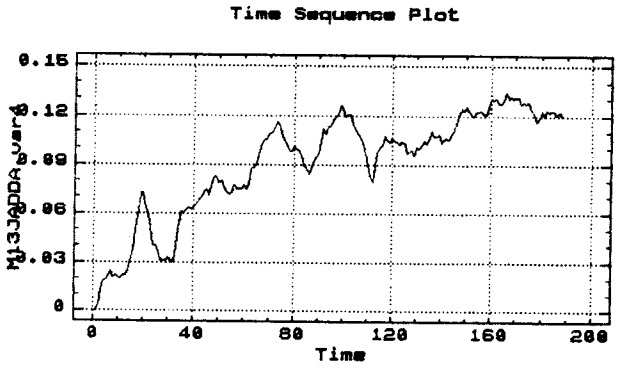

Fig. 10.14a Across-day averaged time series for Sat. 13(A).

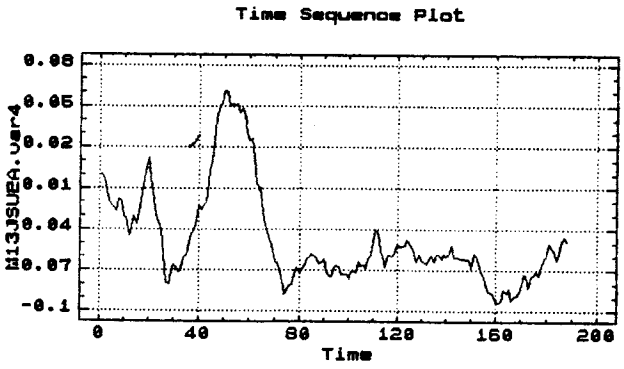

Fig. 10.14b Across-day differenced time series for Sat. 13(A).

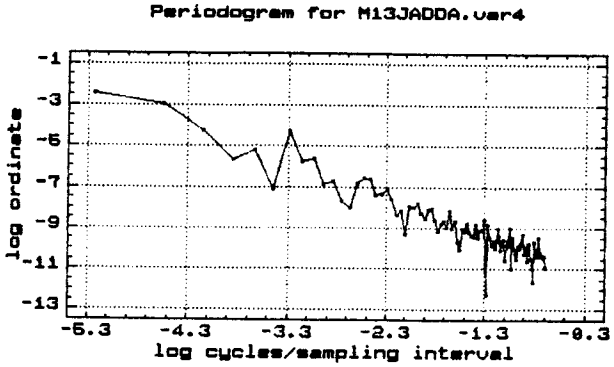

Fig. 10.14c Spectral density of the averaged series.

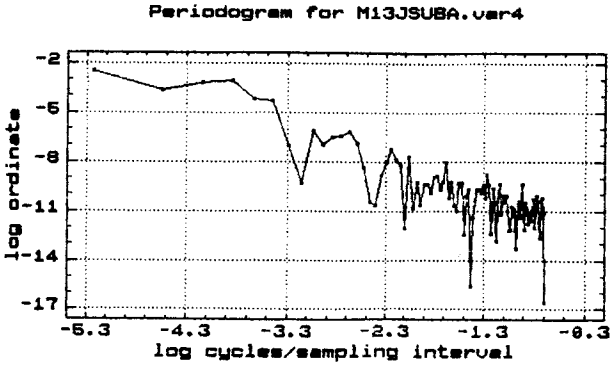

Fig. 10.14d Spectral density of the differenced series.

frequencies of the grid of the overtone series because of insufficient random access memory available on the PC used.

10.7.5 Across-Day Averaging and Differencing (Data Set A)

The spectral density function (Fig. 10.14c) of the averaged file **(ΣΔ##)/2** in Fig. 10.14a shows a clear peak at a 13.5 minute period (-3.3 ln cycles per sampling interval). After the large variation at the beginning of the differenced file **DΔ##** in Fig. 10.14b the across-day differencing seems to be successful in extinguishing the periodicities from epoch 80 to 150 (a 35 minutes interval). The diagrams are presented without further comment.

10.7.6 Time Series Plot of Satellite 13 Data (Set B)

The observations for Satellite 13 (data set B) were recorded from 14:12 UT to 15:38 UT and have been compacted to 173 samples. In order to correlate these time series plots with Table 9.1, the reading at the first occurring 10-minute interval will be identified: observation 17 in Figs. 10.15a,b,c and d was recorded at 00:19:59 AEST. There is a certain amount of spikiness in the Δ## time series plots of the across-site across-frequency differenced data shown in Figures 10.15a and 10.15b that may be due to signal multipathing. But other variations with 50 mm amplitudes seem to be superimposed. This variation is equivalent to a change in the total electron content of the ionosphere of about half a TEC unit of 10^{16} electrons per square metre over the full length of the observation session of 1½ hours.

In the first half hour of day 255 (Fig. 10.15a) the spikes, which are characteristic of signal multipathing, are lacking. It is conceivable (although unlikely) that stationary personnel or stored equipment could have obstructed strong multipath signals. No other reasons for the lack of spikes (which do appear the next day) came to mind.

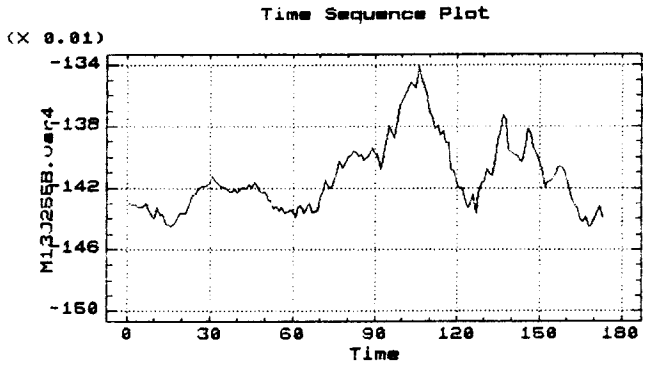

Fig. 10.15a Δ#ᵩ (255).

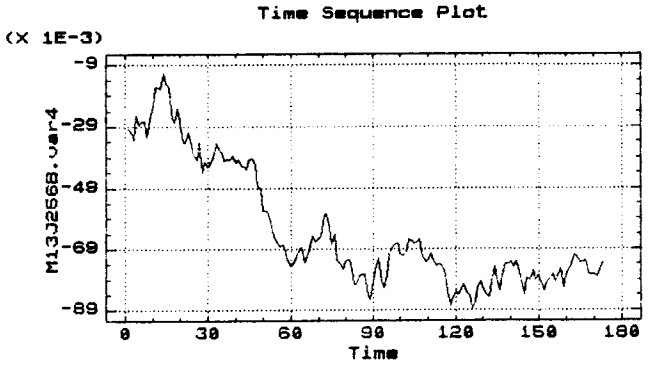

Fig. 10.15b Δ#ᵩ (256).

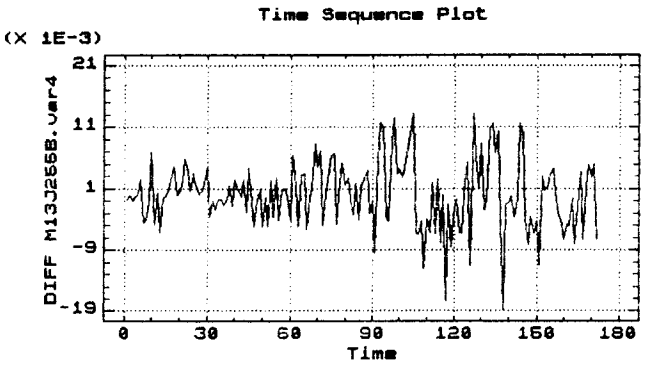

Fig. 10.15c δΔ#ᵩ (255).

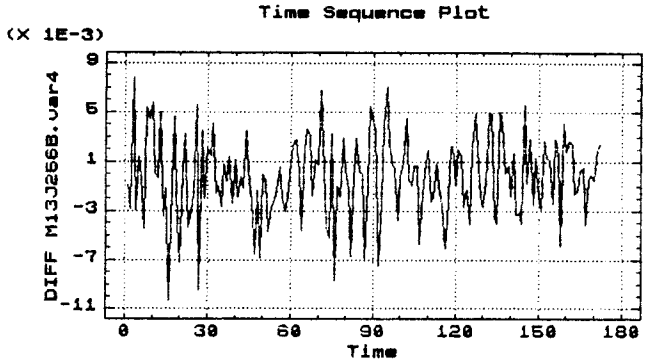

Fig. 10.15d δΔ#ᵩ (256).

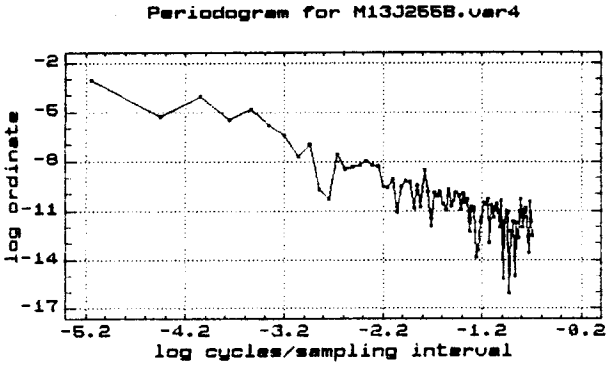

Fig. 10.15e Frequencies.

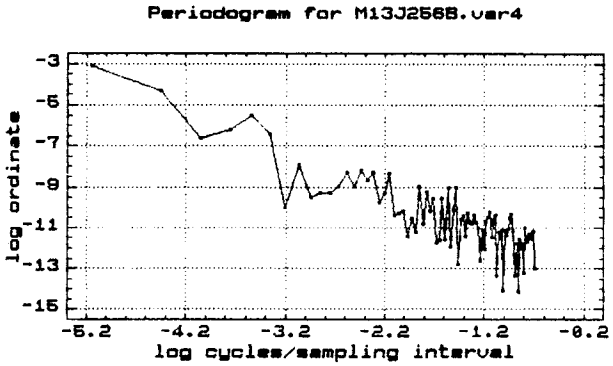

Fig. 10.15f Frequencies.

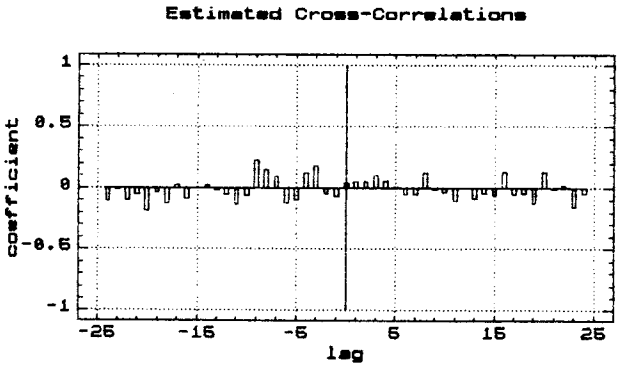

Fig. 10.15g Cross-correlations Sat.13(B), days 255 and 256.

10.7.7 Across-Epoch Differencing of Satellite 13 Data (Set B)

The across-epoch differenced series $\delta\Delta\#\bullet$ for day 256 in Figure 10.15d is contained within a 10 to 12 mm band, while day 255 (Fig. 10.15c) shows a wider band of about 20 mm in the latter half of the session. These plots represent the changes from one thirty second epoch to the next.

10.7.8 Cross-Correlation Function of Satellite 13 Data (Set B)

The cross-correlation function in Figure 10.15g shows a peak at lags between 210 and 300 seconds, with the highest correlation coefficient at a 300 second lag. Although the correlation coefficient at a lag of 240 seconds is almost as large, the peak is not as distinct as in the records of Satellites 3, 6, 8, 9 and 11.

10.7.9 Spectral Density of Satellite 13 Data (Set B)

The spectral density estimates in Figs. 10.15e and 10.15f show peaks on both days at the logarithmic values of -5.2, -3.55, -2.4, -1.85. This corresponds to periods of 91, 17, 5.5 and 3 minutes respectively. Dual peaks at the 120/154 frequency ratio occur at the log values -2.32 and -2.58, as well as at the log values -1.6 and -1.85. These pairs correspond to L1 periods of 5 minutes and 2.5 minutes, respectively.

10.7.10 Across-Day Averaging and Differencing (Data Set B)

The spikes in the averaged file in Fig. 10.16a are more pronounced than those in the differenced file in Fig. 10.16b, even after allowing for the scale difference between the two

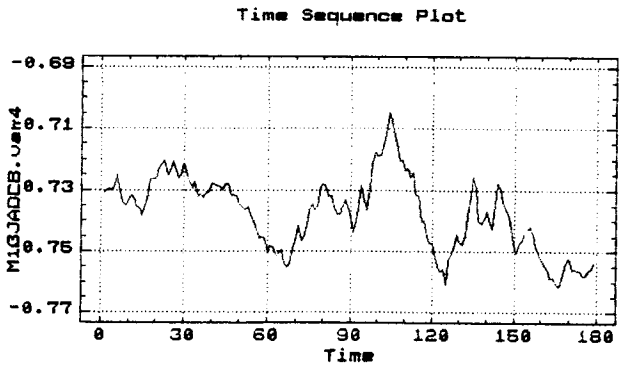

Fig. 10.16a Across-day averaged time series for Sat. 13(B).

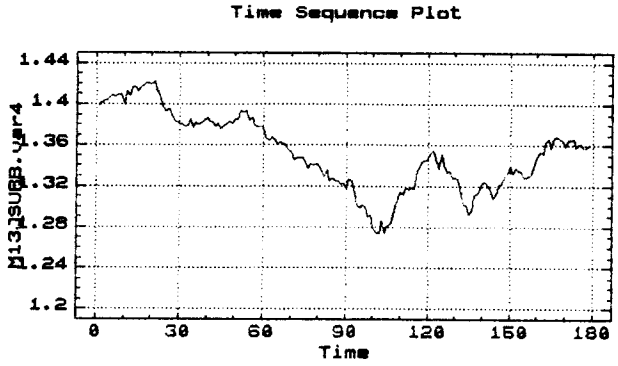

Fig. 10.16b Across-day differenced time series for Sat. 13(B).

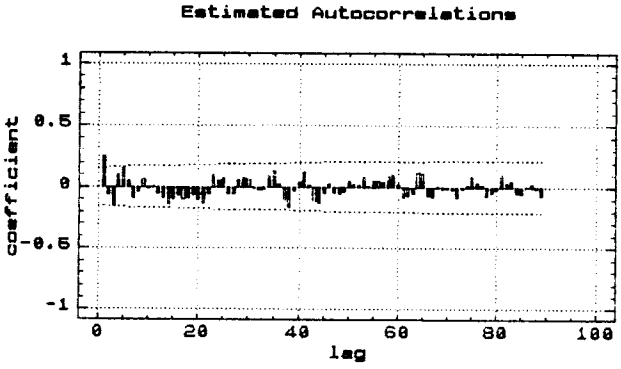

Fig. 10.16c Autocorrelations of the averaged series.

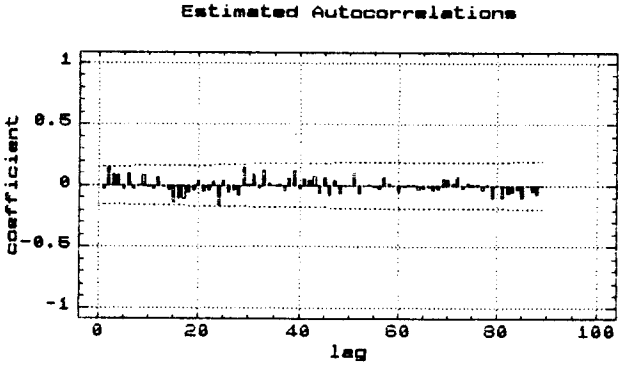

Fig. 10.16d Autocorrelations of the differenced series.

plots. The differencing seems to be especially successful over a 25 minute period between epochs 50 and 100. The spikiness is totally extinguished over this interval. The autocorrelation function (Fig. 10.16c) of the across-day averaged series shows that a period of 2.5 minutes is well represented. This corresponds to the spikes in the averaged series of Fig. 10.16a.

10.8 Summary of Analysis

In the across-site across-frequency records of Satellites 3, 6, 8, 9, 11 and 13 distinct troughs are evident that repeat themselves after 23 hours and 56 minutes. Cross-correlation calculations confirm these conclusions. Some of these deep troughs accompany large amplitude variations which suggest extremely strong reflections with relative signal strength factors α of nearly 1. This is confirmed by the observed pulse function effect caused by a sawtooth phenomenon described in Chapters 10.2.1 and 12.1.

It was possible to identify the occurrence of multipath in various cases through the double peak feature in the spectral density function (Refer to Chapter 12 for an explanation). Positively identified are L1 periods of 4 to 6 minutes in the Satellite 6 data, L1 periods of 10 to 13 minutes in the Satellite 8 data, L1 periods of 10, 13 and 16.5 minutes in the Satellite 9 data, one L1 period of 6 minutes in the Satellite 12 data and L1 periods of 2.5 and 5 minutes in the Satellite 13 data. A possible 20 and 30 minute L1 period exists in the Satellite 3 data. Various of the periods found are consistent with the surrounding reflective surfaces, when considered together with the relevant multipath index.

The averaging and differencing across two consecutive days at a 240 second lag is successful in visually enhancing the occurrence of multipath. This technique also gives an impression of the relative magnitudes of the multipath component and the ionospheric component of the differential

dispersive delay. For Satellite 8 and 13, the multipath component appears larger than the ionospheric component at various times. Of interest is the fact that some of the across-day differenced files DΔ## still show dual peaks in the spectral density function. This suggests that the multipath effect, that repeats the next day, is not necessarily of the same intensity. There can be changes in the reflectivity or conductivity of the surface from one day to the next. Changes in dustcover or moisture content could be the reasons.

Although the cross-correlation functions sometimes show relative maxima which are not the largest at the 240 second lag, it is noticed that there is always a peak at this lag. The other lags now and then also display positive cross-correlation coefficients. But this occurs quite randomly. Averaging of all the cross-correlation plots of this chapter would show only one peak at the 240 second lag. As this is regarded as an indication of multipath, one might even conclude that multipath is more the rule than the exception at the site considered.

Multipath does not necessarily have to occur over the whole five hour observation period. The geometry may perhaps support multipathing during one part of the observational session and not it in another. When calculating the cross-correlation function for the whole five hour session, the cross-correlations of parts with multipath will be attenuated by the zero cross-correlations of parts with no multipath. Even though strong correlations may occur in, say, a few half hour intervals, the overall correlation coefficient for the full five hour session will remain at the 20 to 30 % level. Thus the size of the correlation coefficient for the full five hour session is not as important as the fact that the peak occurs at the 240 second lag. When the data window is partitioned, the cross-correlation function shows much higher peaks in some intervals. For example, the cross-correlation results for carrier phase data of Georgiadou and Kleusberg

(1988) and Müller et al (1989) refer to data spans of 15 to 20 minutes.

Across-epoch differencing is carried out in order to suppress low frequency ionospheric variations and to enhance high frequency variations like multipath. The across-epoch differenced files display a narrow noise band, which is often 3 to 4 millimetres but almost always less than 10 millimetres wide. This shows that the large amplitudes in the Δ## files are accumulated from consistently positive or negative minuscule steps of a few millimetres, between the 30-second data intervals.

11. ANALYSIS OF PSEUDORANGES.

Only a summary will be given of the analysis of the pseudorange information as this study concentrates on carrier phase multipath. The across-site across-frequency pseudorange delay pathlength differences Δ#P showed a typical noise level within a 4 metre band, with most maxima within a 7 or 8 metre band. This is about half of the maximum possible peak-to-peak multipath error expectable from the early/late delay gate error function as described in Chapters 5.1 and 8.2. This suggests that the signal strength of the reflected signal is generally no more than about half the strength of the direct signal in this data set. Most of the spectral content of the data can be found in a band two to three metres wide. The largest maxima are at the ten metre level. A typical plot of a Δ#P time series is shown in Fig. 11.1 and displays the data of day one (day 255) of Satellite 9. The units on the vertical axis are metres; the horizontal axis shows the

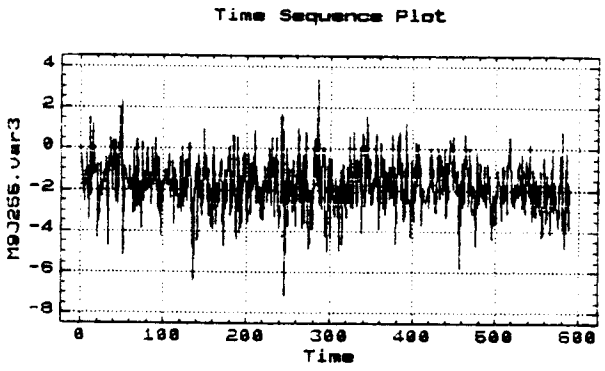

Figure 11.1 The Δ#P time series of day 1 (Satellite 9, 12 September, 1987).

number of 30-second intervals of observations. The frequency spectrum of the pseudorange data of this 150 kilometre line is not very useful. The data appears to be too noisy for a successful decomposition into periodic functions. An example of a typical Δ#P pseudorange spectral density function is

shown in Fig. 11.2. It is clearly very noisy, with comparable energy right across the frequency spectrum. The vertical axis shows the base 10 logarithm of the total variance (in metres squared) contributed by the frequency on the horizontal axis. Some extra energy (in excess of 10^2 m^2) is visible between -1.4 and -2.4 log cycles per sampling interval, which represents periods between 2 and 5.5 minutes.

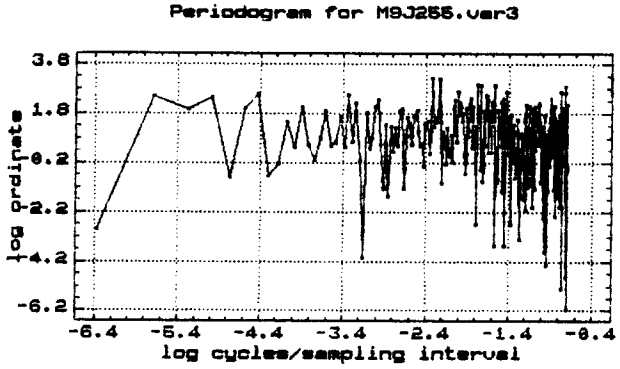

Figure 11.2 The frequency spectrum of a Δ#P pseudorange time series (Satellite 9, 12 September, 1987).

The between-day cross-correlation functions of the across-site across-frequency pseudorange delay pathlength differences Δ#P are shown in Figures 11.3 to 11.11. A point worthwhile noting here is that, in contrast to the carrier phase data of this 150 kilometre baseline, no across-epoch differencing of the pseudorange information is required in order to demonstrate the high between-day cross-correlation at the four minute lag. This phenomenon has been addressed in Chapter 7.1.4. The carrier phase multipath effect and the ionospheric component of Δ#Φ, the across-site across-frequency carrier phase pathlength difference, have similar amplitudes but show a different frequency behaviour and require a further level of differencing in order to analyse the correlations. The across-epoch differenced carrier phase observable δΔ#Φ is successful in separating the high and low frequency components of the differential dispersive delay as shown in Chapter 7.1.4. In contrast, the pseudorange multipath effect is a lot larger than the remaining across-site ionospheric component mentioned above and no across-epoch differencing is required in order to show the across-

day correlations. All the cross-correlation plots in Figures 11.3 to 11.11 show a relatively high correlation between the Δ#P pseudorange time series of two consecutive days at a lag of four minutes. The horizontal axis shows the lag number (in units of 30 seconds) for which the cross-correlation coefficient is calculated. The vertical axis shows the cross-correlation coefficient as a value between 0 and 1, either positive or negative. If all the cross-correlation function plots were averaged a dominant peak centred around the eighth 30-second lag would become evident while the other ordinates would look like random noise.

The Δ#P cross-correlation function plots of Satellites 3, 6, 9, 12, 11(A) and 13(B) show a relative maximum at the eighth lag of 30 seconds (Figs. 11.3, 11.4, 11.6, 11.7, 11.8 and 11.11, respectively). This is equivalent to a high correlation the next day at a time four minutes earlier. The pseudorange records of Satellites 8, 11(B) and 13(A) show a cluster of high cross-correlation coefficients near the eighth lag but the maxima are at the seventh (Figs. 11.5 and 11.9) and ninth lag (Fig. 11.10), respectively.

Data set (Satellite No.)	Cross-correlation maximum Δ#P lag No.	Δ#Φ lag No.
3	8	8
6	8	8
8	7	8
9	8	8
11(A)	8	7
11(B)	7	8
12	8	7
13(A)	9	8
13(B)	8	9

Table 11.1 Cross-correlation function maxima.

In the case of the cross-correlation plots of the carrier phase Δ#Φ records (Refer to Chapter 10) the eighth lag showed a maximum for Satellites 3, 6, 8, 9, 11(B) and 13(A). The maxima for the Δ#Φ cross-correlations of Satellites 11(A), 12

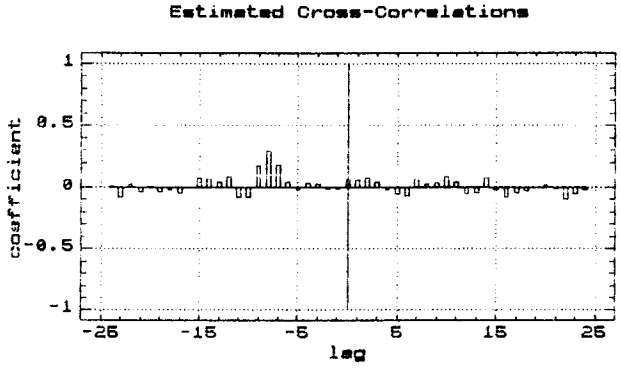

Figure 11.3 Satellite 3 Δ#P cross-correlations, days 255 and 256.

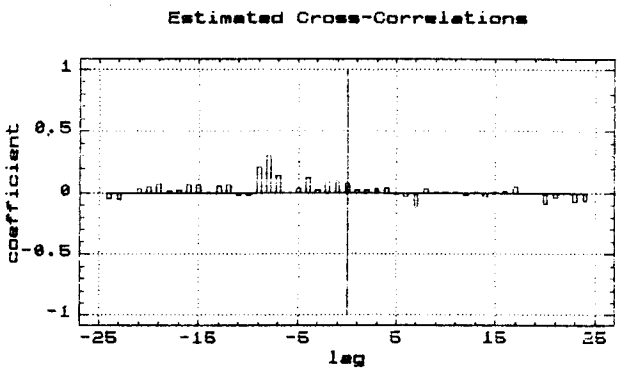

Figure 11.4 Satellite 6 Δ#P cross-correlations, days 255 and 256.

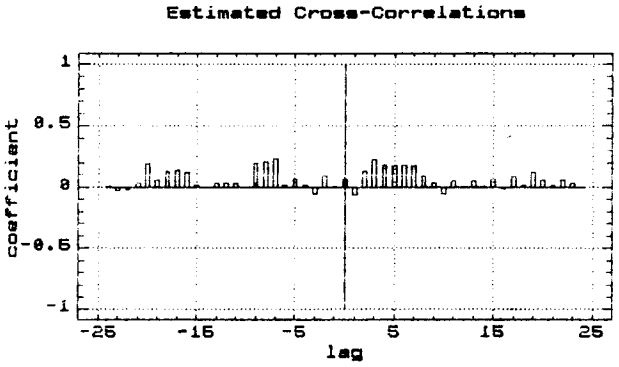

Figure 11.5 Satellite 8 Δ#P cross-correlations, days 255 and 256.

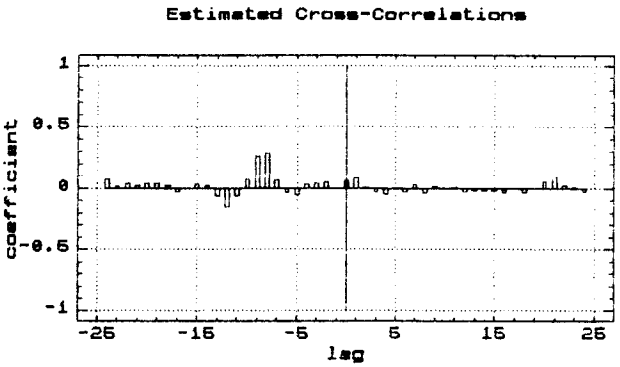

Figure 11.6 Satellite 9 Δ#P cross-correlations, days 255 and 256.

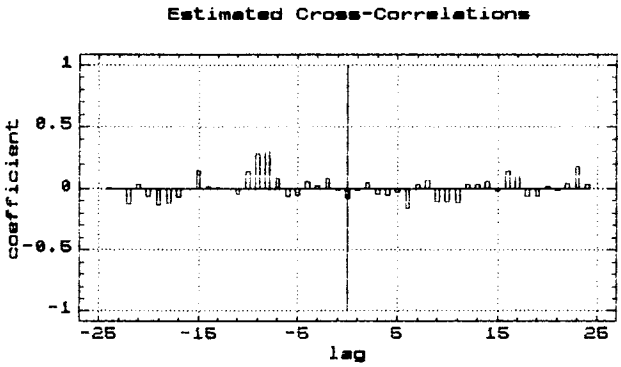

Figure 11.7 Satellite 12 Δ#P cross-correlations, days 255 and 256.

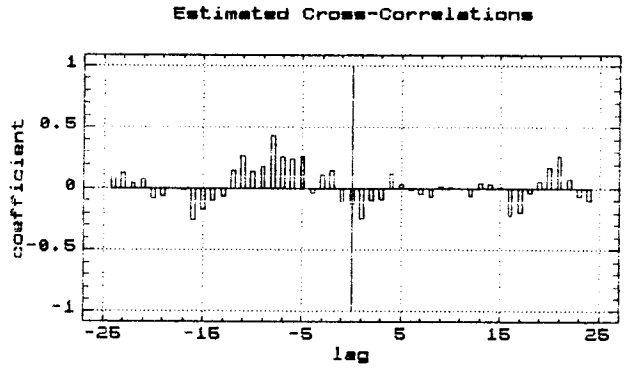

Figure 11.8 Satellite 11 Δ#P cross-correlations, days 255 and 256 (Set A).

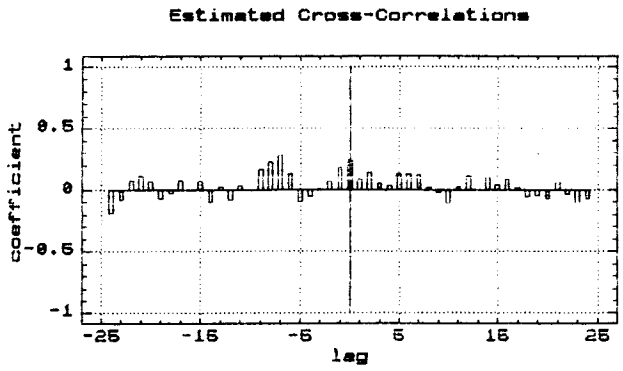

Figure 11.9 Satellite 11 Δ#P cross-correlations, days 255 and 256 (Set B).

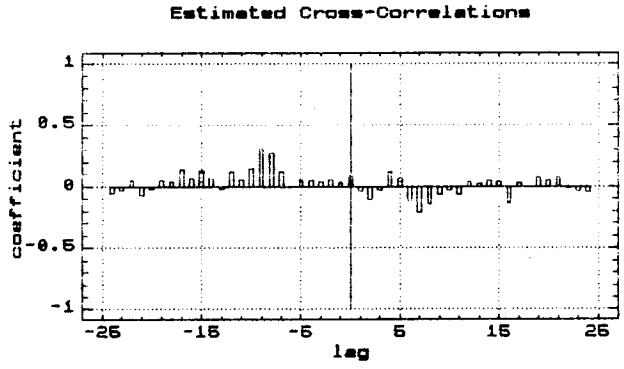

Figure 11.10 Satellite 13 Δ#P cross-correlations, days 255 and 256 (Set A).

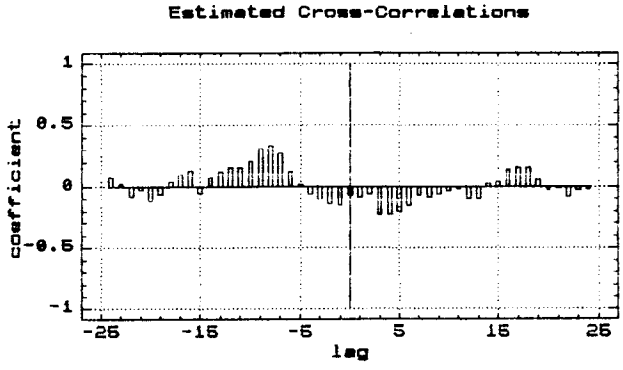

Figure 11.11 Satellite 13 Δ#P cross-correlations, days 255 and 256 (Set B).

and 13(B) are at the seventh, seventh and ninth lag, respectively. Thus part of the data of Satellite 11 and 13 show a pseudorange correlation maximum slightly away from the eighth lag, while the correlation maximum of the phase record of these satellites is right on the eighth lag. For another part of the data of these same satellites the behaviour of phase and pseudorange records is reversed. Noteworthy is also the fact that Satellite 8 shows such a clear correlation example in the case of the carrier phase data but no clear correlation at the eighth lag for pseudorange data. The data of Satellite 12 shows the reverse situation. A summary of this comparison is given in Table 11.1.

The strong negative lobes in Figs. 11.8 and 11.11 are caused

by the use of a relatively short and truncated data series. The cross-correlation function is mathematically defined using an infinite series (Refer to Appendix A.3). The small square data window that truncates the series causes the negative sidelobes through the use of Fourier transforms. Data tapering methods have not been used for reasons given in Appendix A.4. The Figures 11.3 to 11.11 are presented for the sake of completeness only.

12. MULTIPATH SIMULATIONS

12.1 Simulation of Constant Periodicities

Because of sudden changes and large amplitudes in the across-site across-frequency time series plots of Δ## in Chapter 10, it was thought useful to simulate a combination of reflections and look at how the different periodicities interfere with each other. The fading and enhancement of a combination of signals contributes to the generation of a multipath error signature that perhaps can explain signatures found in actual data.

As a starting point, the model of Georgiadou and Kleusberg (1988) was used. A subroutine was written that could generate a multipath error signature for the case of multiple reflections. This programme generates a series of sinusoids with different phases, periods and amplitudes and does so in two frequencies (L1 and L2). The latter have a ratio of 120/154 relative to each other. The two signals are subsequently differenced, to form the across-frequency pathlength difference.

The multipath error signature of a single reflection was generated first (Fig. 7.1), in order to confirm the error curve published by Georgiadou and Kleusberg. Basically the signature shows "three peaks and a squiggle" (Refer to Chapter 7) after which this error signature repeats itself. Alternatingly, the squiggle is either formed by only a point of inflection, or by a low peak and a shallow trough on either side of the point of inflection.

During a satellite pass the multipath period of a reflected signal can easily change by a factor of about 15, because of the changing satellite elevation and the rate of elevation change. Thus reflective surfaces will be contributing towards multipath effects over a range of frequencies, with periods ranging from minutes to hours and more so in the case of multiple reflections. In consequence, a whole range of

frequencies can often be found at any one time in the multipath record. With this in mind the first simulation uses a variety of frequencies right across the plausible spectrum and, for the sake of simplicity, these periodicities are kept constant for the duration of an observation session. This first simulation is carried out in order to gain an appreciation of the ensuing spectral behaviour for the case of a limited number of variables. (In the next simulation more variables are introduced).

In Fig. 7.1 the simulation of the multipath error signature of a single reflection was shown. Figure 12.1 shows the simulation of interference patterns of three periods: 140, 21 and 2.3 minutes, with random voltage amplitude factors of 0.3, 0.45 and 0.07 respectively. The horizontal axis shows the epoch numbers in units of 30-second intervals. The vertical axis shows the amplitude in metres. These indicate the relative signal strengths between the direct and the indirect signal. A long periodic error signature and a short periodic error signature can easily be recognised in the plot. The overall macro behaviour of the curve as well as the sequence of very small spikes show clearly two levels of the "three peaks and a squiggle" artefact in the data. Superimposed upon this is also the third periodicity which is a bit harder to find as it is the very long period.

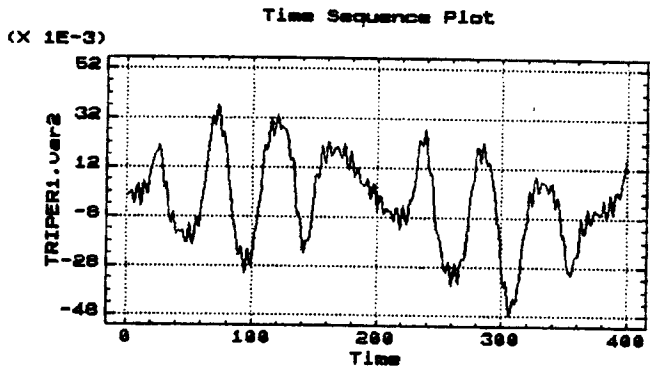

Figure 12.1 Interference pattern of three periods.

The next simulation (Fig. 12.2) combines five periods: 108, 26.4, 14.7, 7 and 1.6 minutes, with random voltage amplitude factors of 0.6, 0.2, 0.07, 0.16 and 0.06 respectively. The axes in Fig. 12.2 are the same as in the previous figure. It

is harder to recognise the error signature, except for the relative large amplitude of one of the periodicities which allows one of the periods to stand out. This error signature doesn't repeat itself until after about five periods of the periodicity with the greatest amplitude. A detailed inspection of the single reflection error signature in Fig. 7.1 shows that although after 4½ cycles a repeat appears to occur, the first authentic repeat occurs after about the

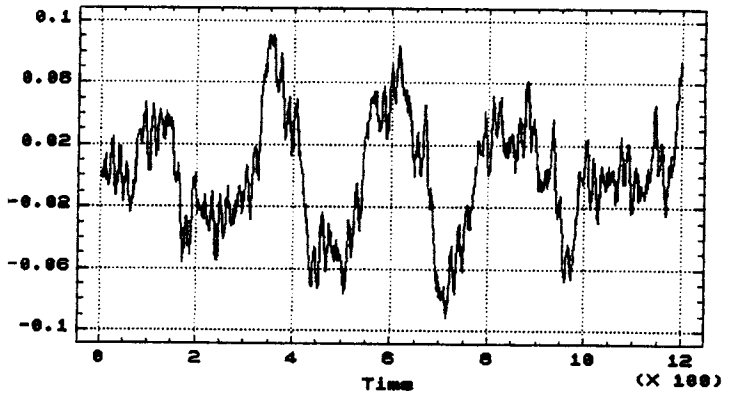

Figure 12.2 The interference pattern of five periods.

ninth cycle. Strictly speaking the first genuine repeat, because of the 120/154 frequency ratio, should only occur at the 60th cycle of L2 or the 77th cycle of L1. When drawing this ratio on an integer grid, one sees that there are various approximate harmonics at a 7/9 ratio.

As a next step the estimate of the spectral density for this last simulation was calculated. The resulting frequency spectrum (Fig. 12.3) shows that each modelled reflective surface impresses two periods into the across-frequency differenced data, an L1 and an L2 based period. This is shown by the dual peaks in the periodogram. Also visible is the lack of noise as the generated data was of course totally deterministic. The horizontal axis shows the natural logarithm of the frequency (in cycles per sampling interval). The vertical axis shows the logarithm of the total variance in metres squared.

Although five periodicities representing reflective surfaces were introduced, the periodogram exhibits only three dual

peaks. The frequencies corresponding with each set of peaks are neatly in a 120/154 ratio with each other. If vertical lines are drawn through the dots on the curve of the periodogram, the grid-lines of the overtone series are obtained.

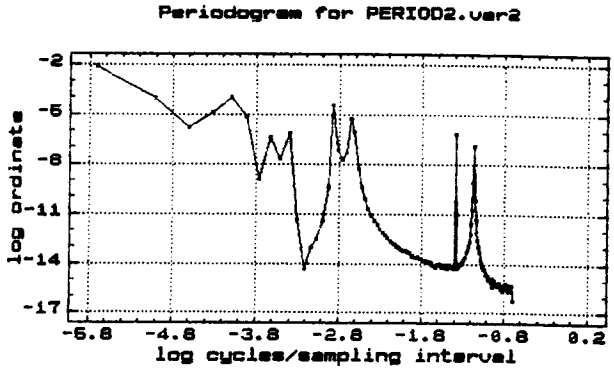

Figure 12.3 Periodogram of the five introduced periods.

The grid is not fine enough to separately capture the double frequencies at longer periods. At these longer periodicities, the width of the gridlines of the overtone series for the decomposition into sinusoids is such that, if the multipath signature of one GPS L-band frequency is captured, the other falls between the grid lines. As mentioned before, the L1 periods introduced were 108, 26.4, 14.7, 7 and 1.6 minutes. The L2 periods follow from the 120/154 ratio. This means the relevant logarithmic values on the horizontal axis for these frequencies are expected to be (using natural logarithms): -5.37 (-5.62), -3.97 (-4.22), -3.38 (-3.63), -2.64 (-2.89) and -1.16 (-1.41). The values in brackets refer to the corresponding L2 periods. The grid line at -5.7 captures both the frequency component at -5.37 and -5.62 and shows a single peak. The next set of frequencies -3.97 and -4.22 also fall between the grid lines and are represented by a single peak at -4.1. In the higher frequency part of the periodogram the grid is dense enough to even show a valley between two frequencies in a 120/154 ratio to each other. The last three periods shown are thus clearly indicated by dual peaks in the periodogram.

The single reflective surface multipath error signature can still be recognised in the main long periodic behaviour of the composite error signature of 5 interfering reflections in Fig. 12.2. This simulation shows that the composite signature exhibits the same steep drops, sudden changes and large amplitudes as those observed in the real data. These signatures

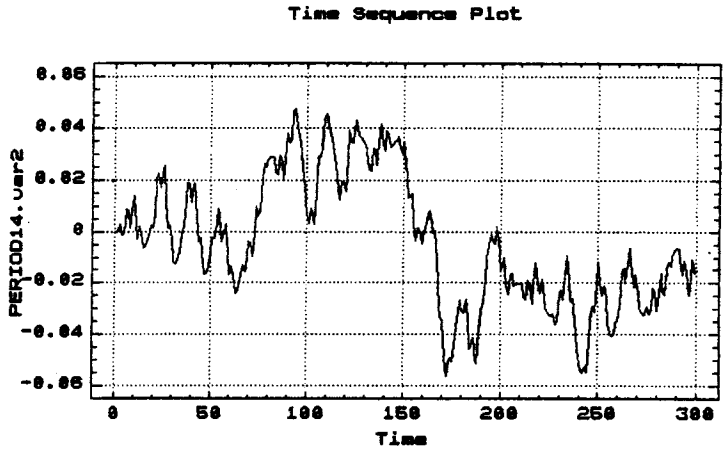

Figure 12.4 Simulated interference of 5 periods, as in Fig. 12.2, displayed in more detail for the first 2½ hours. The horizontal axis shows the number of 30-second sampling intervals. The vertical axis shows the amplitude of the across-frequency difference in metres.

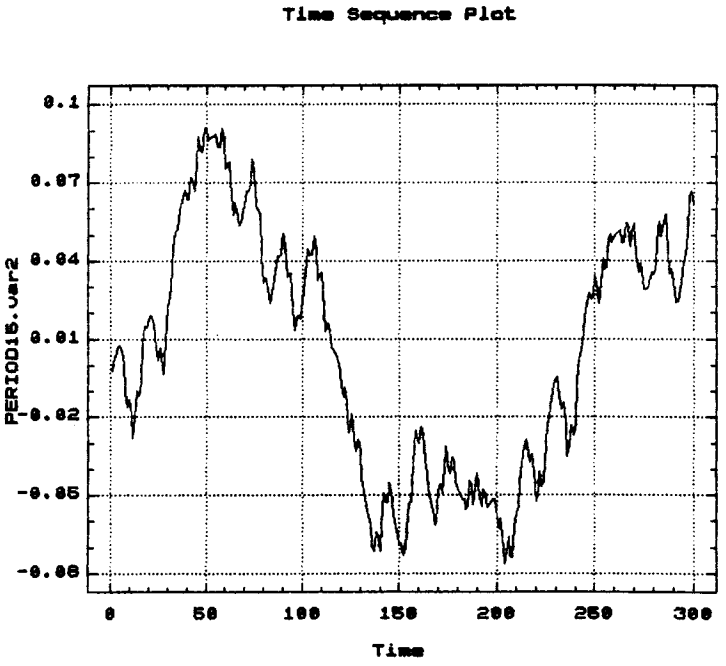

Figure 12.5 The second 2½ hours of simulated interference results for the same signal as in Fig. 12.4.

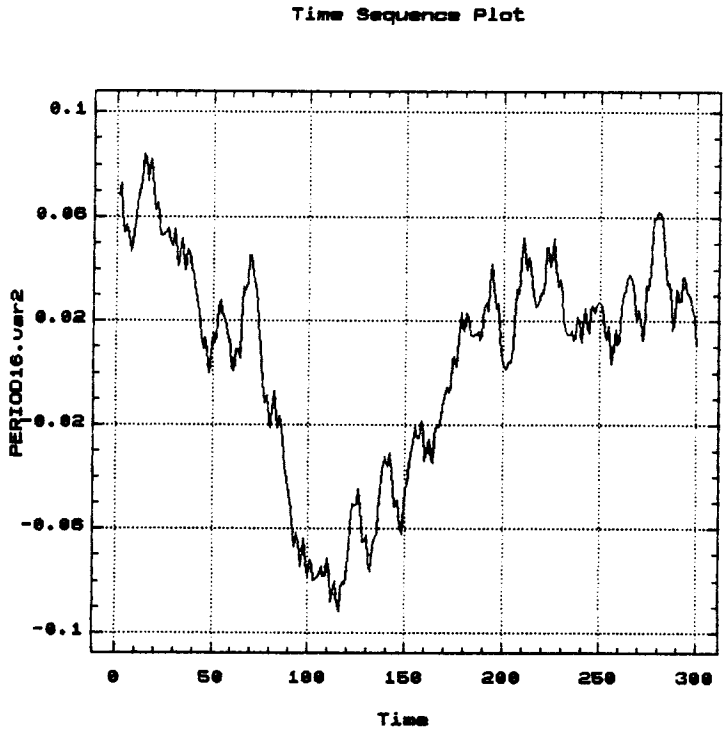

Figure 12.6 The third 2½ hours of simulated interference results for the same signal as in Fig. 12.4.

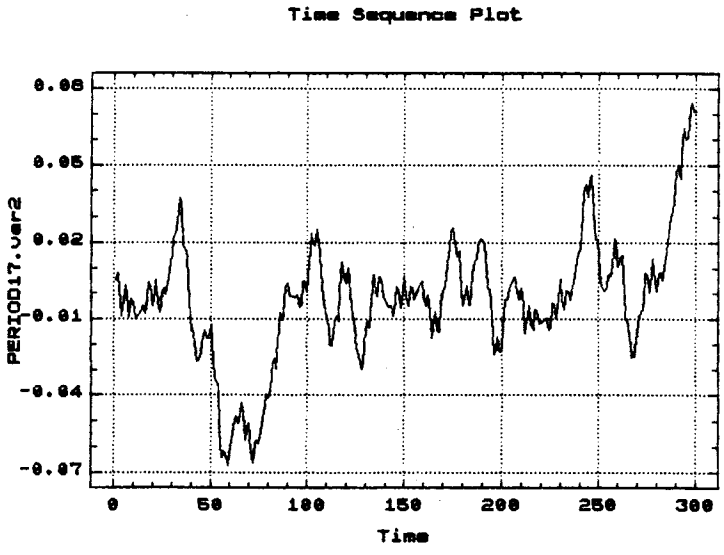

Figure 12.7 The fourth 2½ hours of simulated interference results for the same signal as in Fig. 12.4.

in the real data can therefore be explained by quite normal interference between the constituent sinusoids of various multipath periods.

Often, only small data sets of fifteen minutes or one hour duration are measured. Publications about cross-correlations of carrier phase multipath (Georgiadou and Kleusberg, 1988 and Müller et al, 1989) are usually restricted to data sets of 15 to 20 minutes. The total error signature of a long periodic component is then usually not visible and the short periodic components mask the longer periodic effect in such a way that its error signature is harder to detect. The four plots in Figs. 12.4, 12.5, 12.6 and 12.7 show consecutive 2½ hour intervals of exactly the same continuous error signature caused by the above 5 periodicities. The vertical axis shows the multipath error signature in metres and the horizontal axis displays the number of consecutive 30-second intervals of simulated observations. The time series exhibit continuously changing combinations of phases and amplitudes in response to the underlying periodicities. It is only in the across-epoch differenced time series that a beat pattern emerges.

When a very strong single reflection occurs, the behaviour of the multipath induced phase shift degenerates from an approximate sine-curve to a sawtooth pattern (Fig.12.8). The numerator in Eq.(8.8) is dominant in the case of a weak reflection. The denominator becomes important in the case of a strong reflection when α approaches the value 1. The multipath error signature in the across-frequency carrier phase pathlength difference can then be described as a difference between two sawtooth curves. This results in a pulse function which displays three consecutive pulses on a descending slope, after which the pattern repeats itself (Fig. 12.9). Between the three pulses there is often a sharp spike. Sometimes the spike is a bit wider than at other times. Sharp spikes occur whenever the drops in both sawtooth curves are almost in phase. The wider spikes occur when there is a bit more of a phase difference. The large drops are equidistant

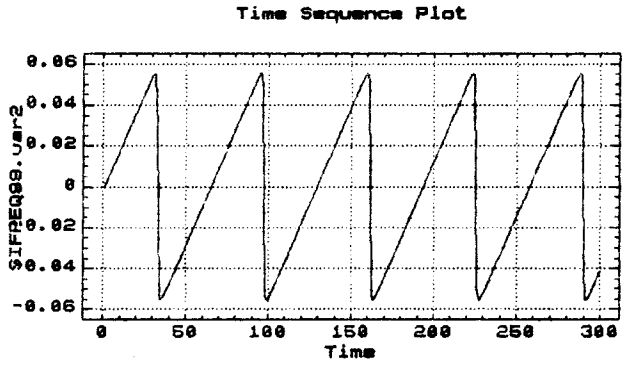

Figure 12.8 The single frequency multipath error curve, normally approximated by a sine-curve, becomes a sawtooth when α approaches 1. The diagram shows the L2 curve corresponding with an L1 period of 50 min. for α = 0.99. The vertical axis is graduated in metres, the horizontal axis shows the number of 30-second sampling intervals.

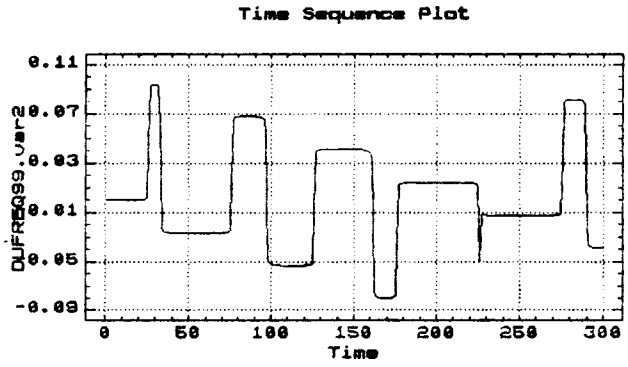

Figure 12.9 When an L1 sawtooth curve is differenced with an L2 sawtooth curve, a pulse-like function results. One of the pulses becomes a spike at the instant that the L1 and L2 signals are nearly in phase with each other. The vertical axis is graduated in metres, showing the across-frequency multipath error curve. The horizontal axis shows the number of 30-second sampling intervals.

from each other and the large rises are equidistant from each other. The distance between the drops is larger than the distance between the rises. The ratio between these distances is 120/154. As a result the pulses change progressively in width until one is reduced to a spike. The pattern then starts all over again.

An example of this spike phenomenon can be seen in Figs. 10.13b (near the tenth observation in the Satellite 13 record) and 10.6a (near the 420-th observation in the Satellite 9 record). Further evidence of the sawtooth phenomenon can be deduced from Figs. 10.2a and 10.2b. When the slopes of the L1 and L2 sawtooth functions are equal and the starting points of the slopes are in phase, Fig. 10.2a results. When the slopes are unequal and the slope starting points are in phase, Fig. 10.2b results. The change in slope can occur through surface roughness of the reflective surface which will attenuate the longer wavelength L2 less than the shorter L1. The resulting across-frequency error curve will then vary between a pulse function (L1 and L2 both reflecting well) and a sawtooth pattern (the L2 reflection becoming dominant). The result will look like Figs. 10.2a and 10.2b.

The following main features assist in recognising the multipath error signature:

1) the "three peaks and a squiggle" attribute in the across-site across-frequency time series;
2) the dual peak incidence in the power spectrum at a frequency ratio of 120/154;
3) the peak in the cross correlation function at a lag of four minutes between the time series of two consecutive days;
4) sometimes a more or less obvious beat pattern can be discerned in the across-epoch across-site across-frequency differenced time series $\delta\Delta\#\Phi$;
5) the above described pulse function nature together with the spikes, in the case of strong reflections which are characterised by 100-200 mm amplitudes in the $\Delta\#\Phi$ time series.

12.2 Simulation of Multipath, with Actual Satellite Elevation and Azimuth Data

The next simulation uses actual elevation and azimuth data of each satellite. The model used for the phase shift of the multipathed signal is derived in Chapter 8.1.4. It is valid for a signal which is hemispherically reflected from an idealised point source. This is combined with the Georgiadou and Kleusberg (1988) model for horizontal reflecting surfaces and their equation for multiple reflecting surfaces (Eq.(8.18)). The author's software treats the point source as hemispherically reflecting. This needs an explanation. This approach is used to approximate reflections from a curved surface like a chimney or a vent with cylindrical characteristics. At each angle of incidence on such a curved surface a ray can be found that will reach the antenna after reflection. For example the "reflective plane" in such a case is tangential to the cylindrical chimney and rotates around the chimney as the angle of incidence changes. As well as this, edges of structures like chimneys and vents often have rounded edges and a more or less constant reflection could be received from this in the form of edge diffraction. A feature of such a reflection is that the distance to the point of reflection is fairly constant. This permits the treating of such reflections as idealised point sources as a first approximation. From there it is rather easy to replace a larger surface by a combination of point sources. An amount of constructive and destructive interference will occur which the model accommodates by accumulating contributions from various points. A vertical string of point sources can represent a chimney or other type of pipe and a horizontal string of point sources can be made to represent a handrail in the vicinity of the receiver station. A matrix of point sources can be made to represent a surface of particular dimensions. The author's software could be refined by allowing for small changes in the distance to the point source while the "reflective surface" rotates. The software

could also be improved by the use of cosine factors of azimuth and elevation. These create a gain in a particular direction, like a particular azimuth of reflection or a particular elevation of reflection, as required by Snell's law. Time has not permitted to develop these ideas further. The software presently adds contributions from surfaces and point sources in response to changing azimuths and elevations. Various reflective surfaces around the antenna have been idealised as a point source and have been allowed to contribute to the total site signature. The roof surface of the observation site and the ground plane level of the antenna have been included using the classical multipath model (employing the perpendicular distance to the reflective surface) as in Georgiadou and Kleusberg (1988). These two reflection models both contribute to the final result, delivering an estimated site signature. It is recognised that the TI 4100 antenna has no appreciable groundplane. The reason for the inclusion of a surface at groundplane height is given below.

The azimuth and elevation prediction record of 12 September 1987 of each of the seven satellites (3,6,8,9,11,12 and 13) has been used to generate a simulated multipath site signature within the time span from 09:00 UT to 16:00 UT. The starting times of the simulations were determined by the predictions in Table 9.1. The times are 23:20, 19:00, 19:00, 20:30, 19:40, 22:20 and 21:20 AEST for Satellites 3, 6, 8, 9, 11, 12 and 13, respectively. For the actual observation times refer to Chapter 10. Twelve objects in the vicinity of the antenna have been represented as idealised point sources, using the model defined in Chapter 8.1.4. All contributions were accumulated through Eq.(8.20) by the subroutine GEKLSMUL3 (written for this purpose) and a result file created. The latter was imported into a statistics programme for plotting and analysis. This was done for each of the 7 satellites. The simulated and satellite-specific site signatures in Figures 12.10 a,b,c,d,e,f and g refer to the 12 chosen point sources and the two horizontal surfaces with which the antenna environment was modelled. The voltage amplitude factors used

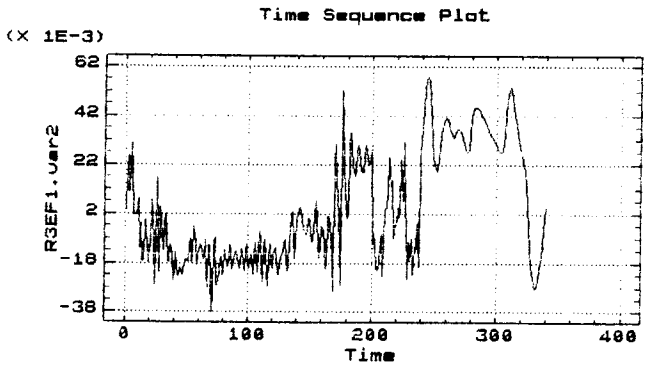

Figure 12.10a Satellite 3.

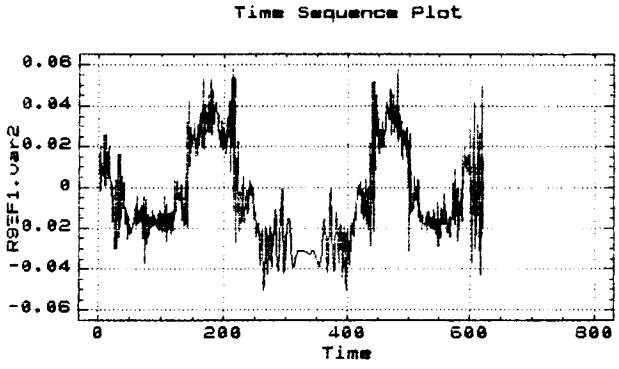

Figure 12.10b Satellite 9.

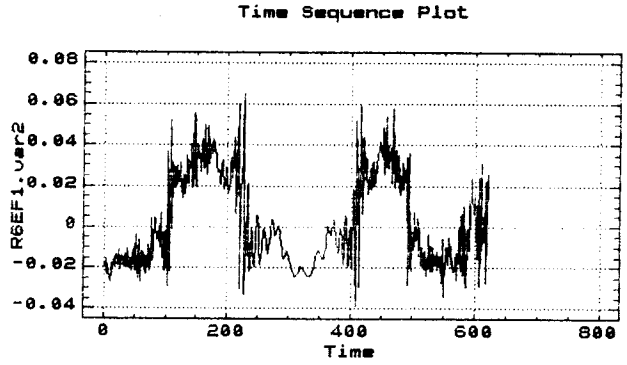

Figure 12.10c Satellite 6.

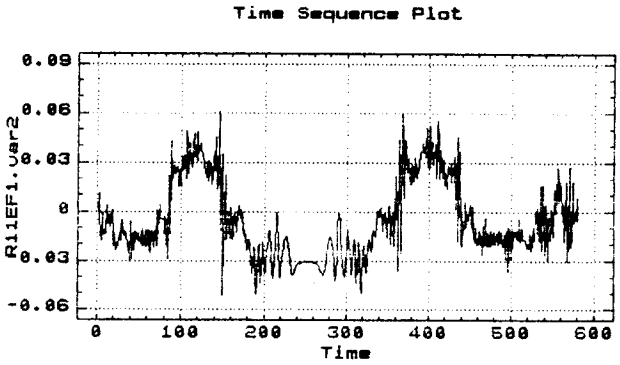

Figure 12.10d Satellite 11.

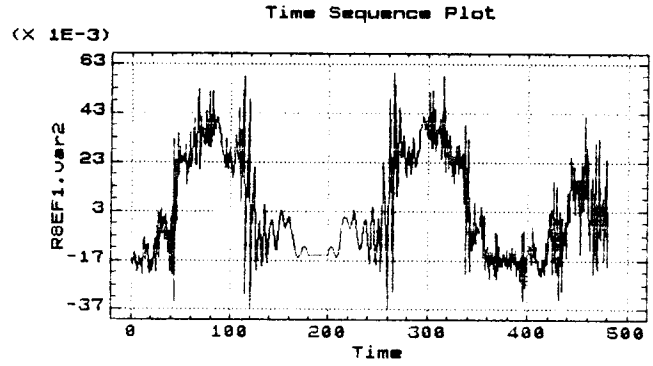

Figure 12.10e Satellite 8.

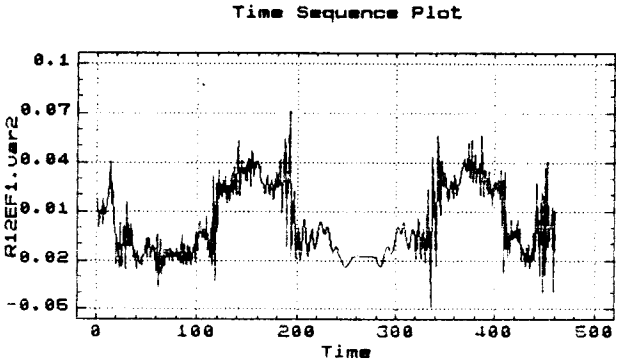

Figure 12.10f Satellite 12.

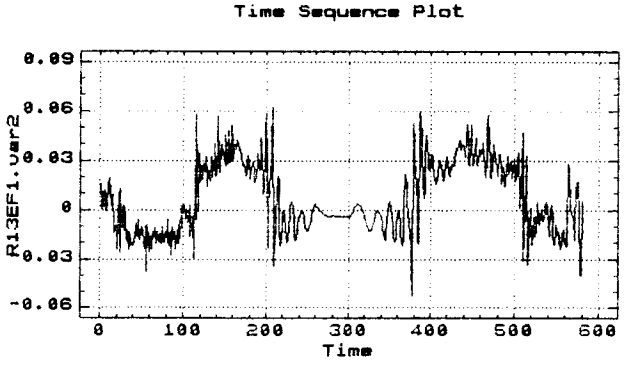

Figure 12.10g Satellite 13

are 0.04 for the 12 point sources, 0.12 for the roof surface and 0.5 for the surface at groundplane level (0.21 m below the phase centre). The horizontal axis shows the number of 30-second intervals and the vertical axis the signal amplitude in metres. Of interest are the similarities and symmetries as well as the differences in these 7 figures.

Generally two peaks are visible, situated 1 to 1¼ hours before and after the point of elevation culmination. The widths of these peaks are of the order of ¾ hours. But the positions of these peaks do vary with respect to the point of satellite elevation culmination. The widths of the peaks vary too. Figures 12.11 and 12.12 show these modelled site signatures, together with the time series plot of the actual observations and after matching the time records. The simulated signature is given in the form of dotted lines and the actual observations in full lines. The horizontal axis shows the number of 30-second intervals. The vertical axis on the left shows the amplitude of the observed signal in metres. The vertical axis on the right shows the amplitude of the simulated signal in metres. In Fig. 12.12 the multiplication factor (xE-3) is not well visible. In both plots the peak-to-peak variation is about 100 mm. The large amplitude long periodic signals, shown in these figures, are the result of the voltage amplitude factor used for the signal reflection at groundplane level and the proximity of this assumed surface to the antenna phase centre. The period of the multipath

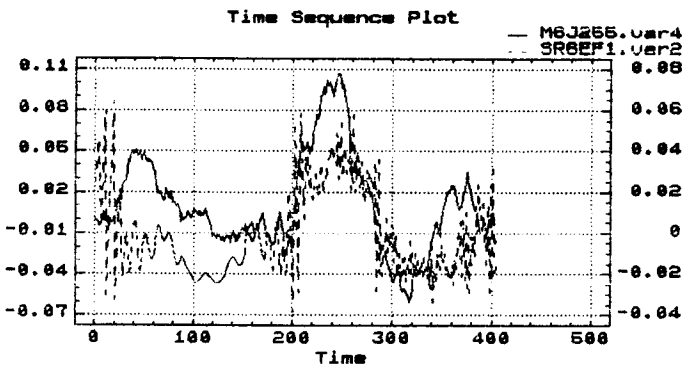

Figure 12.11 Satellite 6: comparison of simulation and observation.

signature is proportional to the reciprocal of the distance to the surface from which the reflection originates. The Figures 12.11 and 12.12 show similarities between the modelled site signatures and the actually observed ones, but there is a difference in period length and a difference in phase. Thus Figures 12.11 and 12.12 seem to indicate that a long periodic reflection effect perhaps plays a part in the forming of this signature. The time series of the other 5 satellites show less obvious or no correlation with the thus modelled site signature. The merit of the modelling is that it shows changes in amplitude and periods of a possible site signature, which resembles the variations seen in the actual data. The conclusion that can be drawn is that this variability can be easily explained in total by the multipath effect, without having to suspect sudden changes in the ionosphere. The investigation shows that even the interference pattern of a dozen sources does not degenerate into a totally random incoherent pattern. Young (1985) suggested multiple reflections would soon result in loss of coherence. The above simulation shows that this is not necessarily so.

The error signature which appears to originate from a 0.2

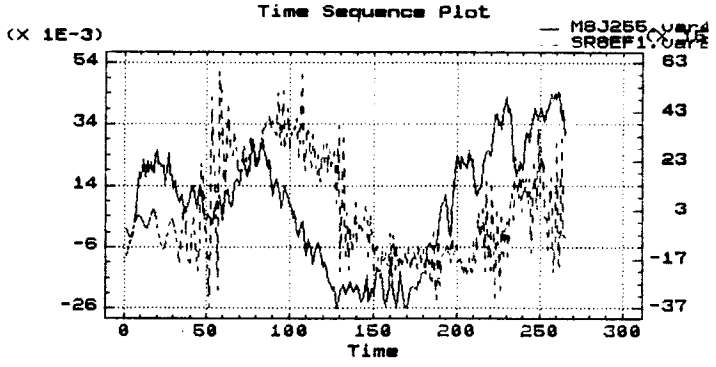

Figure 12.12 Satellite 8: comparison of simulation and observation.

metre distant surface (Figs. 12.9 and 12.10) could be explained by the fact that across-site differenced data is used in this investigation. A reflective horizontal surface at 1.6 metres below the phase centre at one site and 1.4

Local Time	Sat 6 HMI	Sat 6 VMI	Sat 8 HMI	Sat 8 VMI	Sat 9 HMI	Sat 9 VMI	Sat 11 HMI	Sat 11 VMI
20:40	32	22	166	70	18	49	16	13
20:50	36	22	63	28	17	41	18	12
21:00	44	24	39	20	17	35	20	10
21:10	56	28	27	16	18	31	25	10
21:20	69	32	23	16	18	27	34	10
21:30	113	47	19	16	17	22	57	10
21:40	1460	587	17	16	17	19	197	16
21:50	158	66	16	18	18	17	534	28
22:00	80	35	15	20	19	16	68	10
22:10	48	23	14	23	20	14	42	10
22:20	34	19	14	26	23	13	30	11
22:30	27	17	14	31	25	12	25	12
22:40	23	17	14	40	30	11	22	12

Table 12.1 The multipath index at Mulley on 12-9-87. HMI and VMI denote the horizontal and vertical surface multipath indices, respectively, both in minutes times metres.

metres below the phase centre at the other could perhaps result in a long periodic error signature in the differenced variable Δ## resembling one apparent surface at 0.2 metres. Antennas with large groundplanes would reduce the ground reflection effects and a microstrip antenna flush with a large groundplane (Refer to Chapter 5.3.1) would eliminate it (Yunck, 1987). If the antenna phase centre is not flush with the groundplane, multipathing could occur off the groundplane itself.

As given in Eq.(8.29) in Chapter 8.1.4, the multipath period can be derived from the time variation of the satellite elevation. The so derived multipath period has been called the multipath index in this thesis and can be produced for each instant of time for all satellites for which predicted elevation data is available. A horizontal and vertical multipath index was derived, for horizontal and vertical reflective surfaces, respectively. An example is listed in Table 2.2 of Chapter 2. The multipath period is inversely proportional to the distance to the reflective surface. The index uses a standard distance of one metre to the reflective surface. Thus the index should be divided by the perpendicular distance to the suspected reflective surface in order to

obtain the multipath period for a particular surface at a certain instant in time. This index can be used as a planning tool to avoid observations at times with a very long multipath period. The index can also be used to obtain the observation duration necessary to acquire at least one full swing of the multipath error signature and to average out the multipath effect. Table 12.1 shows a possible way to tabulate the multipath indices, and can be used as follows. The table suggests that if reflective surfaces are present, the use of Satellite 6 and Satellite 11 should be avoided between 21:00 and 22:00 (on 12-9-87), if a relative accuracy below the level of multipath effects is required, unless the session is planned to last many hours. The use of Satellites 8 and 9 at this time together with two other Satellites with similarly low multipath indices would be preferable. Even after avoiding satellites 6 and 11, a Satellite 9 signal reflection from a vertical surface, say, at a distance of 5 metres would take 7 minutes to average out. A Satellite 8 signal reflection from a horizontal surface, say, 1.5 metres below the antenna phase centre would take 27 minutes to average out. If the signal of one satellite is subject to the maximum multipath error and the signals of the other three satellites undergo no multipath effects at all, then one quarter of the effect would influence the resulting station position. In the case of multiple reflections this would be $\frac{1}{4} \times \lambda/2$ or 25 to 30 mm. If the satellite elevation is large, the multipath error is likely to map into the station height. If the satellite elevation is very small it will affect the baseline azimuth or the baseline length, depending upon the azimuth to the satellite. When the other satellite signals are also subject to multipath the combined effect could be up to half a cycle. In the case of multiple reflections multipath effects have the potential to bias the apparent ambiguities by half a cycle and thus the ambiguity resolution by one cycle.

13. CONCLUSIONS AND RECOMMENDATIONS

13.1 Conclusions

1) In the past, most of the efforts to reduce multipath effects have been directed towards the improvement of the design of antennas with respect to antenna beam shaping and discrimination of signal polarisation. Not enough emphasis has been placed on reducing multipath through the optimisation of observation time and duration. Some general conclusions can be drawn from the multipath indices developed for this purpose. From about 2½ hours to half an hour before satellite culmination and from half an hour to 2½ hours after satellite culmination the multipath index is the lowest, generally ±20 minutes*metres. This is valid for both the horizontal and vertical multipath indices. The largest horizontal multipath indices occur around the time of satellite culmination. The vertical multipath index is large at low satellite elevations, but also undergoes a rise near satellite culmination. If the extreme low and high elevations (indicated by the above time intervals) are avoided, one can generally assume a multipath index of 20.

Receiver operation in differential mode
when the multipath index = 20 min*m

Required standard dev. of position	Recommended averaging time (multipath periods)	Reflections from: Horiz. surface (1.5 m)	Vert. surface (10 m)
1-5 mm	5 periods	1 hr	10 min
5-20 mm	1 period	13 min	2 min
20-50 mm	1 to ½ period	13-6 min	2-1 min
50-100 mm	½ period to ½ min	6 to ½ min	1 to ½ min

Table 13.1 Recommended averaging times in units of multipath periods in a reflective environment, for various required relative standard deviations of station position.

The lengths of the actual multipath periods will generally depend on the distance and surface orientation of predominating reflective surfaces. In the case of reflections from horizontal surfaces the surrounding ground surface will often be the cause, depending on the type of antenna. If one assumes the ground surface to be at 1.5 metres below the antenna phase centre, the resulting multipath period will be about 13 minutes. Reflections from vertical surfaces will generally originate from further away than 1.5 metres and require a shorter averaging time than multipathing from horizontal surfaces. Some recommendations for minimum lengths of sessions are given in Table 13.1, for an assumed horizontal surface at 1.5 m from the phase centre and a vertical surface at 10 m. If the distances to the reflective surfaces would be twice as much, the periods would be halved. The required averaging time is inversely proportional to the perpendicular distance to the reflective surface. If the multipath index is below 20, these averaging times are also proportionally smaller. It is expected that the use of a microstrip antenna flush with a ground plane will practically eliminate the effect of reflections from horizontal surfaces. In such cases, the vertical surface reflections will determine the required averaging times. Some additional multipath effects may originate from skew surfaces as well as from edge diffractions from objects above the antenna mask angle.

2) The model describing reflections from idealised point sources is helpful in modelling the antenna site signature. It can model edge diffractions and reflections from surfaces that can not be represented as planes.

3) Georgiadou and Kleusberg (1988) used the cross-correlation function to show a high cross-correlation between the files of the Δ## time series on two consecutive sidereal days of data, observed on short baselines. On the long (150 km) baseline tested in this report, a further level of differencing, this time across epochs, was required to show similar cross-correlation results.

4) Analysis of the across-day differenced data suggests that relative ionospheric changes (obtained through differencing between two distant sites) amount to no more than a few tenths of a TEC unit over a number of hours. This is, say, twenty millimetres in the Δ## timeseries. This is remarkably small considering the fact that the two sites are about 150 kilometres from each other. The fact that the survey took place at night and in a year of low solar activity (1987) might have contributed.

5) The simulation study of Chapter 12 leads to the conclusion that the short and the long periodic time variations seen in the measured differential dispersive delay Δ## (Refer to Chapter 10) can be fully explained by interference from multipathed signals. Multiple reflections, when strong, have the potential to bias the position results by 0.1 metres. If the multipath error is not averaged out, the ambiguity resolution can become biased by one full cycle when strong multiple reflections are present.

6) The modelled multipath error signature in the differential dispersive delay was found to show approximate harmonics at a 7/9 ratio which is eight times more frequent than would be expected at first sight from a 120/154 frequency ratio. This makes the multipath error signature easier to recognise.

7) Antenna phase centre variation effects can be corrected in advance by having the antenna phase pattern calibrated and corrections applied to the actual phase readings by the receiver in real-time, thus reducing the effect of any irregularities in the antenna pattern. This is important for high precision work that requires a resolution of a few millimetres. It also enhances multipath analysis. Otherwise it is impossible to separate phase centre variations from multipath effects.

8) The differential dispersive delay Δ## should be renamed the "across-site across-frequency differenced carrier phase pathlength observable" in view of the fact that it is not

solely caused by the ionosphere.

9) The simulations of Chapter 12 show that the long periodic variations seen in the records of Satellites 6 and 8 can be explained by multipathing of a surface about 0.2 metre below the phase centre when one assumes that there is no multipath effect contribution from the second site. If the second site does contribute it can be concluded that the contributions of both sites arise from surfaces that are 0.2 metres different with regard to their respective distances to the relevant phase centres. The across-site across-frequency peak-to-peak variation of this effect observed in the test data is between 70 and 200 millimetres. The larger value would mean the (relative) range to one particular satellite would be biased by ¼λ or at most 60 mm, if no averaging would occur. Under certain circumstances the station position could be affected by a similar amount.

14.2 Recommendations

It is recommended that, apart from avoiding station environments that generate multipath:
1) optimum observation times and durations are chosen using the multipath index as a guide on points where reflections are anticipated. The multipath index provides the time, when the multipath period is shortest and indicates the observation length required to average it out (Refer to Table 13.1). The averaging also benefits the ambiguity resolution. The use of the multipath index is especially important when one of the satellites is within half an hour of either side of its culmination or more than 2½ hours before or after this;

2) observation durations for kinematic surveys are planned with an eye on the previous recommendation when the accuracy sought so requires (Refer to Table 13.1);

3) the accuracy of deformation and crustal motion surveys is enhanced by observing at the same sidereal time (to reproduce receiver multipath) and perhaps in the same month of the year (to reproduce satellite multipath);

4) the ionospheric correction of GPS data and the use of the ionosphere-free linear combination is confined to the use of smoothed data using a moving average method in order to filter out the short periodic multipath component;

5) carrier phase multipath analyses of long baselines are not based on the differential dispersive delay $\Delta\#\#$ but rather on its time variation $\delta\Delta\#\#$;

6) a fast multipath measurement technique be developed following the principles outlined for the "groma" described in Chapter 5.4;

7) antenna calibration data should be part of the reduction software when highest accuracy is sought. Preferably, the receiver should correct the phase observations in real-time for antenna phase pattern irregularities;

8) a similar test (Refer to Chapter 9) be carried out using a microstrip antenna on a large ground plane to confirm the elimination of multipath effects from horizontal surfaces;

9) this test (8) be carried out during a time of maximum solar activity, to test the validity of the method of separating the ionospheric component through across-epoch differencing of the data under these adverse conditions.

ACKNOWLEDGEMENTS

I am very much indebted to the Department of Lands of New South Wales and the Surveyor General Mr. Don Grant for granting me a postgraduate scholarship, at my full salary, which made this study possible. I also wish to express my appreciation to the Land Information Centre (previously Central Mapping Authority) of Bathurst, for making data of the 1987 GPS survey of NSW available.

I want to thank my supervisor Dr. Jean M. Rüeger for his encouragement during the completion of what, for a long time, seemed a daunting task. I am also very thankful for his help and advice. I would like to thank Dr. A. Kleusberg from the University of New Brunswick (Canada) for his helpful remarks. I extend my gratitude to Bernie Hirsch for kindly making some UNSW utilities available that enabled me to access the data for this study which was stored in Nortech binary format.

I am deeply grateful for the great and unending support from my wife Marijke who was very understanding with regards to the time and application that this study required. Without her consideration and endurance I could not have done it.

I would be remiss if I would not also thank my fellow student Doug Kinlyside for shortening my learning curve in the use of a word processor. Finally, I also appreciate very much the pleasant surroundings provided by my accommodation at International House, during the first session of my studies. This accommodation was also paid for by my employer, the Land Information Centre of the Department of Lands of NSW.

REFERENCES

Some of the references listed are published in the two proceedings below and are abbreviated [A] and [B].

[A] Goad, C.C., Ed., Proceedings of the First Symposium on Precise Positioning with the Global Positioning System, Positioning with GPS-1985, Rockville, Maryland, April 15-19, 1985, published by U.S. Department of Commerce, NOAA.

[B] Fell, P.J., Proceedings of the Fourth International Geodetic Symposium on Satellite Positioning, Austin, Texas, April 28-May 2, 1986, The University of Texas at Austin.

Bachynski, M.P. and Kingsmill, M.G., 1962, Effect of Obstacle Profile on Knife-Edge Diffraction, Trans. IRE, AP-10, pp.201-205.

Bendat, J.S. and Piersol, A.G., 1971, Random Data: Analysis and Measurement Procedures, Wiley-Interscience, New York.

Benz, F., 1970, Untersuchungen über die Verringerung des Einflusses der Bodenreflexion bei Entfernungsmessgeräten mittels elektrischer Wellen, Internationaler Kurs für Ingenieursmessungen Hoher Präzision, Graz.

Beutler, G., Bauersima, I., Gurtner, W., Rothacher, M., Schildknecht, T., Mader, G.L. and Abell, M.D., 1987, Evaluation of the 1984 Alaska Global Positioning System Campaign with the Bernese GPS Software, Journal of Geophysical Research, Vol.92, No.B2, pp.1295-1303.

Bishop, G.J., Klobuchar, J.A. and Doherty, P.H., 1985, Multipath Effects on the Determination of Absolute Ionospheric Delay from GPS Signals, Radio Science 20(3), pp.388-396.

Bletzacker, F.R., 1985, Reduction of Multipath Contamination in a Geodetic GPS Receiver, [A], pp.413-422.

Bletzacker, F., Crow, R.B., Najarian, R., Purcell, G., Statman, J. and Thomas, J., 1984, Series-X Test Results, Position Location and Navigation Symposium (PLANS), November, pp.264-271.

Blewitt, G., 1989, Carrier Phase Ambiguity Resolution for the Global Positioning System Applied to Geodetic Baselines up to 2000 km, submitted to Journal of Geophysical Research, 13 pp.

Bloomfield, P., 1976, Fourier Analysis of Time Series: An Introduction, John Wiley and Sons, New York.

Bock, Y., Abbot, R.I., Counselman III, C.C. and King, R.W., 1986a, A Demonstration of 1-2 Parts in $_{10}$-7 Accuracy Using GPS, Bull. Géod. 60(1986), pp.241-254.

Bock, Y., Gourevitch, S.A., Counselman III, C.C., King, R.W. and Abbot, R.I., 1986b, Interferometric Analysis of GPS Phase Observations, Manuscripta Geodaetica (1986), Vol.11, pp.282-288.

Bomford, G., 1971, Geodesy, 3d. ed., Oxford University Press.

Born, M. and Wolf, E., 1965, Principles of Optics, Third ed., Pergamon Press, Oxford.

Bossler, J.D., Goad, C.C. and Bender, P.L., 1980, Using the Global Positioning System (GPS) for Geodetic Positioning, Bull. Géod. 54(1980), pp.553-563.

Brunner, F.K. and Gu, M., 1989, Higher Order Terms of the Dual Frequency Ionospheric Correction of GPS Observations, AGU Fall Meeting, San Francisco, 4-8 December.

Chatfield, C., 1984, The Analysis of Time Series, An Introduction, Chapman and Hall, London.

Coco, D.S. and Clynch, J.R., 1986, System Performance Tests for the TI 4100 Geodetic Receiver, [B], pp.399-417.

Counselman III, C.C. and Shapiro, I.I., 1979, Miniature Interferometer Terminals for Earth Surveying, Proceedings of the Second International Symposium on Satellite Positioning, Austin, Texas, pp.1237-1286.

Counselman III, C.C. and Gourevitch, S.A., 1981, Miniature Interferometer Terminals for Earth Surveying: Ambiguity and Multipath with GPS, IEEE Transactions on Geoscience and Remote Sensing, GE-19, No.4, pp.244-252.

De Jong, G., 1982, The Phase Center of a Monopole Antenna, Radio Science, Vol.17, No.2, pp.349-355.

Dickson, R.G., 1989, Results of New South Wales Combined GPS Survey, Proceedings of the 65th Annual Conference, NSW Staff Surveyors Association.

Dixon, R.C., Spread Spectrum Systems, John Wiley & Sons, New York.

Evans, A.G., 1986, Comparison of GPS Pseudorange and Biased Doppler Range Measurements to Demonstrate Signal Multipath Effects, [B], pp.573-587.

Evans, A.G., Hermann, B.R., Coco, D.S. and Clynch, J.R., 1985, Collocation Tests of an Advanced Geodetic GPS Receiver, [A], pp.245-254.

Evans, A.G. and Hermann, B.R., 1987, On the Reduction of GPS Multipath, EOS 68(44), p.1238, November.

Evans, A.G. and Carr, J.T., 1989, Effect of Signal Multipath Errors at DMA Global Positioning System Satellite Tracking Sites on Orbit Accuracy, Manuscripta Geodaetica Vol.14, pp.143-148.

Faulkenberg, W., Kielland, P. and Lachapelle, G., 1988, GPS Differential Positioning Technologies for Hydrographic Surveying, IEEE, Proceedings of Position Location and Navigation Symposium (PLANS), December, pp.310-317.

Geiger, A., 1987, Einfluss richtungsabhängiger Fehler bei Satellitenmessungen, Bericht Nr. 130, Institut für Geodäsie und Photogrammetrie, Eidgenössische Technische Hochschule Zurich.

Geiger, A., 1988a, Einfluss und Bestimmung der Variabilität des Phasenzentrums von GPS-Antennen, Mitteilung Nr.43, Institut für Geodäsie und Photogrammetrie, Eidgenössische Technische Hochschule Zurich.

Geiger, A., 1988b, Modelling of Phase Center Variation and its Influence on GPS-Positioning,in Groten, E. and Strauss, R., (Eds), 1988, Proceedings of the International GPS Workshop, Darmstadt, April 10-13, pp.210-222.

Georgiadou, Y. and Kleusberg, A., 1987, Ionospheric Refraction and Multipath Effects in GPS Carrier Phase Observations, IUGG XIX General Assembly, Vancouver, Aug. 9-22, Symposium U3, Impact of GPS on Geophysics, 20 pp.

Georgiadou, Y. and Kleusberg, A., 1988, On Carrier Signal Multipath Effects in Relative GPS Positioning, Manuscripta Geodaetica, Vol. 13, pp. 172-179.

Glazer, B.G., 1980, GPS Receiver Operation, Global Positioning System papers published in Navigation, Vol.1, Institute of Navigation, Washington D.C.

Goad, C.C. and Remondi, B.W., 1984, Initial Relative Positioning Results Using the Global Positioning System, Bulletin Géodésique, 58, pp.193-210.

Gottman, J.M., 1981, Time Series Analysis, A Comprehensive Introduction for Social Scientists, Cambridge University Press, Cambridge.

Greenspan, R.L., Ng A.Y., Przyjemski, J.M. and Veale, J.D., 1982, Accuracy of Relative Positioning by Interferometry with Reconstructed Carrier GPS: Experimental Results, Proceedings Third International Symposium for Doppler Positioning, Las Cruces, New Mexico, Feb. 8-12, pp.1177-1195.

Hagger, H.J., 1967, Choice of Wavelength for EDM, Technical System Parameters and Atmospheric Conditions, Paper presented at the XIVth General Assembly of the IUGG, Lucerne.

Hatch, R.R., 1986, Dynamic Differential GPS at the Centimeter Level, [B], pp.1287-1298.

Hemesath, N.B., 1980, Performance Enhancement of GPS User Equipment, Global Positioning System papers published in Navigation, Vol.1, Institute of Navigation, Washington D.C.

Johannessen, R., 1988, The Role of Adaptive Antenna Systems when used with GPS, Proceedings of the Satellite Division Technical Meeting, Institute of Navigation, Colorado, September.

Kanasewich, E.R., 1975, Time Sequence Analysis in Geophysics, University of Alberta, 2ed., Edmonton.

Kip, A.F., 1962, Fundamentals of Electricity and Magnetism, McGraw-Hill Book Company, New York.

King, R.W., Masters, E.G., Rizos, C., Stolz, A. and Collins, J., 1987, Surveying with GPS, Ferd. Dümmlers Verlag, Bonn.

Kleusberg, A., 1986, Ionospheric Propagation Effects in Geodetic Relative GPS Positioning, Manuscripta Geodaetica 11, pp.256-261.

Kleusberg, A., Quek, S.H., Wells, D.E., Lachapelle, G. and Hagglund, J., 1986, GPS Relative Positioning Techniques for Moving Platforms, [B], pp.1299-1310.

Kleusberg, A., 1990, personal correspondence.

Kruczynski, L.R., 1980, Aircraft Navigation with the Limited Operational Phase of the NAVSTAR Global Positioning System, Global Positioning System papers published in Navigation, Vol.1, Institute of Navigation, Washington D.C.

Küpfer, H.P., 1968, Bodenreflexionen und Messtechnik bei der Mikrowellen-Distanzmessung, Schweizerische Zeitschrift fur Vermessung, Photogrammetrie und Kulturtechnik, Vol. 66, No.10, pp.329-348.

Küpfer, H.P. and Hossmann, M., 1971, Die Konzeption des neuen Mikrowellendistanzmessers Distomat DI60, Ein Beitrag zur Lösung des Reflexionsproblems, Allgemeine Vermessungs-Nachrichten, Vol.78, Heft 2, pp.50-64.

Lachapelle,G., Hagglund, J., Falkenberg, W., Bellemare, P., Casey, M. and Eaton, M., 1986, GPS Land Kinematic Positioning Experiments, [B], pp.1327-1344.

Lachapelle, G. and Cannon, E., 1986, Single and Dual Frequency GPS Results for Baselines of 10 to 500 km, Canadian Surveyor, Vol.40, No.2, pp.173-183.

Lachapelle, G., Casey, M., Eaton, M., Kleusberg, A., Tranquilla, J. and Wells, D., 1987, GPS Marine Positioning Accuracy and Reliability, Canadian Surveyor, Vol.41., pp.143-172.

Langley, R.B., Parrot, D., Santerre, R., Vanicek, P. and Wells, D.E., 1986, The Spring 1985 GPS High-Precision Baseline Test: Preliminary Analyses with DIPOP, [B], pp.1073-1088.

Lawrence, R.S., Little, C.G.and Chivers, H.J.A., 1963, A Survey of Ionospheric Effects Upon Earth-Space Radio Propagation, Proc. IEEE, Jan., pp.4-27.

Leick, A., 1989, GPS Evolving, ACSM Bulletin, June, pp.16-22.

Leitinger, R. and Putz, E., 1988, Ionospheric Refraction Errors and Observables, in Brunner, F.K. (ed.), 1988, Atmospheric Effects on Geodetic Space Measurements, Monograph 12, School of Surveying, University of New South Wales, pp.81-102.

Lintz, J.Jr. and Simonett, D.S., 1976, Remote Sensing of Environment, Addison-Wesley Publishing Company, London.

Livingston, D.C., 1970, The Physics of Microwave Propagation, Prentice-Hall Inc., Englewood Cliffs, New Jersey, pp.19-58.

Martin, E.H., 1980, GPS User Equipment Error Models, Global Positioning System papers published in Navigation, Vol.1, Institute of Navigation, Washington D.C.

Melbourne, W.G., 1985, The Case for Ranging in GPS Based Geodetic Systems, [A], pp.373-386.

Merry, C.L. and Rüther, H., 1986, Multipath Effects at Short Ranges, Survey Review, Vol.28, 219, pp.256-266.

Metcalf, J.E., 1986, Multipath Propagation, Febr., Del Norte Technology, Inc.

Meyerhoff, S.L. and Evans, A.G., 1986, Demonstration of the Combined Use of GPS Pseudorange and Doppler Measurements for Improved Dynamic Positioning, [B], pp.1397-1409.

Milliken, R.J. and Zoller, 1980, Principle of Operation of NAVSTAR and System Characteristics, Global Positioning System papers published in Navigation, Vol.1, Institute of Navigation, Washington D.C.

Müller, A., Campbell, J., Lohmar, F.J., 1989, Analysis of Multipath Effects in GPS Data from European Fiducial Stations, Proceedings of the Fifth International Geodetic Symposium on Satellite Positioning, Las Cruces, New Mexico, pp.8-32-841.

Oppenheim, A.V., Willsky, A.S. with Young, I.T., 1983, Signals and Systems, Prentice-Hall Signal Processing Series, Prentice-Hall International, London.

Otnes, R.K. and Enochson, L., 1978, Applied Time Series Analysis, Vol. I, Basic Techniques, John Wiley and Sons, New York.

Poder, K. and Andersen, O.B., 1965, Microwave Reflection Problems, Paper presented at the Electromagnetic Distance Measurement Symposium Special Study Group, IAG, 6-11 Sept.

Remondi, B.W., 1984, Using the Global Positioning System (GPS) Phase Observable for Relative Geodesy: Modelling, Processing and Results, Ph.D. Dissertation, The University of Texas, Austin, Texas, May.

Remondi, B.W., 1985, Global Positioning System Carrier Phase: Description and Use, Bulletin Géodésique, 59, pp.361-377.

Rocken, C. and Meertens, M., 1989, GPS Antenna and Receiver Tests: Multipath Reduction and Mixed Receiver Baselines, Proceedings of the Fifth International Geodetic Symposium on Satellite Positioning, Las Cruces, New Mexico, pp.375-388.

Rikitake, T., Sato, R. and Hagiwara, Y., 1987, Applied Mathematics for Earth Scientists, Terra Scientific Publishing Company, Tokyo.

Rüeger, J.M., 1990, Electronic Distance Measurement, an Introduction, 3rd ed., Springer-Verlag, Berlin, 266 pp.

Santerre, R., Kleusberg, A. and Beutler, G., 1985, The DIPOP Software Documentation, Technical Memorandum TM-5, University of New Brunswick, Fredericton.

Santerre, R., Craymer, M.R., Kleusberg, A., Langley, R.B., Parrot, D., Quek, S.H., Vanicek, P., Wells, D.E. and Wilkins, F., 1987, Precise Relative GPS Positioning with DIPOP 2.0, Paper presented to IAG Section II Scientific Meetings: "Advanced Space Technology", IUGG XIX General Assembly, Vancouver, Canada.

Schanda, E., 1986, Physical Fundamentals of Remote Sensing, Springer-Verlag, Berlin.

Shibuya, S., 1987, A Basic Atlas of Radio-Wave Propagation, John Wiley and Sons, New York.

Sims, M.L., 1985, Phase Centre Variation in the Geodetic TI4100 GPS Receiver System's Conical Spiral Antenna, [A], pp.227-244.

Sims, M.L., 1982, GPS Geodetic Receiver System, Proceedings of the Third Geodetic Symposium of Satellite Doppler Positioning, Las Cruces, New Mexico, pp.1103-1121.

Skolnik, M.I., 1980, Introduction to Radar Systems, 2nd. ed., McGraw-Hill International Book Company, London.

Spilker, J.J., 1980, Signal Structure and Performance Characteristics, Global Positioning System papers published in Navigation, Vol.1, Institute of Navigation, Washington D.C., pp.29-54.

Sukumar, S., Spoelstra, T.A.Th. and Kelder, H., 1987, Multipath Effects in UHF Angle-of-arrival Measurements, Journal of Atmospheric and Terrestrial Physics, Vol. 49, No. 1, pp.99-103.

Talbot, N.C., 1987, G.P.S. Signal Structure and Receiver Operation, Proceedings of the RMIT Centenary GPS Conference, Aug. 24-27, Dept. of Land Information, Royal Melbourne Institute of Technology, Melbourne.

Thornton, C.L., Young, L.E., Wu, S.C. and Thomas, J.B., 1984, GPS-Based Certification for the Microwave Landing System, IEEE Position Location and Navigation Symposium (PLANS), pp.256-263.

Tranquilla, J.M., 1986, Multipath and Imaging Problems in GPS Receiver Antennas, [B], pp.557-571.

Tranquilla, J.M. and Best, S.R., 1986, Phase Centre Considerations for the Monopole Antenna, IEEE Transactions on Antennas and Propagation, Vol. AP-34, No.5, May, pp.741-744.

Tranquilla, J.M. and Colpitts, B.G., 1988, GPS Antenna Design Characteristics for High Precision Applications, ASCE Specialty Conference GPS 88, Nashville, TN, May, 23 pp.

Tranquilla, J.M., Colpitts, B.G. and Carr, J.P., 1989, Measurement of Low-Multipath Antennas for TOPEX, Proceedings of the Fifth International Geodetic Symposium on Satellite Positioning, Las Cruces, New Mexico, pp.356-361.

Tranquilla, J.M. and Colpitts, B.G., 1989, Development of a Class of Antennas for Space Based NAVSTAR GPS Applications, Proceedings Antennas and Propagation, IEEE 1989, pp.65-69.

Vanicek, P., Beutler, G., Kleusberg, A., Langley, R.B., Santerre, R. and Wells, D.E., 1985, DIPOP: Differential Positioning Program Package for the Global Positioning System, Contract Report 85-005, Geodetic Survey of Canada.

Vanicek, P. and Krakiwsky, E., 1986, Geodesy, The Concepts, Second Edition, Elsevier Science Publishing Company, New York.

Ward, P., 1982, An Advanced NAVSTAR GPS Geodetic Receiver, Proceedings of the International Symposium on Satellite Positioning, Las Cruces, New Mexico, pp.1123-1140.

Wassef, A.M. and Kelly, K.M., 1989, Enhancing the Usefulness of GPS Two-Frequency Data for Estimating the Ionospheric Correction, Technical Meeting Preceedings (2nd), Institute of Navigation (ION), Colorado Springs, 1988.

Wells, D.E., Vanicek, P. and Pagiatakis, S., 1985, Least Squares Spectral Analysis Revisited, Technical Report No.84, University of New Brunswick, Fredericton.

Wells, D., 1986, Guide to GPS Positioning, Canadian GPS Associates, University of New Brunswick, Fredericton.

Yaskovich, S.A., 1964, Tellurometer Ground Swing on Geodetic Lines, Canadian Surveyor, Vol.18, No.1, pp.54-66.

Young, L.E., Neilan, R.E. and Bletzacker, F.R., 1985, GPS Satellite Multipath: An Experimental Investigation, [A], pp.423-430.

Yunck, T., 1987, Talk given on suggested antenna configuration, in Draft Minutes from the GPS Antenna Workshop, held at JPL, March 26, 1987.

APPENDIX A. MATHEMATICAL TOOLS AND SOME DEFINITIONS

A.1 Time Series

Data sets are normally not a continuous record of a changing variable, but a record of representative samples given at discrete points in time. The data thus looks like the result of a multiplication of a Dirac comb with the continuous function that is under observation: the Dirac comb periodically multiplies discrete points along the continuous function with 1 and all other points with zero (Fig. A.1). It is the resulting series of numerical values that is called a time series (Rikitake et al, 1987, p.56). A Dirac comb is a train of periodic impulses, in other words a train of Dirac delta functions, where a Dirac delta function is a function that is zero everywhere except in one point.

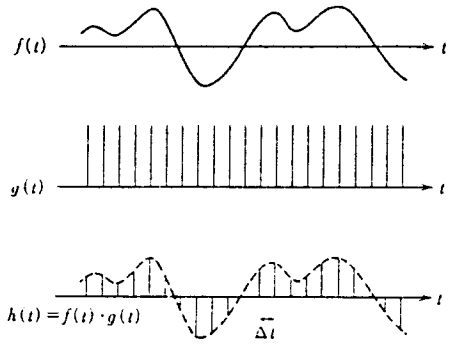

Figure A.1 A time series (after Rikitake et al, 1987).

A.2 Autocorrelation Function

An autocorrelation function is a function which illustrates how the value of the data at one time is correlated with the data at another time (Fig. A.2). The product is determined of two values of the one data set, separated by a lag τ. An estimate of the autocorrelation at a lag τ is obtained by a summation of these products over all the data and by det-

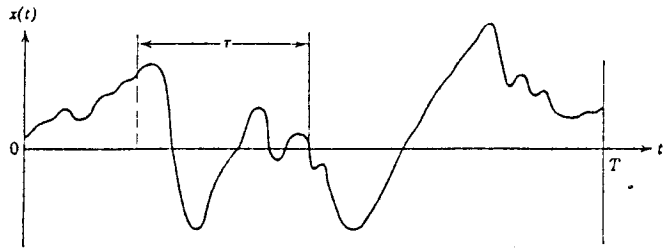

Figure A.2 The autocorrelation function (after Bendat and Piersol, 1971).

ermining an average. This is repeated for a number of different lags. When T, the observation duration, approaches infinity the exact autocorrelation function is obtained. This function (Bendat and Piersol, 1971, pp.18-22) is represented by the equation:

$$R_x(\tau) = \lim_{T\to\infty} \frac{1}{T}\int_0^T x(t)\,x(t+\tau)\,dt \qquad \textbf{(A.1)}$$

where τ is the lag and x(t) is the function in question. The value T can actually be seen as representing the number of observations. The function is symmetrical: for negative lags the same result is obtained as for positive lags and a maximum occurs at a lag of zero. The autocorrelation function is a tool for the detection of deterministic data in a background of random data and is an expression in the time domain. The Fourier Transform (see A.4) of the autocorrelation function leads to the power spectral density function, which is an expression in the frequency domain.

A.3 Cross-Correlation Function

When two sets of random data are compared (for example sets observed on two consecutive days) a function can be derived which shows how the values of the one set depend upon the values of the other set. The value of a function at the time t is multiplied with the value of the other function at the time $t+\tau$. This is carried out for every value of the time series and the average product is determined. The whole

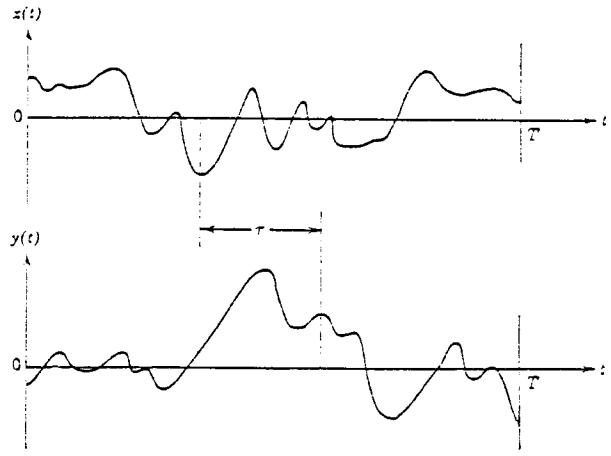

Figure A.3 The cross-correlation function (after Bendat and Piersol, 1971).

sequence of calculations and averaging is repeated for the next value of the lag τ and so on, until the whole sequence of lags has been used (Fig. A.3). When the observation duration T (in fact the amount of sampling intervals) approaches infinity the average of the products approaches the exact cross-correlation function. This function (Bendat and Piersol, 1971, pp.28-31) is represented in the following equation:

$$R_{xy}(\tau) = \lim_{T\to\infty} \frac{1}{T}\int_0^T x(t)\,y(t+\tau)\,dt \qquad \textbf{(A.2)}$$

where τ is the lag and x(t) and y(t) are the two functions. For example the GPS signal, after 23 hours and 56 minutes, encounters the same geometry relative to the reflective surfaces in the antenna's vicinity. Thus one can expect a peak in the cross-correlation function of two consecutive days of observations at the same site at this lag of one day minus 240 seconds. The cross-correlation plots displayed in Chapters 10 and 11 show the cross-correlation coefficient (on a scale from zero to one) as a function of the lag number, which is the number of sampling intervals in the lag. As the sampling interval is 30 seconds in the compacted data used, the eighth lag will be a lag of 240 seconds. This is the difference between a sidereal and a mean solar day.

A.4 Spectral Density and Periodogram

A variation in a time series can be caused by a variation at several different frequencies. This can be represented by a sum of sine and cosine functions. It is known (e.g. Rüeger, 1990, p.213) that a sine wave with phase parameters ϕ and ωt and an amplitude **c** can be represented by the following function:

$$c \sin(\omega t+\phi) \tag{A.3}$$

for which is valid:

$$\begin{aligned} c \sin(\omega t+\phi) &= c(\cos\omega t \sin\phi + \sin\omega t \cos\phi) \\ &= a\cos\omega t + b\sin\omega t \end{aligned} \tag{A.4}$$

$$a = c \sin\phi \tag{A.5}$$

$$b = c \cos\phi \tag{A.6}$$

$$c = \sqrt{a^2 + b^2} \tag{A.7}$$

A sum of sine and cosine functions can be generalised as:

$$\begin{aligned} x_t &= \Sigma\ c \sin(\omega t + \phi) \\ &= \Sigma (a \cos\omega t + b \sin\omega t) \end{aligned} \tag{A.8}$$

Estimates $\bar{\mathbf{a}}$ and $\bar{\mathbf{b}}$ of **a** and **b** are obtained from the actual time series. The constituent frequencies that can be thought to build up the signal is approximated by a grid of frequencies or harmonics, called the **overtone series**. The frequencies of the overtone series are determined as $\mathbf{f} = \mathbf{j/N}$, where $\mathbf{j} = 1,2,.....(\mathbf{N}-1)/2$ and where **N** is the total number of sampling intervals. The **j**-th Fourier frequency refers to a sinusoid which completes **j** cycles during the total data length of **N** sampling intervals. This means one is looking for harmonics with periods of **N**, **N**/2, **N**/3, ... **N**/{(**N**-1)/2}. This grid is sometimes not fine enough to capture all the frequencies present in the data. In such cases it is said that a frequency is trapped in the grid. For each value of $\mathbf{f}_j = \omega_j/(2\pi)$ least square estimates are made of

a_j and b_j in the equation:

$$x_t = \Sigma\ (a_j \cos\omega_j t + b_j \sin\omega_j t) + e_t \qquad \textbf{(A.9)}$$

where e_t is noise. It is well known that the estimates for **a** and **b** for equally spaced data over one or more periods compute as (e.g. Gottman, 1981, p.204; Rüeger, 1990, p.215):

$$\overline{a_j} = \frac{2}{N} \sum_{t=0}^{N-1} x_t \cos\omega t \qquad \textbf{(A.10)}$$

$$\overline{b_j} = \frac{2}{N} \sum_{t=0}^{N-1} x_t \sin\omega t \qquad \textbf{(A.11)}$$

These estimates happen to be the sample autocorrelations. If the sum of squares of the periodic part of equation (A.9) is taken, a quantity is obtained which is called the total energy of the series at frequency **f** (Gottman, 1981, p.205):

$$4\pi I(f) = \sum_{t=0}^{N-1} (\bar{a}\cos 2\pi f t + \bar{b}\sin 2\pi f t)^2 \qquad \textbf{(A.12)}$$

which sums the squares of the data values around the mean value zero. The **periodogram** is defined by dividing this value by 4π and gives the total energy **I(f)** of the series at each frequency **f**. The term **power** is used to denote the average energy contributed by each observation. The power is obtained by dividing the total energy by the width of the frequency interval at that Fourier frequency (Otnes and Enochsen, 1978, p.316). In contrast to the power spectral density function, which gives the average energy of the series, the periodogram gives the total energy of the series at particular frequencies (Gottman, 1981, p.226). The periodogram is a function of the frequencies, which are used to decompose the energy of the series. The periodogram plots the amplitude of the j-th harmonic against the relevant frequency (Chatfield, 1984, p.135) and will have a peak whose height increases with increasing sample size, if there is a deterministic frequency present (Gottman, 1981, p.87). The function x_t can be composed of many frequencies. The latter are estimated by the grid of the overtone series which are consecutive integer

fractions of the total observation duration. A set of estimates for **a** and **b** are obtained for each frequency f_j of the overtone series. It can be shown that the total variance at this frequency becomes (Gottman, 1981, p.206):

$$I(f_j) = \frac{N}{4\pi}\left[\frac{(\overline{a_j})^2}{2} + \frac{(\overline{b_j})^2}{2}\right] \qquad \textbf{(A.13)}$$

Equation (A.13) indicates that the total variability accounted for by each frequency is proportional to the square of the amplitude at that frequency. The periodogram can be represented in complex notation as:

$$I(f) = \frac{1}{2\pi N}\left|\sum_{t=0}^{N-1} x_t e^{-i2\pi ft}\right|^2 \qquad \textbf{(A.14)}$$

and can be shown to be equal to:

$$I(f) = \frac{1}{2\pi}\left[c_o + 2\sum_{k=0}^{N-1} c_k \cos k(2\pi f)\right] \qquad \textbf{(A.15)}$$

where $c_o, \ldots c_k, \ldots . c_{N-1}$ are the autocorrelation estimates. The equivalence of Equations (A.14) and (A.15) is called the Wiener-Khintchine theorem (Gottman, 1981, p.208). This equation transforms the autocorrelation function into the **power spectrum** and is called the **Fourier transform**. Each periodogram ordinate can be written as a series with the same cosine values appearing in each one. When the cosines are gathered in a matrix, it becomes evident that the matrix is symmetrical. The cosine is periodic and reappears in each series. If the number of observations can be factorized in powers of 2, economies are possible. The combination of all possible computational savings leads to a shortened calculation of the Fourier transform, called the **Fast Fourier Transform** (FFT) (Gottman, 1981, p.210).

The power spectral density function is theoretically obtained by an integration of the autocorrelations between $-\infty$ and $+\infty$. To obtain a power density estimate for a limited window from lag $-\tau$ to lag $+\tau$, it is necessary to integrate a convoluted function: the autocorrelation function convoluted with a

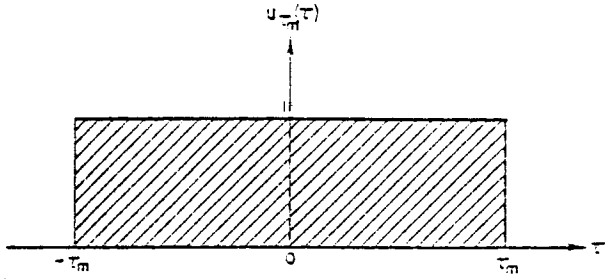

Figure A.4 Boxcar function (after Bendat and Piersol,1971).

square window. The square window is defined as a **boxcar** function (Fig. A.4). The Fourier transform of this boxcar is called a window function and shows "leakage" in the form of side lobes (Fig. A.5), because the data is in fact a truncated infinite series. There are ways of coping with leakage (Bendat and Piersol, 1971, p.316), for example by tapering the data set. This leads to a lower weight for the data at the start and finish of the series. Unfortunately this has been shown to reduce the sharpness of the peaks in the power spectral density function by making them flatter and more spread out (Bloomfield, 1976). As this makes it harder to isolate the closely spaced dual peaks in this analysis of multipath, no attempt was made to taper the data.

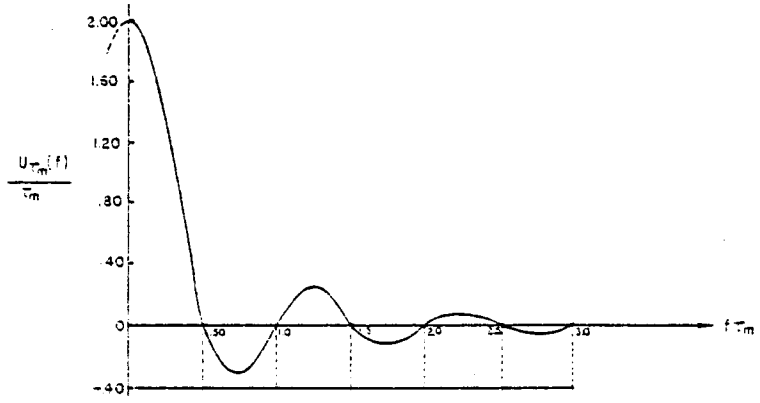

Figure A.5 Window function and its side lobes (after Bendat and Piersol, 1971).

APPENDIX B. IONOSPHERE-FREE OBSERVABLE

According to Lawrence (1964, p.5) the change in phase path length due to the effect of the ionosphere is:

$$\Delta l = \int (n-1)\, dl \qquad \textbf{(B.1)}$$

where **n** is the refractive index of the ionosphere. The phase pathlength is defined as:

$$L = \int n dl \qquad \textbf{(B.2)}$$

and is integrated along the phase path. The refractive index for the ionosphere is derived from the Appleton-Hartree equation for the refractive index in a **plasma** (an electrified gas). Brunner and Gu (1989) expand the Appleton-Hartree equation into a series for **n**, assuming no collision terms. By estimating the size of the terms, they show that only the following three terms are significant for the GPS:

$$n-1 = -\frac{X}{2} - \frac{X^2}{8} \pm \frac{XY}{2}\cos\theta \qquad \textbf{(B.3)}$$

where:

$$X = \frac{\omega_p^2}{\omega^2} \qquad \textbf{(B.4)}$$

$$Y = \frac{\omega_H}{\omega} \qquad \textbf{(B.5)}$$

and where ω_p is the angular plasma frequency, ω_H is the angular gyro frequency of an electron and θ is the angle between the wave normal and the geomagnetic field. The plus/minus sign is the result of a polarisation constant with

value 1 and a sign depending upon the left or right handed sense of circular polarisation. The three significant terms in Eq.(B.3) are a second, third and fourth order term. The second order term has traditionally been applied as an ionospheric correction. The third order term (often called the magnetic term) and the fourth order term (a beam curvature term and a refractive index expansion term) are often neglected. Rough estimates of these terms have been given by Hartmann and Leitinger (1984). Using Eq.(B.1) the equation traditionally used for the ionospheric correction becomes:

$$\Delta l = \int (-\frac{X}{2})\, dl = \int (-\frac{\omega_p^2}{2\omega^2})\, dl$$
$$= -\frac{e^2}{2\epsilon_o m\omega^2}\int N dl = -\frac{40.3\ N^{(TEC)}}{f^2} \qquad \text{(B.6)}$$

where:

$$\omega_p^2 = \frac{Ne^2}{\epsilon_0 m\omega^2} \qquad \text{(B.7)}$$

and **N** is the electron density per cubic metre,

$\mathbf{N^{(TEC)}}$ is the total electron content per square metre (the integrated electron density),

m is the mass of an electron: 9.11×10^{-31} kg (Kip, 1967),

e is the charge of an electron: 1.6×10^{-19} C (Coulomb) or As (Ampere seconds) (Kip, 1967),

ϵ_0 is the electric permittivity of space, which is: 8.85×10^{-12} C^2/Nm^2 (Coulombs squared per Newton metre per metre) or As/Vm (Ampere seconds per Volt metre) (Kip, 1967),

ω is the angular operational frequency ($= 2\pi f$).

When using a dual frequency receiver, the ionospheric correction can be calculated by observing the phase difference between the signals at the separate frequencies and determining the total electron content along the ray path. A popular way of applying the correction has been the use of a linear combination of the phase observables which corrects proportional to the square of the operational

frequencies. This has been called the ionosphere-free observable. Derivations may be found in King et al (1987, p.83), for example. The observable used by King et al (1987) and in Bock (1986) is the following:

$$\phi_{LC} = \phi_1 - \frac{f_1 f_2}{f_1^2 - f_2^2}\left(\phi_2 - \frac{f_2}{f_1}\phi_1\right) \qquad \textbf{(B.8)}$$

and can be shown to be equivalent to:

$$\phi_{LC} = \frac{f_1}{f_1^2 - f_2^2}(f_1\phi_1 - f_2\phi_2) \qquad \textbf{(B.9)}$$

The observable ϕ_{LC} is obtained in phase units. The linear combination used by Blewitt (1989) can be shown to be equivalent to the one used by Kleusberg (1986) but different from Eq.(B.9):

$$\Phi_{LC} = \frac{c}{f_2^2 - f_1^2}(f_1\phi_1 - f_2\phi_2) \qquad \textbf{(B.10)}$$

Eq.(B.10) can be obtained from Eq.(B.9) by multiplication with the wavelength λ_1 and change of sign. The resulting units of the observable Φ_{LC} are metres, in this case. This equation can also be written as a correction to the L1 carrier phase pathlength, analogous to Eq.(B.8) using the notation $\#\Phi$ for the across-frequency carrier phase pathlength difference:

$$\Phi_{LC} = \lambda_1\phi_1 - \frac{\#\Phi}{(\lambda_2/\lambda_1)^2 - 1} \qquad \textbf{(B.11)}$$

The problem with the above approach is that the phase observations are not corrected for multipath before computing the ionosphere-free linear combination. A phase change of 0.1 metres in the phase path length difference through a combination of reflections will erroneously be interpreted as a change in total electron content (TEC) of 1 unit of 10^{16} electrons per m^2. This could be the same size as the total variability of the ionosphere in the same time span, especially at night and more so during years of low solar

caused by ionospheric dispersion, an over-correction of 50 % results. This means the ionospheric correction through the ionosphere-free linear combination is inappropriate when carrying out a multipath analysis, because it destroys the multipath signature by interpreting and correcting it as ionospheric dispersion. This also means in general that the ionosphere-free linear combination should only be applied when the effect of the ionosphere is known to be much greater than the multipath effect. In general the following guidelines should be followed with respect to the use of the ionosphere-free linear combination:

1.) When the baseline is a few tens of kilometres long differencing across sites will be sufficient to reduce the ionospheric effect, while the use of the ionosphere-free observable is likely to degrade the result;

2.) When the ionosphere is calm it is possibly more accurate to use an ionospheric model, than to apply the ionosphere-free linear combination;

3.) It is suggested not to use the ionosphere-free observable when the noise on the signal is below "multipath level" of, say, 50 mm for carrier phase and 7 metres for pseudorange, because the ionospheric effect is then not greater than the possible multipath effect and cannot be removed as easily as before.

The general pre-processor PREGE of the programme DIPOP 2.0 forms a scaled ionospheric correction (Kleusberg, 1990) to the L1 carrier phase pathlength which is tested for discontinuities. (These are the one way phase observations or the one receiver to one satellite phase observations.) The scale factor chosen is such that the size of a possible discontinuity in the resulting time series of the correction is exactly the cycle slip in the L2 carrier phase. This scaled correction is formed by multiplying the correction to the L1 carrier phase pathlength in Eq.(B.11) by a scale factor which is:

$$\frac{\lambda_1 + \lambda_2}{\lambda_1^2} \qquad \text{(B.12)}$$

The result of this is the following time series when no cycle slip occurs:

$$(\Phi_{LC} - \phi_1\lambda_1)\frac{\lambda_1 + \lambda_2}{\lambda_1^2} = \frac{\#\Phi}{\lambda_2 - \lambda_1} \qquad \textbf{(B.13)}$$

When a cycle slip $\mathbf{N_2}$ occurs in the L2 carrier phase the time series of Eq.(B.13) will result in:

$$(\Phi_{LC} - \phi_1\lambda_1)\frac{\lambda_1 + \lambda_2}{\lambda_1^2} = \frac{\#\Phi}{\lambda_2 - \lambda_1} + N_2 \qquad \textbf{(B.14)}$$

A line fit to this time series allows $\mathbf{N_2}$ to be determined and as $\mathbf{N_2}$-$\mathbf{N_1}$ can be determined by finding discontinuities in the widelane time series, $\mathbf{N_1}$ can be determined as the difference between the two.

APPENDIX C. DIPOP (Version 2.0) PREPROCESSOR OUTLINE

In one five hour session of GPS observations with the dual frequency Texas Instruments single channel four satellite multiplex receiver TI 4100, 100000 observations can be expected per receiver. The data consist of P-code transit times in seconds and carrier phases in cycles on both L1 and L2 using the standard three second epochs. When two stations are involved and the observations are repeated on a second day for a multipath study, the amount of information is phenomenal: the equivalent of a total of over 2000 A4 pages of data are collected. This amount of information (about 14 megabytes) has to be validated, checked for outliers and cycle slips and it has to be compacted. A preprocessor with the following features was thus required:

1) reduction of the amount of data to manageable proportions,
2) validation of the large amount of data and detection of discontinuities.

The Land Information Centre in Bathurst (Department of Lands, New South Wales, Australia) had previously acquired the University of New Brunswick DIPOP (Version 2.0) software package (incl. source code), from Canada. This GPS processing software (Santerre et al, 1987; Vanicek et al, 1985) uses dedicated preprocessors, which means that different preprocessors are employed for different receivers (including one for the TI 4100). Following the dedicated preprocessors, the software has a common main and postprocessor. The main processor carries out a sequential adjustment. The postprocessor outputs a variety of desired options. The preprocessor consists of the equivalent of 92 A4 pages (about 6000 lines) of source code of which one third was useful for the data preparation in this multipath investigation. The suite of subroutines called PREGE was used, which is the "general preprocessor": it delivers an "intermediate, quasi-cleaned" file. It samples the raw one-way phase data (1 receiver to 1

satellite) at a nominated interval omitting the remainder, validates it, eliminates obvious data errors, corrects cycle slips detected in the one-way measurements and creates data files containing the sampled and cleaned raw data. A secondary cycle slip detection process, which is normally left to the single difference and double difference processors, was not used in this multipath investigation. When the removal of troublesome observations is completed, the preprocessor returns the remaining raw observations. After the 3-second data have been sampled at 30-second intervals (ignoring 9 out of 10 data values) the reduced files still total about 0.8 megabytes.

The subroutines in this preprocessor PREGE are (apart from subsidiary timing routines and data initialisation routines):
1) Input/Output and data management routines: DAREAD, DAFILL, DAWRIT and SUMPRE.
2) The data cleaning routines are:
ELMNT which eliminates bad observations;
DTECT2 which detects cycle slips (it forms the dispersive delay observable, does line fits to it and forms the wide lane observable);
DETCS which determines cycle slip integer values;
RPCS4 which is a subroutine for the correction of all detected cycle slips.
3) Some additional utilities are:
FIT which computes the average and standard deviation of a sample;
TPOL which computes Chebichev polynomials;
ESPIN which inverts symmetric positive-definite matrices;
DOPRO which computes the dot product;
APPRX2 which approximates the data by polynomial fits.

The cycle slip detector checks the data continuity using the dispersive delay $\#\Phi = \lambda_2\phi_2 - \lambda_1\phi_1$ and the wide lane observable $\#^w\phi = \phi_2 - \phi_1$ to which line fits are applied. The preprocessor calculates the dispersive delay and analyses the across epoch changes in dispersive delay. Each time 5 consecutive (now 30 second) data elements are analysed by forming 4 consecutive

epochs of differences of the dispersive delay. These are line fitted after which the process is shifted to the next data element and repeated. It checks the residuals about the fitted line against a standard deviation of 2 mm in order to detect discontinuities. This process is repeated with the widelane (Refer to Eq.(7.12)) observable and with a linear combination of the L1 and L2 carrier phase observation (Refer to Eqns.(B.12) and (B.13)). The first of the above polynomial fits determines the difference between the L1 and L2 cycle slips. The second one determines the cycle slips in the L2 carrier phase. In Appendix B it is shown that the DIPOP software is using a scaled ionospheric correction for the testing of discontinuities. The linear combination used in the cycle slip detecting subroutine, although not being proportional to the inverse squares of the frequencies, allows an elegant way of determining cycle slips. The difference between the affected (Eq.(B.14)) and unaffected (Eq.(B.13)) time series is exactly the cycle slip in the L2 carrier phase.

As the original data were in Nortech binary format, a few steps were needed to prepare the data for the preprocessor. The recorded data consists of time tagged code measurements, carrier phase measurements, carrier phase rate measurements, satellite positions, satellite velocities and satellite navigation messages (Wells, 1986). The UNSW utility NTRANGE accesses the Nortech binary information and extracts the necessary data in the form of pseudoranges, carrier phases and time tags. A smaller binary file results which can then be read and reformatted in a way acceptable to the DIPOP preprocessor by another UNSW utility DATCARD. This last utility had to be altered by the current author in order to be compatible with one of the DIPOP data entry formats. The University of New Brunswick's "short format" was the most compatible one and DATCARD was altered accordingly.

After the preprocessing with the above described suite of subroutines PREGE from the general preprocessor of the GPS reduction programme DIPOP (Version 2.0) the data were

manipulated in various ways through differencing: across frequencies, across sites, across epochs and across days. Appropriate differencing software was written as described in Chapter 9. This generated many more 0.8 Mb files in preparations for various studies of the data.

Publications from

THE SCHOOL OF SURVEYING, THE UNIVERSITY OF NEW SOUTH WALES.

All prices include postage by surface mail. Air mail rates on application. (Effective Nov. 1990)

To order, write to Publications Officer, School of Surveying, The University of New South Wales, P.O. Box 1, Kensington N.S.W., 2033 AUSTRALIA

NOTE: ALL ORDERS MUST BE PREPAID

UNISURV REPORTS - G SERIES

Price (including postage): $6.00

G14. A. Stolz, "The computation of three dimensional Cartesian coordinates of terrestrial networks by the use of local astronomic vector systems", Unisurv Rep. 18, 47 pp, 1970.

G16. R.S. Mather et al, "Communications from Australia to Section V, International Association of Geodesy, XV General Assembly, International Union of Geodesy and Geophysics, Moscow 1971", Unisurv Rep. 22, 72 pp, 1971.

G17. Papers by R.S. Mather, H.L. Mitchell & A. Stolz on the following topics:- Four-dimensional geodesy, Network adjustment and Sea surface topography, Unisurv G17, 73 pp, 1972.

G18. Papers by L. Berlin, G.J.F. Holden, P.V. Angus-Leppan, H.L. Mitchell & A.H. Campbell on the following topics:- Photogrammetry co-ordinate systems for surveying integration, Geopotential networks and Linear measurement, Unisurv G18, 80 pp, 1972.

G19. R.S. Mather, P.V. Angus-Leppan, A. Stolz & I. Lloyd, "Aspects of four-dimensional geodesy", Unisurv G19, 100 pp, 1973.

G20. Papers by J.S. Allman, R.C. Lister, J.C. Trinder & R.S. Mather on the following topics:- Network adjustments, Photogrammetry, and 4-Dimensional geodesy, Unisurv G20, 133 pp, 1974.

G21. Papers by E. Grafarend, R.S. Mather & P.V. Angus-Leppan on the following topics:- Mathematical geodesy, Coastal geodesy and Refraction, Unisurv G21, 100 pp, 1974.

G22. Papers by R.S. Mather, J.R. Gilliland, F.K. Brunner, J.C. Trinder, K. Bretreger & G. Halsey on the following topics:- Gravity, Levelling, Refraction, ERTS imagery, Tidal effects on satellite orbits and Photogrammetry, Unisurv G22, 96 pp, 1975.

G23. Papers by R.S. Mather, E.G. Anderson, C. Rizos, K. Bretreger, K. Leppert, B.V. Hamon & P.V. Angus-Leppan on the following topics:- Earth tides, Sea surface topography, Atmospheric effects in physical geodesy, Mean sea level and Systematic errors in levelling, Unisurv G23, 96 pp, 1975.

G24. Papers by R.C. Patterson, R.S. Mather, R. Coleman, O.L. Colombo, J.C. Trinder, S.U. Nasca, T.L. Duyet & K. Bretreger on the following topics:- Adjustment theory, Sea surface topography determinations, Applications of LANDSAT imagery, Ocean loading of Earth tides, Physical geodesy, Photogrammetry and Oceanographic applications of satellites, Unisurv G24, 151 pp, 1976.

G25. Papers by S.M. Nakiboglu, B. Ducarme, P. Melchior, R.S. Mather, B.C. Barlow, C. Rizos, B. Hirsch, K. Bretreger, F.K. Brunner & P.V. Angus-Leppan on the following topics:- Hydrostatic equilibrium figures of the Earth, Earth tides, Gravity anomaly data banks for Australia, Recovery of tidal signals from satellite altimetry, Meteorological parameters for modelling terrestrial refraction and Crustal motion studies in Australia, Unisurv G25, 124 pp, 1976.

G26. Papers by R.S. Mather, E.G. Masters, R. Coleman, C. Rizos, B. Hirsch, C.S. Fraser, F.K. Brunner, P.V. Angus-Leppan, A.J. McCarthy & C. Wardrop on the following topics:- Four-dimensional geodesy, GEOS-3 altimetry data analysis, analysis of meteorological measurements for microwave EDM and Meteorological data logging system for geodetic refraction research, Unisurv G26, 113 pp, 1977.

G27. Papers by F.K. Brunner, C.S. Fraser, S.U. Nasca, J.C. Trinder, L. Berlin, R.S. Mather, O.L. Colombo & P.V. Angus-Leppan on the following topics:- Micrometeorology in geodetic refraction, LANDSAT imagery in topographic mapping, adjustment of large systems, GEOS-3 data analysis, Kernel functions and EDM reductions over sea, Unisurv G27, 101 pp, 1977.

G29. Papers by F.L. Clarke, R.S. Mather, D.R. Larden & J.R. Gilliland on the following topics:- Three dimensional network adjustment incorporating ξ, η and N, Geoid determinations with satellite altimetry, Geodynamic information from secular gravity changes and Height and free-air anomaly correlation, Unisurv G29, 87 pp, 1978.

From June 1979 Unisurv G's name was changed to Australian Journal of Geodesy, Photogrammetry and Surveying. These can be ordered from The Managing Editor, Australian Journal of Geodesy, Photogrammetry and Surveying, Institution of Surveyors - Australia , Nos 27 - 29 Napier Close, Deakin, ACT 2600, AUSTRALIA.

UNISURV REPORTS - S SERIES

S8 - S20	Price (including postage):		$10.00
S27 onwards	Price (including postage):	Individuals	$20.00
		Institutions	$28.00

S8 A. Stolz, "Three-D Cartesian co-ordinates of part of the Australian geodetic network by the use of local astronomic vector systems", Unisurv Rep. S 8, 182 pp, 1972.

S9 H.L. Mitchell, "Relations between MSL & geodetic levelling in Australia", Unisurv Rep. S 9, 264 pp, 1973.

S10 A.J. Robinson, "Study of zero error & ground swing of the model MRA101 tellurometer", Unisurv Rep. S 10, 200 pp, 1973.

S12. G.J.F. Holden, "An evaluation of orthophotography in an integrated mapping system", Unisurv Rep. S 12, 232 pp, 1974.

S14. Edward G. Anderson, "The Effect of Topography on Solutions of Stokes` Problem", Unisurv Rep. S 14, 252 pp, 1976.

S15. A.H.W. Kearsley, "The Computation of Deflections of the Vertical from Gravity Anomalies", Unisurv Rep. S 15, 181 pp, 1976.

S16. K. Bretreger, "Earth Tide Effects on Geodetic Observations", Unisurv S 16, 173 pp, 1978.

S17. C. Rizos, "The role of the gravity field in sea surface topography studies", Unisurv S 17, 299 pp, 1980.

S18. B.C. Forster, "Some measures of urban residual quality from LANDSAT multi-spectral data", Unisurv S 18, 223 pp, 1981.

S19. Richard Coleman, "A Geodetic Basis for recovering Ocean Dynamic Information from Satellite Altimetry", Unisurv S 19,332 pp, 1981.

S20. Douglas R. Larden, "Monitoring the Earth's Rotation by Lunar Laser Ranging", Unisurv Report S 20, 280 pp, 1982.

S27. Bruce R. Harvey, "The Combination of VLBI and Ground Data for Geodesy and Geophysics", Unisurv Report S27, 239 pp, 1985.

S29. Gary S. Chisholm, "Integration of GPS into hydrographic survey operations", Unisurv S29, 190 pp, 1987.

S30. Gary Alan Jeffress, "An investigation of Doppler satellite positioning multi-station software", Unisurv S30, 118 pp, 1987.

S31. Jahja Soetandi, "A model for a cadastral land information system for Indonesia", Unisurv S31, 168 pp, 1988.

S32. D. B. Grant, "Combination of terrestrial and GPS data for earth deformation studies" Unisurv S32, 285 pp, 1990.

S33. R. D. Holloway, "The integration of GPS heights into the Australian Height Datum", Unisurv S33, 151 pp.,1988.

S34. Robin C. Mullin, "Data update in a Land Information Network", Unisurv S34, 168 pp. 1988.

S35. Bertrand Merminod, "The use of Kalman filters in GPS Navigation", Unisurv S35, 203 pp., 1989.

S36. Andrew R. Marshall, "Network design and optimisation in close range Photogrammetry", Unisurv S36, 249 pp., 1989.

S37. Wattana Jaroondhampinij, "A model of Computerised parcel-based Land Information System for the Department of Lands, Thailand," Unisurv S37, 281 pp., 1989.

S38. C. Rizos (Ed.), D.B. Grant, A. Stolz, B. Merminod, C.C. Mazur "Contributions to GPS Studies", Unisurv S38, 204 pp., 1990.

S39. C. Bosloper, "Multipath and GPS short periodic components of the time variation of the differential dispersive delay", Unisurv S39, 214 pp., 1990.

S40. John Michael Nolan, "Development of a Navigational System utilizing the Global Positioning System in a real time, differential mode", Unisurv S40, 163 pp., 1990.

S41. Roderick T. Macleod, "The resolution of Mean Sea Level anomalies along the NSW coastline using the Global Positioning System", 278 pp., 1990.

PROCEEDINGS

Prices include postage by surface mail

P1. P.V. Angus-Leppan (Editor), "Proceedings of conference on refraction effects in geodesy & electronic distance measurement", 264 pp., 1968. Price: $10.00

P2. R.S. Mather & P.V. Angus-Leppan (Eds), "Australian Academy of Science/International Association of Geodesy Symposium on Earth`s Gravitational Field & Secular Variations in Position", 740 pp., 1973. Price $15.00

MONOGRAPHS

Prices include postage by surface mail

M1.	R.S. Mather, "The theory and geodetic use of some common projections", (2nd edition), 125 pp., 1978.	Price	$12.00
M2.	R.S. Mather, "The analysis of the earth's gravity field", 172 pp., 1971.	Price	$8.00
M3.	G.G. Bennett, "Tables for prediction of daylight stars", 24 pp.,1974.	Price	$5.00
M4.	G.G. Bennett, J.G. Freislich & M. Maughan, "Star prediction tables for the fixing of position", 200 pp., 1974.	Price	$8.00
M5.	M. Maughan, "Survey computations", 98 pp., 1975.	Price	$11.00
M7.	J.M. Rueger, "Introduction to Electronic Distance Measurement", (2nd Edition), 140 pp., 1988.	Price	$17.00
M8.	A.H.W. Kearsley, "Geodetic Surveying". 77pp., 1988.	Price	$11.00
M10.	W. Faig, "Aerial Triangulation and Digital Mapping", 102. pp., 1986.	Price	$16.00
M11.	W.F. Caspary, "Concepts of Network and Deformation Analysis", 183 pp., 1988.	Price	$25.00
M12.	F.K. Brunner, "Atmospheric Effects on Geodetic Space Measurements", 110 pp., 1988.	Price	$16.00
M13	Bruce R. Harvey, "Practical Least Squares and Statistics for Surveyors", 229 pp., 1990.	Price	$23.00